Quantification of nitrogen in subducting slabs and its recycling in the forearc and sub-arc regions

by

Kan Li

A thesis submitted in partial fulfillment of the requirements for the degree of

Doctor of Philosophy

Department of Earth and Atmospheric Sciences
University of Alberta

Abstract

Nitrogen, a life-essential element, is exchanged between Earth's surface and interior through subduction, which has been acting as a dominant driving force regulating the long-term evolution of Earth's major N reservoirs. However, the nitrogen input fluxes into global subduction zones and the recycling efficiency of subducted slab N inside subduction zones remain loosely constrained. In this thesis, I present six separate studies in two chapters to characterize the nitrogen in the poorly studied mafic-ultramafic components of subducting slab and the recycling of N in the forearc to sub-arc regions.

Chapter 2 is focused on the nitrogen characterization of the entire subducting slab, from top to bottom, including altered basalts, altered sheeted dikes and gabbroic rocks and oceanic serpentinites.

(1) In Chapter 2.1, from the large variation of nitrogen concentrations in global altered basalts (1.3 – 48.4 ppm), I found that the magnitude of nitrogen enrichment in the upper oceanic crust was primarily controlled by the nitrogen availability in the surrounding environment, which is ultimately related to the nitrogen abundance of basal sediments and/or seawater. With the consideration of this primary factor, we estimated a global nitrogen input flux of $3.7^{\pm 0.3} \times 10^{9}$ $\mathrm{mol \cdot yr^{-1}}$ for the 300 – 600 m upper oceanic crust.

(2) In Chapter 2.2, I examined nitrogen features in the sheeted dikes and gabbroic rocks, which were dominantly affected by moderate- to high-temperature hydrothermal alteration. The examined sheeted-dike and gabbroic samples from global ocean floor ubiquitously contain elevated nitrogen concentrations (2.7 – 33.5 ppm). Mixing modeling revealed that the secondary nitrogen was predominantly sourced from seawater with δ^{15}N values of −1‰ – +7‰. Based on the sheeted dike and gabbroic data, I estimated a global nitrogen input flux of $21.8^{+0.9}_{-1.3} - 30.6^{\pm 2.2} \times 10^9$ mol·yr^{-1} for the total oceanic crust.

(3) In Chapter 2.3, I examined oceanic serpentinites with variable serpentinization temperatures, from high temperatures (up to > 350 ºC) at depths to low temperatures (< 150 ºC) near seafloor. The results show that these serpentinites are also enriched in secondary nitrogen (3.2 – 18.6 ppm) predominantly sourced from seawater with δ^{15}N value of −1‰ – +6‰. Based on these data, the serpentinized sub-oceanic mantle is estimated to contribute 3.3×10^9 mol·yr^{-1} nitrogen to global subduction zones.

Chapter 3 is devoted to the characterization of nitrogen recycling inside subduction zones as the slab is subducted into the forearc to sub-arc regions.

(1) In Chapter 3.1, I investigated the nitrogen characteristics of serpentinites exhumed from the mantle wedge in the Izu-Bonin-Mariana (IBM) mud volcanoes, corresponding to a slab depth of 9 – 29 km. The results show that these serpentinites contain variable amounts of recycled nitrogen (3.6 – 16.4 ppm), which is likely sourced mainly from pore fluid with minor

contribution from the subducting sediments. Estimation suggests that the contribution of recycled slab nitrogen ($2.6^{\pm 1.3} \times 10^{6}$ mol·yr^{-1}) to the serpentinized mantle wedge only accounts for up to 0.7% of the nitrogen input flux of subducting sediments solely at IBM, suggesting that recycling of slab N at the early stage of subduction is minor, at least in the IBM subduction zone.

(2) In Chapter 3.2, as a complimentary study to Chapter 3.1, I investigated the nitrogen characteristics of blueschist-facies meta-basalts (peak metamorphic conditions: 320 – 450 ºC and 0.9 – 1.1 GPa) from the Heilongjiang Complex in Northeast China. The results show significant incorporation of sedimentary nitrogen (13.9 to 122.6 ppm) into the meta-basalts inside the subduction channel. This indicates that the labile nitrogen in sediments released during early subduction within the forearc region can be at least partially re-fixed into the more refractory meta-igneous part of the subducting slab, facilitating the retention of nitrogen for deep subduction and recycling.

(3) In Chapter 3.3, through the mass balance between the nitrogen input fluxes estimated from the reference sites offboard the Central America (Holes 1256D and 504B) and IBM (Holes 801C and 1149D) trenches and nitrogen output fluxes through arcs, I showed that, despite of the contrasting thermal regimes between the warm Central America and cold IBM subduction zones, a large fraction (> 50%) of the slab nitrogen is transferred beyond sub-arc depths.

In Chapter 4, I summarized our current state of knowledge about the distribution of nitrogen in subducting slabs and its recycling in the forearc and sub-arc regions, as slabs sink.

Preface

This thesis is an original work by Kan Li. It is composed of six separate manuscripts based on the findings of the author's PhD research supervised by Dr. Long Li. This project was only possible through samples provided by the Deep Sea Drilling Programs, Ocean Drilling Programs and Integrated Ocean Discovery Programs. This project was funded by the Natural Sciences and Engineering Research Council (NSERC) Discovery grant and Canada Research Chairs grant to Dr. Long Li.

Chapters 1 and 4 are original work produced by the author.

Chapter 2 contains three studies:

Study 1 (Chapter 2.1) is pending acceptance with minor revision in *Earth and Planetary Science Letters* as: K. Li and L. Li. *Controlling factors on nitrogen enrichment in the altered upper oceanic crust: a new perspective on constraining the global subducting nitrogen budget and implications for subduction-zone nitrogen recycling.* Sample preparation and analytical work were completed by K. Li. The initial formulation of manuscript was performed by K. Li with valuable intellectual contributions and editing to the manuscript by L. Li.

Study 2 (Chapter 2.2) will be submitted as: K. Li and L. Li. *Alteration enrichment of nitrogen in the gabbroic oceanic crust: implications for global subducting nitrogen budget and subduction-zone nitrogen recycling*. Sample preparation and analytical work were completed by

K. Li. The initial formulation of the manuscript was performed by K. Li with valuable intellectual contributions and editing to the manuscript by L. Li.

Study 3 (Chapter 2.3) will be submitted as: K. Li, A.J. Yu, and L. Li, *Nitrogen enrichment in oceanic serpentinites: A critical reservoir for deep nitrogen recycling*. Sample preparation and analytical work was completed by K. Li. The initial formulation of the manuscript was performed by K. Li with valuable intellectual contributions and editing to the manuscript by A.J. Yu and L. Li.

Chapter 3 also contains 3 studies.

` Study 1 (Chapter 3.1) will be submitted as: K. Li., G-C. Sun, S-B. Zhang and L. Li, *Nitrogen recycling in the forearc: insights from the Izu-Bonin-Mariana mud volcanoes*. K. Li conducted the bulk-rock nitrogen concentration and isotope composition analysis. Major and trace element analysis was performed by G-C. Sun and S-B. Zhang. The initial formulation of the manuscript was performed by K. Li with valuable intellectual contributions and editions to the manuscript from all coauthors.

Study 2 (Chapter 3.2) has been published in CHEMICAL GEOLOGY (2021, Volume 583, Article number: 120474) as: K. Li, G.-Y. Li, Y.-F. Du, W. Han, J. Zhang, L.-H. Chen, J.-B. Zhou, L. Li, *Intraslab remobilization of nitrogen during early subduction facilitates deep nitrogen recycling: Insights from the blueschists in the Heilongjiang Complex in Northeast China*. Sample collection and characterization were performed by G.-Y. Li. K. Li conducted the bulk-rock nitrogen concentration and isotope composition analysis. Major and trace element analysis was performed by Y.-F. Du. The initial formulation of the manuscript was performed by K. Li with valuable intellectual contributions and editing to the manuscript by all co-authors.

Study 3 (Chapter 3.3) has been accepted by GEOCHIMICA ET COSMOCHIMICA ACTA (2022, Volume 335, pp. 197-210) as: K. Li and L. Li, *Nitrogen enrichments in sheeted dikes and gabbros from DSDP/ODP/IODP Hole 504B and 1256D: Insights into nitrogen recycling in Central America and global subduction zones*. Sample preparation and analytical work was completed by K. Li. The initial formulation of the manuscript was performed by K. Li with valuable intellectual contributions and editing to the manuscript by L. Li.

Acknowledgements

I would firstly like to thank my supervisor Long Li for his guidance on every step of my PhD program. His guidance on encouraging me to think about the big picture of science is great treasure for my future academic career. With the seven-years supervisory, from my Master to my PhD program, his patience, support, attitude and creative thinking have taught me invaluable lessons about how to conduct research. I would like to extend my thanks to my candidacy and defense committee members D. Graham Pearson, Thomas Stachel, Thomas Chacko and Ralf Halama. All my co-authors are appreciated for their valuable contribution to my research work.

I am very grateful to Mark Labbe, who has provided immense help in fixing the technical problems of the equipment in our laboratory. His help is always timely and effective.

The friendship and constructive discussions with other graduate student fellows in the stable isotope research group are my good fortune. Thank you to Ji Zhang, Yuhan Qi, Yifan Du, Xueqi Liang, Yingzhou Li and more. When not working, their company has made my life in Edmonton colorful and meaningful.

My doctoral research would not have been possible without the precious drilling samples provided by ODP/ODP/IODP. I am always hoping to participate in future expeditions to obtain the first-hand samples myself.

Thank you to my parents and my wife, who are my biggest source of support.

Table of Contents

List of Tables

List of Figures

Glossary

Abbreviation/Symbol	Definition
‰	Parts per thousand or per mil
wt.%	Weight percent
ppm	Parts per million
~	Approximately
GPa	Gigapascal
Ma	Million years
AOC	Altered oceanic crust
DSDP	Deep Sea Drilling Program
ODP	Ocean Drilling Program
IODP	Integrated Ocean Discovery Program
MORB	Mid-ocean ridge basalt
REE	Rare earth element
HREE	Heavy rare earth element
LREE	Light rare earth element
n.a	Not available
n.p	Not applicable
n.d	Not determined
N	Nitrogen
$\delta^{15}N$	Nitrogen isotopes relative to the international Air standard
$\delta^{18}O$	Oxygen isotopes relative to the international VSMOW standard
σ	Standard deviation of the mean

Chapter 1. Introduction to geological nitrogen cycle

1.1 General introduction

Nitrogen (N) is one of few elements that distribute in all Earth's volatile reservoirs, the atmosphere, hydrosphere/biosphere, crust, mantle and core (e.g., Javoy, 1997; Knoll et al., 2012; Johnson and Goldblatt, 2015; Speelmanns et al., 2018; Mysen, 2019; Bekaert et al., 2021). The exchange of N among different reservoirs is critical for volatile cycles profoundly affecting not only the climate and environment on Earth's surface (e.g., Javoy, 1998; Johnson and Goldblatt, 2015; Johnson and Goldblatt, 2018; Bekaert et al., 2021) but also the physiochemical properties of the mantle and core (Speelmanns et al., 2018; Li et al., 2019a).

The N is recycled in the Earth by two systems (i.e., biological and geological). The biological cycle begins with the fixation of N from the atmosphere and hydrosphere into biomolecules (as $C\text{-}NH_2$) by organisms (e.g., cyanobacteria, phytoplankton) in the euphotic zone. The organic matter surviving water-column degradation eventually sinks and settles in seafloor sediments, where N joins the geological cycle initiated with sedimentation and diagenesis (Mysen, 2019). Before the final preservation in deep-sea sediments, a large fraction of organic N deposited in seafloor sediments is oxidized into bio-available inorganic molecules, including nitrate (NO_3^-), nitrite (NO_2^-) and ammonium (NH_4^+), and returned to the ocean for further assimilation by organisms (Gruber, 2008). Critically, due to the similar ionic radius of NH_4^+ (1.67 Å) and K^+ (1.64 Å; Shannon and Prewitt, 1969; Sidey, 2016), some re-mineralized NH_4^+ can be subsequently incorporated into the crystal lattices of clay minerals in sediments by the substitution for K^+ (e.g., Honma and Itihara, 1981; Sadofsky and Bebout, 2004; Li and Bebout, 2005; Johnson and Goldblatt, 2015). The preservation of N in organic and inorganic forms has caused deep-sea sediments to be conventionally considered as the major N reservoir in subducting slabs and thus the first target to constrain the N input fluxes into global subduction zones based on the recovered seafloor sediments by drill cores from the Deep Sea Drilling Program (DSDP), Ocean Drilling Program (ODP) and International Ocean Discovery Program (IODP) (Sadofsky and Bebout, 2004; Li and Bebout, 2005; Clift, 2017).

Over the last couple of decades, numerous deep-sea drillings reaching the igneous basement have also attracted intensive study of physical properties (e.g., density, porosity and permeability; Purdy, 1987; Carlson and Herrick, 1990b; Fisher, 1998) and geochemical compositions of igneous altered oceanic crust (AOC) (e.g., Kelley et al., 2003; White and Klein, 2014), which is predominantly composed of, from top to bottom, pillow basalts, sheeted dikes and gabbros (Staudigel, 2014a). These studies have revealed that both the physical (e.g., Fisher, 1998; Guerin et al., 2008; Carlson, 2011; Gilbert and Bona, 2016) and chemical compositions of AOC have been profoundly affected by its interaction with seawater-derived hydrothermal fluids (e.g., Muehlenbachs and Clayton, 1976; Muehlenbachs, 1980; Staudigel et al., 1981, 1996, 2014). As hydrothermal fluid comes into contact with oceanic crust, basaltic glass, olivine, pyroxene and plagioclase tend to be intensively altered, releasing cations, such as Ca^{2+}, Mg^{2+} and Fe^{2+} (Gudbrandsson et al., 2011) to facilitate the formation of secondary minerals (e.g., clay minerals, iron-hydroxides, carbonate, secondary plagioclase and amphibole) in their fractures, vesicles and vugs (e.g., Humphris and Thompson, 1978; Seyfried Jr, 1987; Alt, 1999; Alt and Teagle, 1999; Bach and Edwards, 2003; Staudigel, 2014).

Simultaneously, the similar ionic radius and charge between K^+ and NH_4^+ results in the uptake of N into K-bearing secondary minerals, e.g., clay minerals (e.g., Staudigel, 2014). This has been verified by the ubiquitous enrichment of N (< 19 ppm) observed in the altered basalt from DSDP/ODP Holes 1256D, 504B, 801C and 1149D (Li et al., 2007; Bebout et al., 2018; Busigny et al., 2005, 2019). The estimate of N in altered basalts from Holes 801C and 1149D suggests that AOC can be a large N reservoir parallel to seafloor sediments, transferring significant amount of N to subduction zones annually (e.g., Li et al., 2007). Despite of the mafic components of the subducting slab, serpentinization driven by fault-related alteration (e.g., detachment fault and slab-bending-related fault) has long been regarded as a critical process adding volatile components to the subducting slab (e.g., Ranero et al., 2003; Alt et al., 2013), which can be subsequently transferred to the sub-arc affecting arc magma geochemistry (e.g., Hattori and Guillot, 2007; Deschamps et al., 2013) and even beyond sub-arc depth to the deeper mantle (e.g., Kendrick et al., 2011; Smith et al., 2018, 2021). However, due to the lack of investigation of N characteristics of these mafic-ultramafic components in the subducting slab, especially the intrusive section of AOC (i.e., sheeted dikes and gabbroic rocks) and the serpentinized mantle portion (i.e., oceanic serpentinite), which accounts for > 90 vol.% of the material in subducting slab, our understanding on N uptake by these components and their global subducting N budgets is still poorly understood.

Another gap in the geological N cycle is the N recycling efficiency in the subduction channel. Prograde metamorphism could release part of the subducted slab N to the forearc and sub-arc regions and retain the rest to the deeper mantle beyond the sub-arc depth (e.g., Bebout and Fogel, 1992; Mingram and Bräuer, 2001; Pagé et al., 2018; Bekaert et al., 2021). However, several key parameters, including the recycling efficiency of N in the forearc and sub-arc regions (and thus the fraction of deeply subducted N) remain loosely constrained.

1.2 Major objectives

My research in this dissertation aimed to address several important questions that relate to N uptake by the mafic-ultramafic components of the subducting slab and its recycling in subduction zones: (1) Chapter 2 was designed to understand the N uptake by mafic-ultramafic components of subducting slabs and their N budgets from a global perspective. It contains three studies:

Chapter 2.1 is focused on characterizing the controlling factors of N uptake by the upper oceanic crust during low-temperature alteration based on a more extended study of global basaltic oceanic crust samples that are associated with different parameters, such as crust ages, spreading rates, alteration degrees and sedimentary history. The understanding of the controlling factors on N uptake by the altered upper oceanic crust allows me to quantitatively estimate the subducting N budget in the extrusive section of AOC.

Chapter 2.2 is focused on characterizing the N uptake by the sheeted dike and gabbroic section of AOC based on a broad sampling of gabbroic sections from global oceanic crust, which have been predominantly affected by moderate- to high-temperature hydrothermal alteration. The data are used to understand the alteration enrichment of N in the intrusive section of AOC and subsequently quantify the global subducting N budget of AOC by integrating the subducting N budget contributed by the upper basaltic section from Chapter 2.1. Furthermore, through comparison with the N output flux from global arc volcanoes, the efficiency of N that can either be recycled through global arc volcanoes or subducted beyond the sub-arc depth can be constrained.

Chapter 2.3 is focused on characterizing the N uptake of oceanic serpentinites, which represent the sub-oceanic lithospheric mantle exhumed to seafloor by faults. These serpentinites were produced by interaction with high-temperature hydrothermal fluids at depth to low-temperature hydrothermal fluids near seafloor. Understanding N uptake by these serpentinites enables we to quantitatively estimate the subducting N budget contributed by the serpentinized sub-oceanic lithospheric mantle.

(2) Chapter 3 was designed to quantify the recycling efficiencies of slab N within the forearc and sub-arc regions, which further allows to constrain the amount of N that can be transported beyond the sub-arc depth to the deeper mantle. This chapter also includes three studies:

Chapter 3.1 is focused on characterizing the N recycling within the forearc region by investigating the exhumed mantle-wedge serpentinites sampled (9 – 29 km; < 350 ºC) from Izu-Bonin-Mariana forearc mud volcanoes. These data allow me to assess the relative importance of N recycling within the forearc region and the N budget in the mantle wedge.

Chapter 3.2 is also focused on characterizing the N recycling within the forearc region but with samples from a counterpart (i.e., a subduction zone). The investigated blueschist-facies meta-basalts from the Heilongjiang Complex in Northeast China have been subducted to a location slightly deeper (320 – 450 ºC; up to 40 km) than that of the IBM mantle wedge samples. The data in this study allow us to understand the N behavior in the subduction channel during early subduction and their impact on N recycling in the forearc region.

Chapter 3.3 is focused on constraining the N recycling efficiencies in the sub-arc regions of two representatives of modern global subduction zones, i.e., the warm Central America and cold Izu-Bonin-Mariana subduction zones. Based on these data, the effect of the thermal structure of subduction zones on N recycling efficiency in the arc can be quantitatively assessed

1.3 Analytical methods

1.3.1 Analytical methods for bulk-rock N concentrations and δ^{15}N values

The bulk-rock N concentrations and $\delta^{15}N$ values of all the samples in this thesis, including basalts, sheeted dikes, gabbroic rocks, serpentinites and blueschists, were analyzed following an offline sealed-tube combustion and extraction method coupled with carrier-gas isotope ratio mass spectrometry. The analytical details have been described by Li et al. (2021a). In general, sample powders were loaded into a one-end sealed quartz tube together with quartz wool and Cu_xO_x reagents. The tube was put on a custom-made metal manifold to pump overnight and sealed under high vacuum. The sample powder in the sealed tube was then combusted at high temperature in a programmable muffle furnace for complete N extraction (Li et al., 2021a). Following Li et al. (2021a), to ensure a complete N extraction from samples, basalt samples were combusted at 900 °C for 8 hours; sheeted dike and gabbro sample tubes were first put in the heat center of an open-end cylinder-shaped furnace to combust at 1200°C for 30 minutes, then combusted at 900°C for 8 hours; serpentinite and blueschist sample tubes were combusted at 1000 °C for 8 hours. After this high-temperature combustion step, the sample tube was cooled down to and stayed at 600°C for 2 hours before it was naturally cooled down to room temperature. The sample tube was then loaded back into the metal manifold and cracked under high vacuum. The released N_2 was cryogenically purified and quantified by a capacitance manometer. After quantification, the N_2 gas was carried by an ultrahigh-purity helium gas flow to a Thermo Finnegan MAT 253 isotope ratio mass spectrometer for N isotope analysis. All N isotopic data are reported in the δ notation, i.e., $\delta^{15}N_{sample} = (^{15}N/^{14}N)_{sample}/(^{15}N/^{14}N)_{standard} - 1$, where the standard is atmospheric N_2. Based on repeated analyses of samples and two certified reference material, i.e., low-organic content soil standard (reference values: N = 0.133 wt.%; $\delta^{15}N = +6.97‰$) and high-organic content sediment standard (reference values: N = 0.52 wt.%; $\delta^{15}N = +4.32‰$), the analytical error is better than 6% (2σ) for N concentration and 0.2‰ (2σ) for $\delta^{15}N$.

1.3.2 Analytical methods for bulk-rock major and trace elements

Serpentinite rock chips from the Izu-Bonin-Mariana forearc mantle wedge were cleaned by removing surface material and further crushed and ground into fine powders in an agate mortar. Whole-rock major elements were analyzed in the Chinese Academy of Sciences Key Laboratory of Crust-Mantle Materials and Environments at the University of Science and Technology of China (USTC), Hefei. Major elements were measured with a Rigaku PrimusII X-ray fluorescence spectrometer (XRF). Repeated analyses of Chinese national rock standards GBW07112 and USGS BHVO-2 gave an analytical error better than ±2% of the absolute concentrations for major elements. Whole-rock trace element compositions were analyzed with an Agilent 7900 inductively coupled plasma mass spectrometry (ICP-MS). The analytical uncertainty is better than ±10% of the absolute concentrations.

Blueschist rock chips from the Heilongjiang Complex were cleaned by removing surface material and further crushed and ground into fine powders in an agate mortar. Major and trace elements of eleven samples (i.e., the 15HLJ series) were analyzed by Actlabs (Ontario, Canada) using a sequential Thermo Jarrell-Ash ENVIRO II ICP or a Varian Vista 735 ICP. Calibration was achieved using 12 USGS and CANMET certified reference materials. The analytical uncertainties are better than ±5% of the absolute concentrations for major elements depending on abundance and ±10% of the absolute concentrations for trace elements. Major and trace elements of the other sixteen samples (i.e., the 19HLJ and 20HLJ sample series) were analyzed at the State Key Laboratory of Continental Dynamics in Northwest University, Xi'an, China. Major elements were measured using a Rigaku RIX 2000 XRF. Repeated analyses of USGS BCR-2 and two Chinese national rock standards (GSR-1and GSR-3) gave an analytical error better than ±5% of the absolute concentrations for major elements (Wang and Liu, 2016). Trace elements concentrations were analyzed by an Agilent 7500a ICP-MS. The analytical uncertainty is better than ±10% of the absolute concentrations (Liu et al., 2007).

Chapter 2 Constraints on nitrogen input fluxes

Chapter 2.1 Nitrogen enrichment in the altered upper oceanic crust and global subducting nitrogen budget of the altered upper oceanic crust

2.1.1 Introduction

Chemical exchange between seawater and oceanic crust during hydrothermal alteration profoundly affects both the geochemistry of seawater and the physiochemical properties (e.g., volatile contents, density and porosity) of the altered oceanic crust (AOC; Muehlenbachs and Clayton, 1976; Staudigel et al., 1981, 1989; Staudigel and Hart, 1983; Carlson and Herrick, 1990; Brady and Gíslason, 1997; Fisher, 1998; Alt and Teagle, 1999; Chan et al., 2002; Staudigel, 2014; Coogan and Gillis, 2018). Among these reactions, uptake of volatile components, such as water, carbon and halogens, by oceanic crust, has attracted broad interests (e.g., Alt and Teagle, 1999; Staudigel, 2014; Kendrick, 2019) because the budgets of volatile elements in AOC is an important factor for the modeling of subduction of these elements into the deep mantle (e.g., Staudigel et al., 1989; Jarrard, 2003; Hacker, 2008; Shilobreeva et al., 2011; Kendrick et al., 2013; Müller and Dutkiewicz, 2018; Li et al., 2019; Plank and Manning, 2019).

Nitrogen (N) is also a critical volatile element that can be incorporated by AOC during seafloor alteration (Busigny et al., 2005; Li et al., 2007; Bebout et al., 2018). Previous studies on the samples recovered by the Deep Sea Drilling Program (DSDP), Ocean Drilling Program (ODP) and Integrated Ocean Drilling Program (IODP) (e.g., Holes 801C, 1149D, 1256D and 504B) have shown that N in AOC (commonly less than < 19 ppm; Busigny et al., 2005, 2019; Li et al., 2007; Bebout et al., 2018; Li and Li, 2022) is significantly enriched relative to fresh mid-ocean ridge basalts (MORB; ~1.5 ppm; Li et al., 2007; Marty et al., 2020). Because N can be incorporated into minerals/rocks in the form of NH_4^+ by substituting for K^+, and to a lesser extent, Na^+ and Ca^{2+} in mineral crystal lattice (Honma and Itihara, 1981), the K^+-bearing secondary minerals (e.g., smectite, K-zeolites and K-feldspars) formed during low-temperature alteration of upper oceanic crust could be a potential host for secondary N (Hall, 1989; Busigny et al., 2005; Li et al., 2007; Bebout et al., 2018). One interesting observation on the N concentrations of seafloor basalts is that they show remarkably different magnitudes of N enrichments among different sites. For example, offboard the Izu-Bonin-Mariana trench, the entire basalt section in Hole 1149D (average: 2.0±0.5 ppm; n = 6; 1σ) and the lower-section basalts in Hole 801C (average: 2.7±0.8 ppm; n = 11; 1σ) contain very low N (Li et al., 2007). In contrast, offboard the Central American trench, the altered basalts in Holes 1256D (average: 11.8±3.8 ppm; n = 15; 1σ) and 504B (average: 8.0±3.8 ppm; n = 18; 1σ) are characterized by consistently higher N concentrations (Bebout et al., 2018; Busigny et al., 2019; Li and Li, 2022). These cross-site differences in N concentration clearly show that the N enrichment during low-temperature alteration of the upper oceanic crust is variable at the global scale. However, previous studies of individual drill cores could only examine local-scale variability (Busigny et al., 2005; Li et al., 2007; Bebout et al., 2018). Consequently, the global N budget in AOC estimated from the average of local data may have large uncertainty. A better constraint on global N budget in AOC needs to take into account the first-order factors controlling the N enrichment in AOC, which has not been examined due to the lack of data.

Previous studies on alteration enrichment of other volatile components (e.g., carbon) in the upper oceanic crust have revealed that several physiochemical parameters, such as alteration degree, crustal age, seafloor spreading rate and sediment type (e.g., Alt and Teagle, 1999; Bach and Humphris, 1999; Jarrard, 2003; Gillis and Coogan, 2011), may potentially affect the elemental exchange between oceanic crust and hydrothermal fluids. Accordingly, to systematically understand the control of these physiochemical parameters on N uptake by the upper oceanic crust, we selected altered basaltic samples from four additional DSDP/ODP drilling holes that vary in these physiochemical parameters, i.e., DSDP Holes 556 (n = 4), 543A (n = 13), 417A (n = 11) and ODP Hole 1224F (n = 7). The variations of types of overlying sediments, crustal ages, spreading rates, and alteration degrees are described in detail below.

2.1.2 Geological background and sample description

(1) DSDP Hole 543A

Hole 543A was drilled into the ~81-million-year-old slow-spreading oceanic crust (half-spreading rate: 11.5 mm·yr^{-1}) of the Atlantic abyssal plain. The hole is 3.5 km east of the toe of the accretionary prism formed by the westward subduction of the Atlantic Plate beneath the Caribbean Plate (Fig. 1; Shipboard Scientific Party, 1984). The 411 m-thick sedimentary cover is composed of ashy mud, ashy nannofossil mud, radiolarian clay with ashy layers, zeolitic clays and claystone. The basal sediments directly overlying the igneous basement are composed of calcareous ferruginous claystone (Shipboard Scientific Party, 1984). Our analysis of three basal claystone (370 – 390 mbsf) gave high N concentrations of 248 ppm to 325 ppm (average: 297.0±42.8 ppm; 1σ; Table S1).

The recovered 44 m-thick igneous basement is dominated by pillow basalts. Alteration is most intense at the top of the basalt section (Cores 10 – 12), especially in Core 10, where basalts have been moderately altered with production of various secondary minerals such as K-feldspar, iron hydroxides and clay minerals (e.g., celadonite and saponite; Natland et al., 1984). This is also manifested by the significant enrichment of K_2O (up to 5 wt.%) in Cores 10 – 12 (Natland et al., 1984). Deeper in the hole, basalts have been only slightly altered (<5%) with slight enrichment of K_2O contents (average: 0.24±0.18 wt.%; n = 21; 1σ) (Natland et al., 1984; Shipboard Scientific Party, 1984). The studied 13 basalt samples span from the top to the bottom of the hole. Three samples from top of the hole were moderately altered and associated with dark-gray background alteration and brown alteration halos; while the other samples were slightly altered with dark-gray background alterations (see detailed descriptions in Table A1 in Appendix A).

(2) DSDP Hole 556

Hole 556 was drilled into the ~31-million-year-old western flank of the slow-spreading (half-spreading rate: 10 mm·yr^{-1}) Mid-Atlantic Ridge (Fig. 1) at about ~80 km north of the Pico Fracture Zone (Shipboard Scientific Party, 1985). The 461 m-thick sedimentary cover (0 – 461 mbsf), as well as the basal sediments directly overlying the igneous basement, are all carbonate-rich sediments such as nannofossil ooze, foraminiferal-nannofossil ooze and nannofossil chalk (Shipboard Scientific Party, 1985).

The recovered 178 m-thick igneous rocks are composed of (i) basalt-carbonate breccia (i.e., angular basaltic clasts in a matrix of intercalated biogenic limestone) (462 – 469.5 mbsf), (ii) pillow basalts (469.5 – 505 mbsf), (iii) massive flows and pillow breccia (505 – 509 mbsf), (iv) basalt breccia (529– 561 mbsf), and (v) serpentinized gabbro breccia (561 – 639 mbsf) (Shipboard Scientific Party, 1985). The basalts in Hole 556 were fresh to moderately altered with a secondary mineral assemblage dominated by clay minerals, carbonate and iron-oxyhydroxides (Shipboard Scientific Party, 1985). The K_2O contents (average: 0.25±0.11 wt.%; n = 110; 1σ) of these basalts are only slightly enriched relative to fresh MORB (0.14 wt.%; Gale et al., 2013). The 4 samples for this study include one pillow basalt breccia, one basaltic glass and two pillow basalts (Table S1). Three of them were slightly to moderately altered and associated with dark-gray background alteration, while the other one (pillow basalt breccia) was highly altered and associated with dark-gray background alteration and brown alteration halos (Table A1 in Appendix A).

(3) DSDP Hole 1224F

Hole 1224F was drilled into a 48-million-year-old fast-spreading oceanic crust (half-spreading rate: 71 mm·yr^{-1}) generated along a volcanic ridge between the Farallon and Pacific plates (Fig. 1; Stephen et al., 2003). The 28 m-thick sedimentary cover overlying the igneous basement is composed of eolian abyssal clay (Shipboard Scientific Party, 2003a).

The recovered 134 m-thick igneous rock was divided into 3 lithological units (Shipboard Scientific Party, 2003a): (i) 34.7 m-thick sheet flows (28 – 62.7 mbsf); (ii) 70.8 m-thick pillows with minor thin sheet flows (62.7– 133.5 mbsf); (iii) intermixed pillows and sheet flows (133.5 – 161.7 mbsf). Due to the capping of the low-permeability massive sheet flows, most basalts have been only slightly (<5%) altered with a typical low-temperature secondary mineral assemblage of saponite, celadonite, Fe-oxyhydroxides and carbonate (Paul et al., 2006). The K_2O contents (average: 0.29±0.12 wt.%; n = 30; 1σ) of these basalts are slightly enriched relative to fresh MORB (Shipboard Scientific Party, 2003a; Haraguchi and Ishii, 2006). The 7 basalts selected for this study span from units (i) to (iii). Five out of seven samples were slightly altered and associated with dark-gray background alteration; the other two samples were moderately altered and associated with dark-gray background alteration and brown alteration halos (see detailed description in Table A1 in Appendix A).

(4) DSDP Hole 417A

Hole 417A was drilled into the 120-million-year-old slow-spreading (half-spreading rate: 12.5 mm·yr^{-1}) oceanic crust in the western Atlantic at the southern end of the Bermuda Rise (Fig. 1; Shipboard Scientific Party, 1980). The 208 m-thick sedimentary cover (0 – 208 mbsf) is composed of pelagic clay, zeolitic clay and radiolarian ooze (Shipboard Scientific Party, 1980; Mann and Müller, 1979). Hole 417A was drilled on a basement high, where the sediment only started to accumulate 20 Myr after the crustal formation (Shipboard Scientific Party, 1980; Alt and Honnorez, 1984).

The recovered 209 m-thick igneous basement (208 – 417 mbsf) was divided into 19 lithological units, which are dominantly composed of pillow basalts interbedded with thin layers of massive basalts and breccia (Shipboard Scientific Party, 1980). Because the late accumulation of sedimentary cover favored the ingress of seawater-derived hydrothermal fluids, the basalts from Hole 417A were highly altered by low-temperature hydrothermal fluids with a secondary mineral assemblage of K-feldspar, saponite, mixtures of celadonite and nontronite, Fe-oxyhydroxides and calcite (Mevel, 1980; Alt and Honnorez, 1984). Compared to the altered basalts from Holes 556, 1224F and 543A, the basalts from Hole 417A show significant enrichment of alkali elements (e.g., K and Rb) as a result of low-temperature alteration (Humphris et al., 1980; Shipboard Scientific Party, 1980). K_2O contents are 8 wt.% at the top of the hole and decreased progressively to the bottom of the hole (Shipboard Scientific Party, 1980; Table S2). Eleven basalt samples spanning from the top to the bottom of the hole were selected for this study. The majority of these samples were moderately to highly altered showing dark-gray background alteration, but include a highly altered basalt breccia in a matrix of green palagonite, smectite and zeolite (Table A1 in Appendix A).

2.1.3 Results

The N concentrations and $\delta^{15}N$ values of basalts from Holes 556, 1224F, 417A and 543A are listed in Table A1 in Appendix A. In brief, basalts from Holes 556 and 1224F have relatively low N concentrations (6.2 – 13.5 ppm with an average of 8.7±3.3 ppm and 5.2 – 12.9 ppm with an average of 8.1±2.8 ppm, respectively; Fig. 2) and relatively narrow ranges of $\delta^{15}N$ values (+1.3‰ to +3.6‰ with an average of +2.0±1.0‰ and -0.8‰ to +1.5‰ with an average of +0.3±0.8‰, respectively).

Basalts from Hole 417A show bimodal signature. Two samples have high N concentrations (12.8 and 25.8 ppm) with extremely negative $\delta^{15}N$ values (-10.9‰ and -20.9‰), whereas the other 9 samples have lower N concentrations of 2.7 ppm to 11.3 ppm with a narrow $\delta^{15}N$ range of +0.7‰ to +3.4‰. These data are consistent with the N concentrations (11.9 to 14.9 ppm) and $\delta^{15}N$ values (+0.6‰ to +8.3‰) of two basalts from Hole 417A analyzed by Li et al. (2007). Altogether, these Hole 417A data give an average N concentration of 7.3±3.8 ppm and an average $\delta^{15}N$ value of +2.4±2.2‰ (n = 11; 1σ). Basalts from Hole 543A have relatively high N concentrations of 17.5 – 48.4 ppm (average: 24.9±8.3 ppm; n = 11; 1σ) with $\delta^{15}N$ values of -1.0‰ to +7.1‰ (average: +2.9±2.0‰; Fig. 2).

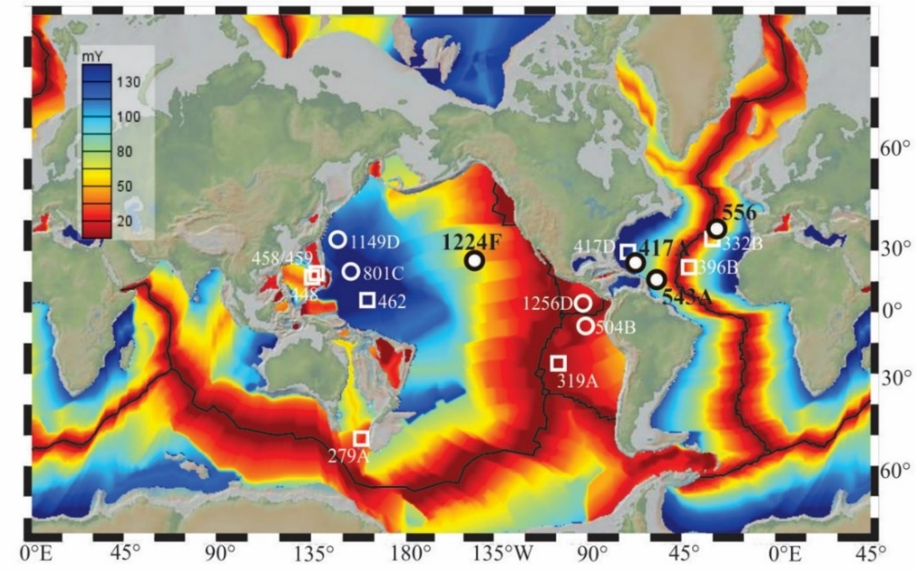

Figure 1. Global oceanic crust map showing sample sites. The crustal ages are generated by GeoMappApp (http://www.geomapapp.org). The DSDP/ODP sites studied here (white filled circles) spread from the northern Pacific Ocean (ODP Hole 1224F) to the Atlantic Ocean (DSDP Holes 543A, 417A, and 556). For reference, the sites that have been previously investigated for nitrogen characteristics (ODP Holes 801C, 1149D, 1256D and DSDP Hole 504B; Li et al., 2007; Bebout et al., 2018; Li and Li, 2022) are marked as white open circles. Some other sites that have been randomly investigated (with less than two data points) for their N characteristics (DSDP

Holes 458, 459, 448, 279A, 319A, 417D, 396B, 332B; Li et al., 2007) are marked as white open squares.

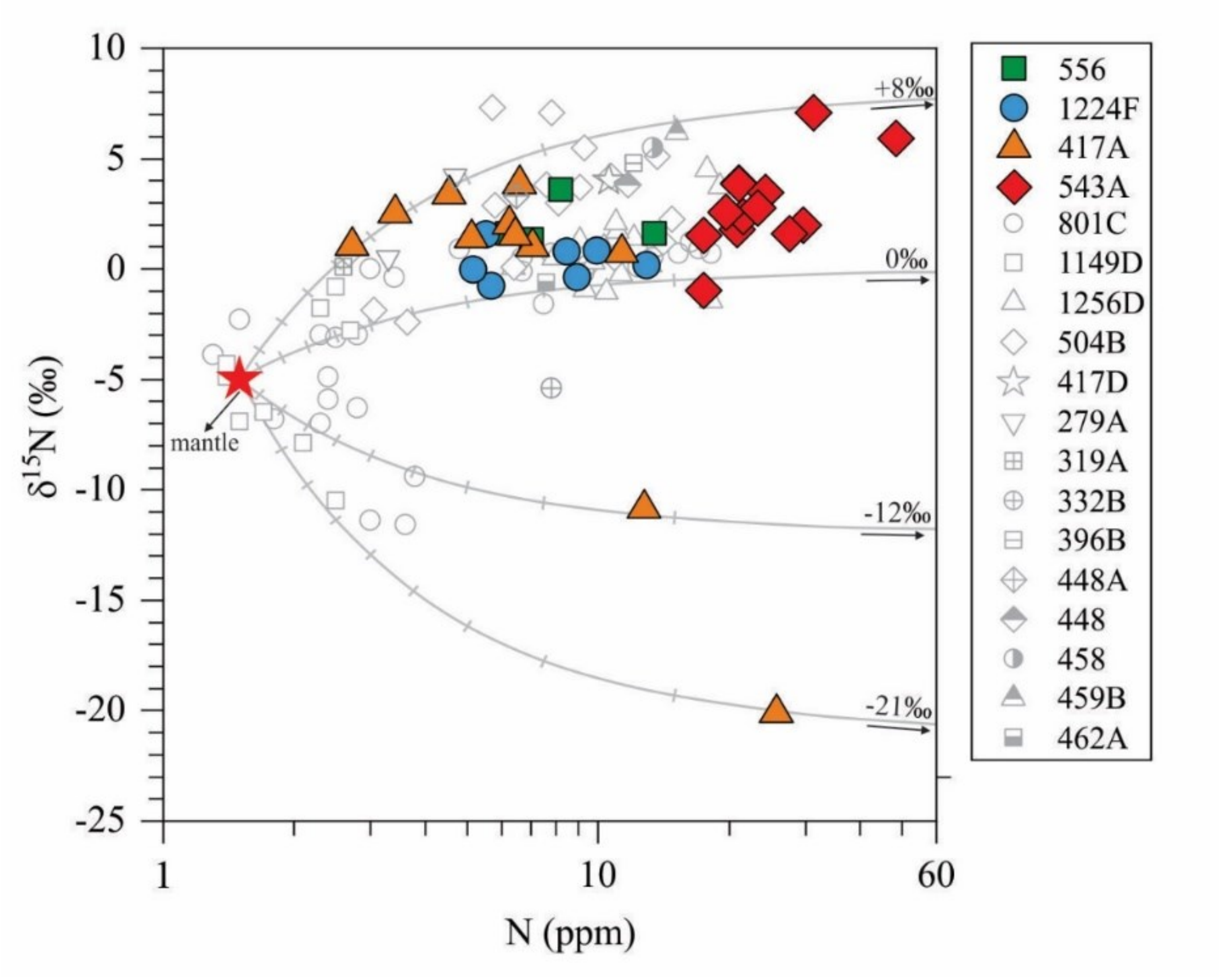

Figure 2. Modeling of N concentrations and $\delta^{15}N$ values of altered basalts (data source: Li et al., 2007; Bebout et al., 2018; Busigny et al., 2019; Li and Li, 2022; this study; see Table S1). The red star represents fresh mid-ridge ocean basalts (MORB) with N inherited from the mantle (N = 1.5 ppm; $\delta^{15}N$ = -5.0‰; Marty and Humbert, 1997; Li et al., 2007; Marty et al., 2020). The grey curves illustrate the results of two-component mixing between fresh MORB and ammonium from (i) sediment/seawater with $\delta^{15}N$ values from 0‰ to +8‰, or (ii) abiotic N_2 reduction with $\delta^{15}N$ values from -12‰ to -21‰. The fraction of the incorporated NH_4^+ in the total N is marked by short gray lines with a 10% increment.

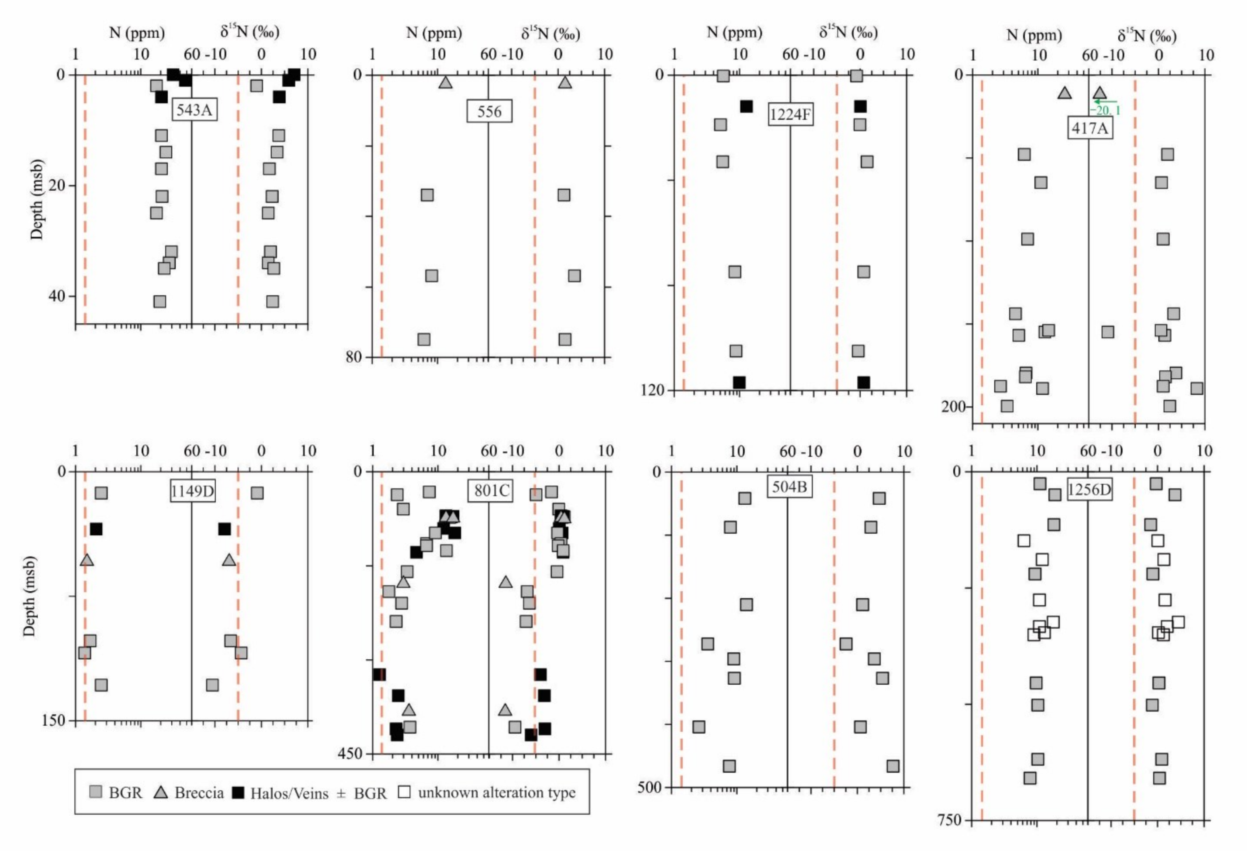

Fig. 3 Downhole variations of N concentrations and $\delta^{15}N$ values of altered basalts from Holes 543A, 556, 1224F, 417A, 1149D, 801C, 504B and 1256D. BGR = background alteration. The top horizontal line (depth = 0) in each panel marks the sediment-basalt boundary and the depth corresponds to the meters subbasement (msb). The vertical red dashed lines mark the N concentration (1.5 ppm) and $\delta^{15}N$ values (-5.0‰) of fresh mid-ocean ridge basalt (Marty and Humbert, 1997; Li et al., 2007; Marty et al., 2020).

2.1.4 Discussion

2.1.4.1 Ubiquitous N enrichment with spatial variations in global upper oceanic crust

In addition to the basalts from previously studied Holes (Holes 801C, 1149D, 504B and 1256D; Li et al., 2007; Bebout et al., 2018; Busigny et al., 2019; Li and Li, 2022), the basalts examined here all show significantly higher N concentrations than fresh MORB (~1.5 ppm; Li et al., 2007; Fig. 2 and Fig. 3). This indicates ubiquitous enrichment of N in the upper oceanic crust at a global scale as a result of hydrothermal alteration, mostly at low temperatures. As has been discussed in previous studies (e.g., Busigny et al., 2005; Li et al., 2007; Bebout et al., 2018), N is primarily incorporated as NH_4^+ into clay minerals through substitution of K^+ in the interlayer sites. The large range in N concentrations (1.3 to 48.4 ppm; Fig. 2) of altered basalts clearly indicates a spatial variation in N uptake. This is possibly attributed to the variations in crustal structure, fluid access, and geochemical properties of hydrothermal fluids across different localities, which are assessed in detail below.

2.1.4.2 Nitrogen sources

The correlation between N concentrations and $\delta^{15}N$ values can be used to interpret the sources of the secondary N in altered basalts. Previous studies of altered basalts from Holes 801C, 1149D, 504B and 1256D have revealed two different sources of secondary N (Li et al., 2007; Busigny et al., 2019; Li and Li, 2022). One is NH_4^+ derived from the overlying sediments and/or seawater, which is characterized by $\delta^{15}N$ values of ~ 0‰ – +10‰ (Sadofsky and Bebout, 2004; Li and Bebout, 2005; Li et al., 2007; Bourbonnais et al., 2012; Jo et al., 2018; Li and Li, 2022). Li et al. (2007) also suggested that, when the availability of sediment/seawater-sourced NH_4^+ is limited in hydrothermal fluids (e.g., in the lower volcanic series in Holes 801C and 1149D), altered basalts may also incorporate NH_4^+ produced by abiotic N_2 reduction, which is characterized by extreme ^{15}N-depletion (~ -12‰ to -16‰) (Li et al., 2007; 2014).

To assess the contribution of these two N sources to altered basalts at a global scale, we fitted the available N concentration and $\delta^{15}N$ data of altered basalts from global oceanic crusts by a two-component mixing model between the pristine N inherited from the mantle and the incorporated secondary N from two sources (Fig. 2). The mixing can be described by Equation (1):

$$\delta^{15}N_S = \left(\frac{C_S - C_0}{C_S}\right) \cdot \delta^{15}N_{ext} + \frac{C_0}{C_S} \cdot \delta^{15}N_0 \qquad (1)$$

in which C_S and $\delta^{15}N_S$ are the measured N concentration and isotope composition of a sample, C_0 and $\delta^{15}N_0$ are the concentration and isotope composition of the inherited mantle N ($C_0 \approx 1.5$ ppm and $\delta^{15}N_0 = -5‰$; Marty and Humbert, 1997; Marty and Dauphas, 2003; Li et al., 2007; Marty et al., 2020). $\delta^{15}N_{ext}$ is the N isotope composition of the incorporated secondary N, which can well represent the N isotope composition of the source due to the small isotope fractionation (< 2‰) as NH_4^+ is incorporated into clay minerals under seafloor low-temperature alteration condition (Li et al., 2021b).

The modeling indicates that the majority of the altered basalt data can be explained by addition of sediment/seawater-derived NH_4^+ with $\delta^{15}N$ value of 0‰ to +8‰ (Fig. 2). We interpret this as an indication that sediment/seawater-derived NH_4^+ is the main source for the secondary N in altered basalts. Meanwhile, two altered basalts from Hole 417A and a number of altered basalts from Holes 801C and 1149D have extremely negative $\delta^{15}N$ values (as low as –21‰). Different to the basalts from Holes 801C and 1149D which were less oxidized, the basalts from Hole 417A were highly oxidized due to its intensive interaction with oxygenated seawater on a basement high (Alt and Honnorez, 1984). However, interactions with reducing hydrothermal fluids can be clearly revealed by the local preservation of Fe(II)-rich pyrite and saponite (Alt and Honnorez, 1984). Therefore, we consistently interpret these extremely low $\delta^{15}N$ values as a result of abiotic N_2 reduction. The relatively few extremely low $\delta^{15}N$ values in global oceanic basalts indicates that abiotic N_2 reduction is not a dominant source for secondary N in global altered basalts. Nevertheless, the high N concentrations in the two basalts from Hole 417A suggest that abiotic N_2

reduction can supply secondary N comparable with the sediment/seawater source in some localities.

2.1.4.3 Factors controlling N enrichment in altered basalt

Despite the ubiquitous N enrichment in altered basalts from global oceanic lavas, the magnitude of N enrichment varies significantly among different holes. For example, mass-balance calculation suggests that secondary N accounts for 94±2% of N in 543A basalts, 86±4% in 1256D basalts, 76±14% in 504B basalts, 22±18% in 1149D basalts, 61±28% in 801C basalts, 74±14% in 417A basalts, 81±6% in 556 basalts and 80±7% in 1224F basalts. To understand the first-order control on this difference, we examined some potential factors, such as alteration degree, crustal age, spreading rate, and sediment type.

2.1.4.3.1 Alteration degree and type

Alteration degree of basalts can be inferred from the average loss on ignition content (LOI in wt.%; Table 1), which can serve as an index of the fraction of hydroxyl minerals (e.g., clays) formed during low-temperature alteration (e.g., Teagle et al., 1996; Shipboard Scientific Party, 2000a). Fig. 4a illustrates no correlation between N concentrations and LOI contents among different holes, indicating that the amounts of clay minerals are not the determining factor for the magnitude of N enrichment. Besides alteration degree, we also compared the possible effect of different types of alteration (e.g., background alteration vs. alteration halos/veins). As illustrated in Fig. 3, no consistent difference in N concentration is observed between samples of different alteration types. It should be noted that alteration veins which could be significantly enriched in N (e.g., 354 – 491 ppm for two phyllosilicate veins in Hole 1256D; Busigny et al., 2005) are not included in the sample set for this study. Their contribution to the total N budget of global oceanic crusts is worth investigating in future studies.

2.1.4.3.2 Potassium content

Because N in the upper oceanic crust has been considered to mostly occur as NH_4^+ in the K^+-bearing secondary minerals (e.g., clays, K-feldspars and zeolites; Hall, 1989; Busigny et al., 2005; Li et al., 2007; Bebout et al., 2018), K content of the upper oceanic crust, which is commonly elevated relative to fresh MORB during low-temperature alteration (Staudigel, 2014), may potentially control the magnitude of N enrichment. However, Fig. 4b shows no correlation between N and K_2O concentrations either. The lack of K control on N enrichment is especially manifested in the volcanic section of Hole 504B and Hole 417A. At Hole 504B, the upper volcanic alteration zone (274 – 594 mbsf) was affected by early-stage open circulation of cold seawater and thus has relatively high K_2O concentrations (up to 0.5 wt.%; Bach et al., 2003), whereas the lower volcanic alteration zone (594 – 846 mbsf) was affected by late-stage restricted circulation of less-oxidative fluids derived from evolved seawater and has relatively low K_2O concentrations (commonly < 0.1 wt.%; Alt et al., 1996; Bach et al., 2003). But this downhole difference in K_2O concentrations does not occur for N concentrations (Fig. 3). At Hole 417A, while intense low-temperature alteration has resulted in significant elevation of K_2O concentrations (up to 8 wt.% in the top section) and formation of K-feldspars in altered basalts (Shipboard Scientific Party, 1980; Alt and Honnorez, 1984), the N concentrations of these altered basalts were not significantly elevated. Overall, these observations suggest that N concentrations are decoupled with K concentrations in altered basalts. This decoupling suggests that N may reside not only in K-bearing secondary minerals, but also in Na- and/or Ca-bearing minerals (Busigny et al., 2011; Li and Li, 2022). Positive correlation between N and K_2O concentrations in altered basalts does show up in the upper ~60 m of Hole 801C (Li et al., 2007), which suggests that the enrichment of N could be controlled by K_2O concentrations locally.

2.1.4.3.3 Crust age

Crust age is speculated to potentially affect the magnitude of N enrichment in altered basalts. This is because if secondary N can be progressively added into basalts over the long-lasting low-temperature seafloor alteration process, older oceanic crust is expected to have higher N concentrations. In addition, the relatively high temperatures of bottom water in Jurassic-Cretaceous oceans have been demonstrated to enhance the uptake of secondary carbon by altered basalts (Gillis and Coogan, 2011; Coogan and Gillis, 2013). If this temperature effect also impacted the uptake of N, older oceanic crust is expected to have higher N concentrations. However, Fig. 4c shows that no N increase trend along aging of oceanic crusts in the range from 6 Ma (Hole 504B) to 170 Ma (Hole 801C; Table 1). This suggests that the uptake of secondary N could have occurred quickly in the young ages (likely < 20 Myr) when the activity of hydrothermal circulation was the greatest (Stein and Stein, 1994). This observation is consistent with previous studies which suggested that the formation of secondary minerals (e.g., celadonite and calcite) and assimilation of volatile elements such as carbon occurred dominantly in the first ~20 Myr after crustal accretion (e.g., Richardson et al., 1980; Coggon et al., 2010; Coogan et al., 2016; Coogan and Gillis, 2018; Laureijs et al., 2021a, b).

2.1.4.3.5 Spreading rate

While spreading rates vary over a range from 11.5 $\mathrm{mm \cdot yr^{-1}}$ to 110 $\mathrm{mm \cdot yr^{-1}}$, a direct comparison between average N concentrations of AOC and spreading rates shows no obvious correlation (Fig. 4d). This suggests that spreading rate does not have significant effect on the N enrichment in AOC.

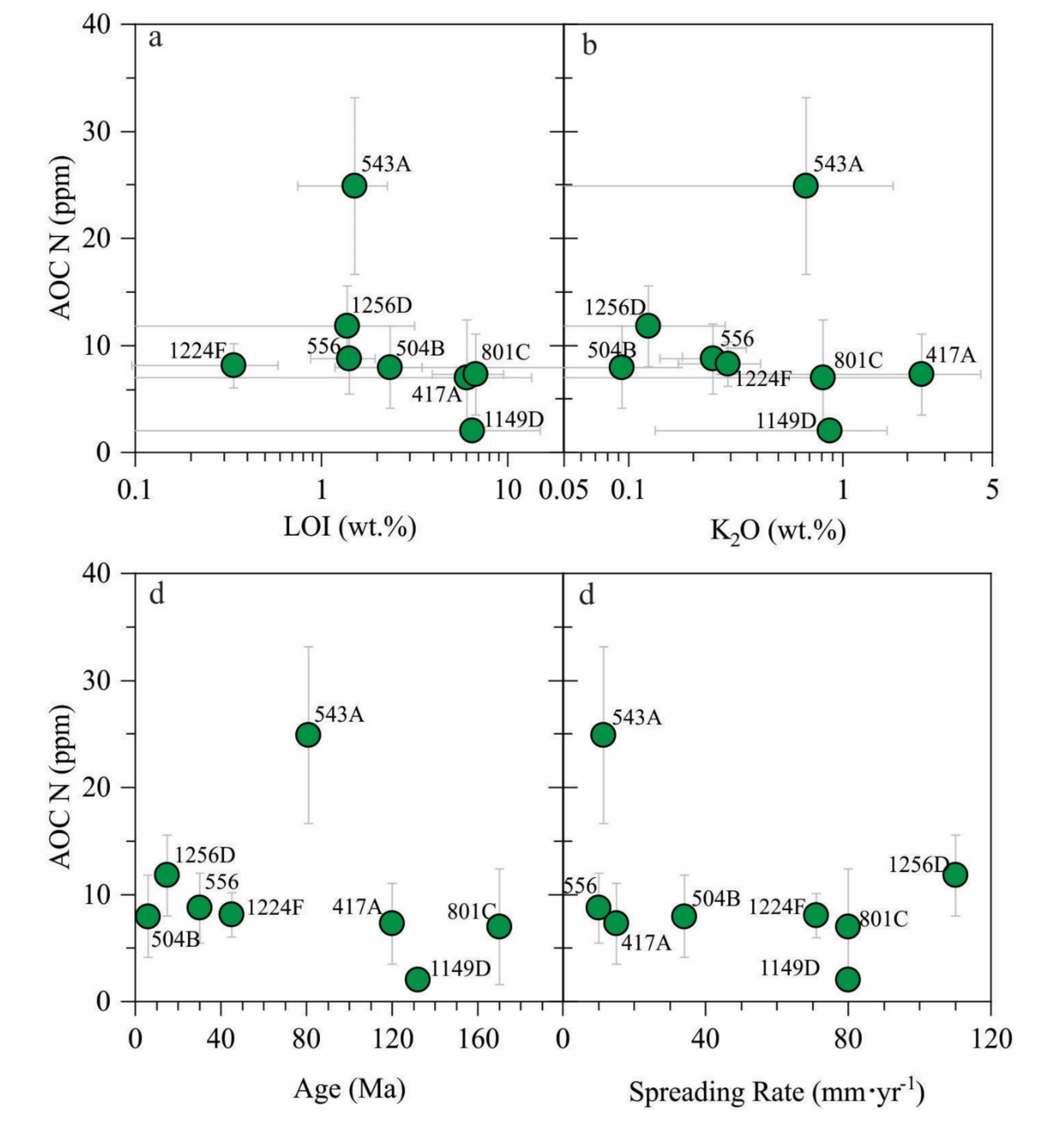

Fig. 4 Comparison of the average N concentrations of altered basalts with their (a) average loss on ignition (LOI) data, (b) average K_2O concentrations, (c) crustal ages, and (d) spreading rates. Error bars represent 1σ. See Table 1 for data source.

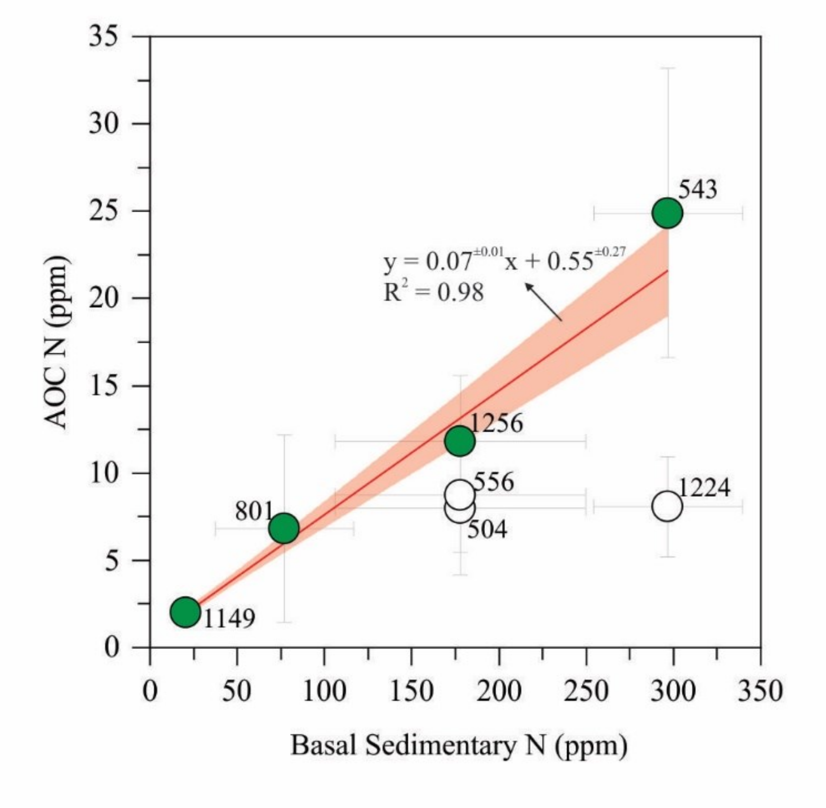

Fig. 5 Comparison of the average N concentrations of altered basalts with the average N concentrations of basal sediment sections. Note that the basal sediment N data for Sites 504, 506 and 1224 (empty circles) are not available but assigned by the data of similar sediment lithologies in sites 543 and 1256. See Table 1 for data. Red lines are linear fitting results with 1σ error band.

2.1.4.3.4 Nitrogen availability from overlying sediments

With the deposition of sediments after crustal formation from mid-ocean ridges, more NH_4^+ could be extracted from overlying sediments and added into hydrothermal fluid for further incorporation into altered basalts (e.g., Wheat et al., 2000). Meanwhile, overlying sediments may also act as a low-permeability layer inhibiting the ingress of seawater-derived fluids into oceanic crust (Snelgrove and Forster, 1996; Coogan and Gillis, 2018). Therefore, it is worth investigating the integrated effect of sediments on N enrichment in altered basalts. Available data from Sites 1149, 801, 1256 and 543 (Fig. 5) show that the average N concentrations of altered basalts positively correlate ($R^2 = 0.98$) with the average N concentrations of basal sediments section. The variation in N concentration of the basal sediments among these sites is primarily controlled by their lithologies (Table 1). The silica-rich radiolarites (interbedded with claystone) at Site 801 and radiolarian cherts (interbedded with nannofossil chalk) at Site 1149 are N-poor (77.0±39.5 ppm at Site 801 and 20.5±3.5 ppm at Site 1149; Sadofsky and Bebout, 2004), whereas the claystones at Site 543 are N-rich (297.0±42.8 ppm) with the calcareous nannofossil oozes at Site 1256 falling in between (177.7±71.8 ppm; Shipboard Scientific Party, 2003b). This good correlation indicates that the availability of N from overlying basal sediments is likely the first-order control on the magnitude of N enrichment in the upper oceanic crust. This is also consistent with the observation from the basement hydrothermal fluids at the eastern flank of Juan de Fuca Ridge (i.e., the Baby Bare to Mama Bare Outcrops), where NH_4^+ in hydrothermal fluid is mainly sourced from overlying sediments and the sediment-derived NH_4^+ is consumed as it flows through the igneous basement (Wheat et al., 2000).

To test the control of overlying sediment on N enrichment in altered basalts at a global scale, we examined the average N concentrations of basalts from Holes 504B, 556, 417A and 1224F relative to their basal sediments. Although the N concentrations of the basal sediments at these sites have not been reported, they can be classified by the lithologies of their basal sediments section accumulated directly overlying the igneous basement for a qualitative test. Sites 504 and 556 are characterized by calcareous basal sediments (e.g., nannofossil chalk, limestone and nannofossil ooze; Table 1) similar to those at Site 1256, whereas Site 1224 is characterized by clay-rich sediments similar to Site 543. For reference, we applied the N concentrations of the basal sediments at Site 543 (claystone) and Site 1256 (carbonate) to Site 1224 (claystone) and Sites 504 and 556 (carbonate), respectively. Consistently, Hole 504B (8.0±3.8 ppm) and Hole 556 (8.7±3.3

ppm) have comparable average N concentrations to Hole 1256D (11.8±3.8 ppm) and lie close to the relationship defined by Sites 1149, 801, 1256 and 543 on Fig. 5. At Hole 417A, sediments were not deposited within the ~20 Myr of crustal formation. Therefore, the secondary N should have mainly come from dissolved NH_4^+ in seawater, which is not as abundant as that derived from clays. Consequently, N concentrations of Hole 417A basalts (7.3±3.8 ppm) are comparable to those associated with relatively N-poor carbonate-rich basal sediments (i.e., Holes 1256D, 504B and 556). Clay-rich sediments started to accumulate after ~20 Myr of crustal formation at Hole 417A, but apparently they did not significantly impact the N enrichment in 417A altered basalts. This is likely due to the sealing of fractures and voids by precipitation of secondary minerals within the first ~20 Myr of crustal formation which inhibits the ingress of fluids carrying sediment-derived N into oceanic crust.

In contrast to the data consistency of Holes 504B, 556, and 417A, Hole 1224F shows an apparent exception (Fig. 5). Although it cannot be excluded that these basal sediments are N-poor, clayey sediments sampled from the clay province of the Pacific Ocean close to Site 1224 are N-rich (hundreds of ppm; Müller, 1977). If the basal sediments are similarly N-rich, the N concentrations of the 1224F basalts would be expected to be much higher than the measured values (8.1±2.8 ppm), or even close to those of the altered basalts from Hole 543A (24.9±8.3 ppm). One possibility to reconcile this discrepancy is attributed to the existence of a low-permeable capping massive flow at the top of Hole 1224F (Paul et al., 2006), which could restrict the flux of downwelling fluid into the crust (Paul et al., 2006; Gillis et al., 2015; Coogan and Gillis, 2018) and consequently decrease the N availability to the oceanic crust.

2.1.4.4 Subducting N budget of the upper oceanic crust

Above quantitative understanding of the controlling factors of N enrichment in altered basalts allows us to better constrain the subducting N budget of the upper oceanic crust. Given that the N concentration of basal sediment are the most important parameter, we firstly examined the basal sediments section from each DSDP/ODP/IODP reference site located offboard individual subduction zones (Clift, 2017; Plank and Langmuir, 1998) to determine the lithologies (and N concentrations) of the basal sediments section accumulated directly overlying the igneous basement (Table A2 in Appendix A). So far, the entire section of subducting sediments has been recovered for 55% of world's subduction zones (i.e., 24252 km out of the 43819 km global subduction zones; Jarrard, 2003) (Table A2 in Appendix A). The lithologies of the basal sediments vary from clay-rich, carbonate-rich to silica-rich, which are similar to what have been observed at Sites 543, 1256, 801, and 1149. Consequently, the average N concentrations of basal sediments at Sites 543, 1256, 801, and 1149 are applied correspondingly (Table A2 in Appendix A). These N concentration data were then employed to estimate the average N concentrations of the upper oceanic crust for individual subduction zones (Table A2 in Appendix A) using the linear relationship in Fig. 5. For the other 45% subduction zones (19567 km in length, including Manila, Negros and Catabato trenches) where basal sediment data are unavailable, an average N concentration (10.1±7.8 ppm; $n = 109$; 1σ) of global altered basalts was applied (Table A2 in Appendix A). Another important parameter in this estimation is the thickness of the upper oceanic crust. In previous models estimating volatile budgets in subducting AOC, a standard stratigraphy of oceanic crust has been commonly employed, in which the thickness of the basaltic upper oceanic crust (or the volcanic section) is 600 m (e.g., Alt and Teagle, 1999; Kelemen and Manning, 2015). We adopted this standard stratigraphy but considered a heterogenous thickness with different spreading rate. The upper oceanic crust formed at fast-spreading (half-spreading rate > ~40 mm·yr^{-1}; Dick et al., 2003) to intermediate-spreading (half-spreading rate 28 – 40 mm·yr^{-1}; Dick et al., 2003) ridges are thicker with continuous layered structure; thus 600 m was used. The upper oceanic crust formed at slow-spreading ridges (half-spreading rate < ~28 mm·yr^{-1}; Dick et al., 2003) are thinner with complex structure (sometimes associated with gabbros and serpentinized peridotites); thus 300 m was used (e.g., Chen, 1992; Cannat, 1993, 1996; Cannat et al., 1995). Applying these parameters, together with the average dry density (2.7 g·cm^{-3}) of basaltic rocks, convergence rate, and trench length (Jarrard, 2003; Table 2), we obtained the N input flux from the upper oceanic crust for individual subduction zones (Table 2) and a global N input flux from the upper oceanic crust of $3.7\pm0.3\times10^9$ mol·yr^{-1}.

The N input flux of the upper oceanic crust has also been estimated by previous studies. For example, Busigny et al. (2011) employed a thickness of 2.5 km for the basaltic crust (Peacock, 1990) and the average N concentrations (6.5±2.6 ppm) of eclogites from Lago di Cignana in western Alps and the Raspas complex in Ecuador (Halama et al., 2010) to yield an N input flux of 9.3×10^9 mol·yr^{-1}. Employing the same thickness of 2.5 km for the subducting basaltic crust, the average N/K_2O ratios of blueschists and eclogites (19.3±2.0) from Jenner in California and the Raspas Complex in Ecuador, as well as the average K_2O contents (0.16 wt.% – 0.62 wt.%) of fresh MORB (Gale et al., 2013) and altered basalts from ODP Hole 801C (Kelley et al., 2003), Harris et al. (2022) obtained an N input flux of $4.4\pm0.4\times10^9$ mol·yr^{-1} to $1.7\pm0.9\times10^{10}$ mol·yr^{-1}. These estimations are up to 5 times higher than our estimate in this study. Besides using different datasets, a big difference among these estimates is the employment of different thickness (300 – 600 m in this study vs. 2.5 km in Busigny et al., 2011 and Harris et al., 2022). However, the 2.5 km of oceanic crust contains not only the upper volcanic section but also part of the lower intrusive sheeted dike and gabbro sections, which have very few data (Busigny et al., 2019; Li and Li, 2022).

If normalized to a unit thickness, our estimate ($6.1\pm0.6\times10^{6}$ mol·yr^{-1}·m^{-1}) is slightly higher than the estimate (3.7×10^{6} mol·yr^{-1}·m^{-1}) by Busigny et al. (2011) and is at the upper end of the range ($1.8\pm0.2\times10^{6}$ mol·yr^{-1}·m^{-1} to $6.9\pm0.6\times10^{6}$ mol·yr^{-1}·m^{-1}) estimated by Harris et al. (2022). It should be noted that these global unit fluxes can only be applied to the upper 300-600 meters of oceanic crust. The N budget in the deeper oceanic crust has to be estimated based on detailed constraints on sheeted-dike and gabbro samples from global oceanic crusts, which are still relatively few by far (Busigny et al., 2019; Li and Li, 2022).

2.1.5 Implications for N recycling in subduction zones

Our new data together with previously published data indicate that, despite ubiquitous addition of secondary N by low-temperature alteration, altered basalts in the upper oceanic crust retain relatively low N contents (1.3 – 48.4 ppm with an average of 10.1 ppm). In addition, although the secondary N in altered basalts is considered to mainly reside in the K^{+} site, the expected positive correlation between N and K_2O concentrations in altered basalts has not been observed, which is shown by a large variation in the N/K atomic ratio (7 ± 7 - $307\pm425 \times 10^{-4}$) (Fig. 6a). This suggests that the low-temperature alteration-induced enrichment of N in basaltic rocks is relatively inefficient and more complicated than previous thought.

Similar to altered basalts, their metamorphic equivalents (i.e., blueschists and eclogites) from several different sites, show highly variable N/K atomic ratios ($15 - 432 \times 10^{-4}$; Fig. 6a). But blueschists and eclogites commonly show a much better correlation between N and K_2O concentrations than altered basalts (Fig. 6B; Halama et al., 2010; Li et al., 2021c; Harris et al., 2022). This suggests that N in altered basalts may be re-organized into K-rich minerals (e.g., mica) during prograde metamorphism inside subduction zones. Another interesting observation is that blueschists contain much more abundant N than global altered basalts (Fig. 6b and 6c), which supports a second N enrichment process inside the subduction channel during the early subduction stage by fluid remobilized sedimentary N in the mélange (e.g., Li et al., 2021c; Harris et al., 2022). This indicates persistent N enrichment of AOC from mid-ocean ridge to the early subduction stage. In contrast, eclogites show lower N concentrations largely overlapping with those of altered basalts (Fig. 6c). Although this difference could possibly be attributed to spatial heterogeneity in their protoliths, it is more likely indicative that the metamorphosed basalts start to lose N rather than continuously gain N during high-grade metamorphism (e.g., eclogite facies). This is best illustrated by the prograde blueschist-eclogite sequence from Tianshan, where the breakdown of phengite from blueschist to eclogite results in progressive loss of N and decrease of N/K atomic ratios (Fig. 6a; Halama et al., 2017). This hypothesis can be further tested by future studies on blueschists and eclogites from broader spatial and age spectra.

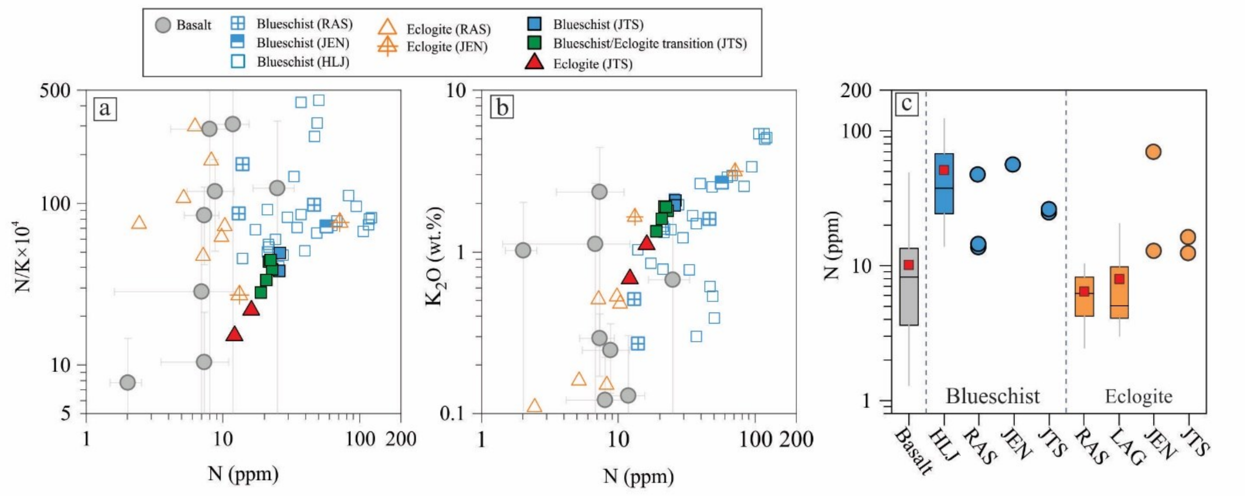

Figure 6. Comparison of N concentrations of altered basalts, blueschists and eclogites with (a) their N/K molar ratios, (b) K_2O concentrations, and (c) difference sites. Note: (1) a progressive loss of N during prograde metamorphism from blueschist to eclogite is observed in the JTS sequence in Southern Central Tianshan Suture Zone (A-B); (2) in panel C, blueschists and/or eclogites with sample numbers > 6 from individual locality are shown as box plot, whereas these

with samples numbers < 6 (i.e., RAS, JEN and JTS) are plotted as individual data points (filled circles). Abbreviations in the diagram: RAS = Raspas Complex in Ecuador (Halama et al., 2010); JEN = Jenner in California (Harris et al., 2022); HLJ = Heilongjiang Complex in Northeast China (Li et al., 2021a); JTS = JTS sequence in Southern Central Tianshan Suture Zone (Beinlich et al., 2010; Halama et al., 2017); LAG = Lago di Cignana in Western Alps (Halama et al., 2010).

2.1.6 Conclusions

Characterization of nitrogen concentrations and isotope compositions of altered basalts is expanded from ODP/IODP Holes 504B, 801C, 1149D and 1256D to DSDP/ODP Holes 417A, 543A, 556, and 1224F. These altered basalts with diverse alteration degree, crustal age, spreading rate, and basal sediment type allow a full investigation of the controlling factors on the magnitude of nitrogen enrichment in the upper oceanic crust during low-temperature hydrothermal alteration. We found that altered basalts in global oceanic crusts are ubiquitously enriched in secondary nitrogen (1.3 – 48.4 ppm), mainly from sediments/seawater with a minor contribution from abiotic N_2 reduction. The magnitude of nitrogen enrichment in the upper oceanic crust is mainly determined by local nitrogen availability, which is further dependent on the nitrogen abundance of basal sediments. Taking this primary controlling factor into consideration, we estimated the nitrogen input flux of each individual subduction zone, from which a global nitrogen input flux of $3.7\pm0.3\times10^9$ $mol\cdot yr^{-1}$ is yielded for the 300 – 600 m altered upper oceanic crust. Our new data also demonstrate that N concentrations are relatively low in global altered basalts. In comparison, blueschists have much higher nitrogen concentrations whereas eclogites have relatively low nitrogen concentrations similar to altered basalts. This implies more nitrogen enrichment to meta-basalts inside subduction channel during early subduction (at least to blueschist facies) but nitrogen devolatilization from meta-basalts during deep subduction (by eclogite facies).

Table 1. Summary of geological characteristics of the investigated DSDP/ODP Holes.

Site	N[a] (ppm)	±[a]	Age (Ma)	LOI[b] (wt.%)	±[b]	K_2O[c] (wt.%)	±[c]	SPR[d] ($mm \cdot yr^{-1}$)	Lithology of basal sediments[e]	Basal sedimentary N (ppm)[f]	±[f]
1256D	11.8	3.8	15	1.37	1.81	0.12	0.16	110	nannofossil ooze	177.7	71.8
801C	7.0	5.4	170	6.04	7.43	0.81	1.26	80	radiolarite interbedded with claystone	77.0	39.5
1149D	2.0	0.5	132	6.50	8.48	0.87	0.74	51	radiolarian chert interbedded with nannofossil chalk	20.5	3.5
504B	8.0	3.8	5.9	2.33	1.14	0.09	0.08	34	nannofossil chalk and limestone	177.7[g]	71.8
556	8.7	3.3	30	1.41	0.53	0.25	0.11	10	nannofossil ooze and chalk	177.7[g]	71.8
1224F	8.1	2.8	46	0.24	0.2	0.34	0.24	71	claystone	297.0[g]	42.8
543A	24.9	8.3	81	1.51	0.76	0.67	1.05	11.5	claystone	297.0	42.8
417A	7.3	3.8	120	6.76	2.81	2.34	2.09	15	no sedimentation	n.a	n.a

a. Average and 1 SD of N concentrations of AOC (data source: Li et al., 2007; Bebout et al., 2018; Li and Li, 2022; this study).

b. Average and 1 SD of loss on ignition data of AOC (data source: Shipboard Scientific Party, 1980, 1984, 1985; Bougault et al., 1984; Natland et al., 1984; Alt et al., 1996; Bach et al., 2003; Kelley et al., 2003; Expedition 309/312 Scientists, 2006; Haraguchi and Ishii, 2006; Seyedali et al., 2021)

c. Average and 1 SD of K_2O concentrations of AOC (data source: Shipboard Scientific Party, 1980; Bougault et al., 1984, 1984, 1985; Natland et al., 1984; Alt et al., 1996; Bach et al., 2003; Kelley et al., 2003; Expedition 309/312 Scientists, 2006; Haraguchi and Ishii, 2006; Seyedali et al., 2021).

d. Spreading rate (SPR; data source: Shipboard Scientific Party., 1990, 2000, 2003b; Jarrard et al., 2003).

e. Lithology of basal sediment section directly overlying the igneous basement at different DSDP/ODP sites (Shipboard Scientific Party, 1980, 1984, 1985, 2003a, b; Alt et al., 1996; Kelley et al., 2003).

f. Average and 1 SD of N concentrations of basal sediments (data source: Shipboard Scientific Party, 2003b; Sadofsky and Bebout, 2004).

g. Nitrogen concentrations of basal sediments were assigned based on the lithologies of the basal sediments directly overlying the igneous basement.

Table 2. Nitrogen input flux of upper oceanic crust of world's major subduction zones.

Subduction Zones	Length[a] (km)	Convergence rate ($mm\cdot yr^{-1}$)[a]	N flux($mol\cdot yr^{-1}$)
Southern Chile[b]	1218	16	$2.3^{\pm1.8}\times10^{7}$
Central Chile[b]	1306	71	$1.1^{\pm0.8}\times10^{8}$
North Chile[c]	1579	74	$1.7^{\pm1.2}\times10^{8}$
Peru[c]	1599	65	$1.5^{\pm1.1}\times10^{8}$
Columbia-Ecuador[c]	1355	65	$1.3^{\pm0.9}\times10^{8}$
Central America[e]	1400	85	$2.1^{\pm0.1}\times10^{8}$
Mexico[c]	1383	49	$1.7^{\pm0.3}\times10^{8}$
Kurile[b]	1243	75	$2.1^{\pm0.4}\times10^{7}$
Kamchatka[c]	900	74	$9.7^{\pm6.8}\times10^{7}$
NE Japan[b]	1061	76	$9.4^{\pm7.3}\times10^{7}$
Izu-Bonin-Mariana[f]	2450	41	$6.2^{\pm0.2}\times10^{7}$
Ryukyu[c]	1153	57	$1.6^{\pm0.3}\times10^{8}$
Philippine[c]	1509	64	$2.4^{\pm0.5}\times10^{8}$
Tonga[b]	1460	148	$2.5^{\pm1.9}\times10^{8}$
Kermadec[b]	1422	52	$8.6^{\pm6.7}\times10^{7}$
Hikurangi[b]	794	21	$1.9^{\pm1.5}\times10^{7}$
South Sandwich[c]	1005	44	$3.2^{\pm2.2}\times10^{7}$
Lesser Antilles[d]	800	24	$2.8^{\pm0.9}\times10^{7}$
Aleutians, W[b]	1102	18	$2.3^{\pm1.8}\times10^{7}$
Aleutians, E[b]	1246	59	$8.6^{\pm6.6}\times10^{7}$
Alaska[c]	1490	56	$2.1^{\pm0.4}\times10^{8}$
Nankai[c]	824	38	$7.7^{\pm1.5}\times10^{7}$
Sumatra[c]	2462	50	$3.0^{\pm0.6}\times10^{8}$
Java[c]	1200	71	$2.1^{\pm0.4}\times10^{8}$
Sunda East[c]	950	71	$1.7^{\pm0.3}\times10^{8}$
Andaman-Burma[b]	1089	23	$2.9^{\pm2.3}\times10^{7}$
Markan[c]	950	37	$8.7^{\pm1.7}\times10^{7}$
Aegean[b]	850	5	$4.9^{\pm3.8}\times10^{6}$
Cascadia[b]	990	36	$4.1^{\pm3.2}\times10^{7}$
Manila[b]	1050	10	$1.2^{\pm1.0}\times10^{7}$
Negros[b]	400	20	$9.3^{\pm7.2}\times10^{6}$
Sulawesi. N[b]	600	30	$2.1^{\pm1.6}\times10^{7}$
Sulu[b]	500	20	$1.2^{\pm0.9}\times10^{7}$
Cotabato[b]	500	20	$1.2^{\pm0.9}\times10^{7}$
San Cristobal[b]	1050	49	$6.0^{\pm4.6}\times10^{7}$
Yap-Palau[b]	550	3	$1.9^{\pm1.5}\times10^{6}$
Torbriand[b]	590	20	$1.4^{\pm1.1}\times10^{7}$
Vanuatu[b]	1189	111	$1.5^{\pm1.2}\times10^{8}$
New Britain[b]	600	110	$7.7^{\pm6.0}\times10^{7}$
Global total	43819		$3.7^{\pm0.3}\times10^{9}$

a. Convergence rate and trench length of global subduction zones are from Jarrard (2003).

b. Global average nitrogen concentration of 10.1±7.8 ppm in the upper oceanic crust is.

c. The N concentration of the upper oceanic crust is calculated based on the equation in Fig. 5.

d. Flux calculated by employing Hole 543A as a reference site.

e. Flux calculated by employing Holes 1256D and 504B as two reference sites (see Li and Li, 2022).

f. Flux calculated by employing Hole 801C as a reference site (see Li and Li, 2022).

Chapter 2.2 Nitrogen enrichment in the altered gabbroic oceanic crust and global nitrogen budget of subducting slabs

2.2.1 Introduction

Seawater-oceanic crust interaction modifies the geochemical compositions of not only seawater (e.g., Humphris and Thompson, 1978; Staudigel and Hart, 1983; Alt and Honnorez, 1984; Seyfried Jr, 1987) but also AOC. The subduction of AOC will further impact the geochemical features, particularly of volatile elements such as N, of the mantle (e.g., Dasgupta, 2013; Mallik et al., 2018; Bekaert et al., 2021). To quantify the N recycling across subduction zones, the N budget of subducting slabs, predominantly composed of AOC, has been a research focus (e.g., Busigny et al., 2005; Li et al., 2007; Busigny et al., 2011; Bebout et al., 2018; Busigny et al., 2019).

A typical AOC section contains the upper volcanic section and the lower intrusive section composed of sheeted dikes and gabbros (Penrose Conference Participants., 1972). So far, most of the N studies on AOC have been focused on the upper 300 – 600-meter volcanic section (e.g., Busigny et al., 2005; Li et al., 2007; Bebout et al., 2018; ***Chapter 2.1***). Those studies show that the volcanic section of AOC, which has been mostly altered at low temperatures (< 100°C) with high water/rock ratios (e.g., Seyfried Jr, 1987; Alt and Bach, 2001; Staudigel, 2014), is variably enriched in secondary N with N concentrations mostly falling into the range of 1.3 to 48.4 ppm (e.g., Busigny et al., 2005; Li et al., 2007; Bebout et al., 2018; ***Chapter 2.1***).

In contrast to the upper volcanic section, sheeted dikes and gabbroic rocks, which comprise the majority of AOC, have been rarely studied for N concentrations and isotope compositions. So far, only 15 sheeted dike samples from ODP/IODP Holes 504B and 1256D and 10 gabbro samples from Hole 1256D have been examined (Busigny et al., 2019; ***Chapter 3.3***). The results show significant N enrichment also in sheeted dikes (N concentrations: 4.0 – 33.5 ppm; $\delta^{15}N$ values: -3.7‰ – +5.0‰) and gabbros (N concentrations: 6.2 – 23.8 ppm; $\delta^{15}N$ values: -0.4‰ – +3.2‰) during moderate- to high-temperature alterations. However, whether such N enrichment is limited in local scale or occurs commonly in global oceanic crust and how this would impact the N budget in global oceanic crust remains unknown.

Benefited from ODP and IODP drillings in global oceanic basement, gabbroic rocks have been widely recovered from 'tectonic windows', where lower gabbroic sections of AOC were tectonically unroofed onto the seafloor by low-angle detachment faults (e.g., in the Hess Deep Rift in the East Pacific Ocean, the Atlantis Bank in the Southwest Indian Ridge and the Atlantis Massif in the Atlantic Mid-ocean Ridge; Shipboard Scientific Party, 1999; Expedition 304/305 Scientists, 2006a; Coogan, 2014). These sites thus provide valuable opportunities to further characterize alteration-induced N enrichment in the gabbroic section of AOC.

In this study, I conducted new analyses of N concentrations and $\delta^{15}N$ values of 38 gabbroic rocks from ODP Hole 735B at the Atlantis Bank, IODP Hole 1415P at the Hess Deep Rift and IODP Hole 1309D at the Atlantis Massif. These selected samples are characterized by background alterations without obvious alteration halos or veins. These new data, integrated with literature data, are expected to provide a better understanding of N enrichment in the gabbroic sections of AOC. This large dataset further facilitates the determination of the global subducting N budget in the entire AOC and quantification of the fractions of slab N that is recycled back to the surface via arc volcanoes and subducted into the deep mantle, respectively.

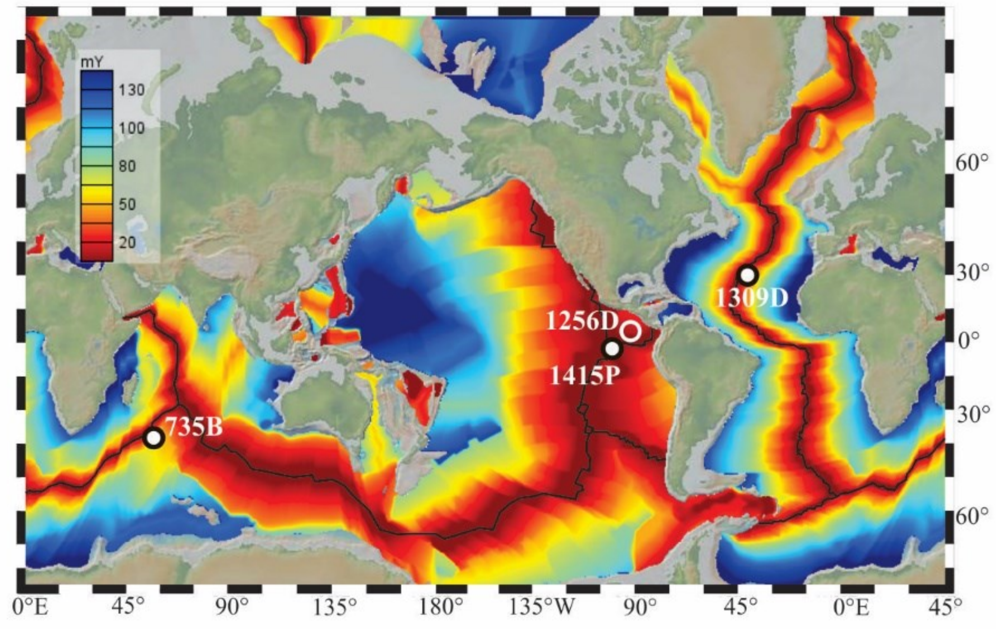

Figure 7. Global oceanic crust map showing sample sites of oceanic gabbroic rocks. The crustal ages are generated by GeoMapApp (http://www.geomapapp.org). The gabbro samples studied here are from ODP Hole 735B at the Atlantis Bank in the Southwest Indian Ridge, IODP Hole 1415P at the Hess Deep in the East Pacific Rise and IODP Hole 1309D at the Atlantis Massif in the Mid-Atlantic Ridge. ODP/IODP Hole 1256D, which is studied in ***Chapter 3.3***, is also shown for reference.

2.2.2 Geological background and samples

The 38 gabbroic rocks studied here include 13 from Hole 1309D, 10 from Hole 1415P and 15 from Hole 735B (Fig. 7). These rocks represent the lower oceanic crustal layers which were rapidly (< ~1 Ma; e.g., Baines et al., 2008; Grimes et al., 2008; Schwartz et al., 2009; Schoolmeesters et al., 2012) unroofed onto seafloor by faulting (e.g., Ildefonse et al., 2007; Smith and Schouten, 2018). Their alteration characteristics are described in detail below.

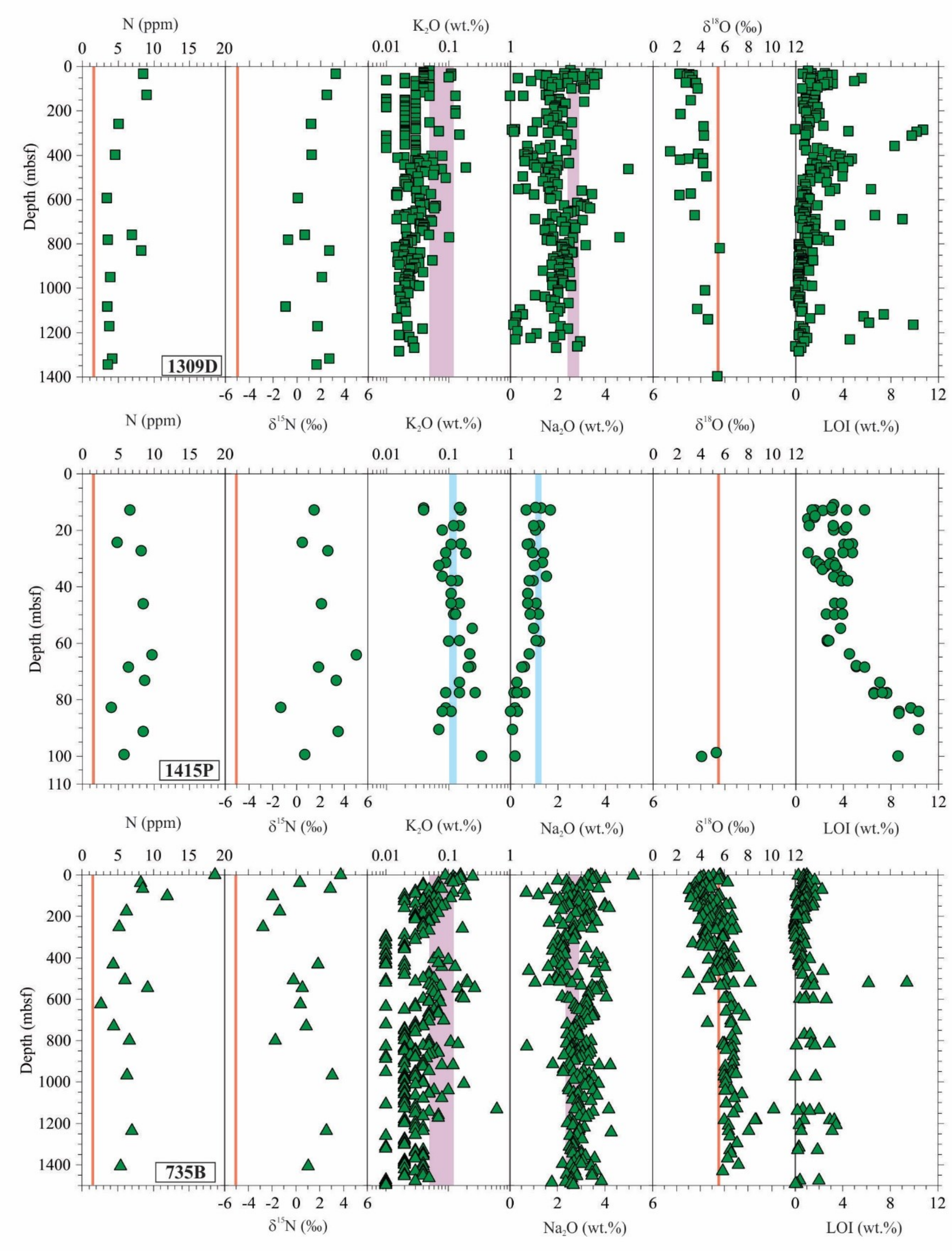

Figure 8. Downhole variations of N concentrations, δ^{15}N values, K$_2$O, Na$_2$O concentrations, δ^{18}O values and LOI contents of gabbroic rocks from IODP Hole 1309D (top row), IODP Hole 1415P

(middle row) and ODP Hole 735B (bottom row). (Data source: Shipboard Scientific Party, 1999; Bach et al., 2001; Alt and Bach, 2006; Castelain, 2011; Expedition 304/305 Scientists, 2006b; Gillis et al., 2014c; McCaig et al., 2018). All data error bars are smaller than the data symbols. The red bars in the panels of N concentration (1.5 ppm), $\delta^{15}N$ value (-5.0‰), and $\delta^{18}O$ value represent the value of fresh MORB (Marty, 1995; Eiler et al., 2000; Li et al., 2007). The pink bars represent the average K_2O concentration ($0.09^{\pm0.04}$ wt.%; VanTongeren et al., 2021) and Na_2O concentration ($2.50^{\pm0.08}$ wt.%; VanTongeren et al., 2021) of the high-level gabbroic lower oceanic crust. The blue bars represent the average K_2O ($0.12^{\pm0.01}$ wt.%) and Na_2O concentration ($1.16^{\pm0.10}$ wt.%) of the low-level gabbroic section estimated by Gillis et al. (2014a).

(1) ODP Hole 735B (Atlantis Bank)

Hole 735B was drilled into the ~12 Ma Atlantis Bank, which is a block tectonically unroofed onto the seafloor by a detachment fault (Ildefonse et al., 2007) and lies ~95 km south of the present-day ultraslow-spreading Southwest Indian Ridge (SWIR; half spreading rate: 6 – 10 $mm \cdot yr^{-1}$). A total of 1506 m gabbroic rocks, dominated by olivine gabbro, were recovered from Hole 735B (Shipboard Scientific Party, 1989, 1999). Fluid inclusions in the upper 500 m of the gabbroic rocks suggest that these rocks were initially emplaced at 1.5 – 2.0 km below the seafloor, which is close to the sheeted dike-gabbro transition (Vanko and Stakes, 1991; Dick et al., 2000, 2019). The lack of layering in these gabbroic rocks suggests that they represent the high-level gabbro section.

The gabbroic rocks in the hole were generally fresh to 40% altered, which is lower than the plutonic section recovered from Hole 1309D, Hole 1415P and other fracture-zone environments (e.g., Mével et al., 1991; Gillis et al., 1993; Shipboard Scientific Party, 1999). Multi-stage alteration history has been revealed from this core, including (i) early stage on-axis high-temperature (~ 450 – >700 ºC) amphibolite- to granulite- facies hydrothermal alteration, which produced amphibole and secondary plagioclase (Shipboard Scientific Party, 1999; Dick et al., 2000); (ii) moderate-temperature (~350 – 450 ºC) greenschist-facies alteration, which produced amphibole, chlorite and secondary plagioclase (Shipboard Scientific Party, 1999; Dick et al., 2000); (iii) low-temperature (< ~350 ºC) zeolite-facies alteration, which produced zeolite, chlorite-smectite mixed layer phases (~100 – 350 ºC), smectite (mainly saponite; <150 ºC), oxyhydroxides and carbonate (~10 ºC; Shipboard Scientific Party, 1999; Alt and Bach, 2001a; Nozaka et al., 2008). Overall, the degree of high-temperature amphibolite-facies to moderate-temperature greenschist-facies alterations is most intense (30% – 45%) in the upper 500 m of the hole and broadly decreases downhole to 2%. The degree of low-temperature alteration remains low throughout the hole (<1% – 2%) but is slightly higher in the intervals of 0 – 40 mbsf (3%), 500 – 600 mbsf (8%) and 1050 – 1300 mbsf (4%), where abundant smectite ± carbonate ± oxyhydroxides were present due to the fracturing in the vicinity of late brittle faults (Shipboard Scientific Party, 1999; Alt and Bach, 2001, 2006; Bach et al., 2001).

Geochemically, the upper section (0 – 500 mbsf) of the hole shows common ^{18}O depletions relative to MORB as a result of interaction with hydrothermal fluids at moderate to high temperatures (400 – >600 °C; Stakes, 1991). In contrast, the lower section (500 – 1506 mbsf) of the hole commonly exhibits ^{18}O enrichments due to reaction with ^{18}O-enriched fluids at moderate to high temperature (250 – 600 °C) with a lesser contribution from low-temperature alteration by seawater (~ 10 to 250 °C; Alt and Bach, 2006). The K_2O concentrations of the gabbroic rocks from the majority part of the hole ($0.04^{\pm0.03}$ wt.%; 1σ; n = 190; Fig. 8) are comparable to that of the high-level gabbroic lower oceanic crust (average: $0.09^{\pm0.04}$ wt.%; VanTongeren et al., 2021), except for the three intervals (i.e., 0 – 40 mbsf, 500 – 600 mbsf and 1000 – 1250 mbsf; Fig. 8) with higher degrees (3 – 8%) of low-temperature alteration (Bach et al., 2001), which resulted in K_2O enrichments (up to 0.61 wt.%; Fig. 8). The Na_2O concentrations of these gabbroic rocks (average:

$2.86^{\pm 0.68}$ wt.%; 1σ; n = 275) are comparable to that of the estimated high-level gabbroic lower oceanic crust (average: $2.50^{\pm 0.08}$ wt.%; VanTongeren et al., 2021).

(2) IODP Hole 1415P (Hess Deep Rift)

The hole was drilled into ~1.3 Ma oceanic crust (Rioux et al., 2012), which was formed at the fast-spreading (half spreading rate: ~75 $\mathrm{mm \cdot yr^{-1}}$; Rowan and Rowley, 2014) East Pacific Rise (EPR). The gabbroic body was tectonically unroofed onto the seafloor due to the westward propagation of the Cocos-Nazca rift towards the east flank of EPR at a rate of ~65 $\mathrm{mm \cdot yr^{-1}}$ (Lonsdale, 1988). A total of ~97 m gabbroic rocks was recovered, including the upper ~54 m of layered olivine gabbro and the lower ~43 m of troctolite (Gillis et al., 2014c). The layering in the olivine gabbros is similar to the layered gabbros from the low-level gabbro sections in ophiolite (e.g., Hopson et al., 1981), suggesting that the initial emplacement depth of these gabbroic rocks was > 2 km beneath the sheeted dike-gabbro transition (Faak and Gillis, 2016). With the assumption that the sheeted dike-gabbro transition occurs at 1.5 – 2.0 km depth in crust formed at fast spreading ridges, as observed in Hole 1256D and the Oman ophiolite (Hopson et al., 1981; Expedition 309/312 Scientists, 2006), this corresponds to an initial emplacement depth of >3.5 – 4.0 km for the gabbroic rocks at Site 1415.

These gabbroic rocks were variably altered with increasing loss on ignition (LOI) from the upper olivine gabbro section to the lower troctolite section, suggesting that olivine gabbros are less altered (10 – 40%) than troctolite (30 – 80%) (Gillis et al., 2014b, c). The hydrothermal alteration spans from high-temperature upper amphibolite facies to low-temperature zeolite facies (Gillis et al., 2014b, c). The secondary mineral assemblage (amphibole + chlorite) formed during amphibolite facies at high temperatures of 450 – 650 °C is widespread in Hole 1415P (Gillis et al., 2014b, c). The predominant alteration occurred at lower greenschist facies (~200 – 400°C) to zeolite facies (~100 – 200°C) as revealed by the assemblage of serpentine, prehnite and chlorite and the assemblages of zeolite and clay minerals, respectively (Gillis et al., 2014b, c).

The available $\delta^{18}O_{VSMOW}$ values (+4.1‰ to +5.3‰; Fig. 8) of two troctolites from the lower section of Hole 1415P indicate alteration temperatures of > 200°C (McCaig et al., 2018). Consistently, the K_2O concentrations of these gabbroic rocks (average: $0.11^{\pm 0.07}$ wt.%; 1σ; n = 36; Fig. 8) are comparable to that of the low-level gabbroic section ($0.12^{\pm 0.01}$ wt.%) estimated by Gillis et al. (2014a). The Na_2O concentrations of these layered gabbroic rocks (average: $0.84^{\pm 0.43}$ wt.%; 1σ; n = 36) are also consistent with the estimated Na_2O concentration (average: $1.16^{\pm 0.10}$ wt.%) of the low-level gabbros given by Gillis et al. (2014a).

(3) IODP Hole 1309D (Atlantis Massif)

Hole 1309D was drilled into ~1.2 Ma oceanic crust, which was tectonically unroofed from depths by a detachment fault to the central dome of the Atlantis massif, located near 30 ºN at the intersection of the slow-spreading Mid-Atlantic Ridge (half-spreading rate of ~11.8 $mm \cdot yr^{-1}$) and the Atlantis Transform Fault (Expedition 304/305 Scientists, 2006a; Grimes et al., 2008). The recovered 1415.5 m gabbroic rocks from Hole 1309D predominantly comprise of gabbro and olivine gabbro with minor proportions of troctolite, Fe-Ti oxide gabbro, diabase and ultramafic rocks (Expedition 304/305 Scientists, 2006b). These gabbroic rocks were probably emplaced at a depth of ~7 km (Grimes et al., 2008). The abundant metadiabase intrusions at the upper 130 m of the hole suggest that these gabbroic rocks were emplaced just below the dike-gabbro transition (McCaig and Harris, 2012). No layering was observed in these gabbroic rocks (Expedition 304/305 Scientists, 2006a).

The drill core samples record a complex alteration history from early-stage high-temperature granulite-/upper-amphibolite-facies to late-stage low-temperature zeolite-facies metamorphism (Expedition 304/305 Scientists, 2006b; Nozaka and Fryer, 2011). The gabbroic rocks were dominantly affected by lower amphibolite-facies to upper greenschist-facies hydrothermal alterations at high temperatures of 400 – 500 °C as revealed by the presence of amphibole, chlorite and secondary plagioclase (Expedition 304/305 Scientists, 2006b; Castelain, 2011). Lower greenschist-facies secondary mineral assemblages formed at moderate temperatures of 300 – 400 °C in the gabbros, including serpentine after olivine and prehnite after plagioclase, are spatially correlated with the olivine-rich rocks (e.g., troctolitic gabbro and olivine gabbro; Expedition 304/305 Scientists, 2006b; Castelain, 2011). Late-stage zeolite-facies alteration at low temperatures of ~120 – 300 °C produced an assemblage of zeolite, clay minerals (e.g., saponite, vermiculite) and carbonate (Expedition 304/305 Scientists, 2006b; Jöns et al., 2013). Especially, saponite formed at ~120 – 150 °C was observed throughout the hole, while vermiculite was only observed at deeper level (> 900 mbsf) at < 200 – 300 °C (Nozaka et al., 2008). Overall, the degree of alteration decreases from moderate (~50%) in the upper ~400 m, to low (~30%) between 400 to 800 mbsf and to minor (~10%) between 800 to 1415 mbsf (Expedition 304/305 Scientists, 2006a, b).

The gabbroic rocks show ^{18}O depletions with $\delta^{18}O$ values of +1.4‰ to +5.4‰, suggesting that the alteration occurred at temperature > 200 – 250 °C (Fig. 8; Castelain, 2011). The K_2O concentrations of these gabbroic rocks (average: $0.03^{\pm0.02}$ wt.%; 1σ; n = 202; Fig. 8) are comparable to that of the high-level gabbroic lower oceanic crust (average: $0.09^{\pm0.04}$ wt.%; VanTongeren et al., 2021). The Na_2O concentrations of these gabbroic rocks (average: $1.92^{\pm0.81}$

wt.%; 1σ; n = 202) are comparable to that of the estimated high-level gabbroic lower oceanic crust (average: $2.50^{\pm 0.08}$ wt.%; VanTongeren et al., 2021).

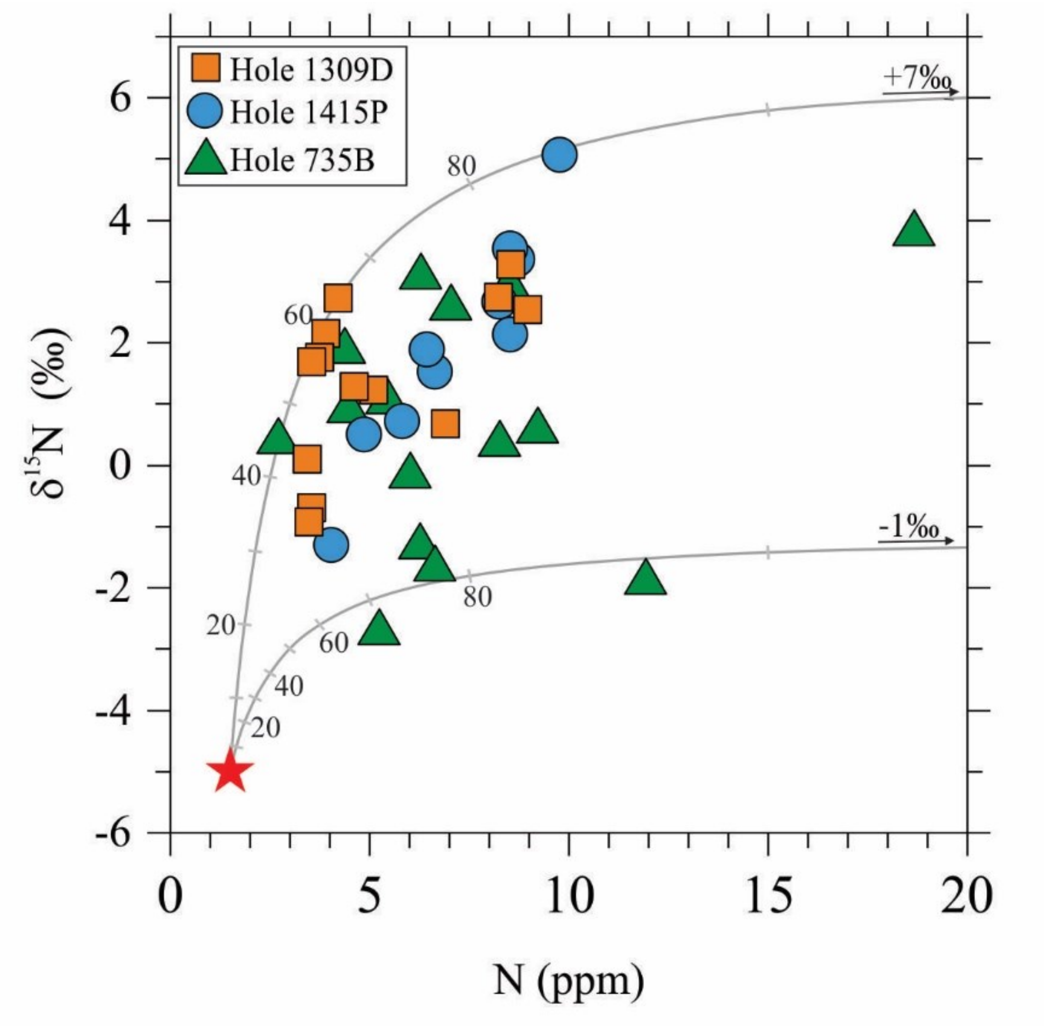

Figure 9. The relationship between N concentrations and $\delta^{15}N$ values of altered gabbros from Holes 1309D, 1415P and 735B. All data error bars are smaller than the data symbols. The red stars represent the N concentration and $\delta^{15}N$ value of fresh mid-ridge ocean basalt (MORB) inherited from the mantle (N = 1.5 ppm; $\delta^{15}N$ = -5.0‰; Marty, 1995; Marty and Humbert, 1997; Marty and Dauphas, 2003; Li et al., 2007; Marty et al., 2020). All the gabbro data fall into the two-component mixing curves between fresh MORB and secondary N derived from seawater/sediments with a $\delta^{15}N$ range from -1‰ – +7‰.

2.2.3 Results

The N concentrations and δ^{15}N values of the studied samples are listed in Table B1 in Appendix B. The gabbroic samples contain 2.7 to 18.7 ppm N (average: $7.4^{\pm 3.8}$ ppm) with δ^{15}N values of -2.7‰ to +3.8‰ (average: $+0.6^{\pm 2.0}$ ‰) for Hole 735B (1σ; n = 15), 4.0 to 9.8 ppm N (average: $7.2^{\pm 1.9}$ ppm) with δ^{15}N values of -2.2‰ to +5.1‰ (average: $+1.9^{\pm 2.0}$‰) for Hole 1415P (1σ; n =10), and 3.5 to 9.0 ppm N (average $5.3^{\pm 2.1}$ ppm) with δ^{15}N values of -0.9‰ to +3.3‰ (average: $1.4^{\pm 1.3}$‰) for Hole 1309D (1σ; n =13), respectively. Neither N concentrations nor δ^{15}N values of these gabbroic rocks show obvious downhole trend (Fig. 8), but a broad positive correlation is observed between N concentrations and δ^{15}N values (Fig. 9).

2.2.4 Discussion

2.2.4.1 Ubiquitous N enrichment in global gabbroic rocks

Compared to the N concentration of fresh MORB (~1.5 ppm; e.g., Sakai et al., 1984; Marty, 1995; Li et al., 2007), the studied gabbroic rocks all show higher N concentrations (2.7 – 18.7 ppm), indicating ubiquitous N enrichment in these gabbroic rocks from global ocean floor. These enrichments have also been observed in the gabbros from Hole 1256D (6.2 – 23.8 ppm; ***Chapter 3.3***). Integrating the data of the 1256D gabbros, an average N concentration of $7.6^{\pm 4.1}$ ppm (1σ; n = 48) is obtained for gabbroic rocks from global oceans, which is close to the average N concentration of $9.7^{\pm 7.7}$ ppm of the upper volcanic rocks from global oceans (***Chapter 2.1***). This suggests that gabbroic rocks are able to assimilate N in comparable amounts to the overlying basalts during hydrothermal alteration.

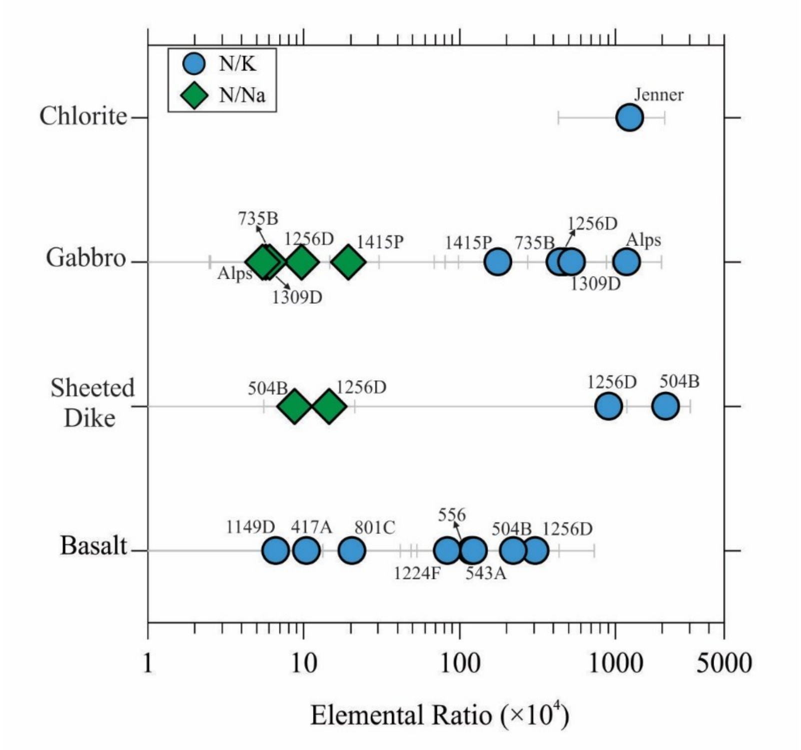

Figure 10. Comparison of bulk-rock N/K and/or N/Na molar ratios among altered basalts, sheeted dikes and gabbros (data source: Li et al., 2007; Bebout et al., 2018; Busigny et al., 2019), the hydrothermally affected meta-gabbros from western Alps (Busigny et al., 2011), and chlorite in high-pressure metamorphic rocks from Jenner, California ($1248^{\pm 818}\times 10^{-4}$; Harris et al., 2022).

Nitrogen in silicate rocks typically occurs as ammonium (NH_4^+) which can substitute for potassium (K^+) and/or sodium (Na^+) in mineral lattices (e.g., mica, plagioclase, clinopyroxene; Honma and Itihara, 1981; Watenphul et al., 2010; Li et al., 2021b). In altered basalts from the upper oceanic crust, N is thought to reside predominantly in clay minerals (e.g., Li et al., 2007; Busigny et al., 2005; Bebout et al., 2018), which are common secondary minerals from low-temperature (< 100 °C) alteration (e.g., Staudigel, 2014). In contrast, the gabbroic rocks in this study experienced complex alterations from early-stage high-temperature granulite facies to late-stage low-temperature zeolite facies. To better understand the potential N residence in altered gabbros, we examined the N/K and N/Na molar ratios of the altered gabbroic samples. The results show that, compared with the highly variable but relatively small N/K molar ratios in altered basalts ($7^{\pm7}$ – $306^{\pm424} \times 10^{-4}$; Fig. 10), the gabbroic rocks from the three sites in this study show much higher N/K molar ratios ($177^{\pm96}$ – $525^{\pm426} \times 10^{-4}$) but slightly lower than the meta-gabbros from western Alps ($1186^{\pm799} \times 10^{-4}$; Busigny et al., 2011). The N/K ratios of these altered gabbros are consistent with those of the altered gabbros from Hole 1256D ($473^{\pm405} \times 10^{-4}$) and the altered sheeted dikes from Holes 1256D ($906^{\pm986} \times 10^{-4}$) and 504B ($906^{\pm986}$ – $2112^{\pm924} \times 10^{-4}$; ***Chapter 3.3***). This suggests that, if NH_4^+ is incorporated into the K^+ site in secondary minerals (e.g., amphibole and feldspar) in altered gabbroic rocks, it requires a much higher NH_4^+ substitution coefficient. While this could be induced by higher temperatures, the extremely high N/K molar ratios in the altered sheeted dikes from Hole 504B (average: $2112^{\pm924} \times 10^{-4}$) suggests occurrence of some NH_4^+-endmember phases of K-bearing minerals (***Chapter 3.3***), which have not been observed in any samples from Holes 1256D and 504B. Moreover, during the moderate- to high-temperature alterations of the gabbroic rocks, the leaching of K^+ out of oceanic crust (Edmond et al., 1979; Von Damm, 1990) forming K-poor secondary minerals does not favor the addition of NH_4^+. Alternatively, as proposed in ***Chapter 3.3***, Na-bearing minerals (e.g., secondary plagioclase and amphibole) in the gabbroic rocks and sheeted dikes, where Na^+ remains unchanged or shows a slight gain by forming Na-rich minerals (e.g., secondary plagioclase; Alt et al., 1996; Staudigel, 2014b), are the most probable host for NH_4^+. Comparison between the N/Na molar ratios of the altered gabbroic rocks and N/K ratios of altered basalts, the N/Na molar ratios of these gabbroic rocks ($6^{\pm3}$ – $19^{\pm11} \times 10^{-4}$; Fig. 10) are at the lower-end of the N/K molar ratios of global altered basalts. This is consistent with the fact that the Na^+ site should have a slightly lower capacity to host NH_4^+ than the K^+ site (Honma and Itihara, 1981). In the altered gabbroic rocks, secondary plagioclase (albite) is likely the predominant Na^+-bearing mineral that can incorporate NH_4^+ in its crystal lattice. Besides the

K- and Na-bearing minerals, Harris et al. (2022) studied chlorite in the high-pressure rocks from Jenner at California and detected N up to 83 ppm with N/K molar ratios of $1248^{\pm 818} \times 10^{-4}$, which stands in the upper end of the N/K range of altered sheeted dikes and gabbroic rocks (Fig. 10). Therefore, the widespread chlorite in the altered gabbroic rocks could also be an important N host, although the incorporation mechanism of N into chlorite remains uncertain (***Chapter 3.3***). Regardless of the exact N residence site in minerals, the incorporation of NH_4^+ in secondary plagioclase/amphibole/chlorite requires that the uptake of N should have occurred in the moderate- to high-temperature alteration stages (> ~ 250ºC; ***Chapter 3.3***).

2.2.4.2 Sources of secondary N

Previous studies on altered basalts from global oceans, as well as the altered sheeted dikes and gabbros from Holes 504B and 1256D, have revealed that the added NH_4^+ was mainly from seafloor sediments and/or seawater with less contribution from abiotic reduction of N_2 (e.g., Li et al., 2007; Bebout et al., 2018; Busigny et al., 2019; ***Chapter 2.1***). Because sedimentary/seawater N is more ^{15}N-enriched and abiotic reduction produced NH_4^+ is more ^{15}N-depleted than mantle N, the addition of N from these two sources would result in positive and negative correlations between N concentrations and $\delta^{15}N$ values, respectively. These correlations have been observed from several sites, including 801C, 1256D and 504B (Li et al., 2007; ***Chapter 3.3***).

To assess the relative contribution from these two NH_4^+ sources in the gabbroic rocks in this study, we modeled the data by employing the same two-component mixing model (Fig. 9), which has been employed in ***Chapter 2.1***. In this modeling, the observed positive N-$\delta^{15}N$ correlations of the altered gabbroic rocks can be well fitted by addition of secondary NH_4^+ with a $\delta^{15}N$ range of -1‰ – +7‰ (Fig. 9). These $\delta^{15}N$ values are consistent with the isotopic composition of NH_4^+ derived from seafloor sediments and seawater (-1‰ to +10‰; Sadofsky and Bebout, 2004; Li and Bebout, 2005; Tesdal et al., 2013; Bourbonnais et al., 2012; Jo et al., 2018). No significant N contribution from abiotic N_2 reduction is observed in these altered gabbros. Mass-balance calculation suggests that secondary N accounts for 55% – 85% of the N in the 1309D gabbroic rocks, 60% – 90% of the N in the 1415P gabbroic rocks, and 45% – 92% of the N in the 735B gabbroic rocks.

2.2.4.3 Controlling factors on N enrichment in global gabbroic oceanic crust

The new data for gabbroic rocks from Holes 735B, 1039D and 1415P, together with previously published data of altered gabbros from Hole 1256D (***Chapter 3.3***), allow a first attempt to understand the controlling factors on N enrichments in the plutonic section of AOC. Our previous study on hydrothermal enrichments of N in altered basalts suggests that N availability, which is related to sediment type, is the major control (***Chapter 2.1***). However, different to the upper volcanic rocks which are often overlain directly or interlayered by sediments, the gabbroic rocks assimilated their N mainly in the moderate- to high-temperature alteration stages beneath the seafloor (e.g., Nozaka et al., 2008; Schoolmeesters et al., 2012). For example, based on the available exhumation path of the 1309D gabbroic rocks (Schoolmeesters et al., 2012), the uptake of the majority of secondary N in these gabbros occurred at ~7 km to ~ 2.5 km below the seafloor. At these depths, there should be no sediments in direct contact with gabbros to provide an abundant N source. Instead, the added NH_4^+ was likely mobilized by seawater-dominated hydrothermal fluid. Thus, the N availability likely remained at similarly low levels for all gabbros. This is consistent with the N concentrations of the altered gabbros (average: $7.9^{\pm 4.1}$ ppm), which is identical to the N concentrations of the altered basalts from Hole 417A (average: $7.3^{\pm 3.8}$ ppm; no sediments deposited over the period of N assimilation; ***Chapter 2.1***), but much smaller than the N concentrations of altered basalts from Hole 543A (average: $24.9^{\pm 8.3}$ ppm) with N-rich overlying sediments. The incorporation of seawater-derived N in these gabbroic rocks suggests that the developed faults, especially the detachment faults developed in the slow/ultraslow-spreading ridges, could facilitate the transfer of seawater to several kilometers beneath the seafloor (deMartin et al., 2007; Tao et al., 2020; Liao et al., 2022).

Previous studies also suggest that some other physiochemical parameters, such as alteration degree, spreading rate and crustal age may potentially affect the enrichment degree of volatile elements in AOC (e.g., Alt and Teagle, 1999; Jarrard, 2003; Li et al., 2019b). On the plot of the average N concentration versus average LOI, which is an index of the overall alteration intensity, no positive correlation is observed (Fig. 11), indicating alteration intensity is not the major control on N enrichment in gabbroic oceanic crust at a global scale. The lack of control of alteration intensity on N enrichment is also shown locally in the along-depth variations of N concentration and LOI in single drill holes, e.g., Hole 1415P (Fig. 8). Fig. 11 illustrates that weak positive correlations between N concentrations and spreading rate (Fig. 11b) and crustal age (Fig. 11c) may exist, but these relationships remain inconclusive because they are largely controlled by the data from Hole 1256D. More data from other sites with different crustal age and spreading rate (if available from future drillings) may provide more insights into their control on N enrichment in gabbroic rocks.

2.2.4.4 A revised N input flux in global AOC

The ubiquitous uptake of secondary N by altered gabbroic rocks from global oceans suggests that the plutonic section of AOC should be a large N reservoir that has been overlooked by previous studies (e.g., Li et al., 2007; Busigny et al., 2019). The data in this study thus enable a first attempt to estimate the subducting N budget in the plutonic section of AOC and to further refine the N input flux into global subduction zones.

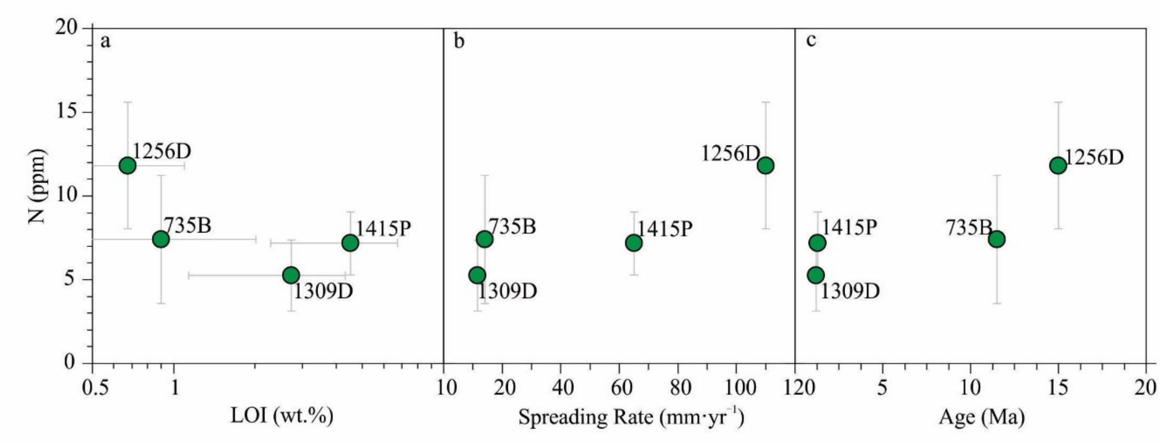

Figure 11. Comparison of the average N concentrations of global oceanic gabbroic rocks with their average loss on ignition (LOI) (a), average K_2O concentrations (b), crustal ages (c) and spreading rates (d). Error bars represent 1σ.

To estimate the subducting N budget of the plutonic section, we followed a number of previous studies (e.g., Alt and Teagle, 1999; Kelemen and Manning, 2015; Li et al., 2019b) to use the standard stratigraphy of oceanic crust, i.e., from top to bottom, 600 m upper volcanics, 200 m transition zone, 1200 m sheeted dikes and 5000 m gabbroic rocks. The N input flux of the upper volcanic section of individual and global subduction zones (43819 km in total length; Table 2; Jarrard, 2003) has been estimated in ***Chapter 2.1***. For the N budgets in the 200 m-thick transition zone and 1200 m-thick sheeted dikes, the available average N concentrations of $5.0^{\pm1.6}$ ppm (1σ; n = 2) from Hole 504B transition zone and $10.6^{\pm6.0}$ ppm (1σ; n = 24) from Holes 504B and 1256D sheeted dikes were applied, which gave a unit N budget of $2.1^{\pm0.7}\times10^2$ mol and $2.6^{\pm1.5}\times10^3$ mol for a 1 m × 1m (in surface area) transition zone and sheeted-dike section, respectively.

To estimate the N input flux contributed by the 5000 m-thick gabbroic section, two endmember case scenarios were applied to bracket the potential heterogeneity in N enrichment in the gabbroic oceanic crust. In the upper-endmember case scenario, the average N concentrations of gabbroic rocks (average: $7.9^{\pm 4.1}$ ppm) from Holes 735B, 1256D, 1309D, and 1415P were applied uniformly to the 5000 m-thick gabbroic section. This gave an upper-end unit N budget of $8.5^{\pm 4.4}\times 10^3$ mol for a 1 m × 1m (in surface area) prism of the 5000 m-thick gabbroic section. In the lower-endmember case scenario, following the exponential decrease in permeability and water-rock ratio along depth (Anderson et al., 1985; Nehlig and Juteau, 1988; Kawahata et al., 2001; Yamaoka et al., 2012), we considered an exponential decrease in N enrichment in gabbroic section. Using the average N concentrations of the gabbroic rocks (i.e., $7.9^{\pm 4.1}$ ppm) for the top section at 2000 mbsf and the inherited mantle value (i.e., 1.5 ppm) for the bottom section at 7000 mbsf, we obtained the lower-end unit N budget of $5.0^{+1.1}_{-2.2}\times 10^3$ mol for a 1 m × 1 m (in surface area) prism of the 5000 m-thick gabbroic section (see Appendix B for methods). It should be noted that the assumption of exponential N decrease along depth gave a very conservative result because the gabbroic rocks from Hole 1309D data show that altered gabbros can still incorporate significant amounts of N (~5.3 ppm N) at depths of ~2.5 km to ~7.0 km.

Integrating the unit budgets of all four AOC sections with subduction rate and trench length, the N input fluxes yielded from AOC of individual subduction zones are listed in Table 3. The total gives a global N input flux from AOC as $21.8^{+0.9}_{-1.3}\times 10^9$ mol·yr^{-1} to $30.6^{\pm 2.2}\times 10^9$ mol·yr^{-1}, in which 53% – 65% is contributed by the gabbroic oceanic crust ($11.5^{+0.5}_{-1.0}\times 10^9$ mol·yr^{-1} to $20.0^{\pm 2.1}\times 10^9$ mol·yr^{-1}). This emphasizes that the lower oceanic crust is an important N reservoir. Integrating the N input flux of 54.3×10^9 mol·yr^{-1} carried by seafloor sediments (Busigny et al., 2003a), a total N input of $76.1^{+0.9}_{-1.3}\times 10^9$ mol·yr^{-1} to $84.9^{\pm 2.2}\times 10^9$ mol·yr^{-1} was obtained for the subducting slab at globe (not accounting from the N in the serpentinized sub-oceanic lithospheric mantle; ***Chapter 2.3***).

Our estimate of total N input flux contributed by AOC ($21.8^{+0.9}_{-1.3}$ – $30.6^{\pm2.2}\times10^{9}$ mol·yr^{-1}) is slightly lower than the estimate (39 $\times10^{9}$ mol·yr^{-1}) by Busigny et al. (2011), who applied the average N concentration ($10.6^{\pm5.1}$ ppm) of the metagabbros from the western Alps evenly for the gabbroic oceanic crust. The metamorphosed AOC could have received further enrichment of N from sediments in the subduction channel (e.g., Halama et al., 2010; Li et al., 2021c). As a result, using the N concentrations of metamorphic rocks to represent those of their protoliths may result in an overestimate of the input N flux.

2.2.4.5 Implications for N recycling across subduction zones

When comparing N concentrations and δ^{15}N values between altered oceanic gabbros and their metamorphic equivalents (Fig. 12a), N concentrations of altered gabbroic rocks are higher whereas δ^{15}N values are lower than those of eclogites. This is also confirmed by the box plots in Fig. 12b and Fig. 12c, where systematic differences in N concentrations and δ^{15}N values exist between altered gabbroic rocks and eclogites. These data differences are consistent with the devolatilization trend caused by prograde metamorphism, which causes preferential release of ^{14}N and results in the increase of δ^{15}N values of the metamorphic rocks (e.g., Bebout and Fogel, 1992). This is consistent with the results in ***Chapter 2.1*** indicating that metamorphosed AOC can lose N by eclogite-facies metamorphism.

2.2.5 Conclusions

Our new data of N concentrations and isotope compositions of the altered gabbroic rocks from ODP Holes 735B, 1309D and 1415P from global oceans demonstrate ubiquitous enrichments of seawater N in the gabbroic oceanic crust. The secondary N in the gabbroic rocks likely resides in secondary minerals such as plagioclase, amphibole and chlorite formed during moderate- to high-temperature alterations. Based on these new data, we estimated the global N input flux to be $21.8^{+0.9}_{-1.3}$ – $30.6^{\pm2.2}\times10^{9}$ mol·yr^{-1} for altered oceanic crust and of $76.1^{+0.9}_{-1.3}\times10^{9}$ mol·yr^{-1} to $84.9^{\pm2.2}\times10^{9}$ mol·yr^{-1} for the entire crustal material (sediments + AOC) in subducting slab. Comparison of N concentrations and isotopic compositions between altered gabbro and its metamorphic equivalents at eclogite facies suggests that N entrained in gabbros may be lost as they are subducted to eclogite-facies conditions.

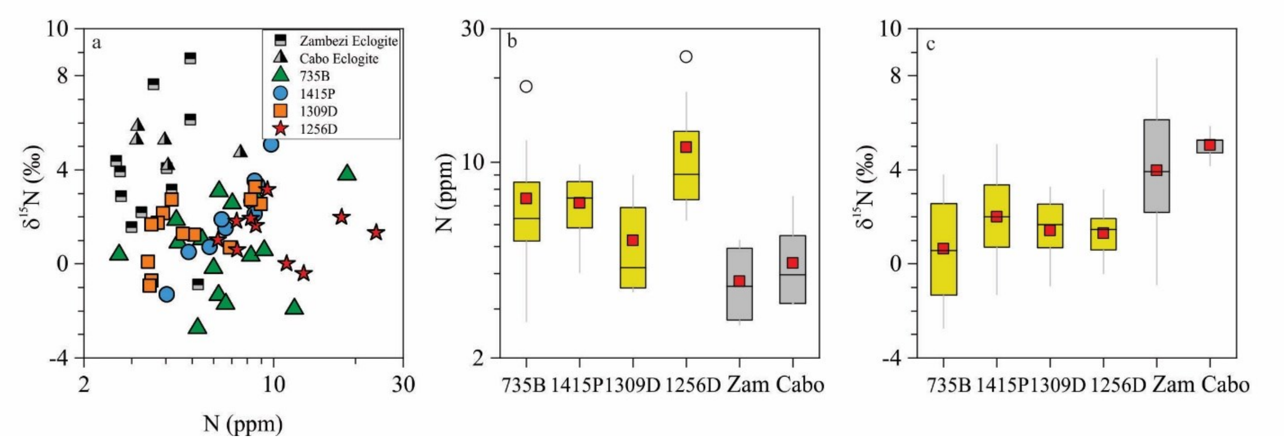

Figure 12. Comparison of N concentrations and δ^{15}N values between altered oceanic gabbroic rocks and their metamorphic equivalents, i.e., eclogites with gabbroic protolith from the Zambezi belt (Zam) and Cabo Ortegal Complex (Cabo; Halama et al., 2010) in forms of individual samples (a) and data ranges (b and c). The red squares represent the mean value of the altered gabbroic rocks and eclogites.

Table 3. Nitrogen input flux of subducting AOC in world's major subduction zones.

Subduction Zones	Length[a] (km)	Convergence Rate[a] (mm·yr^{-1})	N flux (mol·yr^{-1})
Southern Chile	1218	16	$1.8^{+0.4}_{-0.5}$ – $2.4^{\pm 0.9}\times 10^{8}$
Central Chile	1306	71	$0.8^{+0.2}_{-0.3}$ – $1.2^{\pm 0.4}\times 10^{9}$
North Chile	1579	74	$1.1^{+0.2}_{-0.3}$ – $1.5^{\pm 0.6}\times 10^{9}$
Peru	1599	65	$1.0^{+0.2}_{-0.3}$ – $1.3^{\pm 0.5}\times 10^{9}$
Columbia-Ecuador	1355	65	$0.8^{\pm 0.2}$ – $1.1^{\pm 0.4}\times 10^{9}$
Central America[b]	1400	85	$1.1^{\pm 0.1}$ – $2.0^{\pm 0.5}\times 10^{9}$
Mexico	1383	49	$7.0^{+1.3}_{-1.8}$ – $9.3^{\pm 3.2}\times 10^{8}$
Kurile	1243	75	$0.8^{+0.2}_{-0.3}$ – $1.1^{\pm 0.4}\times 10^{9}$
Kamchatka	900	74	$6.2^{+1.3}_{-1.8}$ – $8.5^{\pm 3.1}\times 10^{8}$
NE Japan	1061	76	$0.7^{\pm 0.2}$ – $1.0^{\pm 0.4}\times 10^{9}$
Izu-Bonin-Mariana[b]	2450	41	$4.2^{\pm 0.2}$ – $75^{\pm 5.3}\times 10^{8}$
Ryukyu	1153	57	$6.8^{+1.2}_{-1.8}$ – $9.1^{\pm 3.1}\times 10^{8}$
Philippine	1509	64	$1.0^{+0.2}_{-0.3}$ – $1.3^{\pm 0.5}\times 10^{9}$
Tonga	1460	148	$1.9^{+0.4}_{-0.6}$ – $2.7^{\pm 1.0}\times 10^{9}$
Kermadec	1422	52	$6.6^{+1.5}_{-2.1}$ – $9.2^{\pm 3.5}\times 10^{8}$
Hikurangi	794	21	$1.5^{+0.3}_{-0.5}$ – $2.1^{\pm 0.8}\times 10^{8}$
South Sandwich	1005	44	$3.8^{+0.8}_{-1.2}$ – $5.3^{\pm 2.1}\times 10^{8}$
Lesser Antilles	800	24	$1.8^{+0.4}_{-0.5}$ – $2.4^{\pm 0.9}\times 10^{8}$
Aleutians, W	1102	18	$1.8^{+0.4}_{-0.6}$ – $2.5^{\pm 0.9}\times 10^{8}$
Aleutians, E	1246	59	$6.6^{+1.5}_{-2.0}$ – $9.2^{\pm 3.5}\times 10^{8}$
Alaska	1490	56	$0.9^{\pm 0.2}$ – $1.1^{\pm 0.4}\times 10^{9}$
Nankai	824	38	$3.2^{+0.6}_{-0.8}$ – $4.3^{\pm 1.5}\times 10^{8}$
Sumatra	2462	50	$1.2^{+0.2}_{-0.3}$ – $1.7^{\pm 0.6}\times 10^{9}$
Java	1200	71	$0.9^{\pm 0.2}$ – $1.2^{\pm 0.4}\times 10^{9}$
Sunda E.	950	71	$6.9^{+1.3}_{-1.8}$ – $9.3^{\pm 3.1}\times 10^{8}$
Andaman-Burma	1089	23	$2.2^{+0.5}_{-0.7}$ – $3.1^{\pm 1.2}\times 10^{8}$
Markan	950	37	$3.6^{+0.7}_{-0.9}$ – $4.8^{\pm 1.6}\times 10^{8}$
Aegean	850	5	$3.8^{+0.9}_{-1.2}$ – $5.3^{\pm 2.0}\times 10^{7}$
Cascadia	990	36	$3.2^{+0.7}_{-1.0}$ – $4.4^{\pm 1.7}\times 10^{8}$
Manlia	1050	10	$0.9^{+0.2}_{-0.3}$ – $1.3^{\pm 0.5}\times 10^{8}$
Negros	400	20	$0.7^{\pm 0.2}$ – $1.0^{\pm 0.4}\times 10^{8}$
Sulawesi. N	600	30	$1.6^{+0.4}_{-0.5}$ – $2.2^{\pm 0.9}\times 10^{8}$
Sulu	500	20	$0.9^{+0.2}_{-0.3}$ – $1.2^{\pm 0.5}\times 10^{8}$
Cotabato	500	20	$0.9^{+0.2}_{-0.3}$ – $1.2^{\pm 0.5}\times 10^{8}$
San Cristobal	1050	49	$4.6^{+1.1}_{-1.4}$ – $6.4^{\pm 2.4}\times 10^{8}$
Yap-Palau	550	3	$1.5^{+0.3}_{-0.5}$ – $2.1^{\pm 0.8}\times 10^{7}$
Torbriand	590	20	$1.1^{+0.2}_{-0.3}$ – $1.5^{\pm 0.6}\times 10^{8}$
Vanuatu	1189	111	$1.2^{+0.3}_{-0.4}$ – $1.6^{\pm 0.6}\times 10^{9}$
New Britain	600	110	$5.9^{+1.3}_{-1.8}$ – $8.2^{\pm 3.1}\times 10^{8}$
Global	43819		$21.8^{+0.9}_{-1.3}$ – $30.6^{\pm 2.2}\times 10^{10}$

a. Trench length and convergence rate of global subduction zones is from Jarrard (2003).

b. Nitrogen input flux data adopted from ***Chapter 3.3***.

Chapter 2.3 Nitrogen enrichment in oceanic serpentinites: A critical reservoir for deep nitrogen recycling

2.3.1 Introduction

The N budget in subducting slab is a key parameter to quantify the deep recycling of N. Among the three major components in subducting slabs, i.e., sediments, altered oceanic crust (AOC) and oceanic/slab mantle, N data are most available for seafloor sediments and the input flux of sedimentary N has been relatively well determined (Sadofsky and Bebout, 2004; Li et al., 2007). Recent studies on AOC also observed significant N enrichment not only in the upper basaltic section (see ***Chapter 2.1***) but also in the lower sheeted dike and gabbroic section (see ***Chapter 2.2***). The N in AOC likely resides in the K- and/or Na-bearing secondary minerals formed during hydrothermal alteration (Watenphul et al., 2010; Li et al., 2021b). This makes AOC an important N reservoir in parallel to sediments for subduction-zone N recycling (e.g., Busigny et al., 2005; Li et al., 2007; Bebout et al., 2018; ***Chapter 2.1, 2.2***).

Ultramafic rocks from the mantle (principally peridotite) contain very low N, mainly as N_2 in fluid inclusions (Fischer et al., 2005) and possibly some fixed ammonium in pyroxene. Serpentinization of subducting slabs driven by fault-related alteration (e.g., detachment faults and slab-bending-related faults) has long been regarded as an important process adding volatile components (e.g., Ranero et al., 2003; Alt et al., 2013), which can be subsequently transferred to the sub-arc depth affecting arc magma geochemistry (e.g., Hattori and Guillot, 2007; Deschamps et al., 2013) and even beyond the sub-arc depth to the deeper mantle (e.g., Kendrick et al., 2011; Smith et al., 2018, 2021). However, the N potential in oceanic serpentinites has not been examined so far, except three samples from the Southwest Indian Ridge (Philippot et al., 2007). Recent studies on metamorphosed serpentinites from the Ligurian Alps and Bètic Cordillera, which represent the mantle material in subducting slabs that were subducted to depths of up to ~70 km, showed that they contain remarkable amounts of N (1.3 – 20.6 ppm), with negligible N loss during prograde metamorphism (Philippot et al., 2007; Halama et al., 2014). This highlights the importance of serpentinites as host for deep N recycling (Halama et al., 2014). However, it is uncertain whether the N enrichment in these metamorphosed serpentinites occurred during pre-subduction hydrothermal alteration (i.e., from external seawater N) or inside the subduction channel through intraslab metasomatic addition (i.e., from internal slab N), which both have been observed in meta-basalts (Halama et al., 2014; Li et al., 2021c). The lack of N data for oceanic serpentinites has impeded the quantification of the N budget in global subducting serpentinites and the understanding of the N behavior of N in the subduction channel recorded by meta-serpentinites.

Here, I report the N concentrations and isotope compositions of 26 modern oceanic serpentinites from four sites (Fig. 13a) recovered by the Ocean Drilling Program (ODP), including Hole 895D from the Hess Deep (n = 9) at the East Pacific Rise (EPR), Holes 1271B (n = 5) and 1274A (n = 6) from the 15°20' N fracture zone at the Mid-Atlantic Ridge and Hole 920D (n = 7) from the eastern intersection of the Kane Fracture Zone and the Mid-Atlantic Ridge, together with two serpentine vein minerals from Hole 895D. These data allow for a first investigation of the uptake of N by oceanic serpentinites during hydrothermal alteration. Our results show that sediment- and/or seawater-derived N is ubiquitously added into these oceanic serpentinites during serpentinization and the serpentinized slab mantle could be a critical reservoir transferring N to the deeper mantle.

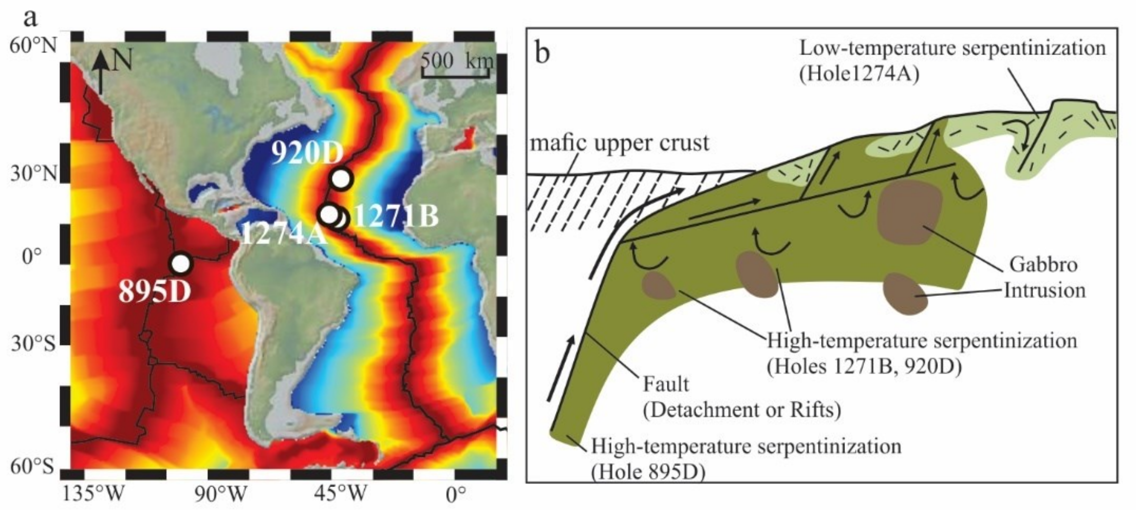

Figure 13. Sample locations and alteration temperatures of oceanic serpentinites. (A) Global oceanic crust map showing sample sites. The map was generated by GeoMappApp (http://www.geomapapp.org). (B) Schematic diagram showing high-temperature (dark green) and low-temperature (light green) serpentinization processes (modified from Alt et al., 2013). High-temperature serpentinization can be induced either by heat and mass transfer associated with gabbroic intrusions (brown) along detachment faults (e.g., Holes 1271B and 920D), or by massive penetration of seawater into hot peridotite along rifting-related faults (e.g., for Hole 895D). Black arrows indicate hydrothermal circulation.

2.3.2 Geological background and sample descriptions

Serpentinites from the four ODP holes were exhumed onto the seafloor by either crustal thinning along long-lived low-angle detachment faults or propagating rifts (Alt et al., 2013; Fig. 13b). Harzburgites and dunites in these holes are commonly highly to completely altered (~60% – 100%) with a secondary mineral assemblage dominated by serpentine and associated with magnetite ± amphibole ± brucite ± chlorite ± talc ± carbonate ± clay ± iron oxyhydroxides (see Appendix C for detailed core description). Following Alt et al. (2013), the oceanic serpentinites from the four holes were classified into two groups based on the temperature of serpentinization:

(1) High-temperature serpentinization:

Samples from Holes 1271B and 920D have experienced high-temperature serpentinization due to gabbroic intrusions (Fig. 13b; Alt and Shanks, 2003; Alt et al., 2013). The low bulk-rock $\delta^{18}O$ values (+2.6 – +4.1‰) of serpentinites suggest that serpentinization predominantly occurred at temperatures of > 350 ºC (Alt and Shanks, 2003; Alt et al., 2007, 2013).

Serpentinization of samples from Hole 895D occurred during the rifting process where seawater was injected into hot peridotites at depth of ~ 5 km (Fig. 13b; Mével and Stamoudi, 1996; Alt et al., 2013). The low $\delta^{18}O$ values (+3.2 – +4.1‰) of serpentine mineral separates indicate serpentinization temperatures of 200 – 400 ºC (Agrinier et al., 1995; Früh-Green et al., 1996; Mével and Stamoudi, 1996; Alt et al., 2013).

It should be noted that these serpentinites have all been slightly affected by late-stage low-temperature alteration as they were uplifted to the seafloor, as revealed by the presence of low-temperature secondary minerals of carbonate ± clay ± iron oxyhydroxides (e.g., Agrinier et al., 1995; Alt et al., 2007).

(2) Low temperature serpentinization:

Hole 1274A is characterized by low-temperature serpentinization, which is affected by exposure of peridotites to seafloor by faulting (Fig. 13b; Alt et al., 2007, 2013). The bulk-rock $\delta^{18}O$ values of serpentinites are mostly high (up to ~+8.1‰), indicating low serpentinization temperature of < 150 ºC (Alt et al., 2007, 2013).

2.3.3 Results

The bulk-rock N concentrations and $\delta^{15}N$ values of serpentinites from all four holes largely overlap in ranges of 3.2 ppm to 18.6 ppm and -3.3‰ to +4.4‰, respectively (Fig. 14**;** Table C1 in

Appendix C). These samples show consistently higher N concentrations and lower $\delta^{15}N$ values than those of the three samples (N = 2.0 – 2.9 ppm; $\delta^{15}N$ = +6.3‰ to +7.5‰) from Southwest Indian Ridge (Philippot et al., 2007), which may be due to different analytical protocols between the labs (Halama et al., 2014; Li et al., 2021; see more analytical comparison in ***Chapter 3.3***). Neither N concentrations nor $\delta^{15}N$ values show downhole trends in individual boreholes, but a broad positive trend between N concentrations and $\delta^{15}N$ values was consistently observed for each borehole (Fig. 14). Compared to the bulk-rock N concentrations and $\delta^{15}N$ values of serpentinites, the two serpentine vein samples from Hole 895D show much higher N concentrations (34.9 – 94.0 ppm) and slightly higher $\delta^{15}N$ values (+5.7‰ – +5.9‰).

2.3.4 Discussion

2.3.4.1 Ubiquitous N enrichment in oceanic serpentinites

The N concentrations (3.2 – 18.6 ppm) of serpentinites from four sites spreading from the Pacific to the Atlantic ridges consistently demonstrate that oceanic serpentinization can add significant amount of N into altered mantle rocks. The magnitude of N enrichment in serpentinites is comparable to those in altered basalts, sheeted dikes and gabbroic rocks (***Chapters 2.1, 2.2***).

Nitrogen can be incorporated into minerals/rocks through NH_4^+ substitution of K^+ and Na^+ in mineral crystal lattice (e.g., clay, mica, plagioclase; Honma and Itihara, 1981; Li et al., 2021b). However, the lack of K- and Na-bearing phases in these serpentinites, as revealed by their near-zero K_2O and Na_2O contents (e.g., Shipboard Scientific Party, 2004a; Mével and Stamoudi, 1996), precludes this substitution mechanism. The high N concentrations of the two serpentine veins (Table C1 in Appendix C) indicate that serpentine is the major N-hosting mineral in serpentinites.

However, the small radii of the trioctahedral (~ 0.75Å) and tetrahedral (~ 0.32Å) sites (Laurora et al., 2011) of serpentine minerals makes it difficult to accommodate the large NH_4^+ with ionic radius of 1.67 Å (Sidey, 2016). In addition to cation exchange mechanism, the adsorption of large cations (e.g., Cs^+; 1.88 Å; Shannon and Prewitt, 1969) onto the serpentine surface has been demonstrated by previous experimental studies (Lafay et al., 2016). Therefore, the adsorption of NH_4^+ onto the negatively charged serpentine surface is a likely mechanism but needs to be tested in future studies. It is interesting to note that, remarkably high N (up to 83 ppm) has also been detected in chlorite (Harris et al., 2022), which is also capable of adsorbing large cations onto its negatively charged surface (Hussain et al., 1996). This suggests that N may occur as a trace element in much more minerals than previously thought.

The positive correlation between N concentrations and $\delta^{15}N$ values in serpentinites can be readily explained by a two-component mixing model (refer to Equation 1 in ***Chapter 2.1***) between the depleted mantle with N concentration of ~1.1 ppm and $\delta^{15}N$ value of -5‰ (Marty et al., 2020) and the secondary N with a $\delta^{15}N$ range of -1‰ – +6‰, consistent with an N source from sediments/seawater (Sadofsky and Bebout, 2004; Li and Bebout, 2005). The $\delta^{15}N$ values of the two serpentine veins (+5.7‰ – +5.9‰; Fig. 14), which are expected to be closer to the fluid endmember, further verify the mixing model. Mass-balance calculation indicates that 66% – 94% of the N in these oceanic serpentinites is secondary.

2.3.4.2 Equivalent N enrichments in low-temperature and high-temperature serpentinites

Despite of the difference in serpentinization temperature, i.e., near-seafloor low-temperature alteration (< 150 ºC; Hole 1274A) and high-temperature alteration at depths (200 – > 350 ºC; Holes 895D, 1271B and 920D) (Alt et al., 2013), no obvious difference in either N concentration or $\delta^{15}N$

value between these sites is observed (Fig. 14). Because N availability is the primary factor controlling the enrichment of N in AOC (Li et al., 2007; ***Chapters 2.1, 2.2***), it is not surprising to observe remarkable N enrichment in serpentinite from low-temperature alteration near the seafloor because abundant NH_4^+ is available in the unlimited seawater environment. It is however surprising to observe equivalent N enrichment by high-temperature serpentinization at depths. This implies that either sufficient surface NH_4^+ can be delivered by seawater-derived fluids along faults to depth to facilitate N assimilation or high-temperature serpentinization can more efficiently assimilate N if the fluid NH_4^+ is limited. Either pathway could induce the serpentinized mantle rocks at depths to contain significant amounts of N.

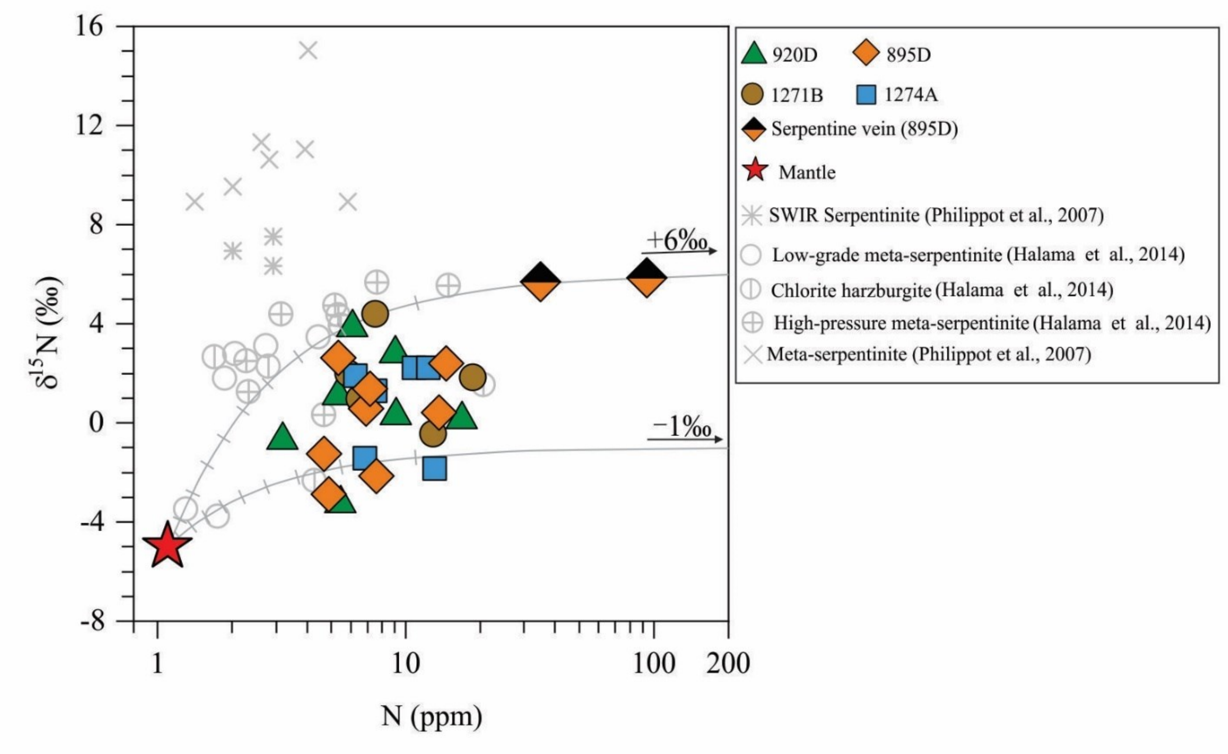

Figure 14. The relationship between N concentrations and $\delta^{15}N$ values of oceanic serpentinites. Error bars are less than the symbol size. The data fall in the range of two-component mixing between mantle N and sediment/seawater N (grey curves). The fraction of the incorporated secondary N is marked by short gray lines with a 10% increment. For comparison, the N concentrations and $\delta^{15}N$ values of oceanic serpentinites from the Southwest Indian Ridge (SWIR)

and meta-serpentinites (Philippot et al., 2007; Halama et al., 2014) are also shown for comparison (see text for discussion).

2.3.4.3 Nitrogen retention in serpentinites during subduction

These new data for serpentinites allow for a first attempt to assess the behavior of N in the subduction channel via a first-order comparison with their metamorphic equivalents (i.e., meta-serpentinite). Nitrogen concentrations and isotopic compositions have been examined for meta-serpentinites with various metamorphic conditions (Fig. 15), such as the low-grade serpentinites (< 0.5 Gpa and < 300 ºC) in the Erro Tobbio and Monte Nero units (Ligurian Alps) or the high-pressure serpentinites experienced partial antigorite dehydration at 550 – 600 ºC and 2.0 – 2.5 Gpa in the Erro Tobbio unit and chlorite harzburgite formed by complete antigorite dehydration at > 650 – 700 ºC and ~2 Gpa in the Cerro del Almirez unit (Bètic Cordillera). Because the protoliths of the other meta-serpentinites were derived from oceanic mantle and mostly experienced serpentinization from low to high temperatures in seafloor settings (Halama et al., 2014). Therefore, the studied oceanic serpentinites here could be used as a reference for the potential N signatures of their protoliths.

As illustrated in Fig. 15, the meta-serpentinite data by Halama et al. (2014) largely overlap (with some of the data sitting slightly above) the ODP serpentinite data. This can be explained by isotopic heterogeneity of NH_4^+ in hydrothermal fluid with a slightly higher $\delta^{15}N$ value (+8‰), or alternatively, by minot N loss during metamorphic devolatilization. In fact, the low-grade serpentinites have lower N concentration than the high-pressure serpentinites, which is inconsistent with metamorphic N devolatilization (Halama et al., 2014). Therefore, N isotopic heterogeneity of alteration fluid is more likely the cause. It is noted that the meta-serpentinites from the Erro Tobbio units analyzed by Philippot et al. (2007) have much lower N concentrations and higher $\delta^{15}N$ values, which are apparently consistent with the isotopic effect of partial N loss (Bebout and Fogel, 1992). This discrepancy has, however, been attributed to be most likely due to the differences in analytical protocols rather than metamorphic N devolatilization (Halama et al., 2014). Overall, these results suggest that serpentinites are capable to retain N during prograde metamorphism inside the subduction channel.

2.3.4.4 Implications for deep N recycling

Our data demonstrate that N can be enriched in serpentine during serpentinization not only near-seafloor in low-temperature conditions but also in high-temperature conditions at depths as hydrothermal fluids penetrated along detachment faults and/or rifting-related faults. Because these serpentinites uplifted to the seafloor are only widely developed at slow- and ultra-slow spreading ridges (e.g., Cannat, 1993), their contribution to the subducting N flux may be limited at a global scale but may be important locally, such as the Antilles and Scotia subduction zones (Alt et al., 2013).

Outboard of trenches, slab bending can produce faults for deep penetration of fluids into the oceanic mantle. Thermal modeling predicts that the slab mantle is cold and well within the serpentinization temperature range (Shirey et al., 2021). Serpentinization of slab mantle has been observed (e.g., Ranero et al., 2003; Alt et al., 2013; Fig. 15). A range of serpentinization degree from low (~1%; Kendrick et al., 2017), to moderate (10%) and high (30%; Kelemen and Manning, 2015; Krantz et al., 2019; Smith et al., 2021) for the uppermost 10 km of oceanic mantle has been used for the calculation of elemental fluxes in subduction zones. Employing the global trench length of 43819 km, an average convergence rate of 0.05 $m \cdot yr^{-1}$, 10 km oceanic mantle with moderate serpentinization degree of 10%, dry density of 2.6 g·cm^{-3} (Jarrard, 2003; Alt et al., 2013; Kelemen and Manning, 2015) and an average N concentration of 8.1 ppm of oceanic serpentinite from Hole 895D, the subducting oceanic mantle can carry an N flux of 3.3×10^{9} mol·yr^{-1} into subduction zones. This value is comparable to that of the most altered upper volcanic section of AOC (Busigny et al., 2011; Harris et al., 2022; ***Chapter 2.1***).

Thermal models of subducting slabs have revealed that the pressure-temperature path of cold slabs passes through the stability field of serpentine to dense hydrous magnesium silicates, acting as a mechanism to transport volatile to the transition zone and beyond (e.g., Ohtani et al., 2004; Shirey et al., 2021). This is supported by blue boron-bearing diamonds from the lower mantle (Smith et al., 2018) and the heavy iron isotope compositions of metallic inclusions in diamonds from a depth of 360 – 750 km (Smith et al., 2021). Therefore, it is expected that, in cold subducting slabs, N in oceanic serpentinites can be carried to the deeper mantle even beyond the transition zone (Fig. 15). This deeply subducted N could be responsible for some enriched N isotopic signatures observed in mantle plumes and deep diamonds (Dauphas and Marty, 1999; Palot et al., 2014).

2.3.5 Conclusions

Low- and high-temperature oceanic serpentinites from four ODP sites spreading from the Pacific to the Atlantic show ubiquitous enrichment (3.2 – 18.6 ppm) of secondary N sourced from sediments/seawater with δ^{15}N value of -1.0‰ – +6.5‰. The largely overlapping N concentrations and δ^{15}N values of oceanic serpentinites and meta-serpentinites that have been subducted to depth of up to ~70 km suggest that N in these meta-serpentinites is well retained during prograde metamorphism inside subduction zones. If N is enriched at a similar degree during serpentinization of the sub-oceanic lithospheric mantle, it can contribute an input N flux of 3.3×10^{9} mol·yr^{-1}. This implies that the serpentinized mantle is a critical reservoir transferring N to the deeper mantle especially in cold slabs. The entrained N in these oceanic serpentinites can be incorporated into diamond-forming fluids, supplying heavy N isotopic signatures.

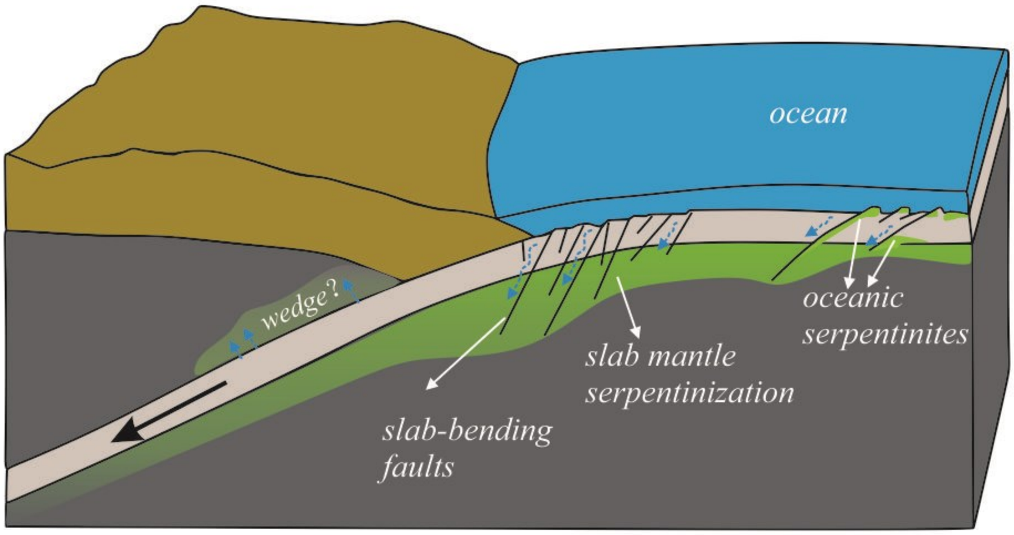

Figure 15. Schematic diagram (not to scale) showing the uptake of N by serpentinization on the seafloor, and the slab mantle.

Chapter 3 Constraints on nitrogen recycling in the forearc and sub-arc regions

Chapter 3.1 Nitrogen recycling in the forearc: insights from the Izu-Bonin-Mariana mud volcanoes

3.1.1 Introduction

Subduction zones are the main conduit for mass exchange between Earth's surface and interior. Volatiles are carried by subducting slabs through the forearc and sub-arc regions and ultimately delivered to the deeper mantle beyond the sub-arc depth (e.g., Hilton et al., 2002; Barry et al., 2019; Plank and Manning, 2019; Bekaert et al., 2021). Deep recycling of volatiles is consistent with isotopic signatures of some mantle-derived materials, such as diamonds (e.g., Walter et al., 2011; Smart et al., 2016; Regier et al., 2020) and plume-related magmas (e.g., Eiler et al., 1997; Dauphas and Marty, 1999; Halldórsson et al., 2016). The subduction-zone recycling of volatile elements has substantially influenced the geochemical evolution of Earth's major volatile reservoirs (e.g., atmosphere, biosphere and mantle) and the habitability of Earth's surface. As such, constraining volatile recycling within the forearc and sub-arc regions is essential to understand the large-scale volatile cycle from subduction to deposition in the deeper mantle.

Over the past several decades, substantial efforts have been put in constraining the recycling of nitrogen (N) via arc volcanos (e.g., Snyder et al., 2001; Hilton et al., 2002; Zimmer et al., 2004; Elkins et al., 2006; Mitchell et al., 2010; Labidi et al., 2021; Füri et al., 2021). The forearc region has also been recently identified as a critical reservoir trapping recycled slab volatile components through the serpentinization of mantle-wedge peridotites (e.g., Bach et al., 2019; Barry et al., 2019; Fullerton et al., 2021). However, although possible entrainment of recycled slab N in the forearc serpentinites has been inferred from studies of their metamorphosed equivalents (Pagé et al., 2018), the flux of recycled N to the forearc mantle wedge and its importance in the subduction-zone N recycling has not been assessed using forearc mantle samples, in our best knowledge.

Along the Izu-Bonin-Mariana (IBM) trench, fluids derived from slab dehydration have led to extensive hydration and uplift of the overlying mantle wedge, resulting in serpentinite mud volcanism on the inner trench slope (e.g., Savov et al., 2005, 2007; Fryer, 2012, 2018a; Debret et al., 2019). Mud flows, including serpentine mud, variably serpentinized ultramafic clasts, together with minor amounts of recycled subducted slab material (e.g., metabasite and cherty limestone), have been erupted to the seafloor (e.g., Fryer, 2012, 2018). The isotopic signatures of Li, B, O, Sr, H, Si, and Tl of serpentinite clasts and serpentine muds have clearly indicated that the alteration fluids were sourced from slab dehydration (e.g., Benton et al., 2001, 2004; Alt and Shanks, 2006; Nielsen et al., 2015; Geilert et al., 2021). This is also consistent with the significant elevation of slab-derived fluid mobile elements (e.g., Li, Cs, Rb, As, B) in these rocks relative to the depleted mantle (DM) (e.g., Savov et al., 2005, 2007; Deschamps et al., 2013). Consequently, the serpentinite clasts and serpentinite muds provide a valuable opportunity to investigate the N recycling during early-stage subduction.

To systematically investigate the recycling of slab N in the IBM forearc and its implications to subduction-zone N recycling, here I investigated N concentrations and δ^{15}N values, together with major and trace elements (i.e., fluid-mobile elements, including Li, Cs, and B), of 38 serpentinite clasts and 5 serpentinite muds recovered from Ocean Drilling Program (ODP) Holes 780C, 779A, 1200A, 784A and International Ocean Discovery Program (IODP) Hole 1498B. These samples represent uplifted mantle wedge materials from a depth range from 9 – 29 km.

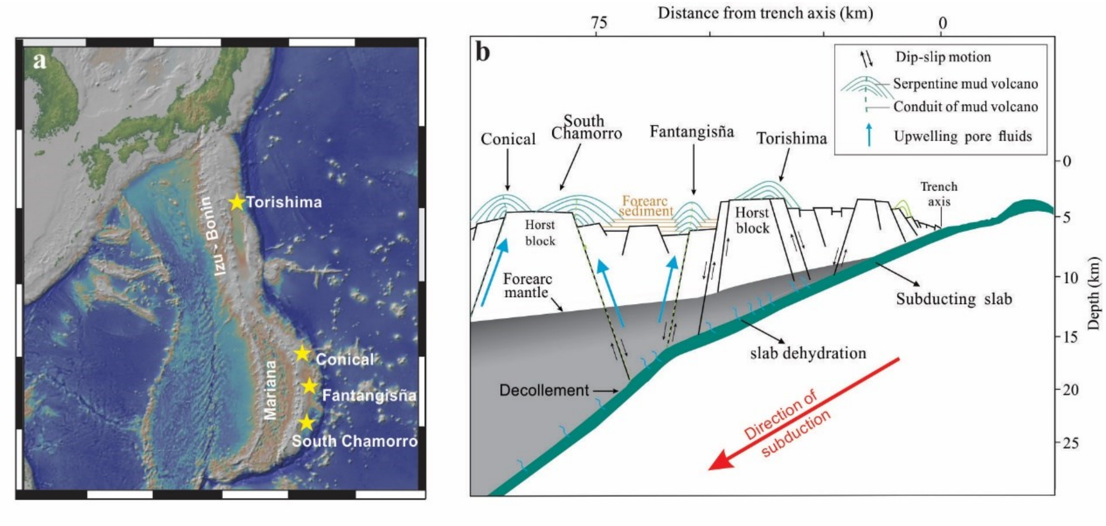

Figure 16. Sample locations of serpentinites from the Izu-Bonin-Mariana forearc mud volcanoes. (a) Study sites (four forearc seamounts) in the Izu-Bonin-Mariana forearc region (generated by GeoMapApp; http://www.geomapapp.org); (b) idealized cartoon showing the cross section of the Izu-Bonin-Mariana forearc region and the spatial distribution of the four forearc seamounts (modified from Fryer, 2018).

3.1.2 Geological background and sample descriptions

The ~2450 km IBM arc system spreads from Tokyo (Japan) in the north to Mariana Islands in the south, where the Mesozoic Pacific Plate has been subducted beneath the West Philippine plate since the Cenozoic (Ishizuka et al., 2011; Sun et al., 2020; Fig. 16). As a non-accretionary subduction system, the multiple horst and graben structures caused by extensional stress from rapid slab roll-back have resulted in the development of numerous serpentinite mud volcanoes (Fryer, 1996). The samples for this study were from 5 ODP/IODP drill holes at 4 mud volcanoes:

(1) The Conical Seamount: 19 serpentinite clasts and 1 serpentine-bearing mud were from ODP Hole 780C (n = 8) and Hole 779A (n = 11) drilled on the summit and flank of the active Conical Seamount, respectively. The Conical Seamount lies 86 km west of the Mariana trench axis and ~29 km above the subducting slab (Mottl et al., 2003; Fryer et al., 2018a). The examined

ultramafic clasts are harzburgites, which have been moderately to completely (~50% – 100%) serpentinized to chrysotile, lizardite, antigorite and brucite (Saboda et al., 1992). Generally, alteration has turned olivine to mesh-textured lizardite, and orthopyroxene to bastitic lizardite (Saboda et al., 1992). The metamorphic conditions at the slab-mantle interface below the Conical Seamount is estimated to be ~250 – 350 ºC, which is in the lawsonite-blueschist facies (Maekawa et al., 1993; Tamblyn et al., 2019; Fryer et al., 2020; Ichiyama et al., 2021).

(2) The South Chamorro Seamount: 7 serpentinized peridotite clasts were from ODP Hole 1200A drilled on the knoll of the South Chamorro Seamount, which lies 78 km west of the Mariana trench axis and ~22 km above the subducting slab (Shipboard Scientific Party, 2002; Mottl et al., 2003; Oakley et al., 2008). The South Chamorro Seamount is the only known site with active blueschist mud volcanism in the world (Shipboard Scientific Party, 2002). The examined ultramafic clasts are highly serpentinized harzburgites (~70% – 100%) with the primary olivine and orthopyroxene commonly replaced by lizardite and brucite (Shipboard Scientific Party, 2002). The serpentinized harzburgites generally show typical mesh and bastitic textures developed by the replacement of olivine and orthopyroxene to lizardite (Shipboard Scientific Party, 2002). The metamorphic conditions at the slab-mantle interface below the South Chamorro Seamount is estimated to be ~250 – 350 ºC, which is in the epidote-blueschist facies (Fryer et al., 2020; Ichiyama et al., 2021)

(3) The Fantangisña Seamount: 6 serpentinized peridotite clasts and 5 serpentine-bearing muds were from IODP Hole 1498B drilled on the southwestern flank of the active Fantangisña Seamount, which lies 62 km west of the Mariana trench axis and 14 km above the subducting slab (Fryer et al., 2018a). The examined ultramafic clasts are highly serpentinized harzburgites composed of lizardite, chrysotile, antigorite and brucite (Fryer et al., 2018b). The serpentinized

harzburgites generally show mesh and bastitic textures developed by the replacement of olivine and orthopyroxene to lizardite/chrysotile (Fryer et al., 2018b). The metamorphic conditions at the slab-mantle interface below the Fantangisña Seamount is estimated to be ~150 ºC, which is in the prehnite-pumpellyite facies (Fryer et al., 2018a; Ichiyama et al., 2021).

(4) The Torishima Seamount: 5 serpentinite clasts were from Hole 784A drilled on the western flank of the inactive Torishima Seamount, which lies 30 km west of the Izu-Bonin trench axis and ~9 km above the subducting slab. The examined ultramafic clasts are highly serpentinized harzburgites with olivine and orthopyroxene replaced by chrysotile and lizardite showing mesh and bastitic textures (Shipboard Scientific Party, 1990). The metamorphic conditions at the slab-mantle interface below the Torishima Seamount are estimated to be ~200 ºC, which is in the prehnite-actinolite facies (Fryer, 1992; Maekawa et al., 1992).

3.1.3 Results

3.1.3.1 Major and trace elements

Major and trace element concentrations are listed in Table D1 in Appendix D. The serpentinite clasts from 5 holes contain comparable MgO (31.50 – 43.96 wt.%), SiO_2 (30.13 – 40.53 wt.%), and $Fe_2O_3^T$ (5.32 – 8.46 wt.%), with other oxides, including Al_2O_3 (0.00 – 0.99 wt.%), CaO (0.00 – 1.84 wt.%), Na_2O (0.09 – 0.52 wt.%) and MnO (0.09 – 0.13 wt.%). The serpentinite clasts from Holes 1200A, 1498B and 784A generally have high LOI varying from 11.16 wt.% to 19.39 wt.%, whereas ultramafic clasts from Holes 779A and 780C have more variable LOI ranging from 3.82 wt.% to 17.42 wt.% and 7.99 wt.% to 16.44 wt.%, respectively. The serpentinite muds from Hole 1498B have major element concentrations comparable to those of serpentinite clasts with MgO (37.37 – 39.34 wt.%), SiO_2 (38.42 – 39.50 wt.%), $Fe_2O_3^T$ (6.04 – 7.07 wt.%), Al_2O_3 (0.33 – 0.68

wt.%), CaO (0.04 – 2.34 wt.%), Na_2O (0.32 – 0.39 wt.%) and MnO (0.10 – 0.11 wt.%). These clast samples also have high LOI from 14.21 wt.% to 15.55 wt.%.

The Li, Cs and B concentrations of the studied serpentinite clasts show ranges of 0.4 – 9.0 ppm, 0.002 – 1.19 ppm and 8.0 – 67.0 ppm, respectively (Fig. D1 in Appendix D). These results are consistent with previous studies on serpentinite clasts from Holes 1200A, 780C, 779A, 784A and 1498B indicating significant gain of these fluid mobile elements relative to the depleted mantle (Savov et al., 2005; Savov et al., 2007; Debret et al., 2019). No downhole trends of Li and Cs concentrations were observed in these holes, but B concentrations decrease gradually with the increase of depth in Hole 779A (Fig. D1 in Appendix D). Noteworthily, B concentrations of the serpentinite clasts from Hole 784A are also all significantly elevated (43.1 – 67.0 ppm) relative to the depleted mantle (Fig. D1 in Appendix D). In contrast to the serpentinite clasts, the serpentinite muds from Hole 1498B show Li concentrations (0.2 – 0.8 ppm) mostly within the range of the depleted mantle, but elevated B (13.2 – 20.2 ppm) and Cs (0.002 – 0.02 ppm) concentrations relative to the depleted mantle (Fig. D1 in Appendix D). In our samples, a broad negative correlation between LOI and Li (Fig. 17a) and Cs (Fig. 17b) concentrations and a broad positive correlation between Li and Cs concentrations were observed (Fig. D2 in Appendix D). The serpentinite clasts and serpentinite muds from Hole 1498B and serpentinite clasts from Hole 784A fall in the lower ends of the Li and Cs concentration ranges (Fig. 17a, b).

3.1.3.2 Nitrogen concentrations and isotope compositions

The N concentrations and $\delta^{15}N$ values are listed in Table D1 in Appendix D. The serpentinite clasts from 5 holes have comparable N concentrations of 3.6 – 12.8 ppm with $\delta^{15}N$ value of -3.4‰ – +2.8‰ (Fig. 18). The serpentinite muds from Hole 1498B have slightly higher N concentrations of 9.7 – 16.4 ppm with δ^{15}N value of -3.8‰ – -0.7‰ (Fig. 18). Overall, the N concentrations of serpentinite clasts and muds show broad negative correlations with Li (Fig. 17c) and Cs contents (Fig. 17d), but a positive correlation with δ^{15}N (Fig. 18).

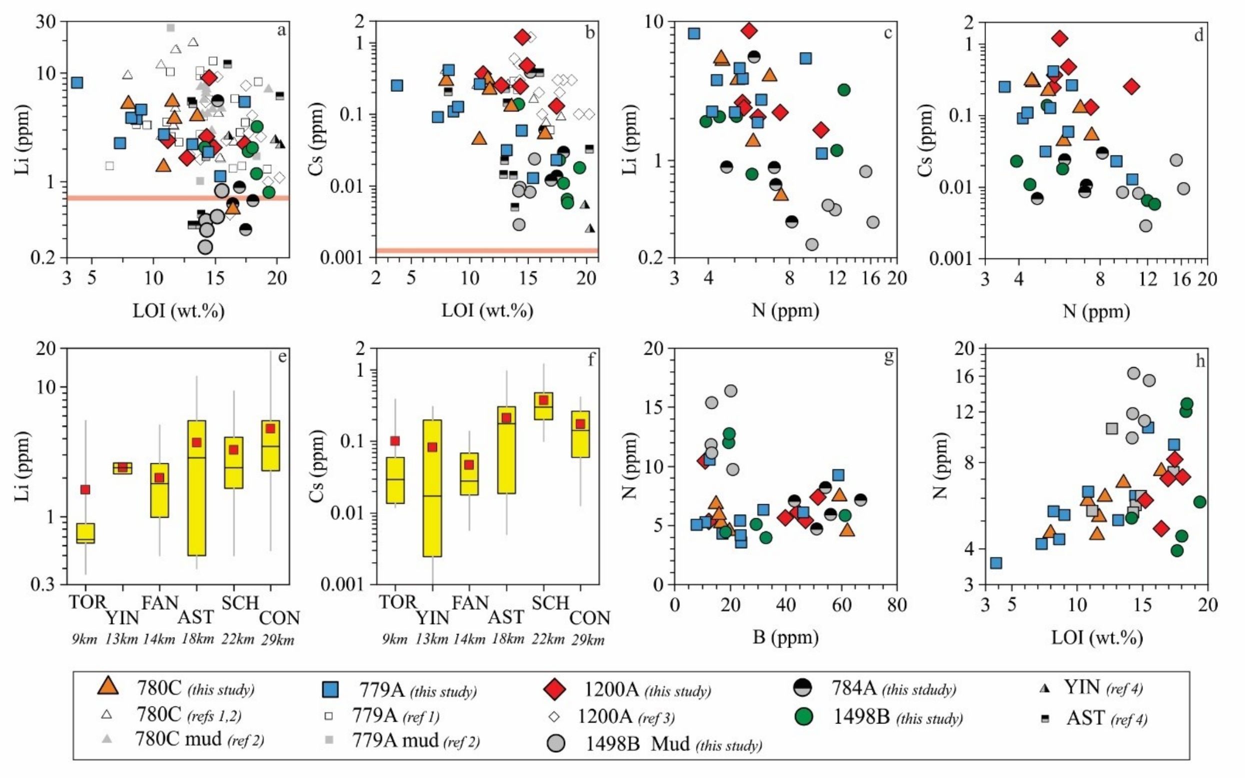

Figure 17. Trace element and N characteristics of the examined serpentinites. (a) and (b): the relationship between LOI contents and Li and Cs concentrations; (c) and (d): the relationship between N concentrations and Li and Cs concentrations; (e) and (f): Box plot of Li and Cs concentrations of serpentinite clasts from the Torishima (TOR), Yinazao (YIN), Fantangisña (FIN), Asùt Tesoru (AST), South Chamorro (SCH) and Conical (CON) seamounts. Note the increase of slab depth from 9 km to 29 km from left to right (data source: Savov et al., 2005, 2007; Debret et al., 2019; Johnston, 2019). The red squares represent the mean Li and Cs concentrations of all the data. The data of serpentinite clasts and muds from Holes 780C, 779A and 1200A are from Savov et al. (2005) (ref 1), Benton et al. (2004) (ref 2), Savov et al. (2007) (ref 3). The serpentinite clasts data from the Yinazao and Asùt Tesoru Seamounts are also shown for comparison. The red shaded area marks the Li (0.7 ppm) and Cs (0.0013 ppm) concentrations of the depleted mantle (Salters and Stracke, 2004).

3.1.4 Discussion

3.1.4.1 Nitrogen enrichment in serpentinites from the IBM mantle wedge

Compared to the low N concentration (~1.1 ppm; Marty et al., 2020) and $\delta^{15}N$ value (-5‰; Marty and Humbert, 1997; Marty and Dauphas, 2003) of the depleted mantle, the N concentrations and $\delta^{15}N$ values of the serpentinite clast and mud samples from the IBM mud volcanoes are significantly elevated. This has to be attributed to addition of external N during hydrothermal alteration, as being demonstrated by the positive correlation between N and LOI contents (Fig. 17h). Previous studies have revealed that two possible fluids, i.e., slab-derived fluids and seawater, were involved in the alteration of the serpentinized clasts from Sites 779, 780 and 1200 (e.g., Benton et al., 2001; Savov et al., 2005; Savov et al., 2007). Therefore, the external N could come from subducting slab and/or seawater. Distinguishing the N between these two sources is required to quantify the recycling of slab N within the forearc region.

3.1.4.2 Source of N in the IBM mantle-wedge serpentinites

Among the enriched fluid-mobile elements (i.e., Li, Cs and B) in the serpentinite clasts, B concentrations can be significantly affected by seawater (Benton et al., 2001). This effect is most prominent in the upper ~15 m at Site 780 and possibly ~100 m at Site 779, where B concentrations of serpentinites are highest (Benton et al., 2001). This effect could also be the cause of the relatively high B concentrations of serpentinized peridotites in Hole 784A at the Torishima Seamount, where seawater is the dominant alteration fluid due to the lack of upwelling deep-sourced fluids (e.g., Savov et al., 2007; Fig. D1 in Appendix D). In contrast, previous studies (Savov et al., 2005, 2007; Deschamps et al., 2013; Albers et al., 2020) have demonstrated that seawater alteration has minor effect on Li and Cs concentrations. Instead, Li and Cs enrichments are more likely caused by slab fluids (Albers et al., 2020) sourced mainly from subducted sediments with contribution of AOC at greater depths (e.g., > 18 km beneath the Asùt Tesoru, the South Chamorro and the Conical Seamounts; Mottl et al., 2004; Hulme et al., 2010).

When plotting the Li and Cs concentrations of the studied serpentinite clasts and muds against the slab depth beneath the seamounts (Fig. 17e and 17f), it shows an increasing trend in Li and Cs concentrations along slab depths, which have been attributed to progressive release of Cs and Li from subducting slab during dehydration along depth (e.g., Benton et al., 2004; Albers et al., 2020). This further supports a slab source for these elements in the serpentinites from the IBM mantle wedge. Accordingly, we can use B concentration as an index of seawater input and Li and Cs concentrations as indices for slab fluid input, with low Li and Cs concentrations indicating shallow slab fluid and high Li and Cs concentrations indicating deeper slab fluid.

When comparing N concentrations with B concentrations of the studied serpentinite clasts and muds, no positive correlation is observed (Fig. 17g). This suggests that the majority of N in the examined samples was sourced from slab-derived fluids. A slab source of the secondary N in the serpentinite clast and mud samples is also supported by their $\delta^{15}N$ data, which fit well with a two-component mixing model (refer to Equation 1 in ***Chapter 2.1***; Fig. 18) between the depleted mantle ($N = \sim 1.1$ ppm, $\delta^{15}N = -5‰$; Marty et al., 2020) and secondary N in the subducting sediments and basalts toward the IBM trench ($\delta^{15}N = -1‰$ to $+5‰$; Sadofsky and Bebout, 2004; Li et al., 2007). While the relative N contribution between sediments and AOC cannot be distinguished by N isotopic data solely, it is most likely that the majority of N was from sediments because the loss of N from AOC during the early subduction stage up to blueschist-facies metamorphism (< ~40 km) is negligible (Halama et al., 2010; Li et al., 2021c; ***Chapter 3.2***).

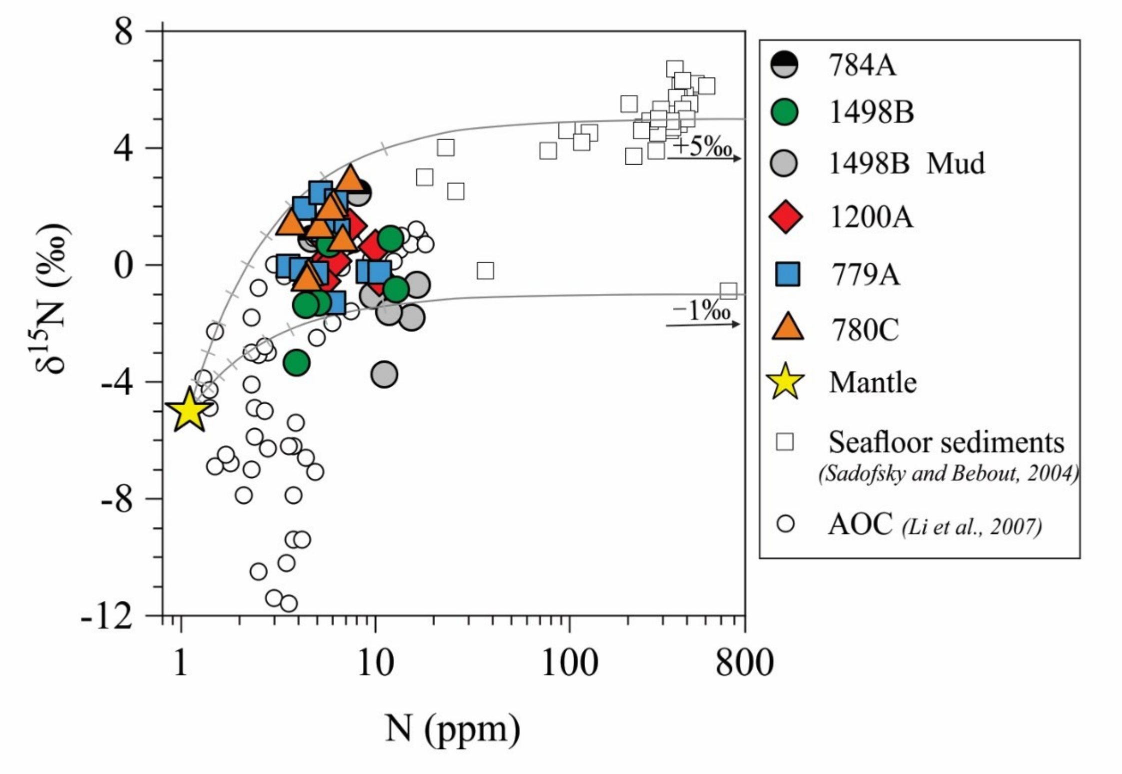

Figure 18. Two-component mixing modeling of the N concentrations and δ^{15}N values of the IBM serpentinite clasts and muds. The yellow star marks the depleted mantle endmember (Marty et al., 2020; N = 1.1 ppm; δ^{15}N = -5.0‰;). The grey curves illustrate the addition of NH_4^+ with δ^{15}N values of -1‰ to +5‰. The fraction of the incorporated NH_4^+ in the total N is marked by short gray lines with a 10% increment. The data of subducting seafloor sediments (Sadofsky and Bebout, 2004) and AOC (Li et al., 2007) offboard the IBM trench are also shown for comparison.

3.1.4.3 Waning of N recycling along depth in the IBM forearc

It is interesting to observe broad negative correlations between N and both Li (Fig. 17c) and Cs concentrations (Fig. 17d). As discussed earlier, the increase of Li and Cs concentrations in serpentinite clasts is a result of interactions with slab-derived fluids with progressively more enriched Li and Cs at greater slab depths. Consequently, the negative correlations between N and Li or Cs indicate that the recycling of slab N to the forearc mantle wedge is progressively waning with the increase in depth. This suggests that the shallow slab fluid contained relatively higher N whereas the deeper slab fluid contained little N. Given the shallow depth and the relatively low-temperature conditions, the shallow fluid was likely mainly sourced from compacted pore fluid with high fluid fluxes, whereas the deep fluid with low fluid flux could contain more contributions from decomposition of hydrous minerals (Hyndman and Peacock, 2003). This is supported by two lines of evidence. One is the positive correlation between N concentration and LOI content (Fig. 17g), which indicates that the shallow fluid with high flux generated high N concentrations and high LOI contents in the rocks and vice versa. The other is the N signature (high N concentrations but low $\delta^{15}N$ values) of the serpentinite muds. The mud samples from ~54 – 201 mbsf of Hole 1498B have low Li, Cs and B concentrations (Fig. 17a, b and g), indicating they are most closely related to shallow slab fluids. The pore fluid in sediments and AOC generally has slightly lower $\delta^{15}N$ values due to the isotope fractionation between fluid and clay minerals (Li et al., 2021b), which is consistent with the slightly low $\delta^{15}N$ values observed in the serpentinite mud samples.

Overall, our data suggest that most of the recycled slab N in the IBM serpentinized mantle wedge is dissolved N in pore fluids (which is not accounted in the calculations of input N flux; Sadofsky and Bebout, 2004; Li et al., 2007; ***Chapter 3.3***) rather than the fixed N in sediments and/or AOC. This apparently conflicts with the observation that the increasing slab temperature along depth favors the progressive devolatilization of slab N during prograde metamorphism (e.g., Bebout and Fogel, 1992; Bebout et al., 1999). However, it should be noted that the samples in this study represent the very early stage of subduction up to epidote-blueschist facies (9 – 29 km; < 350 ºC). Studies on metasediments from both cold and warm subduction zones indicated no significant N loss up to blueschist facies (Bebout et al., 1992; Busigny et al., 2003; ***Chapter 3.3***), which is consistent with this study. Significant N loss in subducting slabs only appears in the greenschist and amphibolite facies (Bebout et al., 1992) or eclogite facies (***Chapters 2.1-2.3***).

3.1.4.4 Flux of slab N recycled to the forearc mantle wedge

These new data of N in the serpentinite clasts exhumed from the hydrated forearc mantle wedge allow for the first attempt to estimate the flux of slab N recycled to the forearc region. Using the water flux of 7.1×10^{11} $g \cdot yr^{-1}$ into the IBM forearc mantle wedge (Abers et al., 2017), together with the assumption that all the water is incorporated into the mantle wedge to produce serpentine with ~12 wt.% of water (Schmidt and Poli, 1998) , the quantity of serpentinite is estimated to be 5.9×10^{12} $g \cdot yr^{-1}$. With the average N concentration of $6.1^{\pm 3.1}$ ppm (after correcting the N concentration inherited from the depleted mantle) for the serpentinite clasts and muds examined in this study, the slab N that is fixed by the serpentinized forearc mantle wedge is calculated to be $2.6^{\pm 1.3} \times 10^6$ $mol \cdot yr^{-1}$, which only accounts for ~0.7 % of the N input flux of subducting sediments ($3.6^{\pm 0.2} \times 10^8$ $mol \cdot yr^{-1}$) and 0.2 – 0.3% of the total N input flux of the entire subducting slab into the IBM trench ($7.8 - 11 \times 10^8$ $mol \cdot yr^{-1}$; see ***Chapter 3.3***). From a global perspective, if the serpentinite in global forearc mantle wedge has comparable N concentration to that of the IBM, the recycled slab N that is fixed in the serpentinzied mantle wedge would be $1.5^{\pm 0.7} \times 10^8$ $mol \cdot yr^{-1}$ employing the water flux of 4.0×10^{13} $g \cdot yr^{-1}$ to the global forearc mantle (Abers et al., 2017). Similarly, this only accounts for ~0.2% of the total N input flux ($7.6 - 8.5 \times 10^{10}$ $mol \cdot yr^{-1}$; ***Chapter 2.3***) contributed by global subducting slab. It should be noted that the recycled N flux quantified here is only the fixed portion of the recycled slab N. Future studies constraining the N characteristics of the upwelling fluids from these mud volcanoes could gain additional insights on the recycled N flux in the un-fixed forms of N.

3.1.4.5 Implications to subduction-zone N recycling

The estimation of the recycled slab N to the forearc mantle wedge suggests that little (< 1%) slab N (sediments + AOC) is devolatilized during the early-stage of shallow subduction recorded by the serpentinite samples up to blueschist facies (e.g., Maekawa et al., 1993). Therefore, it is expected that the forearc region may not play an important role for the N recycling in most of modern-style subduction zones that pass through blueschist-eclogite facies metamorphism (van Keken et al., 2018). In contrast, in extremely hot subduction zones (e.g., Catalina Schist) passing through greenschist and amphibolite facies, a large portion of slab N (> ~70%; Bebout et al., 1999) could be devolatilized within the forearc region and subsequently fixed by the serpentinized mantle wedge. As a result, the serpentinized forearc mantle wedge could be a relatively important sink for recycled slab N. This might be applicable to subduction zones in deep time (e.g., Archean), which had geotherms hotter than the modern ones (e.g., Dasgupta, 2013). If the serpentinized forearc mantle wedge can be dragged down by vertical movement of mantle flow along slab subduction (e.g., Chen et al., 2017; Fig. 19), it may act as a more efficient carrier than subducting sediments for deep N recycling due to the broader stability field of serpentine toward high temperature-pressure conditions (Ohtani et al., 2004). If the mantle wedge cannot be dragged down but becomes a stagnant reservoir (e.g., Wada et al., 2008), the recycled slab N accumulated in this isolated mantle reservoir over time can be significant and thus contribute to mantle heterogeneity.

3.1.5 Conclusions

Serpentinized forearc material at depths of ~ 9 km to ~ 29 km recovered from four Izu-Bonin-Mariana (IBM) forearc mud volcanoes show diminished (along depth) enrichment of secondary N sourced from subducting slab. The stronger enrichment of N at shallow depth of the mantle wedge was likely from compaction-derived fluid. The waning N enrichment along depth is a combined effect of decreasing flux of pore fluid and little release of fixed N in subducting sediments and altered oceanic crust. The flux of recycled slab N to the serpentinized forearc mantle wedge below IBM is estimated to be $2.6^{\pm 1.3} \times 10^6$ mol·yr^{-1}, which only accounts for ~0.7% of the N input flux from the subducting sediments into the IBM trench. This suggests that N recycling in the forearc is minor at least in the IBM subduction zone, and likely in most of the modern-style subduction zones with cold geotherms. However, the serpentinized mantle wedge could assimilate a significant amount of slab N over time and potentially contribute to the mantle heterogeneity.

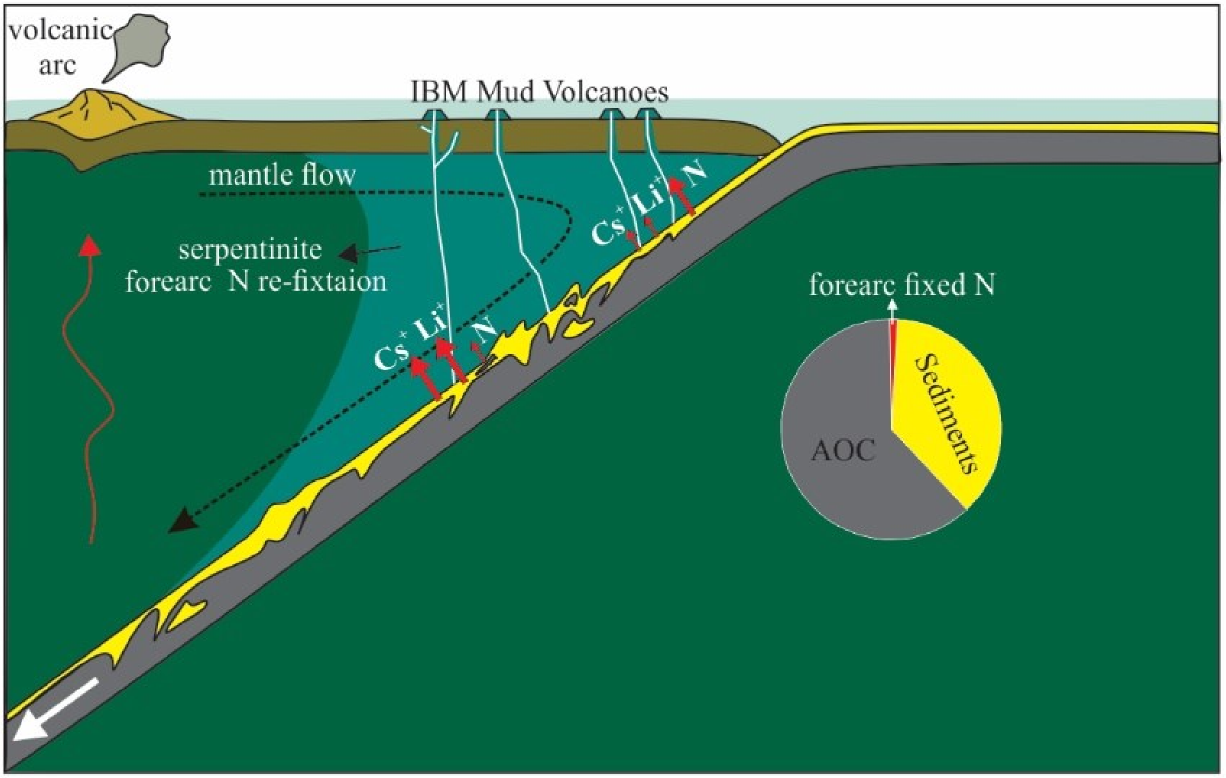

Figure 19. Schematic diagram (not to scale) showing the N and fluid-mobile element recycling in the IBM subduction zone. The inset pie chart illustrates the fraction of the recycled N flux to the forearc mantle wedge relative to the N input flux of subducting sediments and AOC. Note that the size of the red arrows indicates the intensity of element mobilization into the forearc mantle wedge.

The recycling of slab N to the forearc mantle wedge is progressively waning along depth, while more Li and Cs can be mobilized to the forearc mantle wedge during prograde metamorphism.

Chapter 3.2 Intraslab remobilization of nitrogen during early subduction recorded by blueschists from Heilongjiang Complex

3.2.1 Introduction

Nitrogen recycling across subduction zones is a critical part of the geological N cycle on Earth (e.g., Hilton et al., 2002; Johnson and Goldblatt, 2015; Bekaert et al., 2021). Nitrogen in the surface reservoirs (e.g., the atmosphere, hydrosphere and biosphere) can be incorporated into seafloor sediments (by precipitation of organic matter and clay minerals) and AOC (by hydrothermal and/or microbial alteration). The N concentrations of subducting sediments can vary depending on lithology from as low as ~ 10 ppm in sandstones, carbonates and cherts, to as high as ~2400 ppm in the organic-rich top sediments (e.g., Sadofsky and Bebout, 2004; Li and Bebout, 2005). In contrast, AOC commonly show much lower N concentrations in a range of 1.3 – 18.2 ppm (e.g., Busigny et al., 2005, 2019; Li et al., 2007; Bebout et al., 2018). Nevertheless, AOC may contain a large N inventory, at least of the same order of magnitude to the overlying sediments in the subducting slab, because of its much larger volume (Li et al., 2007). In subduction zones, part of the slab N may be released back to the surface by metamorphic devolatilization and stored in mantle wedge serpentinites by the infiltration of slab-derived fluids (***Chapter 3.1***); the remainder will be subducted into the deep mantle (e.g., Hilton et al., 2002; Halama et al., 2010; Bebout et al., 2013b; Pagé et al., 2018), which could be subsequently sampled by plume-related magmas (e.g., Dauphas and Marty, 1999; Barry and Hilton, 2016; Halldórsson et al., 2016). Subduction-zone N recycling could thus have potentially impacted the long-term evolution of Earth's surface and interior reservoirs (e.g., Sano et al., 2001; Marty and Dauphas, 2003; Mallik et al., 2018; Bekaert et al., 2021), which, however, cannot be quantitatively assessed so far because critical knowledge on N retention in slabs in subduction zones is missing.

Metamorphic rocks from ancient subduction zones provide a window to examine the N behavior in subduction zones (e.g., Haendel et al., 1986; Bebout and Fogel, 1992; Bebout, 1997; Busigny et al., 2003a; Sadofsky and Bebout, 2003; Jia, 2006; Halama et al., 2010; Li et al., 2014; Sievers et al., 2017). Nitrogen isotope ratios can be used as a robust tool to assess N devolatilization because of large magnitudes of isotope fractionations between minerals and the common devolatilized N species (NH_3 or N_2; Li et al., 2021b, d). In general, ^{14}N is preferentially taken by the released NH_3 or N_2, which can result in progressive ^{15}N enrichment in the remaining rocks along prograde metamorphism (e.g., Haendel et al., 1986; Bebout and Fogel, 1992; Mingram and Bräuer, 2001).

Nitrogen devolatilization modeling of metasedimentary rocks subducted from the forearc to sub-arc depths in four ancient subduction zones suggested high-degree (~70%) N loss (in form of N_2) in the Catalina Schist (Bebout and Fogel, 1992), medium-degree (~30%) N loss (in form of NH_3) in the European Variscan (Mingram and Bräuer, 2001), and nearly no N loss in the Schistes Lustrés (Busigny et al., 2003a) and Franciscan Complex (Sadofsky and Bebout, 2003). These results imply that the fate of N in the subducted sediments could be strongly variable among different subduction zones, which is speculated to be dependent on the thermal structure of individual subduction zone (e.g., warm for the Catalina Schist vs. cold for the Schistes Lustrés; Busigny et al., 2003b; Bebout, 2007b).

In contrast, studies on high-pressure (HP) to ultrahigh-pressure (UHP) eclogites observed little loss but retention of N in AOC to the sub-arc depth (Philippot et al., 2007; Halama et al., 2010, 2014; Busigny et al., 2011). This implies that AOC could be more resistant to metamorphic devolatilization than sediments. More interestingly, based on correlations of N and trace element concentrations, Halama et al. (2010) observed potential addition of sediment-derived N to the eclogites in the Raspas Complex (Ecuador) by fluid-rock interactions inside the subduction zone. Similarly, relatively high N concentrations (3 – 74 ppm) have also been observed in some HP peridotites from the Central Alps, Raspas Complex (Ecuador) and Almirez Massif (Spain), which are speculated to be a result of admixing of sedimentary N during prograde metamorphism within the subduction zone (e.g., Halama et al., 2010, 2014; Cannaò et al., 2020), although N addition during seafloor alteration is also possible. Nevertheless, these studies imply that part of the sedimentary N could be recaptured by the meta-igneous part of the subducting slab during prograde metamorphism. This process, if occurs widely inside subduction zones, may play a critical role to promote the deep recycling of slab N. However, it is still unclear how common this process is inside subduction zones, and in particular, whether it can occur in the forearc region where significant N devolatilization from sediments could be initiated (e.g., Bebout and Fogel, 1992).

In this study, aiming to understand the N behavior in the early subduction stage in the forearc region, we investigated the N concentrations and isotope compositions, as well as major and trace elements of epidote-blueschist facies meta-basalts (hereafter refered to as blueschists) from the Heilongjiang Complex in Northeast China (NE China). These blueschists still retain pillow shapes, which clearly indicates that their protoliths were from the topmost parts of ancient AOC. The epidote-blueschist facies metamorphism occurred at 198 – 175 Ma (see Zhou and Li, 2017 and reference therein) with peak metamorphic conditions of 320 – 450°C and a peak pressure of 0.9 – 1.1GPa (e.g., Zhou et al., 2009), which is equivalent to a subduction depth of ~40 km.

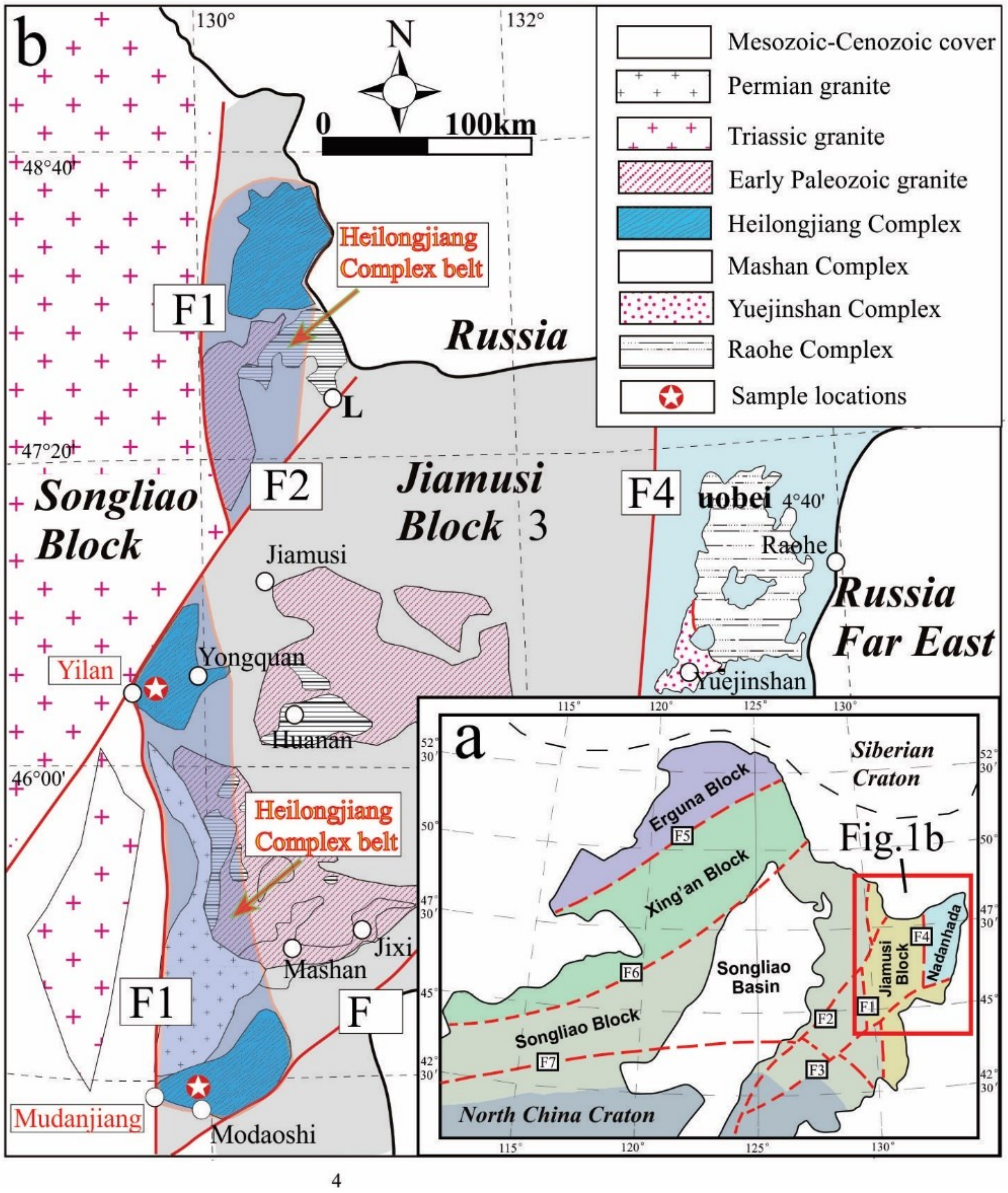

Figure 20. Geological sketch map of Northeast China (modified after Han et al., 2020). (a) Tectonic subdivisions of Northeast China showing multiple micro-continental blocks. (b) Map of the Jiamusi Block and adjacent areas showing the spatial distribution of the Heilongjiang Complex from the Mudanjiang area in the south, the Yilan area in the center, to the Luobei area in the north. The sample locations for this study are marked by stars. Abbreviations: F1 = the Mudanjiang Fault; F2 = the Yilan-Yitong Fault; F3 = the Dunhua-Mishan Fault; F4 = the Yuejinshan Fault; F5 = the Tanyuan-Xiguitu Fault; F6 = the Hegenshan-Heihe Fault; F7 = the Xar Moron-Changchun Fault.

3.2.2 Geological background and samples

(1) Regional geology

Northeast China is geologically comprised of several micro-continental blocks (Fig. 20; Şengör et al., 1993; Jahn, 2004; Li, 2006). Its western part consists of the Songliao, Xing'an and Erguna blocks, which all belong to the Central Asian Orogenic Belt. These blocks mark the broad collision zone between the North China Craton in the south and the Siberian Craton in the north following the closure of the Paleo-Asian Ocean (Fig. 20a). Its eastern part consists of the Heilongjiang Complex in the west, the Jiamusi Block in the middle, and the Nadanhada Terrrane in the east (Fig. 20b), which is a late Triassic-Cretaceous accretionary terrane formed by the westward subduction of the Paleo-Pacific Plate (e.g., Zhou et al., 2014).

The Heilongjiang Complex is an HP metamorphic belt over-thrusted onto the western margin of the Jiamusi Block along the north-south directed Mudanjiang Fault (F1 in Fig. 20b), which was later truncated by the Yilan-Yitong Fault (F2; Zhou et al., 2009; Zhou and Li, 2017). The HP Heilongjiang Complex is characterized by occurrence of blueschists, together with serpentinites, greenschist-facies marble, two-mica schists, muscovite-albite schists, quartz schists, quartzites and minor amphibolites (e.g., Li et al., 1999; Wu et al., 2007; Zhou and Li, 2017). Previous studies have identified that the Heilongjiang Complex was a tectonically juxtaposed mélange (Wu et al., 2007; Zhou et al., 2009, 2010; Zhu et al., 2015, 2017) as a result of an east-west directed closure of an ancient ocean, which was likely related to the Paleo-Pacific Ocean (Li et al., 2021e).

The blueschists in the Heilongjiang Complex are mainly exposed in three areas, i.e., from south to north, Mudanjiang, Yilan, and Luobei (Fig. 20b). Most previous studies on the blueschists in the

Heilongjiang Complex have been focused on the Mudanjiang and Yilan areas (e.g., Zhou et al., 2009; Zhu et al., 2015, 2017; Ge et al., 2017). The Luobei blueschist outcrops are relatively difficult to access and have not been well studied yet. The dating of detrital zircons gave a maximum protolith ages of 288 – 258 Ma for the Yilan blueschists and 224 – 213 Ma for the Mudanjiang blueschists, respectively (Zhou et al., 2013; Ge et al., 2017). Ar-Ar and Rb-Sr dating of these blueschists gave ages of the blueschist-facies metamorphism of 198 – 175 Ma in these two places (Wu et al., 2007; Zhou et al., 2009, 2010, 2013; Zhou and Li, 2017).

(2) Sampling

Twenty-seven blueschist samples were collected from the Mudanjiang (n = 13) and Yilan (n = 14) areas for this study. The Mudanjiang blueschists commonly preserve pillow structures and occur as tectonic lenses dominantly in greenschist-facies mica schist with locally preserved stratigraphic layers supporting a sedimentary origin (see Zhou et al., 2009; Zhu et al., 2015; Ge et al., 2016 for detail). The Yilan blueschists occur as small blocks, boudins or sheets that range from meters to hundreds of meters in length with well-preserved pillow structures and spread in in greenschist-facies mica-schist (Fig. 21a and 21b; see Zhou et al., 2009; Zhu et al., 2015; Ge et al., 2016 for detail). All the samples for this study were collected from the inner parts of pillows or lenses. The rims of the pillows or lenses and veins were carefully excluded to avoid retrograde metamorphic influence.

(3) Petrographic description

Detailed petrographic descriptions of both the Mudanjiang and Yilan blueschists have been given by several previous studies (Zhou et al., 2009; Zhu et al., 2015; Ge et al., 2016). Some key information is summarized here. Meta-basalts from the Mudanjiang area have the typical mineral assemblage of sodic amphibole (20 – 25%), albite (45 – 50%), epidote (20 – 25%), phengite (5 – 10%) and chlorite (10 – 15%) (Fig. 21b and 21c). The sodic amphibole is small (0.5-1 mm; Fig. 21b) and its composition ranges from glaucophane to magnesio-riebeckite (Zhou et al., 2009). Chlorite occurs either in the matrix or around glaucophane (Fig. 21b). The schistosity is defined by sodic amphibole, epidote and chlorite (Fig. 21b and 21c). The abundance of fluid inclusions is low and a few fluid inclusions (1 um to 5 μm) were found in some of the phengite crystals.

Meta-basalts from the Yilan area are dominantly characterized by the mineral assemblages of sodic amphibole (20 – 25%), albite (35 – 40%), epidote (25 – 35%), phengite (5 – 10%) and chlorite (<10%). (Fig. 21). The sodic amphibole is small (0.5 – 1 mm; Fig. 21e and 21f) and its composition is dominated by ferro-glaucophane (Zhou et al., 2009; Ge et al., 2016). Chlorite occurs either in the matrix or around glaucophane and albite (Fig. 21f). The schistosity is defined by sodic amphibole, epidote and chlorite (Fig. 21e and 21f). The abundance of fluid inclusions is low and few fluid inclusions (1 – 5 um) were found in some of the phengite crystals.

Overall, the presence of glaucophane and ferro-glaucophane, associated with epidote and phengite, indicates epidote-blueschist facies metamorphism in the Yilan and Mudanjiang meta-basalts (Zhou et al., 2009). The presence of chlorite indicates these samples experienced retrograd metamorphism as well. However, the preservation of the high-Si signature (3.38 – 3.46 per formula unit) of phengite (Zhou et al., 2009) indicates that the retrograde metamorphic effect on the meta-basalts is relatively small.

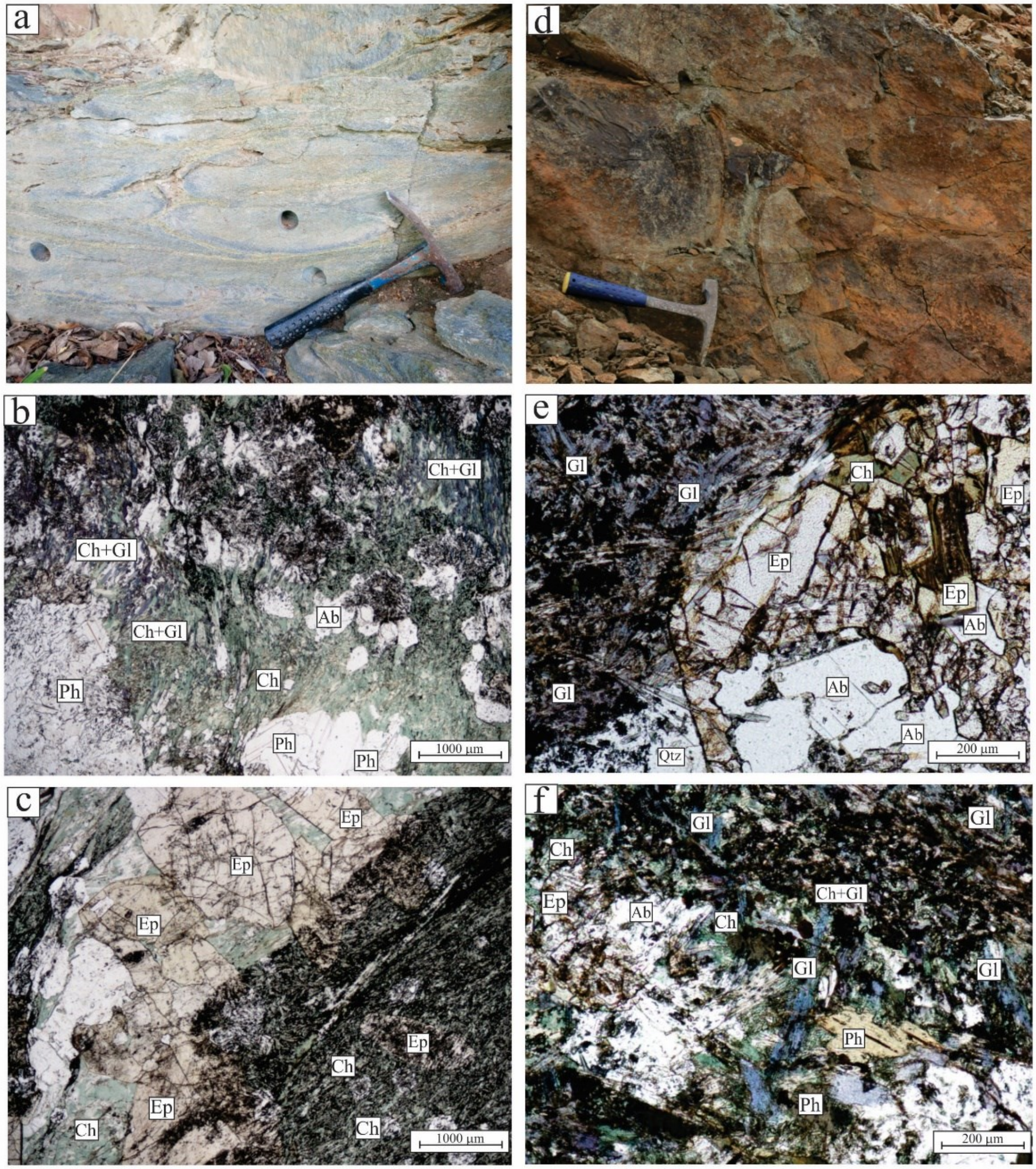

Figure 21. Photographs of field outcrops and thin sections of blueschists from the Heilongjiang Complex. (a) outcrop of the Mudanjiang blueschist showing well-preserved pillow structure; (b) thin section of blueschist sample 15HLJ-05B from Mudanjiang (plane polarized light); (c) thin section of blueschist sample 15HLJ-01 from Mudanjiang (plane polarized light); (d) outcrop of the Yilan blueschist showing well-preserved pillow structure; (e) thin section of blueschist 15HLJ-39 from Yilan (plane polarized light); (f) thin section of blueschist 15HLJ-41 from Yilan (plane

polarized light). Abbreviations: Gl: glaucophane; Ab: albite; Ph: phengite; Ep: epidote; Ch: chlorite; Qtz: quartz.

3.2.3 Results

3.2.3.1 Major and trace elements

Whole-rock major and trace element compositions of the Mudanjiang and Yilan blueschists are listed in Table E1 in Appendix E. Overall, the blueschist samples have SiO_2 concentrations from 39.81% to 52.32%, total FeO concentrations from 9.58% to 15.91%, MgO concentrations from 2.69% to 6.93%, TiO_2 concentrations from 1.57% to 4.56%, and Na_2O concentrations from 2.09% to 5.48%. Both the Mudanjiang and Yilan blueschist samples have high concentrations of rare earth elements (REE) with ΣREE varying from 52.2 to 196.6 ppm for the Mudanjiang blueschists and 104.4 to 295.3 ppm for the Yilan blueschists, respectively. On the diagram of chondrite-normalized REE patterns, the Mudanjiang blueschists show slight enrichments in light REE (LREE), with $(La/Yb)_N$ ratios of 2.5 to 4.2 and $(La/Sm)_N$ ratios of 1.3 to 1.9, and relatively gentle right-dipping REE patterns similar to those of enriched mid-ocean ridge basalts (E-MORB; Fig. 22a). Most of the Yilan blueschists display strong enrichments in LREE, with $(La/Yb)_N$ ratios of 5.6 to 18.5 and $(La/Sm)_N$ ratios of 1.6 to 5.9, and steep right-dipping patterns similar to those of ocean island basalts (OIB; Fig. 22b). Three Yilan samples (15HLJ-39, 15HLJ-40 and 15HLJ-41) display a flat distribution of LREE and strong depletion in heavy REE (HREE), with $(La/Yb)_N$ ratios of 26.4 to 28.5 and $(La/Sm)_N$ ratios of ~1.3 (Fig. 22b). The REE patterns of these three samples have been attributed to the low-degree partial melting of garnet-facies peridotites in which HREEs were retained in garnet in the residue (Zhu et al., 2015). Nevertheless, consistent with previous studies (Zhou et al., 2009; Zhu et al., 2015; Ge et al., 2017), the overall REE patterns of the Yilan blueschists are indicative of an origin similar to OIB.

3.2.3.2 Nitrogen concentrations and isotope compositions

The N concentrations and $\delta^{15}N$ values of the blueschist samples from Mudanjiang and Yilan are listed in Table E1 in Appendix E. The Mudanjiang blueschists display a large range in N concentrations from 13.9 ppm to 83.6 ppm, but a relatively small $\delta^{15}N$ range from −0.5‰ to +3.7‰ (Fig. 23). The Yilan blueschists show a large variation in both N concentrations and $\delta^{15}N$ values, which can be subdivided into two groups: group A samples are characterized by relatively high N concentrations (21.2 ppm to 122.6 ppm; average: 87.4 ppm) and positive $\delta^{15}N$ values within a small range of +0.9‰ to +3.2‰ (average: $+2.5^{\pm 0.7}$‰; 1σ; n = 8); whereas group B samples show relatively low N concentrations (17.3 ppm to 46.9 ppm; average: 33.9 ppm) and large $\delta^{15}N$ variations with unusual negative values (−3.3‰ to −10.9‰; Fig. 23). It should be noted that the two sets of samples in group B with distinct REE patterns (Fig. 22b) show no difference in N concentrations and $\delta^{15}N$ values: 17.3 to 39.7 ppm and −3.3‰ to −10.1‰ for samples with strong HREE depletion, 24.3 to 46.9 ppm and −3.8‰ to −10.9‰ for the other group B samples, respectively. This indicates that their N signatures more likely reflect secondary N rather than original magmatic N. Overall, the $\delta^{15}N$ values of the blueschists from the Heilongjiang Complex overlap with those of basaltic portion of AOC from global oceans, but the N concentrations of the blueschists are significantly higher than those of global basaltic AOC (< 19 ppm; Fig. 23).

3.2.4 Discussion

3.2.4.1 Nitrogen residence in blueschist

Fixed N in minerals is generally accepted to be in form of ammonium (NH_4^+). Because of the similar ionic radius (IR) and charges between K^+ (IR = 1.64 Å; Shannon and Prewitt, 1969) and

NH_4^+ (IR = 1.67 Å; Sidey, 2016), N can be easily enriched in K-bearing minerals (e.g., micas and alkali feldspars; Yamamoto and Nakahira, 1966; Honma and Itihara, 1981; Bos et al., 1988). The substitution of K^+ by NH_4^+ has been well supported by the positive correlations between N and K_2O concentrations observed in several metamorphic suites (e.g., Bebout, 1997; Busigny et al., 2003a; Busigny and Bebout, 2013; Sievers et al., 2017). Surprisingly, such a correlation has not been observed in AOC (e.g., Li et al., 2007; Busigny et al., 2019). This may be attributed to more complicated incorporation of N in AOC involving multiple secondary minerals (Staudigel, 2014a) and organic matter (Ménez et al., 2012) during alteration of oceanic crust. In addition, NH_4^+ can also be assimilated by Na^+- or Ca^{2+}-bearing minerals due to the similar ionic radius between NH_4^+ and Na^+ (IR = 1.39 Å; Shannon and Prewitt, 1969) and the replacement of Ca^{2+}+Mg^{2+} by Al^{3+}+NH_4^+ (e.g., Honma and Itihara, 1981; Watenphul et al., 2010; Li et al., 2021b).

In the studied blueschists, the N concentrations do not correlate with Na_2O and MgO concentrations, but K_2O concentrations (Fig. 24). This suggests that most N resides as NH_4^+ in the K-bearing minerals, which are dominated by phengite in the studied samples. Phengite has also been demonstrated to be the major host mineral for N in rocks that have experienced HP and UHP metamorphism (e.g., Li et al., 2014; Halama et al., 2017). In addition, few fluid inclusions observed in the phengite crystals may also contain N but their contribution to the overall N concentrations of phengite should be small due to their minor abundance. Nevertheless, although some degree of retrograde metamorphism has been observed in the samples (Fig. 21), the majority of N hosted by phengite should not be significantly affected because of the good preservation of phengite (Zhou et al., 2009).

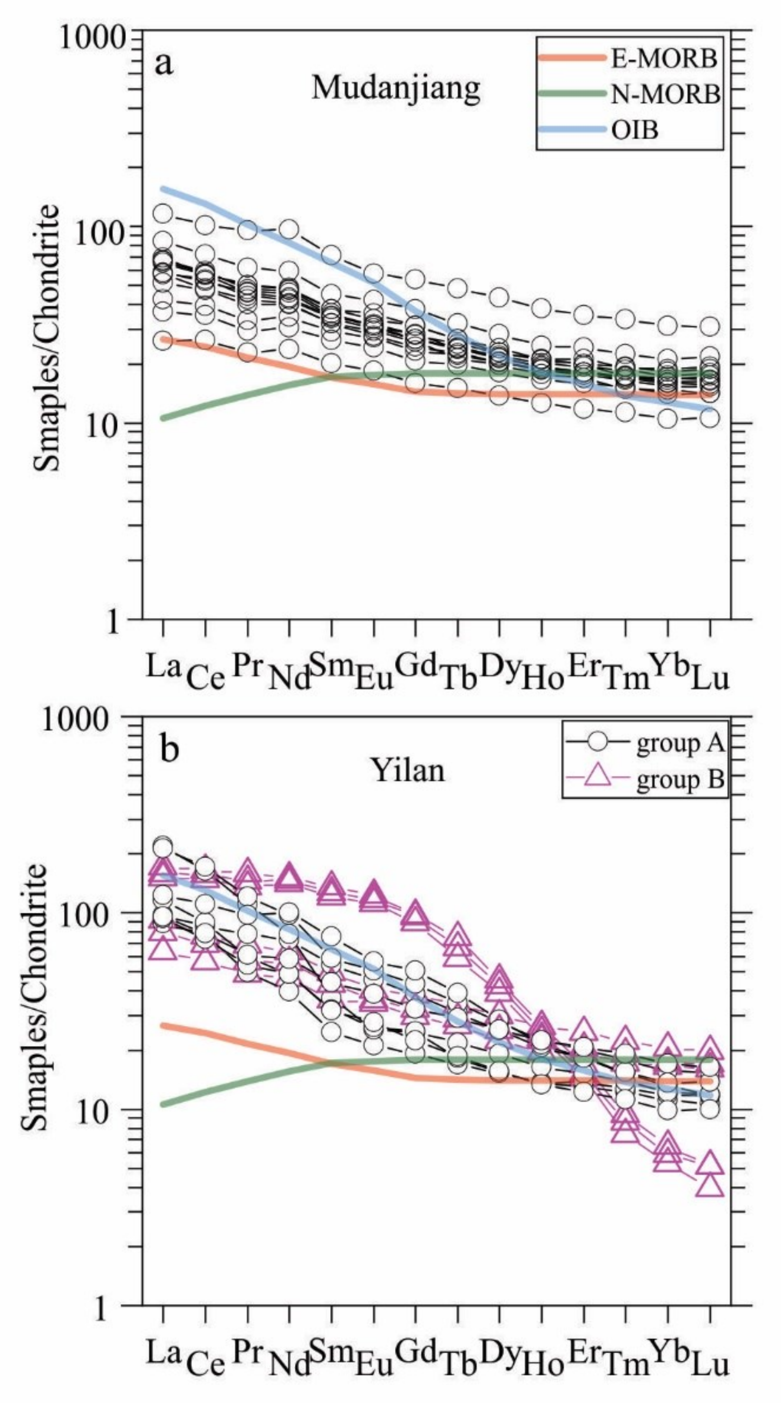

Figure 22. Chondrite-normalized REE patterns for blueschists. (a) the Mudanjiang blueschists show an affinity of enriched mid-ocean ridge basalts (E-MORB); (b) the Yilan blueschists show an affinity of ocean-island basalts (OIB). The compositions of E-MORB and N-MORB are from Gale et al. (2013); and OIB from Sun and McDonough (1989).

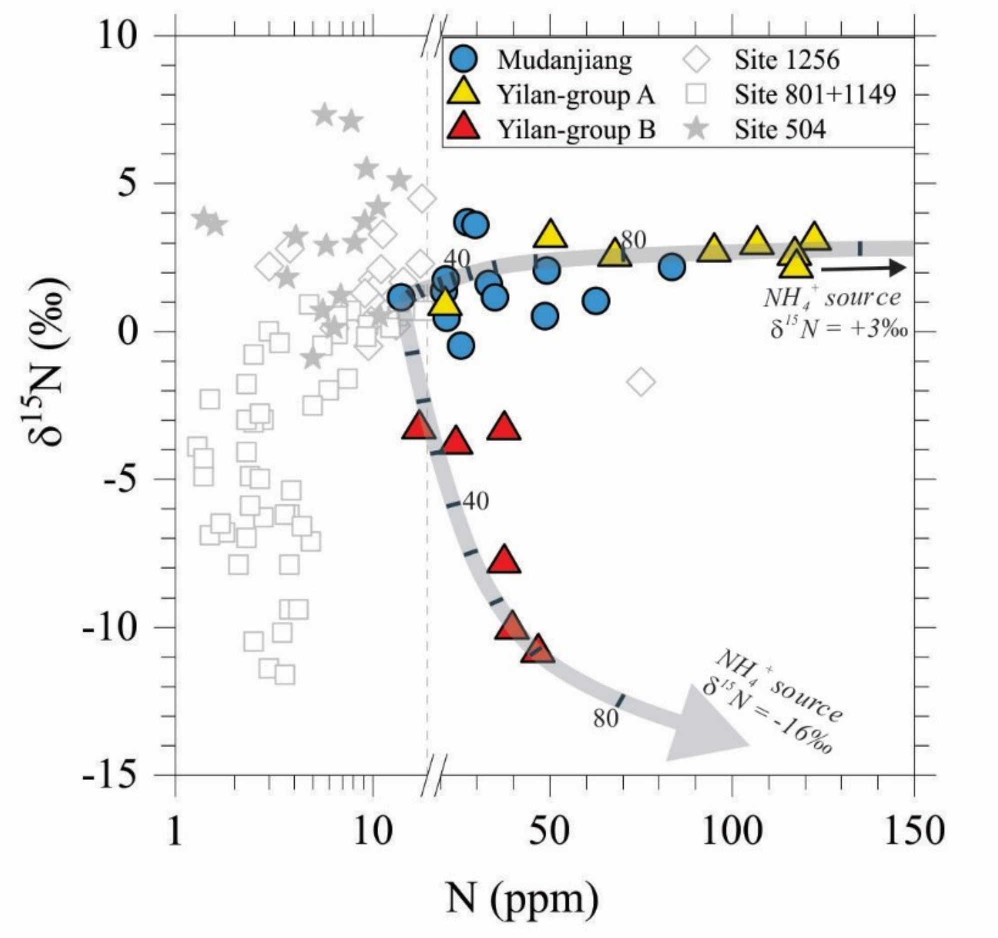

Figure 23. Diagram showing the nitrogen concentrations and $\delta^{15}N$ values of the blueschists from the Heilongjiang Complex. For comparison, the data of global altered oceanic crust (AOC), including Site 801 and 1149 (Li et al., 2007), Site 1256 (Bebout et al., 2018) and Site 504 (Busigny et al., 2019), are also shown. Compared with AOC ($N < 19$ ppm), the blueschist samples are significantly more enriched in N, but show similar $\delta^{15}N$ distribution patterns. The blueschist data can be interpreted by mixing with two types of NH_4^+: one with $\delta^{15}N$ value of +3‰, and the other with $\delta^{15}N$ value of ~ −16‰. Numbers along the curves mark the fractions of added ammonium by increments of 10%. See text for detailed discussion. Note that on the x-axis, the N concentration is plotted in logarithmic scale from 1 ppm to 19 ppm and non- logarithmic scale from 19 ppm to 150 ppm. The vertical grey dashed line marks a N concentration of 19 ppm. The error bars of N concentrations and $\delta^{15}N$ values are smaller than the symbols and not shown in the diagram.

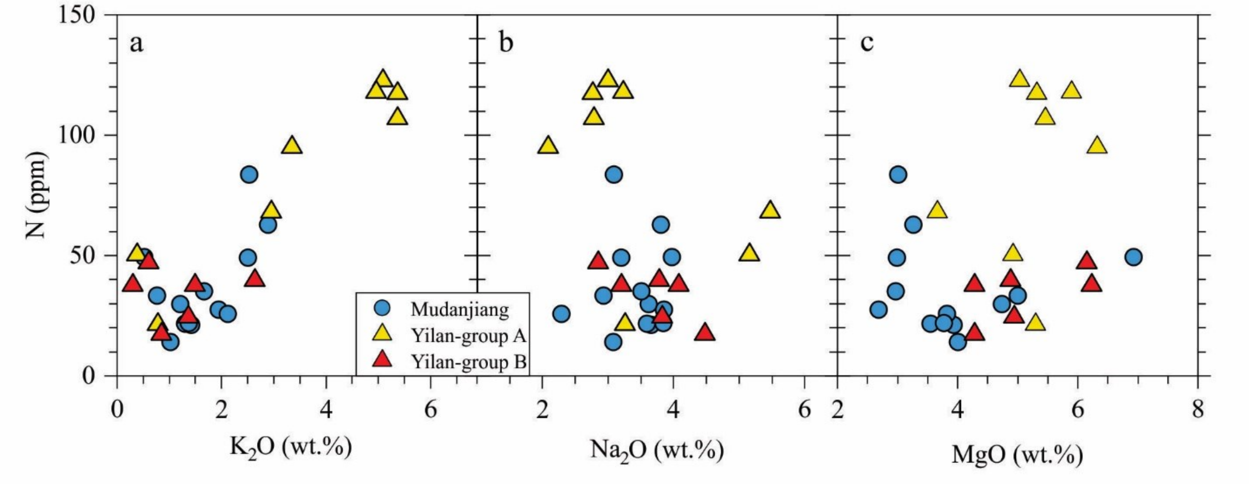

Figure 24. Comparison of N concentrations with the concentrations of major elements. (a) the relationship between N concentrations and K_2O concentrations; (b) the relationship between N concentrations and Na_2O concentrations; (c) the relationship between N concentrations and MgO concentrations. A positive correlation is only observed between N and K_2O concentrations. This suggests that nitrogen (in form of NH_4^+) is primarily residing in K-bearing minerals (i.e., phengite in blueschists), rather than Na- or Ca-bearing minerals.

3.2.4.2 Effect of metamorphic devolatilization

To assess the metamorphic devolatilization effect on the blueschist samples, we adopted the method of Busigny et al. (2003a) by comparing the variations of multiple fluid-mobile elements (e.g., K, Rb and Cs). This model is based on the different compatibilities among K, Rb and Cs during devolatilization, in which Cs is most strongly fractionated into the fluids, followed by Rb and K (Melzer and Wunder, 2000). The changes of Rb, Cs and K abundances through progressive devolatilization can be described by Equation (2):

$$R_{rock}^{f} = R_{rock}^{0} \times F^{(1/K_D - 1)} \tag{2}$$

where R^0_{rock} and R^f_{rock} represent the initial and final elemental ratios (e.g., Rb/K and Cs/Rb) of rock before and after devolatilization, respectively. F is the fraction of element remaining in the rock after devolatilization. K_D is the ratio of distribution coefficients for the Cs-Rb (K_D^{Cs-Rb}) or Rb-K (K_D^{Rb-K}) system (Busigny et al., 2003a for detail). Considering that K, Rb, Cs and NH_4^+ dominantly reside in K-bearing minerals (i.e., phengite in our case), elemental ratios among K, Rb, Cs and NH_4^+ in phengite largely reflect those of whole rock (Zack et al., 2001). Consequently, K_D^{Cs-Rb} and K_D^{Rb-K} values of phengite are employed in the modeling (Table 4). It should be noted that the employed K_D^{Cs-Rb} and K_D^{Rb-K} values of phengite in the modeling are from experiments at 600 °C and 2 GPa (Table 4), which are so far the lowest temperature and pressure experiments with available K_D values for phengite (Busigny et al., 2003a). Because the K_D^{Cs-Rb} and K_D^{Rb-K} values of phengite decrease with decreasing temperature and pressure (Busigny et al., 2003a), their values at 320 – 450°C and 0.9 – 1.1GPa for the studied blueschist (Zhou et al., 2009) would be smaller. Thus, the employment of data from high temperature and pressure in our modeling may cause some uncertainty, but it should not affect the semi-quantitative constraint on the devolatilization effect. On the diagram of molar abundances of Rb versus Cs (Fig. 25a) and K versus Rb (Fig. 25b), blueschists from Mudanjiang and Yilan are broadly distributed along a linear line instead of following the devolatilization trends illustrated by the dashed curves. This suggests that the effect of metamorphic devolatilization on these fluid-mobile elements is minor. To further examine the effect of metamorphic devolatilization on N, N/K molar ratios are plotted against $\delta^{15}N$ values on Fig. 25c. Because ^{15}N is more enriched in minerals than in N_2 or NH_3 (Li et al., 2021b, d), metamorphic devolatilization would lead to a progressive decrease in the N/K ratio with increase in the $\delta^{15}N$ value of the rocks (e.g., Bebout and Fogel, 1992; Mingram and Bräuer, 2001).

However, this trend is not observed in the studied blueschists (Fig. 25c), which consistently suggests that the effect of metamorphic devolatilization on N in these blueschists is minor.

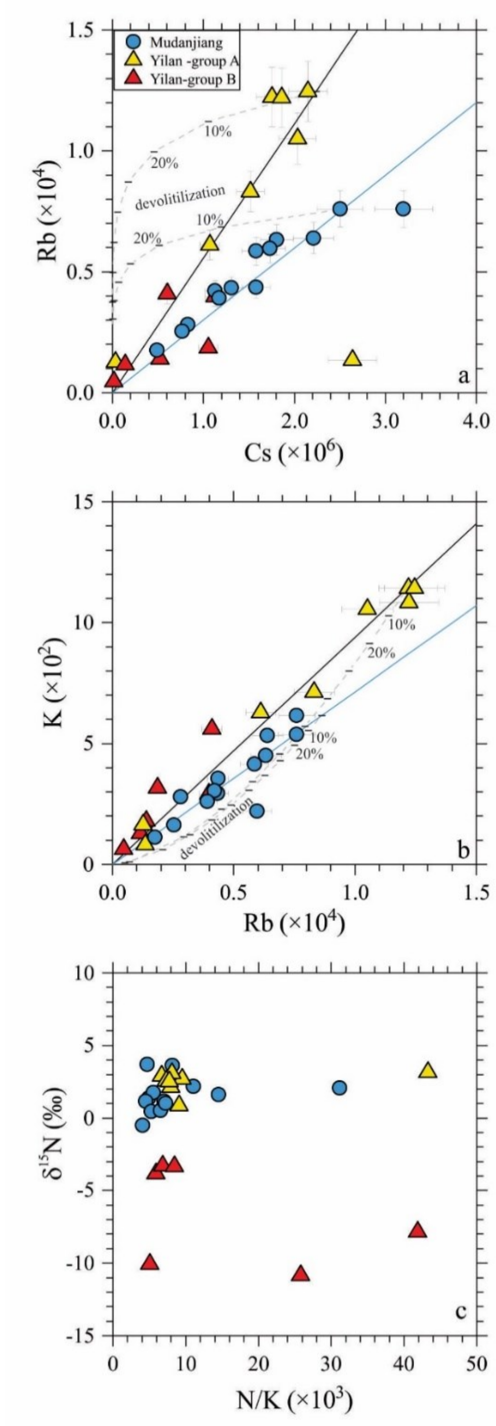

Figure 25. Diagrams comparing the molar abundances of Rb, Cs, K, N and $\delta^{15}N$ values of the blueschists to infer the devolatilization effect. In panels a and b, the solid blue and black lines are

linear fittings of the Mudanjiang and Yilan blueschist data (note that one outlier from Yilan group A blueschists, which clearly falls obviously falling outside the other datasets in Fig. 25a, was excluded for linear fitting); grey dashed curves represent the devolatilization trends modeled by Equation (2) for Mudanjiang and Yilan blueschist data. Numbers along the curves are the fractions of elemental loss after devolatilization. In panel c, the lack of negative correlations between the N/K molar ratios and δ^{15}N values suggests that the effect of metamorphic devolatilization on N is minor.

Table 4. Exchange coefficients and initial elemental ratios employed in the progressive devolatilization modeling.

	K_D	R^0_{rock}
Rb-K	1.62 [a]	0.11[b]
Cs-Rb	0.14 [a]	1.80 [b]

a. The K_D values of Rb-K and Cs-Rb between phengite and fluid at 600 °C, 2GPa were used.

b. The highest molar abundances of K ($\times 10^2$), Rb ($\times 10^4$) and Cs ($\times 10^6$) in each location were employed as their initial molar abundances to derive the initial elemental ratios.

3.2.4.3 Nitrogen enrichment in protoliths on seafloor

It is noted that the protoliths of the blueschists from Mudanjiang (E-MORB) and Yilan (OIB) are different to normal mid-ocean ridge basalts (N-MORB; Zhou and Li, 2017; Fig. 22). As a result, the initial N inherited from the magmatic sources of these protoliths could be slightly different. Both fresh N-MORB and less contaminated E-MORB have δ^{15}N values of ~ −3‰ to −5‰ (e.g., Javoy and Pineau, 1991; Marty and Humbert, 1997; Marty and Zimmermann, 1999; Marty and Dauphas, 2003; Li et al., 2007). In contrast, OIB show highly variable δ^{15}N values from −3‰ to +15‰ (e.g., Exley et al., 1987; Marty and Dauphas, 2003; Halldórsson et al., 2016), which could be attributed to recycling of crustal N into their magmatic sources. Nevertheless, the initial N inherited from their magmatic sources should be very low in abundance (< 2 ppm) due to the low solubility of N in mafic magmas (Libourel et al., 2003). Consequently, their original magmatic N signature can be easily overprinted by addition of secondary N during seafloor weathering. Because the protoliths of all the studied blueschist samples were pillow basalts, they should have undergone low-temperature alterations on the seafloor similar to those of the topmost part of global oceanic crust. Consequently, we can reasonably assume that the N concentrations and isotope signatures of the protoliths of the Mudanjiang and Yilan blueschists, despite their origin, should be similar to those of the upper section of AOC, which are commonly characterized by sedimentary-like positive $\delta^{15}N$ values (Fig. 23; Busigny et al., 2005, 2019; Li et al., 2007; Bebout et al., 2018), although some negative $\delta^{15}N$ values were observed in the basalts of ODP sites 801 and 1149 as the availability of sedimentary N was diminished (Li et al., 2007).

3.2.4.4 Element remobilization inside the subduction zone

3.2.4.4.1 Major and trace element evidence

Besides seafloor alteration, fluid-rock interactions in subduction zones may also add N into the meta-igneous part of the slab (e.g., Halama et al., 2010, 2017). Some elements, such as Ba, U, Th and K, can be used to distinguish between these two processes (e.g., Bebout, 2007a, b; Halama et al., 2010).

Fluid-rock interactions in the subduction zones can result in greater enrichment of Ba than K in the rock, whereas seafloor alteration does the opposite (Bebout, 2007a, b). Fig. 26a illustrates the comparison between Ba and K concentrations that are normalized to Th concentrations to remove the effect of magmatic fractional crystallization (e.g., Bebout, 2007b; Halama et al., 2010). The blueschist samples from the Heilongjiang Complex show higher Ba/Th ratios that deviate from the seafloor alteration trend defined by modern AOC (e.g., ODP Sites 801, 1149 and 504) but are close to the metamorphic enrichment trend defined by high-grade eclogites (e.g., those from the Raspas Complex and Samana Peninsula; Sorensen et al., 1997; John et al., 2004; Halama et al., 2010). In addition, oceanic crust can assimilate significant amounts of U during seafloor alteration (Staudigel et al., 1996, 2014), which produces a steep trend in the Th/U and Th diagram (Fig. 26b). In contrast, the studied blueschists have high Th concentrations and high Th/U ratios, which display a trend opposite to the seafloor alteration trend but again consistent with the metamorphic enrichment trend defined by high-grade eclogites. Therefore, the Th enrichment observed in these blueschists is likely indicative of reaction with HP metamorphic fluids, which has been observed in other HP and UHP metabasite blocks (Fig. 26b; e.g., Sorensen et al., 1997; Saha et al., 2005; also see data compilation in Bebout, 2007a, 2007b, 2013). In summary, major and trace elemental data of the studied blueschists show clear signatures of metasomatic overprint by HP metamorphic fluids inside the subduction zone.

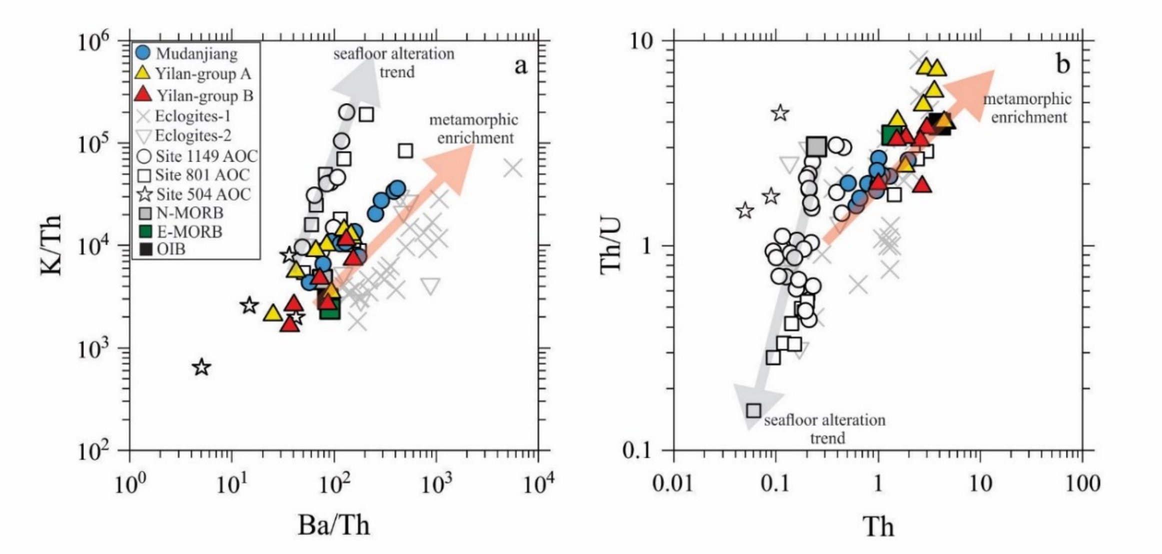

Figure 26. Diagrams showing the different effects of low-temperature seafloor alteration and subduction-zone metamorphism on major and trace element compositions. (a) K and Ba concentrations (both normalized to Th concentration) and (b) Th/U ratios and Th concentrations.

The seafloor alteration trends (grey arrows) are defined by data for modern altered oceanic crust (AOC), including ODP sites 801 and1149 (Kelley et al., 2003), Site 801 (Kelley et al., 2003) and Site 504 (Bach et al., 2003). The subduction-zone metamorphic trends (pink arrows) are defined by high-grade eclogites from the Raspas Complex (Eclogites-1) (John et al., 2004; Halama et al., 2010) and Samana Peninsula (Eclogites-2) (Sorensen et al., 1997). The compositions of E-MORB and N-MORB (Gale et al., 2013) and OIB (Sun and McDonough, 1989) are also plotted for reference. The blueschists from the Heilongjiang Complex show trends distinct to the seafloor alteration effect but consistent with the subduction-zone metamorphic effect.

3.2.4.4.2 Subduction-zone N enrichment in blueschists

Resolving fluid-rock metasomatism in the subduction zones from seafloor alteration in the above discussion provides a framework to explain the N data. The N concentrations of the Mudanjiang blueschists and the Yilan-group A blueschists positively correlate with Ba (Fig. 27a) and Th concentrations (Fig. 27b). Since these Ba and Th enrichments are attributed to fluid-rock interactions in the subduction zone (Bebout, 2007a, 2007b, 2013), the majority of N enrichment in these blueschists samples can be consistently considered to take place in the subduction zone as well. Compared with the Yilan-group A blueschists, the Yilan-group B blueschists commonly show much lower Ba and Th concentrations, suggesting much less metasomatic effect on the group B blueschists. It should be noted that the group A and B samples occur randomly in the outcrops without a specific distribution pattern. This indicates that fluid-rock interaction in the subduction zone is highly heterogeneous, consistent with observations from other subduction-zone mélange settings (e.g., Breeding et al., 2004; Spandler et al., 2008). Nevertheless, the Yilan-group B blueschists are much richer in N than global AOC, indicating that these blueschists were able to assimilate significant amounts of N. Overall, the significantly higher N concentrations in blueschists relative to AOC may reflect that low-temperature alteration on the seafloor is less efficient to enrich N, whereas the high-temperature and high-pressure conditions in the subduction zone may promote more efficient N fixation into meta-igneous rocks (Fig. 23).

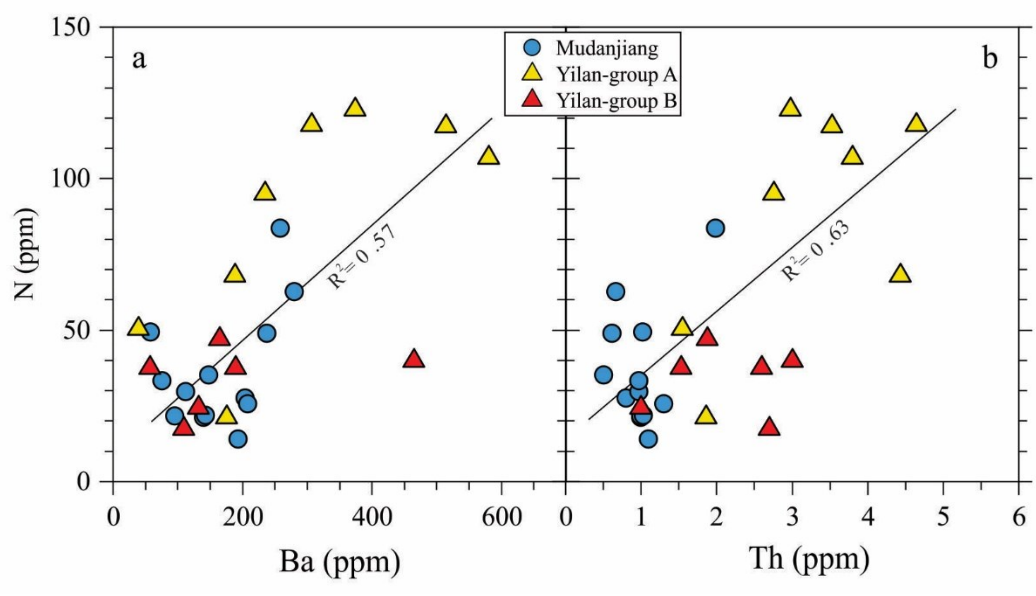

Figure 27. Correlations of N concentrations with Ba concentrations (a) and Th concentrations (b) of the blueschists. The solid lines are linear regressions for the Mudanjiang blueschists and the Yilan-group A blueschists (see text for discussion).

3.2.4.4.3 Source and mechanisms for N enrichment of blueschists

To determine the N source and detailed mechanism for the N enrichment in the blueschists inside the subduction zone, we examined the relationship between N concentrations and $\delta^{15}N$ values of the blueschists (Fig. 23). The Mudanjiang blueschists and the Yilan-group A blueschists show a $\delta^{15}N$ range of −0.5‰ to +3.7‰, falling into the isotopic range (−0.9‰ to +7.3‰) of the top section of AOC, which is considered to assimilate dissolved NH_4^+ in seawater or derived from overlying sediments (Busigny et al., 2005, 2019; Li et al., 2007). The high N concentrations (up to ~123 ppm) of the Mudanjiang blueschists and the Yilan-group A blueschists also require a source containing abundant N, consistent with sediments (e.g., Sadofsky and Bebout, 2004; Li and

Bebout, 2005). Consequently, the N source of the Mudanjiang blueschists and the Yilan-group A blueschists can be attributed to the sedimentary component in the mélange (Fig. 28). This is also supported by the elevated Th and Ba concentrations in these blueschists (Figs. 26, 27). The Mudanjiang and Yilan-group A blueschists have Ba/Th ratios of 25 to 421, consistent with those of clay-rich sedimentary rocks of 21 to 458 but smaller than those of sedimentary carbonate of 700 to 2751 (Plank, 2014). This clearly points to a pelitic sedimentary source in the mélange, which is consistent with the field observation that blueschists of Heilongjiang Complex are closely associated with pelitic mica schist (Zhou et al., 2009).

Employing a two-endmember mixing model (Li et al., 2007; refer to Equation 1 in ***Chapter 2.1***), the N concentrations and isotope compositions of the Mudanjiang blueschists and the Yilan-group A blueschists can be fitted by the addition of ^{15}N-enriched NH_4^+ with a $\delta^{15}N$ value of +3‰ into rocks with an initial N concentration of about 14 ppm and a $\delta^{15}N$ value of ~ +1‰ (Fig. 23). This mixing trend could be interpreted as heterogeneous addition of sedimentary N into the blueschists protoliths. The mixing trend is still valid if we consider that the protoliths of the blueschists had heterogeneous N concentrations and isotope compositions similar to the upper branch of data of ODP Sites 801 and 1149 samples (Li et al., 2007; Fig. 23). In a simplified scenario of heterogeneous addition of sedimentary NH_4^+ with $\delta^{15}N$ value of +3‰ into the protoliths of the blueschists with relatively homogenous N (~14 ppm and ~+1‰), this gives $\delta^{15}N$ value of +2.0‰ to +2.2‰ for sediment-derived dissolved NH_4^+ in fluids employing an isotope fractionation of +1.0‰ to +0.8‰ (Li et al., 2021b) between phengite and dissolved NH_4^+ in fluids at temperature condition (320 – 450 ºC; Zhou et al., 2009) of epidote-blueschist facies metamorphism.

Furthermore, a mass-balance calculation suggests that 36-89% of N in the Mudanjiang and Yilan-group B blueschists could come from sedimentary NH_4^+.

The Yilan-group B blueschists all have negative $\delta^{15}N$ values as low as ~ −11‰, apparently different from those of subducting sediments ($+5.2^{\pm1.6}$‰; see data complication in Li et al., 2014). Instead, the Yilan-group B data can be fitted by addition of ^{15}N-depleted NH_4^+ with a $\delta^{15}N$ value of ~ −16‰ (Fig. 23). Notably, a similar ^{15}N-depleted NH_4^+ source has been observed in the ODP sites 801 and 1149 basalts (Li et al., 2007) and the UHP rocks with hydrothermally altered protoliths from the Sulu belt in eastern China (Li et al., 2014). An abiotic reduction of N_2 to NH_4^+ by Fe^{2+}-bearing minerals associated with kinetic isotope fractionation has been proposed to account for the formation of this extremely ^{15}N-depleted NH_4^+ (Li et al., 2007, 2014). Although abiotic N_2 reduction in these cases occurs before subduction, it does not preclude the occurrence of abiotic N_2 reduction in the subduction zone if favorable conditions for the reaction are met. In mafic rocks such as the studied blueschists, Fe(II) is abundant and can act as an efficient reductant to abiotically reduce N_2 at 300 – 500 ºC and high-pressure conditions (Brandes et al., 1998; Li et al., 2014). Therefore, we still employ this mechanism to account for the ^{15}N-depleted NH_4^+ endmember (−16‰) in the Yilan-group B blueschists, which is equivalent to a $\delta^{15}N$ of −15.0‰ to −15.2‰ for dissolved NH_4^+ in fluids if we consider the isotope fractionation of +1.0‰ to +0.8‰ between phengite and dissolved NH_4^+ in fluids at 320 – 450 ºC (Li et al., 2021b). Although N_2 inside the subduction zone could come from both metamorphic devolatilization of sediments (e.g., Bebout and Fogel, 1992) and partial melting of the mantle wedge, the latter is unlike to occur given the low-temperature conditions (320 – 450 ºC) for the formation of the blueschists in the Heilongjiang Complex. Therefore, the enriched N in the Yilan-group B blueschists should be still sourced from the ambient sediment components in the mélange. At 320 – 450 ºC, the $\delta^{15}N$

difference between NH_4^+ and N_2 in fluids released from a sedimentary source with the same N isotope composition is +5.6‰ to +4.2‰ (Li et al., 2021d), which implies that the $\delta^{15}N$ value of N_2 in fluids is −3.6‰ to −2.0‰. This requires a kinetic isotope fractionation of −11.4‰ to −13.2‰ between the product NH_4^+ and source N_2 in fluids, which is consistent with the kinetic isotope fractionation of –11‰ to –16‰ for abiotic N_2 reduction observed in previous studies (Li et al., 2007; Li et al., 2014). Accordingly, a mass-balance calculation suggests that a minimum of 19 – 72% of N (corresponding to 3.3 – 36.0 ppm N) in the Yilan-group B blueschists could come from abiotic N_2 reduction (Fig. 23).

The oxygen fugacity may vary strongly at a small local scale in the mélange zone (Tumiati et al., 2015), which could result in coexistence of N_2 and NH_4^+ in subduction-zone fluids (e.g., Jackson et al., 2021) although the relative abundances of N_2 and NH_4^+ in fluids could be highly variable. This could induce different N-fixation mechanisms between the Mudanjiang and Yilan-group A blueschists (i.e., direct NH_4^+ assimilation) and the Yilan-group B blueschists (abiotic N_2 reduction to NH_4^+). The Mudanjiang and Yilan-group A blueschists were likely able to access abundant fluids that interacted with sediments, as revealed by their significantly elevated Ba, Th and N concentrations (Fig. 26, 27), which favors direct NH_4^+ assimilation. In contrast, the relatively low Ba, Th and N concentrations of the Yilan-group B blueschists indicate that the fluids reacting with these blueschists contained much less Ba, Th and NH_4^+, likely due to interactions with other blueschists along their flow path. The lack of NH_4^+ in fluids made N_2 contribute dominantly to blueschists through abiotic N_2 reduction, although this reaction is less efficient in supplying NH_4^+. Consequently, the Yilan-group B blueschists gained smaller amounts of NH_4^+ with strong ^{15}N depletion.

3.2.4.5 Implications to N recycling in subduction zones

The discussion above demonstrates that devolatilized sedimentary N (either in form of NH_4^+ or N_2) can be at least partially re-fixed by the meta-igneous components of a subducting slab in subduction zones. This process can transfer N from susceptible sediments to more refractory meta-igneous components in the mélange at the early stage of subduction.

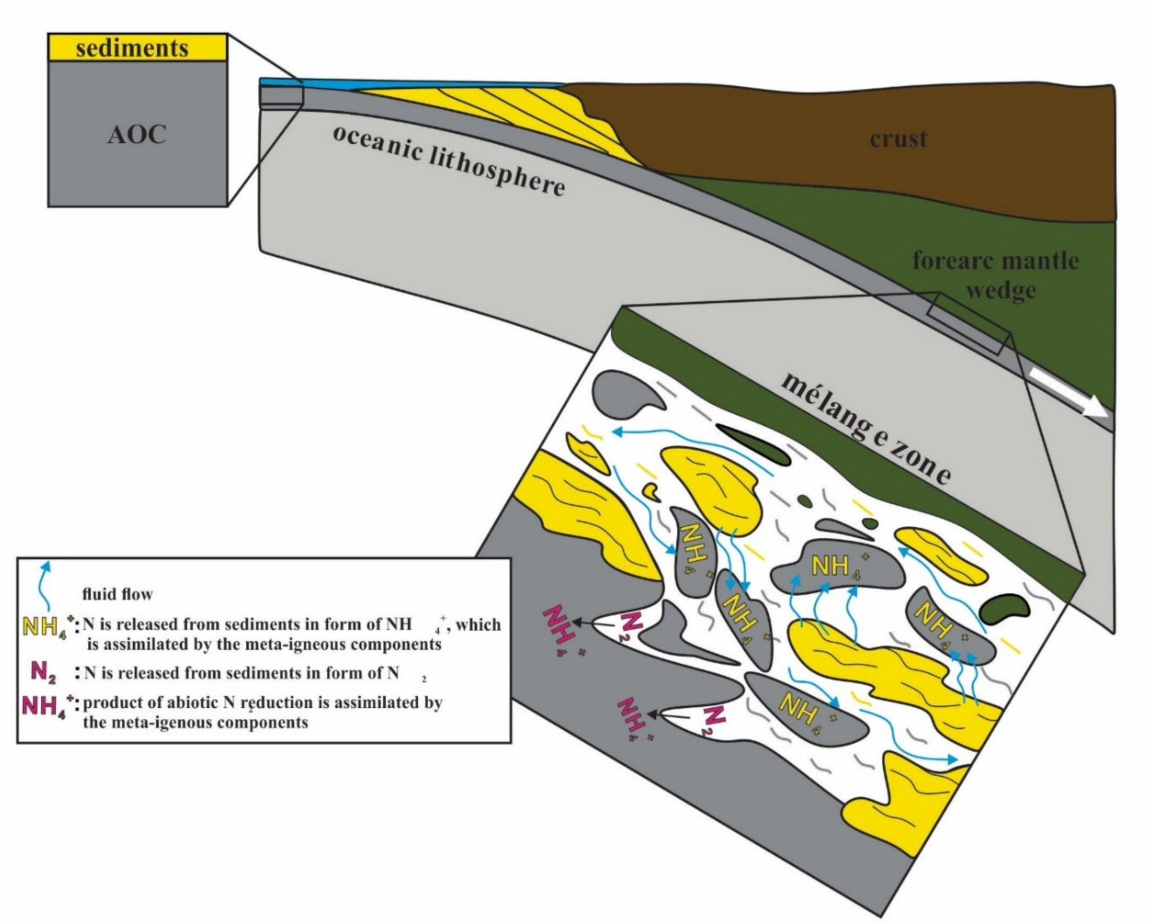

Figure 28. Schematic diagram (not to scale) showing N transfer from sedimentary components to meta-igneous components in the mélange of a subduction zone (modified from Bebout and Penniston-Dorland, 2016). Two N transfer pathways are illustrated in the diagram. One is that N is released from sediments as NH_4^+, which is subsequently re-fixed by the meta-igneous

components through fluid-rock interaction. The other is that N is released from sediments as N_2, which is reduced into NH_4^+ and subsequently re-fixed by the meta-igneous components.

Mélanges are common feature of modern-style subduction zones (Nielsen and Marschall, 2017). Field studies on exhumed HP mélange zones suggested that the thickness of mélange zones could vary from hundreds of meters to several kilometers (Bebout, 1991; Marschall et al., 2006). The low-seismic-velocity materials on the upper part of several modern subduction zones (Abers, 2005), which possibly represent the mélange material, vary from 1 to 10 km in thickness (Marschall and Schumacher, 2012). If we assume that the mélanges are composed of subducting sediments with an initial weighted average N concentration of 299 ppm (Sadofsky and Bebout, 2004; Li and Bebout, 2005) and AOC with an initial weighted average N concentration of 7 ppm (Li et al., 2007; Bebout et al., 2018; Busigny et al., 2019), a ballpark estimate of the N re-fixation efficiency (i.e., the fraction of the devolatilized sedimentary N that can be re-fixed by the igneous components in the mélange) is illustrated in Fig. 29. The modeling results show that the re-fixation efficiency is strongly controlled by the relative thicknesses of sediments and AOC that are incorporated into the mélange zone (Fig. 29). Taking the modern Circum-Pacific subduction zones (representing ~70% of global subduction zones in length) as an example, even applying the maximum sedimentary N loss (~40%; Bebout and Fogel, 1992; Bebout et al., 1999) during the epidote-blueschist metamorphism in the Catalina Schist (an exceptionally hot subduction zone), the released N from the sediments (average thickness: 794 m) can be efficiently re-fixed if the mélange contains >850-meter AOC (Fig. 29). The required thickness of AOC for efficient re-fixation of devolatilized sedimentary N is even smaller to account for the diminished N devolatilization in cold subduction zones with geotherm of $8°C \cdot km^{-1}$ (Busigny et al., 2003a), which may be the case for most of modern subduction zones (Penniston-Dorland et al., 2015). It should be noted here that our modeling of the AOC thickness is conservative because (i) samples in this study were from inner parts of pillow basalts, which likely experienced a lower degree of metasomatism than the rims of the pillows, and thus a lower degree of N enrichment; (ii) the devolatilized sedimentary N could also be re-fixed by the meta-peridotites of subducting slabs or serpentinites in the mantle wedge (Halama et al., 2014; Pagé et al., 2018; Cannaò et al., 2020), which are also common components of mélanges in subduction zones (e.g., Spandler et al., 2008) but not considered in our modeling due to the loose constraints of N characteristics on these components. Incorporating these parameters can further reduce the thickness of AOC required to re-fix the devolatilized sedimentary N. Therefore, the meta-igneous components in the mélange in most of subduction zones can efficiently re-fix the devolatilized sedimentary N.

The K-bearing phases, such as phengite, are the major host of N in metamorphosed AOC (e.g., blueschists, eclogites). Attributed to the stability of phengite over large temperature and pressure ranges (up to ~300 km) in subduction zones (Poli and Schmidt, 1995; Schmidt, 1996; Watenphul et al., 2010), N can be well retained beyond the sub-arc depth. Although some degree of N loss from phengite may occur during further prograde metamorphism (Halama et al., 2017), significant amounts of N have been observed in phengite in UHP eclogites from the Sulu belt (eastern China), which has been subducted to >120 km or even > 200 km (Xu et al., 1992; Ye et al., 2000). This suggests that N can be well retained and recycled into the deep mantle.

3.2.5 Conclusions

The pillow-shaped blueschists in Northeast China provide a good opportunity to examine the N behavior at the early stage of subduction. These blueschists contain average N concentrations seven times higher than AOC. The concentration correlations between N and other elements, such as Ba, Th, indicate that most of the N in the blueschists was added in the subduction zone. The relationship between the N concentrations and $\delta^{15}N$ values of these blueschist indicates that two types of NH_4^+ were added to the studied blueschists. The first type of NH_4^+ is characterized by a positive $\delta^{15}N$ value, likely directly derived from devolatilization of sediments. This type of N is significantly enriched in the blueschists that have undergone intensive interaction with metamorphic fluid. The other type of NH_4^+ is characterized by strong ^{15}N depletion, likely generated by abiotic reduction of sediment-derived N_2. This type of N is enriched in the blueschists that have undergone limited interaction with metamorphic fluid. These results show that the meta-igneous components of the slab can efficiently re-fix the devolatilized N from the sedimentary portion of the slab, which facilitates the retention of slab N for deep subduction and recycling.

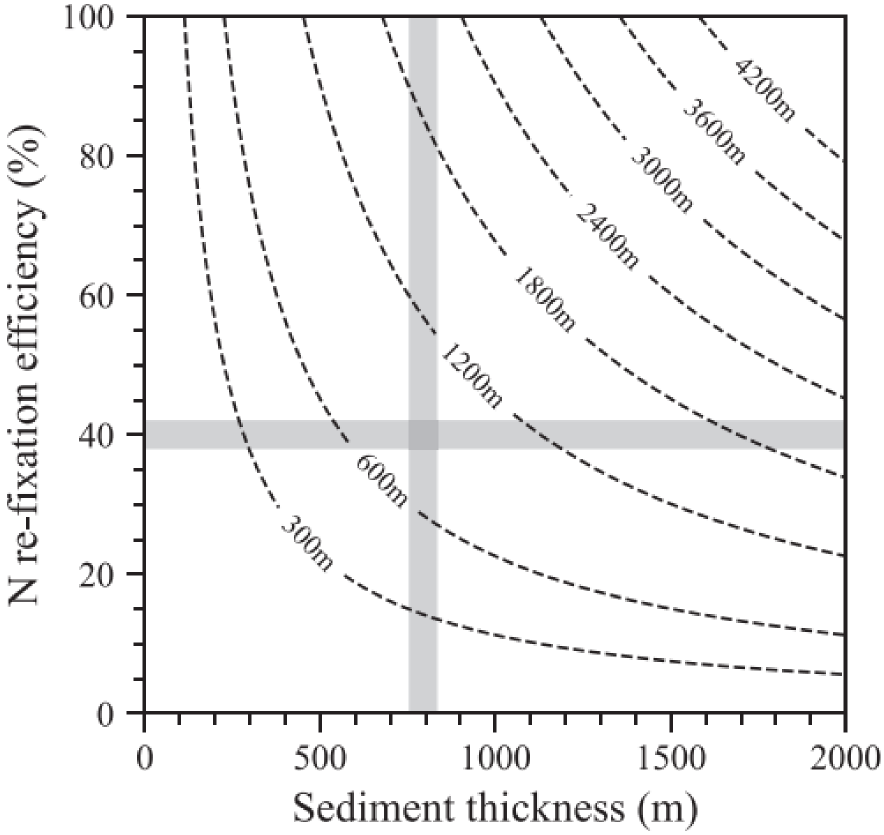

Figure 29. Diagram showing the relationship between the N re-fixation efficiency and the thickness of sediments and AOC that are incorporated into the mélange. The numbers on the curves represent the thickness of AOC. The parameters used in the modeling include average density (1.64 g·cm^{-3}) and porosity (38.5%) of subducting sediments from Plank and Langmuir (1998), average density (2.93 g·cm^{-3}) and porosity (12%) of subducting AOC from Johnson and Pruis (2003), the initial weighted average N concentrations of 299 ppm for sediments (Sadofsky and Bebout, 2004; Li and Bebout, 2005) and 7 ppm for AOC (Busigny et al., 2005, 2019; Li et al., 2007; Bebout et al., 2018), and the final average N concentration of 51 ppm (this study) for the blueschist-facies igneous rocks. The horizontal grey bar represents the maximum fraction of N loss of sediments during the early-stage subduction. The vertical grey bar represents the average thickness of the subducting sediments along the Circum-Pacific subduction zones (Plank and Langmuir, 1998; Clift, 2017). The python code for modeling is available at https://github.com/GeoCan22/N-Re-fixation-Efficiency-Modeling.

Chapter 3.3 Nitrogen recycling at the arcs of the warm Central American and cold Izu-Bonin-Mariana subduction zones

3.3.1 Introduction

Subduction zones are key channels for mass exchange between Earth's surface and interior. In particular, volatile recycling in the forearc and sub-arc regions (e.g., Hilton et al., 2002; Kelemen and Manning, 2015; Barry and Hilton, 2016; Plank and Manning, 2019; Bekaert et al., 2021) could have substantially impacted the geochemical signatures of volatile components in Earth's major reservoir (e.g., atmosphere, biosphere and mantle) and the habitability of Earth's surface environment (e.g., Galvez and Pubellier, 2019; Bekaert et al., 2021).

Nitrogen is one of the few elements playing important roles in all Earth's reservoirs. The extent of N recycling down to sub-arc depth inside the subduction channel is a key parameter for the understanding of the long-term evolution of Earth and its sub-reservoirs, but has been poorly constrained so far. Two major approaches have been used for such s study. One is through examinations of N retention in exhumed metamorphic rocks from ancient subduction zones. For example, Busigny et al. (2003) found that N could be well retained in the ultrahigh-pressure metamorphic rocks subducted to 90 km in the Schistes Lustrés metasedimentary unit in Western Alps, which had a cold geotherm. In contrast, significant N loss was observed in the prograde metasedimentary rocks (up to ~70% in the amphibolite-facies rocks; Bebout and Fogel, 1992; Bebout et al., 1999) of the Catalina Schist, which had an extremely hot geotherm (Bebout, 2007). Accordingly, the thermal structure of subduction zones has been proposed to be a main control in subduction-zone N recycling (e.g., Busigny et al., 2003b, 2019; Mallik et al., 2018; Halama and Bebout, 2021; Jackson et al., 2021). The other approach is through direct mass balance between subducted N into the trench (or input N) and recycled N from the arc (or output N) in modern subduction zones. Nitrogen recycling efficiency at the arc, which is defined as the ratio between the output and input N fluxes, is commonly used to quantify subduction-zone N recycling (Fischer et al., 2002; Hilton et al., 2002; Mitchell et al., 2010; Busigny et al., 2019). This approach has been applied to two representative modern subduction zones, i.e., the cold Izu-Bonin-Mariana (IBM) and the warm Central America (CA) subduction zones (Syracuse et al., 2010). One study by Mitchell et al. (2010) reported a low N recycling efficiency of 4% – 17% for the IBM arc. The N recycling efficiency at the CA arc has been more intensively studied but is hotly debated from nearly complete recycling (e.g., Fischer et al., 2002; Labidi et al., 2021) to partial recycling (e.g., Li and Bebout, 2005; Busigny et al., 2019; Halama and Bebout, 2021). One of the major barriers that caused these discrepancies is the loose constraint on the N input flux – although the N data of seafloor sediments are relatively abundant (e.g., Sadofsky and Bebout, 2004; Li and Bebout, 2005), the N residing in AOC, particularly in the intrusive sections (sheeted dikes and gabbros), is poorly known.

Based solely on the data of altered basalts, AOC has been already considered to be a large N reservoir with an inventory at least of the same order of magnitude to the overlying sediments (Li et al., 2007). This is because a significant amount of N, mostly in form of ammonium (NH_4^+), can be fixed into the crystal lattice of K-bearing secondary minerals formed by seawater alteration (Hall, 1989; Busigny et al., 2005, 2019; Li et al., 2007; Bebout et al., 2018). A number of studies have examined the N in basaltic rocks across global ocean basins recovered by the DSDP/ODP/IODP, with a focus on DSDP/ODP Hole 504B (Busigny et al., 2019), ODP/IODP Hole 1256D (Busigny et al., 2005; Bebout et al., 2018) and ODP Hole 801C and 1149D (Li et al., 2007). The results show that in the basaltic section of AOC, which was mostly altered at low temperatures (<100°C) and high water/rock ratios (e.g., Seyfried Jr, 1987; Staudigel, 2003), the bulk-rock N concentration can be elevated from the initial low N content (~1.5 ppm) in fresh mid-ocean ridge basalts (MORB) inherited from the mantle (Marty, 1995; Li et al., 2007) to up to 19 ppm (Busigny et al., 2005, 2019; Li et al., 2007; Bebout et al., 2018). Most of the basaltic samples from the upper AOC section have typical $\delta^{15}N$ signatures of seawater and/or seafloor sediments (Sadofsky and Bebout, 2004; Li and Bebout, 2005). Because the equilibrium N isotopic fractionation between aqueous NH_4^+ and secondary minerals (e.g., clay) is small (Li et al., 2021b), this isotopic consistency suggests that the secondary N in basaltic AOC was mainly sourced from seawater and/or seafloor sediments. Additionally, abiotic reduction of N_2 in hydrothermal fluid could also contribute to the secondary N in AOC (e.g., Li et al., 2007). This source can be easily distinguished from the sedimentary sources by the extremely low $\delta^{15}N$ value as a result of significant kinetic isotopic effect associated with abiotic N_2 reduction (Li et al., 2007, 2014, 2021c).

In contrast to the extrusive section of AOC which has been relatively well studied, the sheeted-dike and gabbroic sections, which comprise the majority of crustal material in the subducting slab, have been rarely studied for N content and isotopic composition. So far, only seven sheeted dike samples from Hole 504B have been examined, which gave N concentrations from 1.4 ppm to 6.9 ppm with $\delta^{15}N$ values from −0.9‰ to +4.5‰ (Busigny et al., 2019). However, N concentrations of sheeted dikes could be underestimated in these samples because of analytical bias (see details in Section 3.3.3 below). Greater N enrichment has been observed in some metagabbros (N: 12 to 30 ppm; $\delta^{15}N$: +1.2‰ to +4.7‰) from an ophiolitic sequence of Western Alps (Busigny et al., 2011). But it is uncertain whether the N enrichment occurred under seafloor or during metamorphism or both (see discussion in Li et al., 2021c; ***Chapter 3.2***).

The sheeted-dike and gabbro section could be potentially enriched in N by fluid-rock interaction under the seafloor. High-temperature hydrothermal fluids, represented by those from the 'black smokers', can contain up to 20 mM·kg^{-1} NH_4^+ when the venting site is associated with sediments (e.g., Von Damm, 1990; Lilley et al., 1993; Pedersen et al., 2010). Most of the sheeted dikes and gabbros recovered from modern and ancient AOC have experienced various degrees of high-temperature alteration by such fluids. As a result, significant amounts of N could be potentially incorporated into secondary minerals.

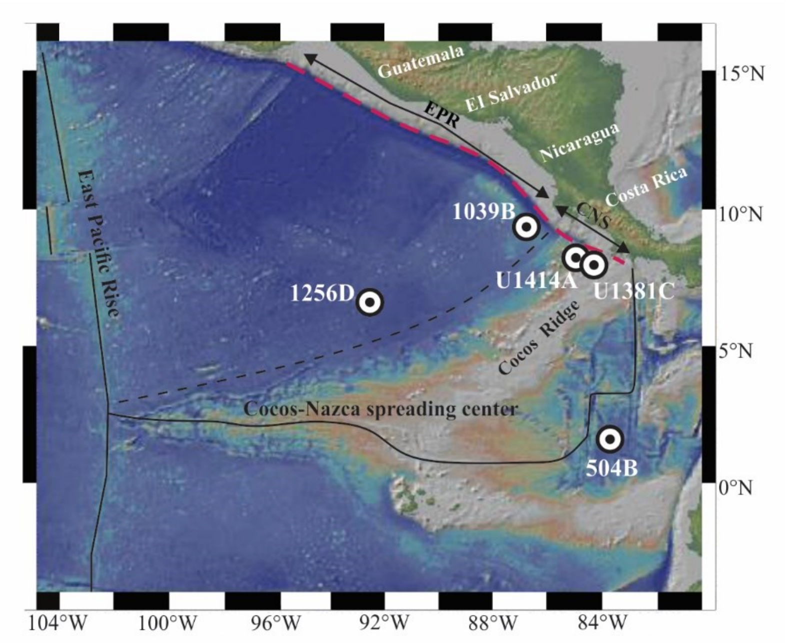

Figure 30. Bathymetric map showing ODP/IODP Hole 1256D and DSDP/ODP Hole 504B outboard the 1400 km Central America trench (marked by the red dashed line). Also shown in the map is ODP Hole 1039B, IODP Holes 1381C and U1414A, which are reference sites for subducting sediments. The solid black lines mark the fast-spreading East Pacific Rise (EPR) center and the intermediate-spreading Cocos-Nazca spreading center (CNS). The black dashed line marks the boundary between the crusts formed at the EPR and the CNS. The map was generated by GeoMapApp (http://www.geomapapp.org).

In this study, we examined the N concentrations and isotopic compositions of AOC from ODP/IODP Hole 1256D and DSDP/ODP Hole 504B (Fig. 30), with a focus on the less studied intrusive sections, but also including some basaltic samples from sections not studied by previous studies. These two drill holes are the only two in modern ocean basins that have penetrated to the intact intrusive oceanic crust (Wilson et al., 2006; Expedition 335 Scientists., 2012). Thus, these samples provide a valuable opportunity to unravel the N enrichment mechanism in the poorly studied deeper AOC sections. In addition, the rocks from these two drill holes represent the reference materials that have been subducted into the CA margin. The data will enable us to re-assess the N recycling efficiency in the warm CA margin, which can further shed lights into the deep N recycling at a global scale.

3.3.2 Geological background and samples

ODP/IODP Hole 1256D was drilled in the ~15 Myr-old oceanic crust of the Cocos Plate formed at the fast-spreading (~110 mm·year^{-1}) East Pacific Rise (EPR; Shipboard Scientific Party, 2003c) (Fig. 30). The hole penetrated 1507 meters below seafloor (mbsf). The lithostratigraphy of Hole 1256D is characterized by, from top to bottom, (i) a 250 m-thick of sediment section (0 – 250 mbsf) composed of an upper 41 m-thick clay-rich section and a lower 210 m-thick biogenic carbonate section, (ii) a 754 m-thick lava section (250 – 1004 mbsf) dominated by massive flows, sheet flows and minor pillow lava, (iii) a 57 m-thick transition zone (1004 – 1061 mbsf) composed of lavas and dikes, (iv) a 346 m-thick sheeted dike complex (1061 – 1407 mbsf), and (v) two gabbro bodies intruded into the sheeted dike complex (1407 – 1507 mbsf) at or near ridge axis (Hayman et al., 2019). The upper (52 m in thickness) and lower (24 m in thickness) gabbro bodies are separated by two granoblastically recrystallized dike screens (Wilson et al., 2006).

The igneous rocks in Hole 1256D are characterized by increasing alteration temperatures and decreasing water/rock ratios along depth (Shipboard Scientific Party, 2003a; Expedition 309/312 Scientists, 2006; Alt et al., 2010). The lava section has been persistently altered under sub-greenschist facies (< 200 °C; Expedition 309/312 Scientists, 2006), resulting in ^{18}O enrichment (δ^{18}O: +6.1‰ – +9.2‰; Gao et al., 2012; Fig. 31) relative to fresh MORB. The secondary mineral assemblage in the upper 600 m lava section (250 – 850 mbsf) is dominated by saponite and celadonite, which indicate an alteration at low temperatures (< 100 °C; Expedition 309/312 Scientists, 2006). The presence of mixed-layer chlorite-smectite in the base lavas at ~981 mbsf suggests that the alteration temperature increases to ~200 °C (Expedition 309/312 Scientists, 2006; Alt et al., 2010). The transition zone, which spreads from 1004 to 1061 mbsf, is marked by subvertical intrusive contacts and mineralized breccias. The secondary mineral assemblage in this transition zone is characterized by the presence of mixed layer of chlorite-smectite and chlorite (after primary plagioclase and olivine), actinolite (after primary clinopyroxene), and albite (after primary plagioclase). This indicates moderate-temperature alteration (~250 °C) at sub-greenschist to greenschist facies (Fig. 31**;** Expedition 309/312 Scientists, 2006; Alt et al., 2010). Deeper in the hole, rocks show consistent ^{18}O depletion (δ^{18}O: +3.0‰ – +5.5‰) relative to fresh MORB, suggesting an alteration temperature of > 250 °C (Fig. 31; Gao et al., 2012). The secondary mineral assemblage in sheeted dikes above ~1300 mbsf is dominated by chlorite (after primary olivine and plagioclase) and anorthitic secondary plagioclase (after primary plagioclase), indicating an alteration under greenschist facies (> 250 °C; Expedition 309/312 Scientists, 2006). The secondary mineral assemblage in sheeted dikes below ~1300 mbsf changes to actinolite and hornblende replacing primary clinopyroxene, indicating that the alteration temperature has increased to ~ 400°C (Shipboard Scientific Party, 2003a). The gabbros have been predominantly hydrothermally altered under amphibolite-facies conditions with temperature of 400 – ~ 800 °C (Expedition 309/312 Scientists, 2006; Alt et al., 2010), characterized by replacements of primary clinopyroxene by actinolitic hornblende and primary plagioclase by albite and anorthitic secondary plagioclase (Fig. 31**;** Expedition 309/312 Scientists, 2006; Alt et al., 2010).

DSDP/ODP Hole 504B was drilled in the ~6 Myr-old oceanic crust of the Nazca Plate formed at the intermediate-spreading (~36 mm·year^{-1}) Cocos-Nazca spreading center (CNS; Becker et al., 1989) (Fig. 30). From top to bottom, the hole was further divided into (i) a 275 m-thick sedimentary section (0 – 275 mbsf) dominantly composed of siliceous ooze, (ii) a 571 m-thick volcanic zone (275 – 846 mbsf) dominated by pillow basalt, (iii) a 209-m thick transition zone (846 – 1055 mbsf), (iv) a 445 m-thick upper sheeted dike complex (1055 – 1500 mbsf), and (v) a 611-m thick lower sheeted dike complex (1500 – 2111 mbsf; Fig. 32; Alt et al., 1996). Similarly, the igneous section in Hole 504B shows increasing alteration temperatures and decreasing water/rock ratios along depth (Bach et al., 2003). The volcanic zone has been ubiquitously affected by low-temperature (< 250 ºC) alteration at zeolite facies, which is manifested by the presence of celadonite, saponite, chlorite-smectite mixed phases, zeolite and oxyhydroxide, and ^{18}O enrichment (δ^{18}O: +6.1‰ – +8.5‰; Fig. 32**;** Alt et al., 1986, 1996) relative to fresh MORB. A steep transition to moderate-temperature (> 250 ºC) alteration at greenschist facies can be observed in the upper part of the transition zone as being revealed by the presence of chlorite, albite, actinolite after primary olivine, plagioclase and clinopyroxene (Bach et al., 2003) and the appearance of ^{18}O depletion relative to fresh MORB (Fig. 32; Alt et al., 1986, 1996). The typical secondary mineral assemblage of greenschist facies alteration prevails down to ~1600 mbsf of the hole, below which hornblende (from primary clinopyroxene) and anorthitic secondary plagioclase (from primary plagioclase) become more abundant (Shipboard Scientific Party, 1993a; Bach et al., 2003). This indicates an on-axis peak alteration temperature of > 500 ºC approaching the amphibolite facies (Shipboard Scientific Party, 1993a; Bach et al., 2003).

In Hole 1256D, a total of 26 representative samples, including 8 from the upper lava section, 8 from the sheeted dike complex and 10 from the gabbro section, were selected. In Hole 504B, a total of 21 representative samples, including 4 from the upper volcanic zone, 2 from the transition zone, 3 from the upper sheeted dike complex and 13 from the lower sheeted dike complex (Table F2 in Appendix F). These selected samples are characterized by dark gray and green background alterations. Veins were avoided during the sampling.

3.3.3 Results

The bulk-rock N concentrations and $\delta^{15}N$ values of the samples from Hole 1256D and Hole 504B are listed in Table F1 in Appendix F.

Among the 1256D samples examined in this study, N concentrations of basalts range from 7.9 ppm to 19.1 ppm with $\delta^{15}N$ values varying from -1.4‰ to +3.8‰. These data are consistent with the data (6.4 – 17.8 ppm) from Bebout et al. (2018) but significantly higher than the data (1.4 – 4.3 ppm) from Busigny et al. (2005) (Fig. 33). This discrepancy has been explained by Bebout et al. (2018) as a result of the pre-heating of samples at 450 ºC in an oxidizing environment overnight employed by Busigny et al. (2005), which could have induced release of N in secondary minerals. This is further verified by a comparison between 400 ºC heating and for heating on AOC samples by Li et al. (2021a). Integrating our data with those in Bebout et al. (2018) gives an average N concentration of $11.8^{\pm 3.8}$ ppm and an average $\delta^{15}N$ value of $+0.9^{\pm 1.7}$‰ for 1256D altered basalts (n = 15; 1σ). Nitrogen concentrations and $\delta^{15}N$ values of sheeted dikes range from 11.2 ppm to 33.5 ppm (average: $16.4^{\pm 7.2}$ ppm; n = 8; 1σ) and -3.7‰ to +1.4‰ (average: $-1.3^{\pm 1.5}$‰; n = 8; 1σ), respectively. Nitrogen concentrations and δ^{15}N values of gabbros range from 6.2 ppm to 23.8 ppm (average: $11.3^{\pm 5.6}$ ppm; n = 10; 1σ) and -0.4‰ to +3.2‰ (average: $+1.3^{\pm 1.0}$‰; n = 10; 1σ), respectively. Both N concentrations and δ^{15}N values of basalts, sheeted dikes and gabbros largely overlap. Neither N concentrations nor δ^{15}N values show a downhole trend (Fig. 31). Nitrogen concentrations and δ^{15}N values show no correlation in basalts and gabbros, but an inverse correlation in sheeted dikes (Fig. 33).

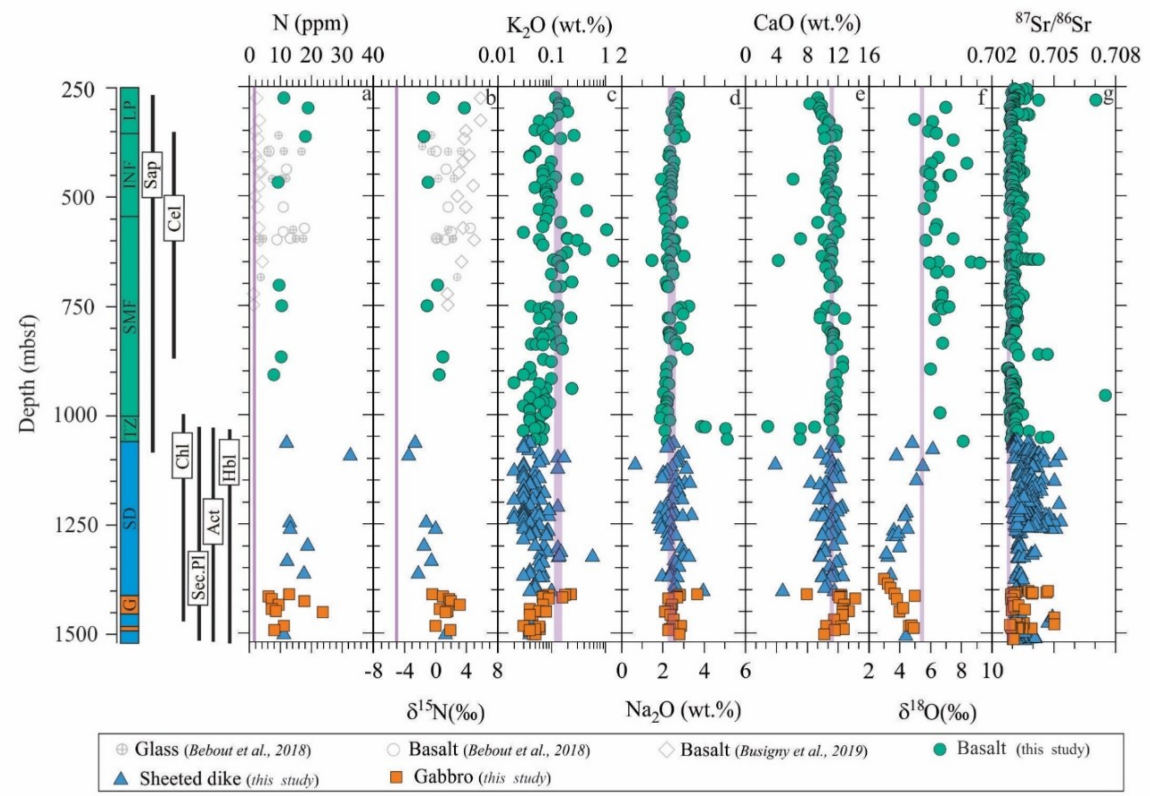

Figure 31. Downhole variations of ODP/IODP Hole 1256D. From left to right, lithology, major assemblage of secondary minerals, N concentration and δ^{15}N value (Bebout et al., 2018 and this study), K_2O, Na_2O and CaO concentrations (Shipboard Scientific Party, 2003b; Expedition 309/312 Scientists, 2006), δ^{18}O value (Gao et al., 2012) and ^{87}Sr/^{86}Sr ratio (Harris et al., 2015) of ODP/IODP Hole 1256D are displayed. Note that the whole-rock N concentrations of upper volcanic basalts reported by Busigny et al. (2005) (grey empty diamond) are systemically lower than those obtained by Bebout et al. (2018) (grey empty circle) and in this study (filled green

circle). The volcanic glass samples (grey empty circle with cross) from Bebout et al. (2018) are also shown for comparison. All data error bars are less than the symbol size. The purple vertical line in each panel represents the value of fresh MORB (Marty and Humbert, 1997; Eiler et al., 2000; Li et al., 2007; Alt and Shanks, 2011; Gale et al., 2013; Geldmacher et al., 2013; Harris et al., 2015). Abbreviations of the main lithological units: LP = lava pond; INF = inflated flows; SMF = sheet and massive flows; TZ = transition zone; SD = sheeted dikes; G = gabbros. Abbreviations of minerals: Sap = saponite; Cel = celadonite; Chl = chlorite; Sec. Pl = secondary plagioclase (i.e., albite and anorthite); Act = actinolite; Hbl = hornblende.

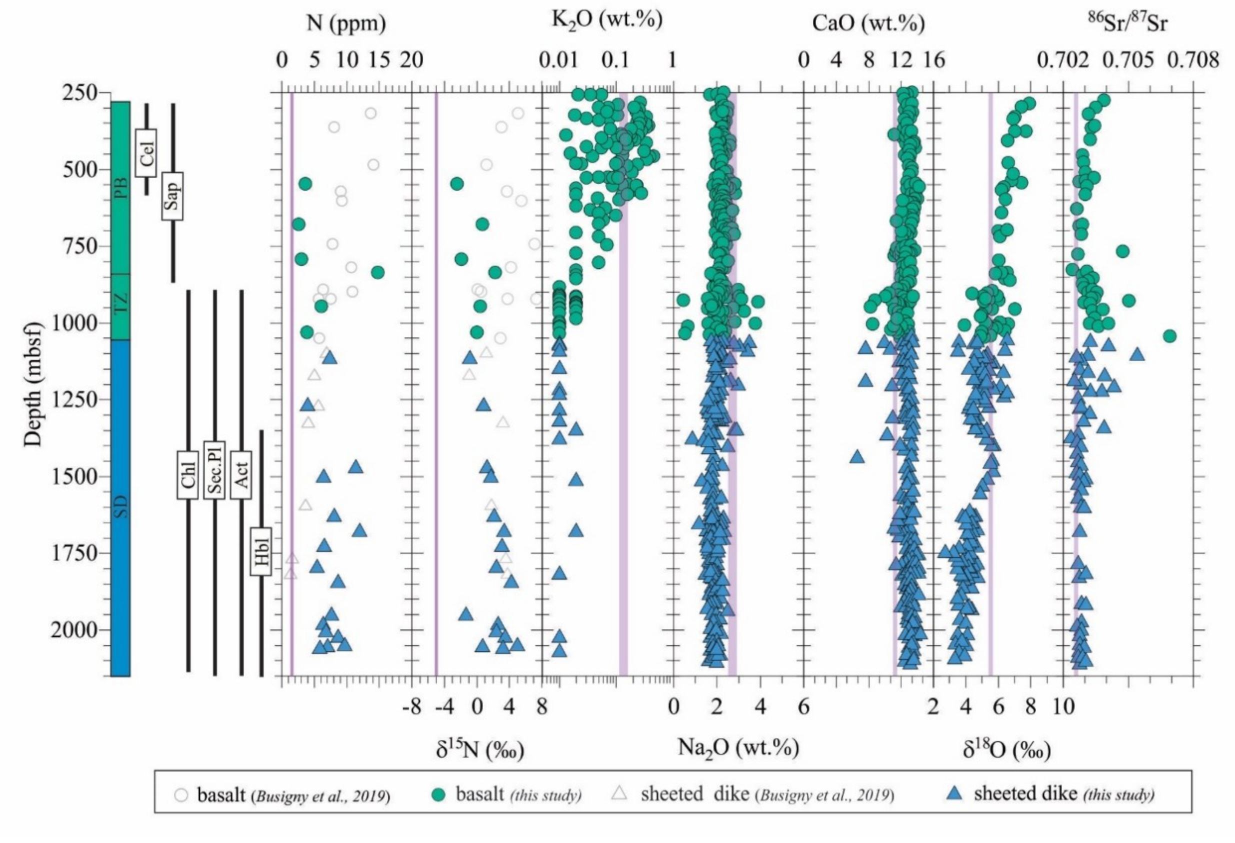

Figure 32. Downhole variations of DSDP/ODP Hole 504B. From left to right, lithology, major assemblage of secondary minerals, N concentration and δ^{15}N value (Busigny et al., 2019 and this study), K_2O, Na_2O and CaO concentrations (Alt et al., 1996; Bach et al., 2003), δ^{18}O value (Alt et al., 1986, 1996) and ^{87}Sr/^{86}Sr ratio (Alt et al., 1996) of DSDP/ODP Hole 504B are displayed. Note that compared with the data reported by Busigny et al. (2019), our data are consistent for basalts but systematically higher for sheeted dikes. The purple vertical line in each panel represents the value of fresh MORB (Alt et al., 1996; Marty and Humbert, 1997; Eiler et al., 2000; Li et al., 2007;

Gale et al., 2013). Abbreviations for the main lithological units: PB = pillow basalts; TZ = transition zone; SD = sheeted dikes. Abbreviations of minerals are the same as those in Fig. 31.

In Hole 504B, N concentrations and δ^{15}N values range from 2.7 ppm to 14.8 ppm (average: $5.7^{\pm4.6}$ ppm; n = 6; 1σ) and -2.4‰ to +2.3‰ (average: $+1.5^{\pm2.2}$‰; n = 6; 1σ) for basalts from the volcanic zone and transition zone (Fig. 32), and 4.0 ppm to 12.0 ppm ($7.6^{\pm2.1}$ ppm; n = 16; 1σ) and -1.3‰ to +5.0‰ (average: $+2.1^{\pm1.7}$‰; n = 16; 1σ) for sheeted dikes (Fig. 32). Compared with the data (5.8 – 14.1 ppm for basalts and 1.4 – 6.9 ppm for sheeted dikes) reported by Busigny et al. (2019), our data are consistent for basalts but higher for sheeted dikes. While the pre-heating of samples at a lower temperature (350 ºC) in an oxidizing environment was employed for 504B samples by Busigny et al. (2019), the overlapping of some of data makes it uncertain whether the N concentration difference in sheeted dike samples is a result of pre-heating or heterogeneity of samples. The shifts of N concentrations to lower values and δ^{15}N to higher values for the sheeted dike data in Busigny et al. (2019) mimic a trend of partial N loss (Fig. 31 and Fig. 32). A clear trend of partial N loss, however, was not observed in the basalt data reported by Busigny et al. (2019). With this caution, we will not include the sheeted dike data but include the basalt data of Busigny et al. (2019) in the following discussions. Integrating our basalts data with those from Busigny et al. (2019) gives an average N concentration $8.0^{\pm3.8}$ ppm and an average δ^{15}N value of $+2.4^{\pm2.9}$‰. Similar to 1256D, the N concentrations and δ^{15}N values of both basalts and sheeted dikes at 504B largely overlap and neither N concentrations nor δ^{15}N values show a downhole trend (Fig. 32), which is inconsistent with the downhole decrease in N concentrations observed by Busigny et al. (2019). A broad positive correlation between N concentrations and δ^{15}N values was observed in the altered basalts and sheeted dikes samples (Fig. 33).

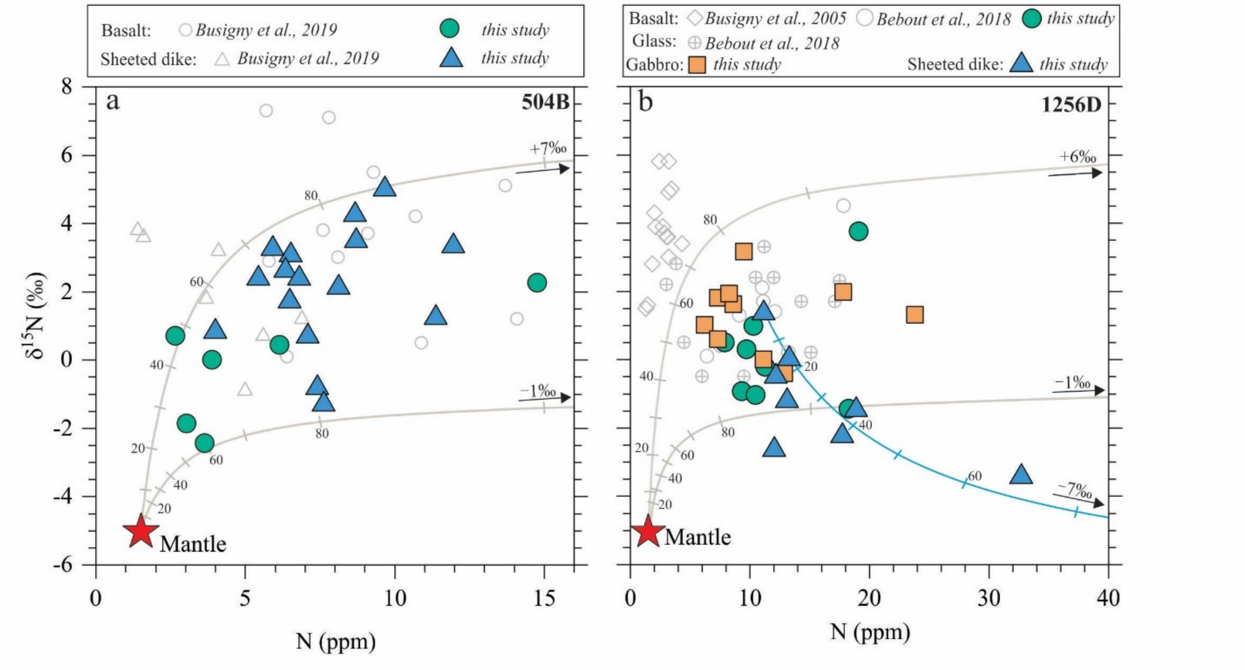

Figure 33. The relationship between N concentrations and δ^{15}N values of basalts, sheeted dikes and gabbros from Hole 504B (panel a) and Hole 1256D (panel b). All data error bars are smaller than data symbols. The two-component mixing model (grey lines) between fresh MORB and sedimentary sources with δ^{15}N value of -1‰ – +7‰ can explain most of the data except the 1256D sheeted dike data, which show a negative trend toward a ^{15}N-depleted source, likely related to abiotic N_2 reduction (blue line). See text for discussion.

3.3.4 Discussion

3.3.4.1 Hydrothermal enrichment of N in the intrusive section of AOC

3.3.4.1.1 Significant N enrichment in sheeted dikes and gabbros

Nitrogen typically occurs as ammonium (NH_4^+) in crustal rocks substituting for potassium (K^+) and to a lesser extent of sodium (Na^+) and calcium (Ca^{2+}) in the lattice of minerals (e.g., clay, mica, feldspar and clinopyroxene; Honma and Itihara, 1981; Pöter et al., 2004; Watenphul et al., 2010; Li et al., 2021e; Yang et al., 2022). In the upper volcanic section of AOC (including the basaltic rocks from Holes 1256D and 504B), enrichment of K^+ has been widely observed as a result of the formation of clay minerals, which are typical secondary minerals after low-temperature hydrothermal alteration of AOC (Figs. 31 and 32; e.g., Bloch and Bischoff, 1979; Seyfried and Bischoff, 1979; Alt, 1999). Consequently, the enriched N in the upper volcanic AOC section is likely associated with the K enrichment in clay minerals (e.g., Busigny et al., 2005; Li et al., 2007; Bebout et al., 2018).

Surprisingly, the underlying intrusive sections in Holes 1256D and 504B contain comparable N to their overlying volcanic sections (Figs. 31 and 32). This indicates that the studied intrusive sections of Holes 1256D and 504B experienced significant N enrichment at the same magnitudes as their extrusive sections.

Nitrogen could be possibly added into AOC in form of biomass through microbial alteration. Nitrogen enrichments have been found in the bio-alteration textures (e.g., microtubules) in volcanic glass from the Troodos ophiolite (Wacey et al., 2014) and some modern oceanic crust (Torsvik et al., 1998). Microbial activities in the AOC (particularly in basalts) from both Hole 1256D (e.g., Alt and Shanks, 2011; Li et al., 2019b) and Hole 504B (e.g., Furnes et al., 1999; Furnes and Staudigel, 1999; Li et al., 2019b) have also been inferred by isotopic fingerprints. This raises the possibility of a microbial contribution to the obtained bulk-rock N in this study. However, based on detailed counting of bio-alteration textures in the basaltic glass from Hole 417D/418A and Hole 504B, Furnes and Staudigel (1999) demonstrated that the influence of bio-alteration consistently decreases downhole to a very minor level by ~500 mbsf. It is thus expected that the added microbial N (if there is any) should be more pronounced in the upper volcanic rocks, which were persistently altered at low temperatures (< 100 °C) and thus favor microbial activity

(Furnes et al., 2008). However, in the upper volcanic section of Hole 1256D, whole-rock samples and basaltic glasses (Fig. 33), which are susceptible to microbial colonization, have comparable N concentrations, i.e., there is no downhole decrease in N concentration. This suggests an even lower contribution of microbial N in the intrusive sections of AOC. The sheeted dikes and gabbros were recovered from > 780 mbsf where in-situ temperature is > ~100°C (Guerin et al., 1996; Expedition 309/312 Scientists, 2006) and does not favor microbial activities. This further supports a minor contribution of microbial N in the intrusive sections of AOC. Other N species, such as N_2 in fluid inclusions or N^{3-} in crystal lattices (Pagé et al., 2018) could also exist in rocks, but they are likely minor in abundance compared to the NH_4^+fixed in crystal lattices. Accordingly, the following discussions are based on the assumption that the majority of N in the studied samples is in form of NH_4^+ fixed in the crystal lattice of secondary minerals.

A first speculation about the potential hosting minerals for the enriched N in sheeted dikes and gabbros are K- and/or Na-bearing secondary minerals, such as secondary plagioclase and amphibole. Their capabilities of hosting NH_4^+ have been demonstrated by previous studies (e.g., Honma and Itihara, 1981; Yokochi et al., 2009; Li et al., 2021b; Yang et al., 2022). It is interesting to observe that, compared to the upper volcanic section, the lower intrusive section contains similar Na_2O concentrations but much smaller K_2O concentrations (Fig. 31 and Fig. 32). If NH_4^+ is predominantly incorporated into the K^+ site, it would require a higher substitution coefficient between NH_4^+ and K^+. For example, the N/K molar ratios in the altered sheeted dikes (average: $906^{\pm 986} \times 10^{-4}$) and gabbros (average: $474^{\pm 405} \times 10^{-4}$) of Hole 1256D and sheeted dikes (average: $2112^{\pm 924} \times 10^{-4}$) of Hole 504B are consistently higher than those of the altered basalts ($7^{\pm 7} – 307^{\pm 425} \times 10^{-4}$) from Sites 504, 1256, 1149 and 801 (Fig. 34). Although the substitution coefficient between

NH_4^+ and K^+ has not been studied for these minerals, experimental work by Pöter et al. (2004) has revealed that the partition coefficient of NH_4^+ between muscovite/K-feldspar and fluids increases slightly with temperature from 400 ˚C to 600 ˚C. Therefore, one possible reason for a higher substitution capacity in sheeted dikes and gabbros may be their higher alteration temperatures. However, moderate- to high-temperature alterations intend to leach K out of oceanic crust by forming K-poor secondary minerals (Edmond et al., 1979; Von Damm et al., 1985; Staudigel, 2014b), which has been observed in the 504B sheeted dikes (Alt et al., 1996) and some of the 1256D sheeted dikes and gabbros (Expedition 309/312 Scientists, 2006). This does not favor the addition of NH_4^+ associated with the addition of K^+ as being observed in basalts. In addition, if NH_4^+ is mainly hosted in the K^+ site, the extremely high N/K molar ratios in the altered sheeted dikes from Hole 504B (average: $2112^{\pm 924} \times 10^{-4}$) suggest occurrence of some NH_4^+-endmember phases of K-bearing minerals, which are, however, not observed in Holes 1256D and 504B. Therefore, most of the N in sheeted dikes and gabbros may not be hosted in the K^+ site.

In contrast to K^+, Na^+ remains unchanged or shows a slight gain during the moderate- to high-temperature alterations of sheeted dikes and gabbros (Alt et al., 1996; Laverne et al., 2001; Expedition 309/312 Scientists, 2006; Staudigel, 2014). Therefore, NH_4^+ may be more likely added to the Na^+ site during moderate- to high-temperature alterations. A comparison of NH_4^+ substituting ratios between K^+ in basalts and Na^+ in sheeted dikes and gabbros indicates that N/Na molar ratios in sheeted dikes and gabbros ($9^{\pm 3} – 15^{\pm 7} \times 10^{-4}$) fall in the range of, but close to the lower end of the N/K molar ratios in basalts ($7^{\pm 7} – 307^{\pm 425} \times 10^{-4}$; Fig. 34), suggesting Na^+ has a similar or slightly lower capacity to host NH_4^+ even at higher temperatures. These hypotheses are worth testing in future studies.

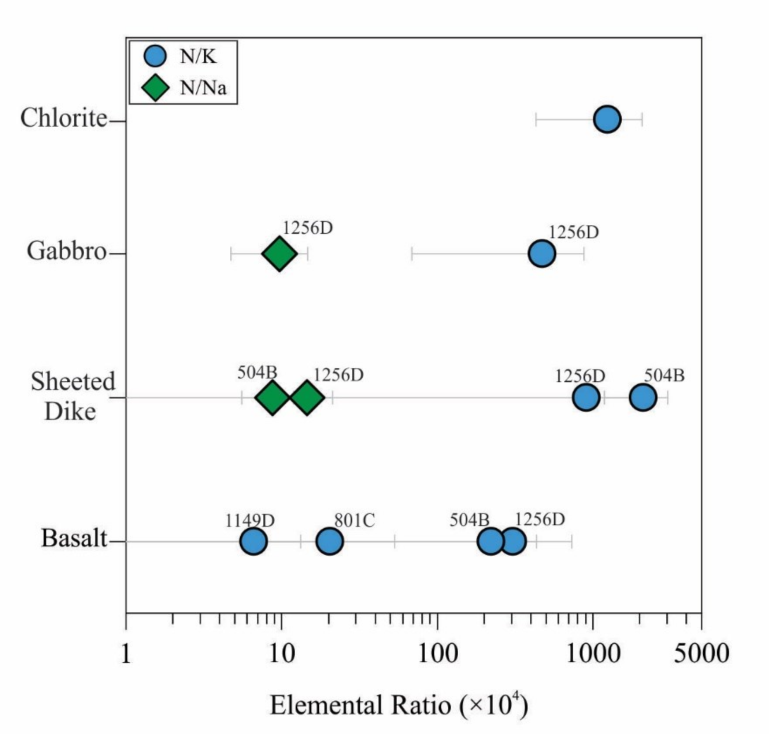

Figure 34. Comparison of bulk-rock N/K and/or N/Na molar ratios among basalts, sheeted dikes and gabbros, including Hole 1256D, Hole 504B, Hole 801C, Hole 1149D (data from: Li et al., 2007; Bebout et al., 2018; Busigny et al., 2019). The N/K molar ratio of chlorite in high-pressure metamorphic rocks ($1248^{\pm818}\times10^{-4}$; Harris et al., 2022) is also plotted for comparison. Note that the N/K ratios of sheeted dikes and gabbros are close to those of chlorite.

Another possible N hosting mineral is chlorite, which is a common secondary mineral in the studied sheeted dikes and gabbros. A recent study on chlorite in high-pressure metamorphic rocks suggested that tens of ppm N can be incorporated into chlorite, although the N-hosting site in the mineral remains unclear (Harris et al., 2022). Interestingly, the N/K ratios of chlorite in high-pressure metamorphic rocks ($1248^{\pm818}$ $\times10^{-4}$; Harris et al., 2022) are consistent with those in the intrusive AOC from Holes 1256D and 504B (Fig. 34). This consistency implies that chlorite could be the main N-hosting mineral in the altered sheeted dikes and gabbros. Regardless of the exact sites for hosting the secondary N, it requires NH_4^+ incorporation into the altered sheeted dikes and gabbros to occur during the early alteration stages at moderate- to high-temperature greenschist to amphibolite facies.

3.3.4.1.2 Sources of secondary N

The combined N concentration and $\delta^{15}N$ data can be used to infer the sources of the secondary N in AOC. Previous studies on the volcanic section of AOC (Li et al., 2007; Busigny et al., 2005; Bebout et al., 2018; Busigny et al., 2019) show that, with the addition of secondary N, the $\delta^{15}N$ values drift progressively from the mantle endmember (N = ~1.5 ppm; $\delta^{15}N$ = -5.0‰; Marty and Humbert, 1997; Li et al., 2007) to two external endmembers. One is isotopically identical to seafloor sediments, suggesting that part of the incorporated NH_4^+ in altered extrusive AOC was mobilized from organic matter and/or clay in overlying sediments. This is best illustrated by the positive correlation between N concentrations and $\delta^{15}N$ values in the altered basalts from the top section of ODP Holes 801C and 1149D (Li et al., 2007). In case that less sediment-sourced NH_4^+ is available to hydrothermal fluids (e.g., in the lower volcanic series at Holes 801C and 1149D), altered basalts may also incorporate NH_4^+ from a less abundant source, i.e., the NH_4^+ generated by abiotic N_2 reduction, which is characterized by an extremely ^{15}N-depleted signature as a result of a kinetic isotopic effect from breaking the strong N≡N bond (Li et al., 2007).

To assess the relative importance of these two NH_4^+ sources in the AOC (particularly the intrusive sections) from Holes 504B and 1256D, we employ a two-component mixing model between the mantle and external secondary N (Fig. 33; refer to Equation 1 in ***Chapter 2.1***).

For Hole 504B, the broad positive N – $\delta^{15}N$ correlation observed in the altered basalts and sheeted dikes can be well fitted by addition of secondary NH_4^+ with $\delta^{15}N$ values of -1‰ – +7‰ into fresh

MORB (Fig. 33a). These $\delta^{15}N$ values of secondary N are consistent with the those of seafloor sediments (-0.9‰ to +10‰; Sadofsky and Bebout, 2004; Li and Bebout, 2005; Tesdal et al., 2013), indicating that seawater/sedimentary sources are mostly responsible for the secondary N in the 504B AOC. Mass balance calculation suggests that 40% – 90% of the N in the AOC from Hole 504B is secondary.

For Hole 1256D, although no positive N – $\delta^{15}N$ correlation is observed in the altered basalts and gabbros, these data can still be well explained by the same mixing model by adding secondary NH_4^+ with $\delta^{15}N$ value of -1‰ – +6‰ (Fig. 33b). Mass-balance calculation suggests that 60% – 94% of the N in the altered basalts and gabbros from Hole 1256D is secondary, higher than Hole 504B. In contrast, the sheeted dikes from Hole 1256D show a negative N – $\delta^{15}N$ correlation (Fig. 33b). However, this negative trend does not mimic the one observed in the altered basalts from Holes 801C and 1149D, which shows simple mixing between fresh MORB and NH_4^+ from abiotic N_2 reduction (Li et al., 2007). Instead, best fitting of the negative correlation of the 1256D sheeted dikes points to mixing between an endmember with low N and high $\delta^{15}N$ (> +1.4‰) and an endmember with high N and low $\delta^{15}N$ (< -7‰) (Fig. 33b). This may imply that at least two hydrothermal fluids have been involved in the alteration of these sheeted dikes. The high $\delta^{15}N$ endmember can be linked to seawater-derived fluid, whereas the low $\delta^{15}N$ endmember requires a fluid component from deeper source, where abiotic N_2 reduction may account for at least part of the NH_4^+ in the fluid. The involvement of deeper fluids is also consistent with the significantly elevated $^{87}Sr/^{86}Sr$ signature of the 1256D sheeted dikes. These high $^{87}Sr/^{86}Sr$ ratios have been attributed to the steep thermal gradient in the thin sheeted dikes at a fast-spreading ridge axis (e.g., ~350 m at 1256D, in comparison to ~1000 m at 504B), which facilitated vigorous circulation of high-temperature hydrothermal fluids and consequently intensive alteration (Harris et al., 2015, 2017). This alteration effect could also explain the difference in N concentration of sheeted dikes between Hole 1256D ($16.4^{\pm 7.2}$ ppm) and Hole 504B ($7.6^{\pm 2.1}$ ppm).

3.3.4.2 Re-visiting the N recycling efficiency in the warm Central America subduction zone

3.3.4.2.1 Nitrogen flux into the Central America trench

The new constraints on the N enrichment in the intrusive sections of AOC from Holes 1256D and 504B enable us to better estimate the N input flux into the 1400 km CA trench (Hilton et al., 2002). Following de Moor et al. (2022), AOC from Hole 1256D formed at EPR and from Hole 504B formed at CNS represent the altered igneous components subducted into the 1100 km Guatemala-Northern Costa Rica trench and the 300 km Central-Southern Costa Rica trench, respectively (Van Avendonk et al., 2011). It should be noted that the heterogeneous alteration of AOC (e.g., different alteration degree and type) could lead to different distribution patterns of volatile elements (e.g., carbon) as has been observed by several previous studies (e.g., Gillis and Coogan, 2011; Staudigel, 2014). Therefore, it is expected that the heterogeneous alteration of AOC could cause some variabilities in the distribution of N among different AOC sections. However, the control of these factors on N distribution in AOC is still poorly understood so far. This may be the largest uncertainty in calculating the input fluxes of volatile elements into individual and global subduction zones.

To determine the N input flux into the CA trench, we employ the same modeling method that has been employed by a number of previous studies that calculated the C and/or N input fluxes of seafloor sediments (Plank and Langmuir, 1998; Sadofsky and Bebout, 2004; Li and Bebout, 2005) and AOC (Li et al., 2007, 2019b, 2020).

From the modeling (see Appendix F2), we obtained an N input flux of $3.1^{\pm 0.1} \times 10^8$ mol·yr^{-1} (weighted average δ^{15}N: +0.1‰) into the Guatemala-Northern Costa Rica trench solely from the upper 1257 m-thick AOC sections recovered from Hole 1256D (811 m upper volcanics + 446 m sheeted dikes and gabbros; Table 5), and another $2.8^{\pm 0.2} \times 10^8$ mol·yr^{-1} (weighted average δ^{15}N: +2.5‰) into the Central-Southern Costa Rica trench solely from the upper 1836 m-thick AOC section recovered from Hole 504B (780 m upper volcanics + 1056 m sheeted dikes and gabbros; Table 5; Fig. 35).

To calculate the N input flux from the residual sections of AOC that are dominantly composed of gabbroic rocks (Staudigel, 2014), two case scenarios are applied to provide the upper- and lower-end estimates. In the upper-end case scenario, the average N concentrations and isotopic compositions of the intrusive sections recovered by Hole 1256D ($11.3^{\pm 5.6}$ ppm; δ^{15}N = $+1.3^{\pm 1.0}$‰) and Hole 504B ($7.6^{\pm 2.1}$ ppm; δ^{15}N = $+2.1^{\pm 1.7}$‰) were applied uniformly to their underlying AOC sections in the EPR and CNS crusts. Seismic studies have revealed that the oceanic crust accreted at EPR is 5.5 – 6 km in thickness (Walther et al., 2000), whereas the oceanic crust accreted at CNS is thickened to 8 – 11 km due to the magmatism associated with the Cocos ridge (Walther, 2003; Van Avendonk et al., 2011). Employing the maximum crustal thickness (6 km for the EPR crust; 11 km for the CNS crust; Fig. 35), we obtained an the upper-end N input flux of $1.0^{\pm 0.5} \times 10^9$ mol·yr^{-1} for the residual 4743 m-thick EPR crust and $3.7^{\pm 1.0} \times 10^8$ mol·yr^{-1} for the residual 9164 m-thick CNS crust (Table 5; Fig. 35; See Appendix F2 for detail). The lower-end case scenario assumes that the N enrichment in AOC follows the exponential decrease trend of permeability and water-rock ratios along depth (Anderson et al., 1985; Nehlig and Juteau, 1988; Kawahata et al., 2001; Yamaoka et al., 2012), which may ultimately control the availability of sediments- or seawater-derived N. Therefore, using the minimum crustal thickness (5.5 km for the EPR crust; 8

km for the CNS crust) and the average N concentrations of recovered samples (i.e., $11.3^{\pm 5.6}$ ppm at 1257 m of Hole 1256D and $7.6^{\pm 2.1}$ ppm at 1836 m of Hole 504B) for the values at the top and the fresh MORB value (i.e., both 1.5 ppm at 5500 m of Hole 1256D and 8000 m of Hole 504B) for the value at the bottom of the un-recovered sections (Fig. 35**;** See Appendix F2 for methods), we obtained a lower-end N input flux of $3.7^{\pm 1.1} \times 10^8$ mol·yr^{-1} for the residual 4243 m EPR crust, and $1.2^{\pm 0.2} \times 10^8$ mol·yr^{-1} for the residual 6164-m thick CNS crust (Table 5). Combing the N input flux contributed by the upper crust calculated from the recovered basaltic sections from Holes 1256D and 504B, the total N input flux of AOC (F_{AOC_N}) into the entire CA trench contributed by the EPR and CNS crusts ranges from $1.1^{\pm 0.1} \times 10^9$ mol·yr^{-1} to $2.0^{\pm 0.5} \times 10^9$ mol·yr^{-1} (Table 5), with a weighted average $\delta^{15}N$ value of $1.0^{\pm 0.4}$‰.

Besides AOC, seafloor sediments also contribute an N input flux of $9.3^{\pm 0.5} \times 10^8$ mol·yr^{-1} into the 1100 km Guatemala-Northern Costa Rica trench (Table 5; Fig. 30; Li and Bebout, 2005) based on the N concentrations of the sediments recovered from Hole 1039B offboard the Northern Costa Rica trench. A sedimentary N input flux into the 300 km Central-Southern Costa Rica trench has not been estimated by previous studies. Following de Moor et al. (2022), we employed the average N composition of sediments (Harris, 2013a, b) recovered from Hole U1414A and U1381C offboard the Central-Southern Costa Rica trench (Fig. 30) to calculate the sedimentary N input flux (see Appendix F2 for detail). This gave an N input flux of $3.1^{\pm 0.5} \times 10^8$ mol·yr^{-1} (Table 5). Overall, we obtained a total sedimentary N input flux (F_{Sed_N}) of $1.2^{\pm 0.1} \times 10^9$ mol·yr^{-1} into the entire CA trench.

In the CA margin, tectonic erosion of the overriding plate (Meschede et al., 2002; Freundt et al., 2014) can also be an important factor contributing to the N input flux. A ball-park estimation by an early study (Li and Bebout, 2005) gave an approximate unit N input flux of $6.8^{\pm 5.5} \times 10^4$ mol·yr^{-1}·km^{-1} from tectonic erosion. Employing the trench length of 1400 km, an N input flux of $7.7^{\pm 6.3} \times 10^8$ mol·yr^{-1} was obtained (F_{Ero_N}; Table 5).

Adding F_{Ero_N}, F_{AOC_N} and F_{Sed_N} together, we obtained a total N input flux of $3.1^{\pm 0.6} \times 10^9$ mol·yr^{-1} to $4.0^{\pm 0.8} \times 10^9$ mol·yr^{-1} (Table 5) for the entire subducting slab (F_{Slab_N}) into the CA trench.

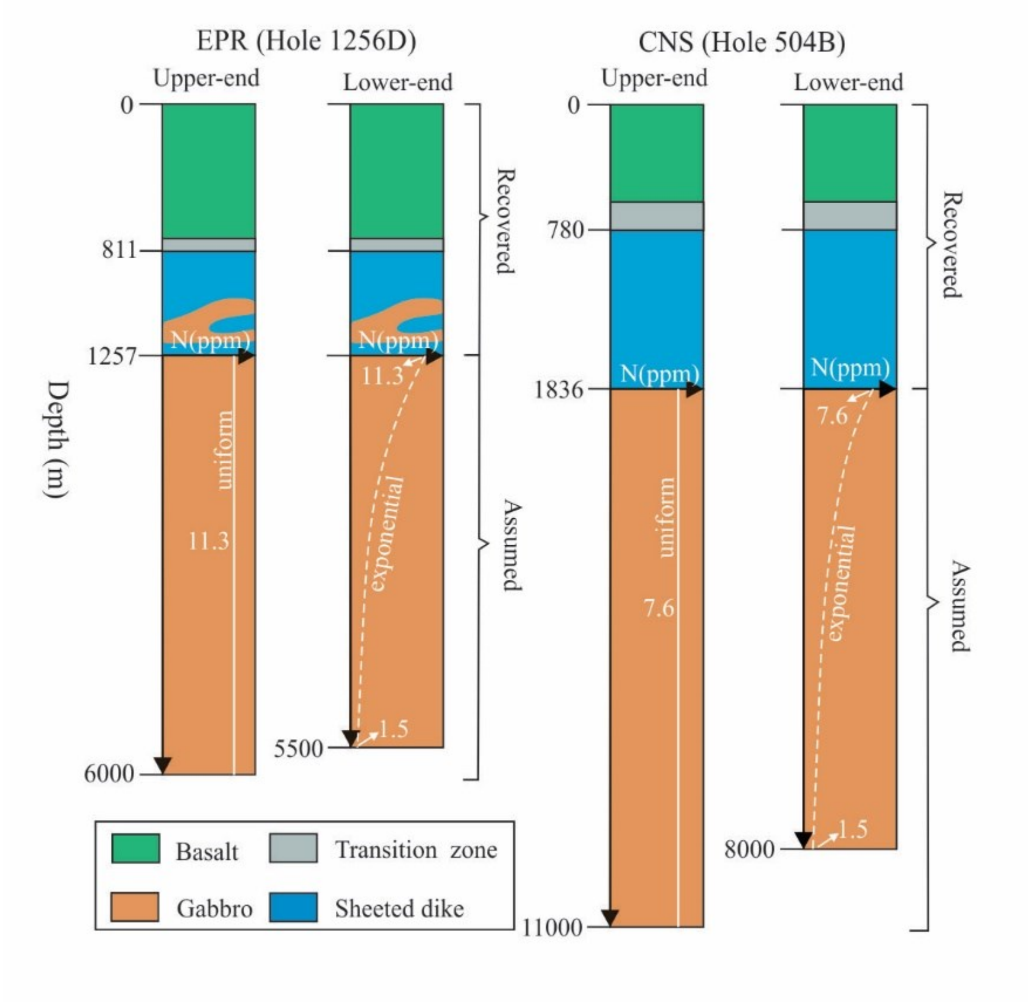

Figure 35. Schematic diagram (not to scale) showing the calculation of N input flux contributed by the EPR and CNS crusts under two endmember scenarios: (1) the upper-endmember scenario applies a uniform N concentration from the top to the bottom of AOC; (2) the lower-endmember scenario employs an exponential decrease in N concentrations along depth. See text for detailed explanation.

3.3.4.2.2 Nitrogen recycling efficiency at the Central America arc

With these new constraints on the N input flux into the CA trench, the N recycling efficiency at the CA arc can be calculated through comparison with the output flux of N from the recycled slab (F_{Output_N}) through arc volcanoes. Several previous studies have attempted to determine the output flux of N from the recycled slab N in the CA arc using different methods, which gave very different results (Table 5) (e.g., Fischer et al., 2002; Hilton et al., 2002; Snyder et al., 2003; Zimmer et al., 2004; Elkins et al., 2006; Labidi et al., 2021). For example, integrating the SO_2 flux in the entire CA arc with the average SO_2/CO_2 molar ratio (~2.7) and air-corrected (using noble gas components) CO_2/N_2 molar ratio (~195.4) of volcanic gases in the CA arc, Hilton et al. (2002) and Fischer et al. (2002) obtained a non-air N flux of 5.8×10^8 $mol \cdot yr^{-1}$ in the CA arc, which is considered to be close to the F_{Output_N} because the fraction of mantle derived N is very small in the samples (Fischer et al., 2002). A recent study by Labidi et al. (2021) employed a $^{15}N^{15}N$ index for air correction to obtain air-corrected $N_2/^3He$ molar ratios (8×10^7 to 2×10^8), which were then combined with the CO_2 flux of the entire CA volcanic arc (9.4×10^{10} $mol \cdot yr^{-1}$; Fischer et al., 2019) and the $CO_2/^3He$ molar ratios of gas samples (2×10^{10}; Kagoshima et al., 2015) to give an F_{Output_N} of $1.4^{\pm 0.6} \times 10^9$ $mol \cdot yr^{-1}$ (Labidi et al., 2021)

It is noted that some unconstrained parameters in both input N and output N may potentially cause uncertainties in the calculation of the N recycling efficiency in the CA margin. In the input part, one unknown parameter is the N stored in the slab mantle in the CA subduction zone, which has been hydrated due to extensive bend-faulting down to the mantle depths (Grevemeyer et al., 2007). A significant amount of N could be potentially trapped in this section and thus increase the total N input flux (e.g., Halama et al., 2014) but has not been well constrained so far. In the output part, there are two unconstrained parameters. One is the loss of slab N within the forearc region

(Inguaggiato et al., 2004). The recycling of slab N to the CA forearc region has not been well-studied yet. Lee et al. (2017) examined the gas components in forearc springs from four localities in Costa Rica and found minor contribution of subducted sedimentary N at two localities (Nicoya and Santa Elena) but somewhat higher contribution of subducted sedimentary N in the other two locality (Osa and Burica). This raises the possibility of N loss to the forearc region. However, the relative portion of the slab N recycled in the forearc region has not been quantified yet. Meanwhile, a recent study on blueschist-facies meta-basalts revealed that the labile N in sediments that is potentially released in the forearc region can be re-fixed into the igneous part of the slab for deep subduction (Li et al., 2021c). Because the geotherm of the CA subducting slab passes through blueschist to eclogite metamorphic facies (van Keken et al., 2018), re-fixation of labile N in sediments could be an alternative mechanism for preventing significant loss of slab N within the forearc region. Even if some fraction of subducted N is removed out of the slab, it may be potentially re-fixed again in the mantle-wedge as serpentinized peridotite, which could be further dragged down to sub-arc depth or even deeper (Pagé et al., 2018). The other unknown parameter in the output part is the recycled N trapped in the arc rocks (Freundt et al., 2014). A recent study by Füri et al. (2021) observed ~1 ppm non-gas N in olivine-hosted melt inclusions from Klyuchevskoy volcano. How much of this fixed N comes from the recycled slab and contributes to the slab N output flux is worth future investigation.

Nevertheless, in comparison with the F_{Slab_N} ($3.1^{\pm0.6} – 4.0^{\pm0.8} \times 10^9$ mol·yr^{-1}) estimated in this study, the F_{Output_N} of 5.8×10^8 mol·yr^{-1} estimated by Hilton et al. (2002) and Fischer et al. (2002) accounts for an N recycling efficiency of $15^{\pm3}\% – 19^{\pm4}\%$ at the CA arc (Table 5); while the N output flux of $1.4^{\pm0.6} \times 10^9$ mol·yr^{-1} estimated by Labidi et al. (2021) accounts for an N recycling efficiency of $35^{\pm4}\% – 45^{\pm5}\%$ at the CA arc (Table 5). Despite of this large uncertainty in the N output flux, our new data suggests that $55^{\pm5}\% – 85^{\pm3}\%$ of subducted N is not degassed via arc volcanoes and could be transported further downward beyond the sub-arc depth in the warm CA subduction zone (Fig. 36). This conclusion is different from the complete recycling of slab N via the CA volcanic arc proposed by Labidi et al. (2021).

3.3.4.3 Effect of thermal structure on N recycling in subduction zones

A thermal structural control on subduction-zone N recycling has been proposed based on the obvious difference in N loss from metamorphic rocks between a cold (Western Alps; Busigny et al., 2003a) and an extremely hot subduction zone (Catalina Schist; Bebout and Fogel, 1992), which is also supported by experimental studies (Mallik et al., 2018; Jackson et al., 2021). However, subduction zones in modern-style tectonics rarely reach the extremely high temperature/pressure gradient of the Catalina Schist. Most of subduction zones in modern-style tectonics fall between warm and cold geothermal gradients represented by the CA and IBM subduction zones, respectively (Bebout, 2007b; van Keken et al., 2018). Therefore, a comparison of the N recycling efficiency between CA and IBM can provide more insights into the effect of thermal structure on N recycling in the modern-style subduction zones.

The N recycling efficiency at the IBM arc has been examined by a previous study (Mitchell et al., 2010). This study employed the elemental ratios (CO_2/N_2 and $CO_2/^3He$) of volcanic gases and magmatic CO_2 and/or ^3He fluxes to give an average F_{Output_N} of $1.3^{\pm0.9} \times 10^8$ mol·yr^{-1} for the IBM arc (Table 5). Based on the sediments and basaltic AOC recovered from the two reference sites (i.e., Sites 801 and 1149) offboard the IBM trench (Sadofsky and Bebout, 2004; Li et al., 2007), the N input flux contributed by sediments and AOC into the IBM trench was previously estimated to be 4.4×10^8 mol·yr^{-1} (Mitchell et al., 2010) and 8.9×10^8 mol·yr^{-1}, respectively, in which the fresh MORB-like N concentration (1.5 ppm) was assigned to the subducting intrusive section (Li et al., 2007; Mitchell et al., 2010). Based on these values, Mitchell et al. (2010) obtained an N recycling efficiency of 4% – 17% for the IBM subduction zone. However, the lack of N data for the intrusive sections of AOC in the IBM margin leaves a large uncertainty to the estimation of the N input flux.

In the IBM margin, the incoming extrusive sections of AOC contain relatively low N concentration ($7.0^{\pm5.4}$ ppm) with a large proportion of secondary N from abiotic N_2 reduction (Li et al., 2007). This suggests that, although the sediment-derived NH_4^+ in hydrothermal fluids was deficient, NH_4^+ from other sources (e.g., abiotic N_2 reduction) can still increase the N budget in AOC. Consequently, employing the same method for the CA margin (see Appendix F2 for detail), a crustal thickness of 5500 m for the oceanic crusts formed at the fast-spreading center (i.e., AOC recovered from Sites 801 and 1149; Chen, 1992; Shipboard Scientific Party, 2000b, c) and the updated convergence rate of 4.1 $cm{\cdot}yr^{-1}$ along the IBM trench (Plank, 2014), we obtained an F_{AOC_N} of $4.2^{\pm2.2} \times 10^8$ $mol{\cdot}yr^{-1}$ to $7.5^{\pm5.3} \times 10^8$ $mol{\cdot}yr^{-1}$ (Table 5) for the IBM margin. The F_{AOC_N} of 8.9×10^8 $mol{\cdot}yr^{-1}$ calculated by Mitchell et al. (2010) and Li et al. (2007) is consistent with the upper end of our new estimation. This is because, although a higher N concentration was assigned to the intrusive section of AOC, the updated convergence rate (4.1 $cm{\cdot}yr^{-1}$) used in our new calculation was smaller than the one used in previous models (see Appendix F2 for detail). The consistency between these two estimations is simply a result of a smaller convergence rate of 4.1 $cm{\cdot}yr^{-1}$ employed in this study (see Appendix F2 for methods). Integrating the revised F_{Sed_N} of $3.6^{\pm0.2} \times 10^8$ $mol{\cdot}yr^{-1}$ (see Appendix F2 for methods), an upper-end F_{Slab_N} of $7.8^{\pm2.2}\times 10^8$ $mol{\cdot}yr^{-1}$ and a lower-end F_{Slab_N} of $1.1^{\pm0.5} \times 10^9$ $mol{\cdot}yr^{-1}$ are obtained for the IBM margin.

These new estimates give an N recycling efficiency of $12^{\pm10}\%$ – $17^{\pm12}\%$ at the IBM arc (Table 5), suggesting that $83^{\pm12}\%$ – $88^{\pm10}\%$ of slab N could be subducted beyond the sub-arc depth at the cold

IBM subduction zone (Fig. 36). Our new estimation of N recycling efficiency at the IBM arc is consistent with the result of 4% – 17% obtained by Mitchell et al. (2010).

When comparing the N recycling efficiencies between the CA and IBM margins, if we apply the N recycling efficiency of $15^{\pm 3}\%$ – $19^{\pm 4}\%$ at the CA arc estimated by the F_{Output_N} of 5.8×10^8 $mol{\cdot}yr^{-1}$ from Hilton et al. (2002) and Fischer et al. (2002), which employed a dataset and methodology more consistent with those for the IBM calculations (Mitchell et al., 2010), it appears that there is no (or only a very small) control of the thermal structure on the N recycling efficiency at arcs of cold to warm subduction zones. If we apply the N recycling efficiency of $35^{\pm 4}\%$ – $45^{\pm 5}\%$ at the CA arc estimated using the F_{Output_N} of $1.4^{\pm 0.6} \times 10^9$ $mol{\cdot}yr^{-1}$ of Labidi et al. (2021), it appears that thermal structure may play a notable role in the N recycling at arc. Despite different thermal structures, the CA and IBM subduction zones also differ in some other parameters, i.e., type of incoming sediments (carbonate-poor pelagic clay, volcaniclastic rocks and silica-rich chert at IBM vs. nearly pure carbonate ooze at CA), heterogeneous N enrichment degree in AOC (i.e., the N content is higher in the incoming AOC at CA compared to IBM) and overriding pate (oceanic crust at IBM vs. continental crust at CA). These factors may potentially affect the recycling of N inside subduction zones but are poorly constrained so far. Nevertheless, the obtained N recycling efficiencies at the IBM and CA arcs consistently support that a large fraction of slab N (> 50%) could be subducted to the deeper mantle beyond the sub-arc depth at either cold or warm subduction zones.

At a global scale, except the Cascadia, Mexico and British Columbia subduction zones, which have hotter geotherms than the CA subduction zone (Syracuse et al., 2010; van Keken et al., 2018), the majority of modern subduction zones (94% in trench length) have geotherms lying within the range bracketed by the cold IBM and warm CA subduction zones (Syracuse et al., 2010; van Keken et al., 2018). This implies that a majority of N (> 50%) in global slabs is not degassed through arc volcanoes but instead could be subducted beyond the sub-arc depth. This ingassed slab N could then be ultimately recycled into other deep reservoirs, such as the sources of mantle plumes (Dauphas and Marty, 1999; Halldórsson et al., 2016).

It is also worth noting that, early in the Earth history, subduction zones could have had much hotter geotherms resembling that of the Catalina Schist. Thus, the recycling of N through arc volcanoes may have been more efficient in modern subduction zone. This difference may cause variable feedbacks on the geochemical evolution of Earth's major volatile reservoirs (e.g., atmosphere and mantle) and be worth examining in the future studies.

3.3.5 Conclusions

Our new data of N concentrations and isotopic compositions of sheeted dikes and gabbros from ODP/IODP Hole 1256D and sheeted dikes from DSDP/ODP Hole 50B indicate that the N enrichments in the intrusive sections of altered oceanic crust are comparable to those in their overlying volcanic sections. The enriched N in sheeted dikes and gabbros was mainly incorporated during moderate- to high-temperature alteration and likely resides in chlorite, secondary plagioclase and amphibole. Employing these new data, we obtained the N recycling efficiency of $15^{\pm 3}\%$ – $45^{\pm 5}\%$ at the Central America arc and $12^{\pm 10}\%$ – $17^{\pm 12}\%$ at the Izu-Bonin-Mariana arc. The effect of thermal structure on subduction-zone N recycling efficiency is not conclusive from these data. Importantly, despite of the very different thermal regime at the cold IBM subduction zone and the warm CA subduction zone, our estimates indicate that > 50% of slab N is not degassed through arc volcanoes but can be possibly subducted into the deeper mantle beyond the sub-arc depth at a global scale.

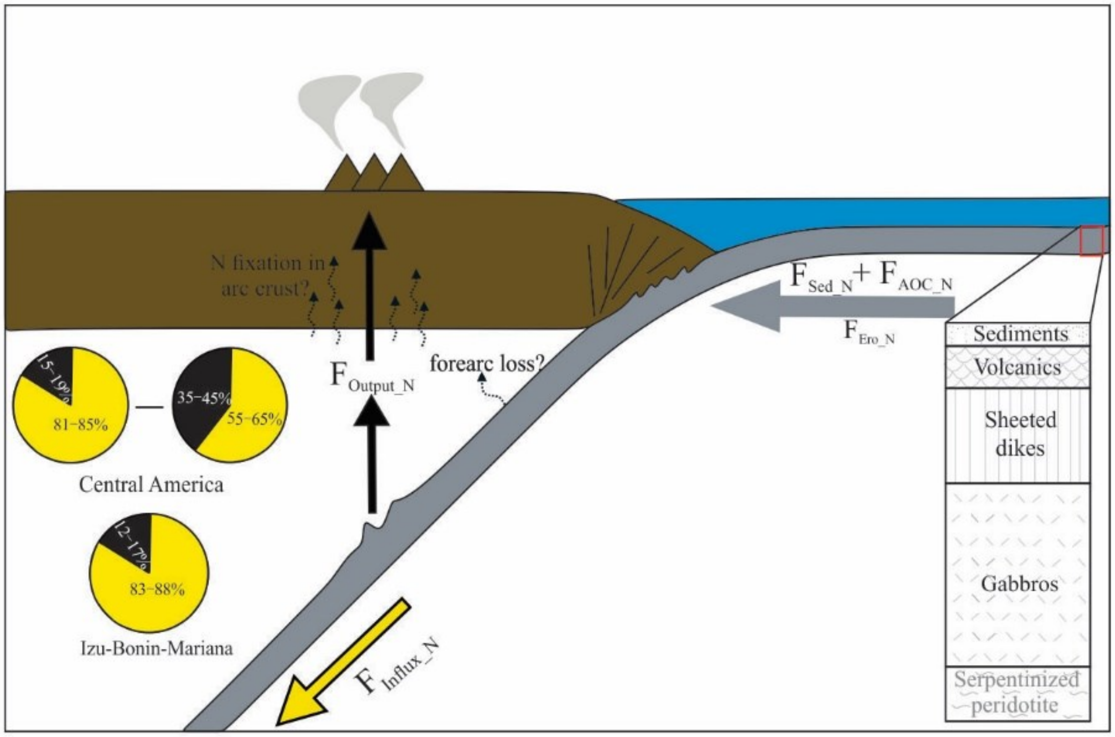

Figure 36. Schematic diagram (not to scale) showing the N recycling model in the Central America margin and Izu-Bonin-Mariana margin. The pie charts show the fractions of slab N that are recycled by arc volcanism (in black) and subducted beyond the sub-arc depth (in yellow), respectively.

Table 5. Calculation of N recycling efficiency at arcs of the Central America (CA) and Izu-Bonin-Mariana (IBM) subduction zones.

Subduction zone	Trench	Length (km)	Input flux ($\times10^8$ mol·yr^{-1})						Output flux (F_{Output_N}) ($\times10^8$ mol·yr^{-1})	Efficiency (%)
			Sediment (F_{Sed_N})	Upper crust	Lower gabbroic crust	AOC (F_{AOC_N})	Tectonic erosion (F_{Ero_N})	Total (F_{Slab_N})		
CA	G-NCR [a]	1100	$9.3^{\pm0.5}$ [c]	$3.1^{\pm0.2}$	$3.7^{\pm1.1} - 10^{\pm5}$	$11^{\pm1} - 20^{\pm5}$	$7.7^{\pm6.3}$	$31^{\pm6} - 40^{\pm8}$	5.8 [b] $-14^{\pm6}$ [c]	$15^{\pm3} - 19^{\pm4}$ [*] to $35^{\pm4} - 45^{\pm5}$ [†]
	CSCR [a]	300	$3.1^{\pm0.5}$ [c]	$2.8^{\pm0.2}$	$1.2^{\pm0.2} - 3.7^{\pm1.0}$					
IBM	n.a.	2450	$3.6^{\pm0.2}$ [e]	$0.6^{\pm0.1}$ [f]	$3.6^{\pm2.2} - 6.9^{\pm5.3}$ [f]	$4.2^{\pm2.2} - 7.5^{\pm5.3}$	n.d.	$7.8^{\pm2.2} - 11^{\pm5}$	$1.3^{\pm0.9}$ [d]	$12^{\pm10} - 17^{\pm12}$

a. G-NCR: Guatemala-Northern Costa Rica trench; CSCR: Central-Southern Costa Rica trench.

b. Data from Hilton et al. (2002) and Fischer et al. (2002).

c. Data from Labidi et al. (2021).

d. Data from Mitchell et al. (2010).

e. See Appendix F2 for detail.

*. Calculated lower-end and the upper-end nitrogen recycling efficiency at CA arc employing the F_{Output_N} from Hilton et al. (2002) and Fischer et al. (2002).

†. Calculated lower-end and the upper-end nitrogen recycling efficiency at CA arc employing the F_{Output_N} from Labidi et al. (2021).

Chapter 4 Conclusions

In Chapters 2 and 3 of my dissertation, I have utilized a suite of altered oceanic crust samples (altered basalts, sheeted dikes and gabbros) and oceanic serpentinite samples across global ocean floors, together with a suite of metamorphic rocks representing the serpentinized forearc mantle wedge and blueschist-facies meta-basalts, to constrain the N input fluxes of subducting slabs into subduction zones and their recycling within the forearc and sub-arc regions. The work in this dissertation fills several research gaps in the geological N cycle by providing detailed and fundamental information on the N uptake by mafic and ultramafic components of oceanic crust and mantle in the subducting slab and the recycling pathways of subducted N during prograde metamorphism inside subduction zones. In this chapter, I summarize the main findings and discussion points that have led to these conclusions.

4.1 Nitrogen uptake in subducting slabs and input N fluxes into subduction zones

4.1.1 The upper basaltic oceanic crust

Chapter 2.1 contributed new N concentration and $\delta^{15}N$ data of four more DSDP/ODP/IODP sites, which combined with published data of ODP Sites 801, 1149, 504 and 1256 allows to configure a N dataset covering the full spectrum for a number of variables of oceanic crust, such as crust age, spreading rate, alteration degree, and sediment type. This dataset enables a detailed assessment of the controlling factors on N enrichment in the most altered upper basaltic oceanic crust. The work in this section demonstrated that: (i) the secondary N (in the form of ammonium) in altered basalts was sourced from sediment/seawater with $\delta^{15}N$ values of 0‰ to +8‰, with a minor source from abiotic N_2 reduction with $\delta^{15}N$ values of -12‰ to -21‰; (ii) N enrichments in the upper oceanic crust do not correlate with crustal age, suggesting that the N uptake should mainly occur over early ages (likely within ~20 Myr of crustal formation); (iii) the magnitude of N enrichment in the upper oceanic crust is primarily controlled by the N availability in the surrounding environment, which is ultimately related to the N abundance of basal sediments and/or seawater. The highest degree of N enrichment occurs in the upper oceanic crust overlain by N-rich basal sediments (claystone), i.e., at Hole 543A (N = 24.9±8.3 ppm; 1σ). In contrast, the lowest degree of N enrichment occurs in the upper oceanic crust overlain by N-poor basal sediments (chert), i.e., at Hole 1149D (N = 2.0±0.5 ppm; 1σ). With the consideration of this primary controlling factor, a global N input flux of $3.7\pm0.3 \times10^9$ $mol\cdot yr^{-1}$ for the 300 – 600 m upper oceanic crust is calculated. These new data also demonstrate that N concentrations are relatively low in global altered basalts (average: 10.1±7.8 pm; 1σ). In comparison to their metamorphic equivalents, blueschists have much higher N concentrations (up to ~122 ppm) whereas eclogites have N concentrations comparable to altered basalts. This implies further N enrichment in basaltic oceanic crust during early subduction and N devolatilization during deep subduction (by eclogite facies).

4.1.2 The lower intrusive oceanic crust

Chapter 2.2 and part of Chapter 3.3 contributed new N concentration and $\delta^{15}N$ data of the moderate- to high-temperature altered sheeted dike and gabbroic oceanic crust, which accounts for ~70 vol% of the crustal material in subducting slabs but has been rarely studied. The new data of sheeted dikes from Holes 1256D and 504B and gabbroic rocks from Holes 1256D, 735B, 1309D and 1415P across the global ocean floors demonstrate that the intrusive section of AOC is able to incorporate significant amount of secondary N (2.7 – 33.5 ppm) from seawater-derived hydrothermal fluids with $\delta^{15}N$ value of -1‰ – +7‰ during the moderate- to high-temperature hydrothermal alteration stage, comparable to that of the upper basaltic oceanic crust. From these data, a global N input flux from AOC as $21.8^{+0.9}_{-1.3}$ ×10^9 mol·yr^{-1} to $30.6^{\pm 2.2}$×10^9 mol·yr^{-1} (not accounting for serpentinized suboceanic lithospheric mantle), in which 53% – 65% is contributed by the gabbroic oceanic crust ($11.5^{+0.5}_{-1.0}$ ×10^9 mol·yr^{-1} to $20.0^{\pm 2.1}$×10^9 mol·yr^{-1}).

4.1.3 The oceanic serpentinites

Chapter 2.3 contributed N concentration and $\delta^{15}N$ data of a set of oceanic serpentinites from four DSDP/ODP/IODP sites (Holes 895D, 1271B, 920D and 1274A) in the Pacific and Atlantic oceans. These samples represent oceanic lithospheric mantle that was altered at variable temperatures (<150 ºC to > 350 ºC). The new data demonstrated that: (i) oceanic serpentinites are ubiquitously enriched in secondary N (3.2 – 18.6 ppm) sourced from sediments/seawater with $\delta^{15}N$ value of -1‰ – +6‰; (ii) N enrichment in these oceanic serpentinites is at similar magnitude despite of variable serpentinization temperatures; and (iii) the N enrichment in serpentinites is of similar magnitude to that in altered oceanic basalts, sheeted dikes and gabbroic rocks. Based on these new data, we estimated that the serpentinized oceanic mantle can contribute 3.3×10^9 mol N to global subduction zones annually, which is comparable to that of the most altered part (i.e., the upper volcanic section) of oceanic crust. A further comparison between these oceanic serpentinites and meta-serpentinites that have been subducted to depths of up to ~70 km suggests that N can be well retained in serpentinites during subduction. These results imply that the serpentinized slab mantle could be a critical reservoir for deep N recycling. The entrained N could subsequently be incorporated into diamond-forming fluids, resulting in the heavy N isotopic signatures observed in diamonds.

4.1.4 Total N input fluxes into global subduction zones

The input fluxes and corresponding δ^{15}N values of each section of the subducting slab studied above are summarized in Fig. 37 and Table 6.

Table 6. Summary of N input fluxes (±1σ) and δ^{15}N values (±1σ) of the subducting slab.

Subducting components	Input flux (×10^{9}; mol·yr^{-1})	δ^{15}N (‰)
Basalts	$3.7^{\pm 0.3}$	$0.2^{\pm 4.4\dagger}$
Transition zone + Sheeted dike	$6.8^{\pm 0.7}$	$1.0^{\pm 2.3\dagger}$
Gabbro	$11.5^{+0.5}_{-1.0} - 20.0^{\pm 2.1}$	$1.3^{\pm 1.8\dagger}$
Serpentinite	3.3	$0.7^{\pm 2.0\dagger}$
Sediments	$54.3^{\dagger\dagger}$	$5.2^{\pm 1.5*}$
Total	$79.4^{+0.9}_{-1.3} - 88.2^{\pm 2.2}$	$3.9^{\pm 1.1} - 3.6^{\pm 1.0\ddagger}$

†. Average δ^{15}N values (±1σ) of the examined samples.

*. Average δ^{15}N values (±1σ) of the subducting sediments offboard the Central America and Izu-Bonin-Mariana trenches.

††. Data from Busigny et al. (2003a).

‡. Weighted average δ^{15}N value (±1σ) of the entire subducting slab.

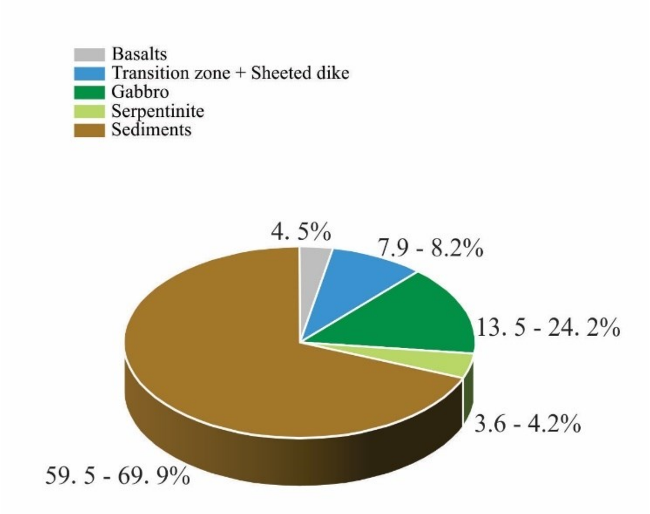

Figure 37. Pie chart showing the relative contributions of N input fluxes from basalt, transition zone, sheeted dike, gabbro, serpentinite and sediments.

4.2 Nitrogen recycling across subduction zones

4.2.1 Nitrogen recycled to the forearc mantle wedge

In Chapter 3.1, the first set of N concentration and $\delta^{15}N$ data of mantle wedge serpentinites were reported, based on the serpentinites from the 9 – 29 km IBM mantle wedge. These serpentinites show ubiquitous N enrichment (3.6 – 16.4 ppm) with $\delta^{15}N$ values of -3.4‰ – +2.8‰, consistent with addition of external N with $\delta^{15}N$ values of -1‰ – +5‰. Comparison of N concentrations and $\delta^{15}N$ values with seawater indicators of B concentration and slab-fluid indicators of Li and Cs concentrations suggests that the secondary N was not from seawater but from the subducting slab with main contributions from pore fluids and, very minor, from mineral devolatilization. The recycled slab N in serpentinites in the IBM forearc mantle wedge is estimated to be $2.6^{\pm 1.3} \times 10^6$ mol·yr^{-1}, which only accounts for up to 0.7% of the N input flux of subducting sediments alone. This suggests that recycling of slab N to the forearc mantle wedge may only play a minor role in subduction-zone N recycling, at least in the IBM subduction zone and possibly in most of the world's subduction zones with subducting slabs passing through blueschist-eclogite facies.

4.2.2 Intraslab remobilization of N during early subduction facilitates deep N recycling

Chapter 3.2 examined the N behavior in subducting slabs through the pillow-shaped meta-basalts in the Heilongjiang Complex in Northeast China, which have been subducted to a pressure-temperature condition slightly higher than the IBM mantle wedge samples. The blueschist data demonstrate that the labile N in sediments released during early subduction can be re-fixed into the more refractory meta-igneous part of the subducting slab. This provides an explanation why little N is released into the mantle wedge, as observed in Chapter 3.1. The redistribution of labile sedimentary N to refractory minerals in meta-igneous rocks in subducting slabs facilitates the retention of N for deep subduction and recycling.

4.2.3 Nitrogen recycling in the sub-arc region

Chapter 3.3 examined the N recycling efficiencies at arcs of the warm Central America and the cold IBM subduction zones, from which the thermal structure control on N recycling in subduction zones was assessed. Based on the mass balance between N input fluxes estimated from the reference sites offboard the trenches and the published N output fluxes through arc volcanoes, the N recycling efficiency at the arc was estimated to be $15^{\pm3}$% – $45^{\pm5}$% for the warm Central America subduction zone and $12^{\pm10}$% – $17^{\pm12}$% for the cold IBM subduction zone. While these new estimates do not provide a conclusive constraint on the effect of subduction-zone thermal structure on N recycling, they consistently suggest that a large fraction of slab N (>50%) survives the sub-arc filter and is delivered beyond arc depths in global subduction zones.

4.2.4 Summary of N recycling from forearc to sub-arc regions

The three studies above consistently suggest that the majority of slab N is able to be retained, at least to blueschist-facies metamorphism, which is well-within the temperature and pressure conditions of the forearc region (Syracuse and Abers, 2006). However, when the subducting slabs reach the sub-arc depth, some degree of N loss is expected. The mass balance between the input fluxes of N contributed by sediments and AOC and the output fluxes of N at arcs of the warm CA and the cold IBM subduction zones suggest that > 50% of slab N is able to be transferred beyond the sub-arc depth in most of world's subduction zones.

Table 7. Summary of global N input flux, output flux and influx (±1σ).

	Global input flux (×10^9; mol·yr^{-1})	Global output flux (×10^9; mol·yr^{-1})	Recycling efficiency at arc (%)	Influx* (×10^9; mol·yr^{-1})
Case 1	$79.4^{+0.9}_{-1.3}$ – $88.2^{\pm2.2}$	39†	$46^{\pm1}$ – $52^{\pm1\dagger}$	$40.0^{+0.9}_{-1.3}$ – $48.8^{\pm2.2}$
Case 2	$79.4^{+0.9}_{-1.3}$ – $88.2^{\pm2.2}$	$67^{\pm2\ddagger}$	$79^{\pm3}$ – $83^{\pm3\dagger}$	$12.2^{+0.9}_{-1.3}$ – $21.0^{\pm2.2}$

†. Data from Hilton et al. (2002).

‡. Data from Bekaert et al. (2021).

*. The flux of N that can be transferred beyond the sub-arc depth.

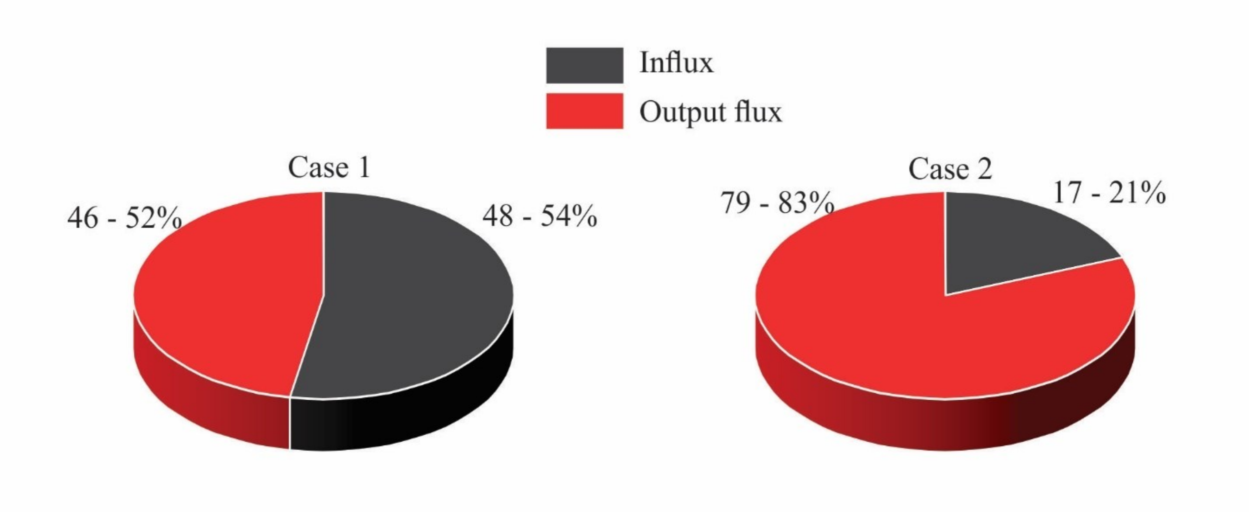

Figure 38. Pie charts showing the relative fractions of N that is recycled through arc volcanoes (output flux) and subducted beyond the sub-arc depth (influx). Case 1 employs the N output flux at arcs estimated by Hilton et al., (2002), while Case 2 employs the N output flux at arcs estimated by Bekaert et al. (2021).

When comparing the total N input flux into global trenches with the total N output flux at global arcs (Table 7), the N recycling efficiency at arcs can be estimated to be $46^{\pm1}$ – $52^{\pm1}$% if we employ the estimate of 39×10^{9} mol·yr^{-1} by Hilton et al. (2002), $79^{\pm3}$ – $83^{\pm3}$% if employ the estimate of $67^{\pm2}\times10^{10}$ mol·yr^{-1} by Bekaert et al. (2021). The former suggests that a large fraction (48 – 54%) of slab N can be transferred beyond the sub-arc depth to the deeper mantle, whereas the latter suggests that only a small fraction (17 – 21%) of slab N can be deeply subducted (Fig. 38). However, given that the thermal regime of subduction zones may play a major role in the recycling of slab N via arcs (Mallik et al., 2018; Jackson et al., 2021), the N recycling efficiency of global arcs should not be more than that of the Central American subduction zone because the average geotherm of global subduction zone is colder than that of the Central America subduction zone (e.g., Syracuse et al., 2010). In this perspective, the estimated arc N recycling efficiency of $46^{\pm1}$ – $52^{\pm1}$% employing the data from Hilton et al. (2002) is more consistent.

This point can also be verified by metamorphic rocks from subduction zones. Based on the comparison between altered basalts and gabbros and their blueschist-facies and eclogite-facies metamorphic equivalents, progressive loss of slab N is expected to occur during eclogite facies metamorphism. This is consistent with the release of N at sub-arc regions, where the subducting slab may go through the blueschist- to eclogite-facies transition and a large amount water released from this transition may induce arc magmatism (Peacock, 1993, 1996). However, when comparing the temperature-pressure paths between modern subduction zones and exhumed ancient subduction-related metamorphic units, eclogite-facies meta-basalts and meta-gabbros show hotter pressure-temperature paths than the warm CA subduction zone but similar to the few hot subduction zones in the world (Cascadia, Mexcio and British Columbia) with young oceanic crusts in their subducting slabs (< 10 Ma; Jarrard, 2003; Fig. 39). This discrepancy has been attributed to the preferential exhumation of metamorphic units under relatively warm conditions due to the subduction of young oceanic crust and/or during the initial warmer stage of subduction (van Keken et al., 2018). The Schistes Lustrés metasedimentary unit (up to eclogite facies), which has been demonstrated to show nearly no (Busigny et al., 2003a) to small amounts (Bebout et al., 2013a) of N loss, has a reconstructed pressure-temperature path close to that of the Central America subduction zone (Fig. 39). Consequently, if thermal structure plays a major role in the recycling of slab N via arcs (Mallik et al., 2018; Jackson et al., 2021), the majority of slab N could be largely retained for deep subduction. Alternatively, the temperature-pressure models of the modern subduction zones are inaccurate, due to a miscount of some heat sources (e.g., exothermic hydration and carbonation of mantle wedge induced by fluids dehydrated from slab, heat transport by dehydrated fluids), which resulted in an underestimation of the geotherms of modern subduction zones (Penniston-Dorland et al., 2015). More studies are needed in the future to reconcile this discrepancy.

It is also interesting to note that, in contrast to meta-basalts and meta-gabbros which show variable N loss doing eclogite-facies metamorphism, N in meta-serpentinites can be well retained to temperature and pressure conditions comparable to eclogite facies (Fig. 39). This again suggests that serpentinites could be a critical reservoir for deep N recycling.

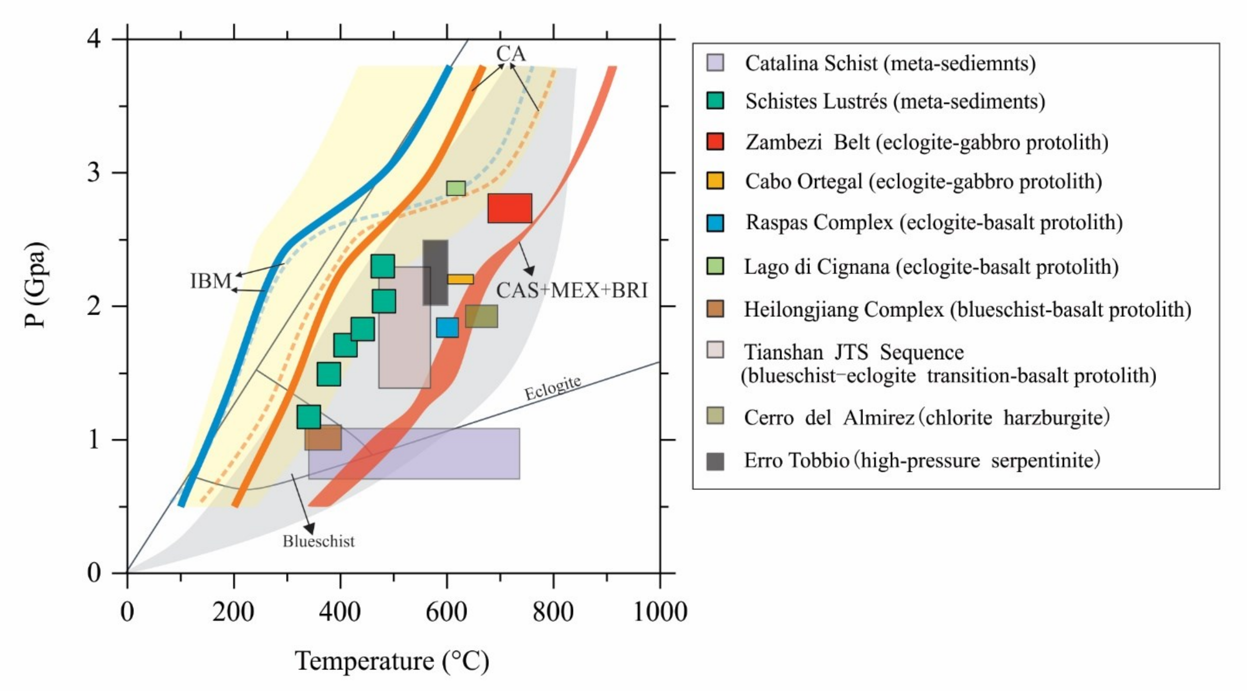

Figure 39. Comparison of pressure-temperature paths between modern subduction zones and ancient exhumed metamorphic units. The pressure-temperature paths of bulk slabs for Central America (CA; orange solid line), Izu-Bonin-Mariana (IBM; blue solid line), the majority of modern subduction zones (94% in trench length; yellow shaded area) and three hot subduction zones (CAS: Cascadia; MEX: Mexico; BRI: British; red shaded area) are from van Keken et al. (2018). The pressure-temperature paths of the slab tops for Central America (orange dashed line) and Izu-Bonin-Mariana (blue dashed line) are also shown for comparison (van Keken et al., 2018). The reconstructed pressure-temperature conditions of the Schistes Lustrés (green filled squares; Agard et al., 2000; Busigny et al., 2003a; Plunder et al., 2012) and Catalina Schist (purple filled

rectangle; Bebout, 2007b), which form end-member of the exhumed metamorphic units (grey shaded area; data from Penniston-Dorland et al., 2015), are characterized by cold and extremely hot geotherms, respectively. Note that modern subduction zones follow pressure-temperature paths in the blueschist-eclogite domains. Data source of the pressure and temperature conditions of metamorphic units are: eclogite-facies meta-gabbros (Zambezi Belt and Cabo Ortegal; Halama et al., 2010), eclogite-facies meta-basalts (Raspas Complex, Lago di Cignana and Tianshan JTS sequence; Halama et al., 2010, 2017), blueschist-facies meta-basalts from the Heilongjiang Complex (Zhou et al., 2009), high-pressure serpentinites and chlorite harzburgite (Halama et al., 2014), the pressure domains of blueschist and eclogite facies metamorphism (Penniston-Dorland et al., 2015).

4.3 Future directions

The ideas presented here have opened various avenues of research to move forward in the future:

4.3.1 Determine the N isotope fractionation during abiotic reduction of N_2, NO_3^-, NO_2^- to NH_4^+

The extreme negative $\delta^{15}N$ values (down to -21‰) observed in the seafloor altered basalts and blueschists from the Heilongjiang Complex were attributed to the kinetic isotope effect during the abiotic reduction of N_2 during fluid-rock interaction (***Chapter 2.1 and Chapter 3.2***; Li et al., 2007; Li et al., 2021b). Similarly, the extreme negative $\delta^{15}N$ values (down to -16‰) observed in the ultrahigh-pressure metamorphic rocks from the Sulu Orogenic belt were also consistently attributed to abiotic reduction of N_2 during fluid-rock interaction (Li et al., 2014). As demonstrated by these studies, this process could potentially be critical to fix N into crustal rocks. Although the abiotic reduction of N_2, NO_3^- and NO_2^- by elemental Fe or Fe(II)-bearing minerals has been experimentally demonstrated (Brandes et al., 1998), N isotope fraction during this abiotic reduction process has not been experimentally constrained so far. This impedes our overall understanding on N isotopic compositions of different reservoirs.

4.3.2 Determine the exact hosts of N in crustal rocks and their ultimate fate during subduction

a. Because the analytical target in this thesis is bulk rock, it is impossible to detect the exact N hosts in these crustal rocks (i.e., basalts, sheeted dikes, gabbros and serpentinized peridotites). Secondary plagioclase, amphibole, chlorite, pyroxene and serpentine are all expected to be capable of hosting NH_4^+. However, their relative importance in hosting N in altered oceanic crust and the serpentinized mantle rocks remains uncertain. Recent advancement in the in-situ analysis of N concentrations by *Nano-SIMS* (Füri et al., 2021; Harris et al., 2022) could make this possible.

b. The incorporation mechanism of NH_4^+ into some minerals (e.g., serpentine, chlorite) is not clear. Whether NH_4^+ can be incorporated into the crystal lattice or simply adsorbed onto the surface of these minerals remains uncertain. These are important directions for us to understand the mechanism of NH_4^+ incorporation into minerals.

c. The behavior of N in these minerals during prograde metamorphism in subduction zones needs to be examined in detail, e.g., by laboratory experiments (e.g., Yang et al., 2022).

4.3.3 Hidden N reservoirs affecting N recycling in subduction zones

As discussed above, the N inventories in some reservoirs, such as the extrusive and plutonic arc crust which can potentially fix the recycled slab N, have not been studied. This is an important missing piece in the geological N recycle.

4.3.4 Determine the impact of subduction on the deep N cycle

The result in this thesis supports that a large fraction (> 50%) of the crustal N, with $\delta^{15}N$ values (~ +3.8‰) heavier than the convecting mantle value (-5‰; Marty et al., 2020), is able to be subducted to the mantle beyond sub-arc depth. This raises several broad directions that are worth further exploring.

a. The first and foremost question that needs to be answered is: will subduction affect the N isotopic composition of the mantle over geological times since the initiation of subduction (e.g., 3.0 – 4.0 Ga; Shirey and Richardson, 2011; Dhuime et al., 2012; Turner et al., 2014)? As demonstrated by the numerical modeling in Labidi et al. (2020), with the subduction of N at an input flux of ~9.4×10^{10} mol·yr^{-1} over ~4 Ga of Earth's history, similar to the estimated total N input flux in this study, the δ^{15}N value of the mantle with an enstatite chondrite N isotopic composition ($-20^{\pm11}$‰; Grady and Wright, 2003) could be significantly elevated to a value (~+3‰) even heavier than that of the modern value (-5‰; Marty et al., 2020). However, if the N input flux contributed by subduction is persistently lower than the volcanic N output flux over the majority of Earth's history, δ^{15}N value could remain steady at ~ -5‰ over Earth's history (Labidi et al., 2020). These modeling results support the idea that the heavy δ^{15}N values observed in fresh MORB and plumes could be primordial (Labidi et al., 2020; Labidi and Young, 2022). Although the results in this study support subduction of massive N into the deeper mantle, which may potentially affect the δ^{15}N value of the mantle on a long-term scale, one of the unconstrained key parameters here is the timing of the initiation of the massive N subduction to the deeper mantle. As stated in ***Chapter 3.3***, compared to the geotherms of modern subduction zones, the geotherms of subduction zones in the deep time (e.g., Archean) may be hotter than the modern ones (e.g., Dasgupta, 2013). Therefore, it is expected that the efficiency of N that can survive the 'subduction filter' to the deeper mantle is different between the modern and ancient subduction zones (e.g., Jackson et al., 2021). This could result in different feedbacks on the evolution of Earth's major N reservoirs (e.g., the atmosphere and mantle). Therefore, more parameters should be taken into account in future modelling to constrain the exchange of N among these reservoirs through geological history.

Bibliography

References for Chapters 1 – 4 and Appendices A – F

Abers, G., Van Keken, P., Hacker, B. (2017) The cold and relatively dry nature of mantle forearcs in subduction zones. *Nat. Geosci* **10**, 333-337.

Abers, G.A. (2005) Seismic low-velocity layer at the top of subducting slabs: observations, predictions, and systematics. *Phys. Earth Planet. Inter.* **149**, 7-29.

Agard, P., Goffé, B., Touret, J.L.R., Vidal, O. (2000) Retrograde mineral and fluid evolution in high-pressure metapelites (Schistes lustrés unit, Western Alps). *Contrib. to Mineral. Petrol.* **140**, 296-315.

Agrinier, P., Cannat, M. (1997) Oxygen isotope constraints on serpentinization processes in ultramafic rocks from the Mid-Atlantic Ridge (23°N). In *Proc. ODP, Sci. Results* (eds. Karson, J.A., Cannat, M., Miller, D.J., Elthon, D.), Ocean Drilling Program, College Station, TX. pp. 381–388.

Agrinier, P., Hékinian, R., Bideau, D., Javoy, M. (1995) O and H stable isotope compositions of oceanic crust and upper mantle rocks exposed in the Hess Deep near the Galapagos Triple Junction. *Earth Planet Sci. Lett.* **136**, 183-196.

Albers, E., Kahl, W.-A., Beyer, L., Bach, W. (2020) Variant across-forearc compositions of slab-fluids recorded by serpentinites: Implications on the mobilization of FMEs from an active subduction zone (Mariana forearc). *Lithos* **364-365**, 105525.

Alt, J.C. (1999) Very Low-Grade Hydrothermal Metamorphism of Basic Igneous Rocks. In *Low-Grade Metamorphism* (eds. Frey, M., Robinson, D.). Blackwell Science Ltd. pp. 169-201.

Alt, J.C., Bach, W. (2001) Data report: low-grade hydrothermal alteration of uplifted lower oceanic crust, Hole 735B: mineralogy and isotope geochemistry. In *Proc. ODP, Sci. Results* (eds. Natland, J.H., Dick, H.J.B., Miller, D.J., and Von Herzen, R.P. (Eds.)). College Station, TX (Ocean Drilling Program). pp. 1–24.

Alt, J.C., Bach, W. (2006) Oxygen isotope composition of a section of lower oceanic crust, ODP Hole 735B. *Geochem. Geophys. Geosyst.* **7**, Q12008.

Alt, J.C., Honnorez, J. (1984) Alteration of the upper oceanic crust, DSDP site 417: mineralogy and chemistry. *Contrib. to Miner. Petrol.* **87**, 149-169.

Alt, J.C., Laverne, C., Coggon, R.M., Teagle, D.A., Banerjee, N.R., Morgan, S., Smith-Duque, C.E., Harris, M., Galli, L. (2010) Subsurface structure of a submarine hydrothermal system in ocean crust formed at the East Pacific Rise, ODP/IODP Site 1256. *Geochem. Geophys. Geosyst.* **11**, Q10010.

Alt, J.C., Laverne, C., Vanko, D.A., Tartarotti, P., Teagle, D.A., Bach, W., Zuleger, E., Erzinger, J., Honnorez, I., Pezard, P.A. (1996) Hydrothermal alteration of a section of upper oceanic crust in the eastern equatorial Pacific: A synthesis of results from Site 504 (DSDP Legs 69, 70, and 83, and ODP Legs 111, 137, 140, and 148). In *Proc. ODP, Sci. Results* (eds. Alt, J.C., Kinoshita, H., Stokking, L.B., and Michael, P.J.), Ocean Drilling Program, College Station, TX. pp. 417-434.

Alt, J.C., Muehlenbachs, K., Honnorez, J. (1986) An oxygen isotopic profile through the upper kilometer of the oceanic crust, DSDP Hole 504B. *Earth Planet Sci. Lett.* **80**, 217-229.

Alt, J.C., Schwarzenbach, E.M., Früh-Green, G.L., Shanks III, W.C., Bernasconi, S.M., Garrido, C.J., Crispini, L., Gaggero, L., Padrón-Navarta, J.A., Marchesi, C. (2013) The role of serpentinites in cycling of carbon and sulfur: seafloor serpentinization and subduction metamorphism. *Lithos* **178**, 40-54.

Alt, J.C., Shanks, W.C. (2003) Serpentinization of abyssal peridotites from the MARK area, Mid-Atlantic Ridge: sulfur geochemistry and reaction modeling. *Geochim. Cosmochim. Acta* **67**, 641-653.

Alt, J.C., Shanks, W.C. (2006) Stable isotope compositions of serpentinite seamounts in the Mariana forearc: Serpentinization processes, fluid sources and sulfur metasomatism. *Earth Planet Sci. Lett.* **242**, 272-285.

Alt, J.C., Shanks, W.C. (2011) Microbial sulfate reduction and the sulfur budget for a complete section of altered oceanic basalts, IODP Hole 1256D (eastern Pacific). *Earth Planet. Sci. Lett.* **310**, 73-83.

Alt, J.C., Shanks, W.C., Bach, W., Paulick, H., Garrido, C.J., Beaudoin, G. (2007) Hydrothermal alteration and microbial sulfate reduction in peridotite and gabbro exposed by detachment faulting at the Mid-Atlantic Ridge, 15°20′N (ODP Leg 209): A sulfur and oxygen isotope study. *Geochem. Geophys. Geosyst.* **8**, Q08001.

Alt, J.C., Teagle, D.A. (1999) The uptake of carbon during alteration of ocean crust. *Geochim. Cosmochim. Acta* **63**, 1527-1535.

Anderson, R.N., Zoback, M.D., Hickman, S.H., Newmark, R.L. (1985) Permeability versus depth in the upper oceanic crust: In situ measurements in DSDP hole 504B, eastern equatorial Pacific. *J. Geophys. Res. Solid Earth* **90**, 3659-3669.

Bach, W., Alt, J.C., Niu, Y., Humphris, S.E., Erzinger, J., Dick, H.J. (2001) The geochemical consequences of late-stage low-grade alteration of lower ocean crust at the SW Indian Ridge: Results from ODP Hole 735B (Leg 176). *Geochim. Cosmochim. Acta* **65**, 3267-3287.

Bach, W., Edwards, K.J. (2003) Iron and sulfide oxidation within the basaltic ocean crust: implications for chemolithoautotrophic microbial biomass production. *Geochim. Cosmochim. Acta* **67**, 3871-3887.

Bach, W., Humphris, S.E. (1999) Relationship between the Sr and O isotope compositions of hydrothermal fluids and the spreading and magma-supply rates at oceanic spreading centers. *Geology* **27**, 1067-1070.

Bach, W., Klein, F., Menzies, C., Lucassen, F., Teagle, D. (2019) Fluid–rock interactions in the shallow Mariana forearc: carbon cycling and redox conditions. *Solid Earth discuss.* **10**, 907-930.

Bach, W., Peucker-Ehrenbrink, B., Hart, S.R., Blusztajn, J.S. (2003) Geochemistry of hydrothermally altered oceanic crust: DSDP/ODP Hole 504B – Implications for seawater-crust exchange budgets and Sr- and Pb-isotopic evolution of the mantle. *Geochem. Geophys. Geosyst.* **4(3)**, 8904.

Baines, A.G., Cheadle, M.J., John, B.E., Schwartz, J.J. (2008) The rate of oceanic detachment faulting at Atlantis Bank, SW Indian Ridge. *Earth Planet Sci. Lett.* **273**, 105-114.

Barry, P., de Moor, J., Giovannelli, D., Schrenk, M., Hummer, D., Lopez, T., Pratt, C., Segura, Y.A., Battaglia, A., Beaudry, P. (2019) Forearc carbon sink reduces long-term volatile recycling into the mantle. *Nature* **568**, 487.

Barry, P., Hilton, D. (2016) Release of subducted sedimentary nitrogen throughout Earth's mantle. *Geochem. Perspect. Lett.* **2**, 148-159.

Bebout, G.E. (1991) Field-Based Evidence for Devolatilization in Subduction Zones: Implications for Arc Magmatism. *Science* **251**, 413-416.

Bebout, G.E. (1997) Nitrogen isotope tracers of high-temperature fluid-rock interactions: Case study of the Catalina Schist, California. *Earth Planet Sci. Lett.* **151**, 77-90.

Bebout, G.E. (2007a) 3.20 - Trace Element and Isotopic Fluxes/Subducted Slab. In *Treatise on Geochemistry* (eds. Holland, H.D., Turekian, K.K.). Pergamon, Oxford. pp. 1-50.

Bebout, G.E. (2007b) Metamorphic chemical geodynamics of subduction zones. *Earth Planet Sci. Lett.* **260**, 373-393.

Bebout, G.E. (2013) Metasomatism in subduction zones of subducted oceanic slabs, mantle wedges, and the slab-mantle interface. In *Metasomatism and the Chemical Transformation of Rock*. Springer. pp. 289-349.

Bebout, G.E., Agard, P., Kobayashi, K., Moriguti, T., Nakamura, E. (2013a) Devolatilization history and trace element mobility in deeply subducted sedimentary rocks: Evidence from Western Alps HP/UHP suites. *Chem. Geol.* **342**, 1-20.

Bebout, G.E., Banerjee, N., Izawa, M., Kobayashi, K., Lazzeri, K., Ranieri, L., Nakamura, E. (2018) Nitrogen concentrations and isotopic compositions of seafloor-altered terrestrial basaltic glass: implications for astrobiology. *Astrobiology* **18**, 330-342.

Bebout, G.E., Fogel, M.L. (1992) Nitrogen-isotope compositions of metasedimentary rocks in the Catalina Schist, California: implications for metamorphic devolatilization history. *Geochim. Cosmochim. Acta* **56**, 2839-2849.

Bebout, G.E., Fogel, M.L., Cartigny, P. (2013b) Nitrogen: Highly volatile yet surprisingly compatible. *Elements* **9**, 333-338.

Bebout, G.E., Penniston-Dorland, S.C. (2016) Fluid and mass transfer at subduction interfaces—The field metamorphic record. *Lithos* **240-243**, 228-258.

Bebout, G.E., Ryan, J.G., Leeman, W.P., Bebout, A.E. (1999) Fractionation of trace elements by subduction-zone metamorphism – effect of convergent-margin thermal evolution. *Earth Planet Sci. Lett.* **171**, 63-81.

Becker, K., Sakai, H., Adamson, A., Alexandrovich, J., Alt, J., Anderson, R., Bideau, D., Gable, R., Herzig, P.M., Houghton, S. (1989) Drilling deep into young oceanic crust, Hole 504B, Costa Rica Rift. *Rev. Geophys.* **27**, 79-102.

Bekaert, D., Turner, S., Broadley, M., Barnes, J., Halldórsson, S., Labidi, J., Wade, J., Walowski, K., Barry, P. (2021) Subduction-Driven Volatile Recycling: A Global Mass Balance. *Annu. Rev. Earth Planet. Sci.* **49**, 2021.

Benton, L.D., Ryan, J.G., Savov, I.P. (2004) Lithium abundance and isotope systematics of forearc serpentinites, Conical Seamount, Mariana forearc: Insights into the mechanics of slab-mantle exchange during subduction. *Geochem. Geophys. Geosyst.* **5**, Q08J12.

Benton, L.D., Ryan, J.G., Tera, F. (2001) Boron isotope systematics of slab fluids as inferred from a serpentine seamount, Mariana forearc. *Earth Planet Sci. Lett.* **187**, 273-282.

Bloch, S., Bischoff, J.L. (1979) The effect of low-temperature alteration of basalt on the oceanic budget of potassium. *Geology* **7**, 193-196.

Bos, A., Duit, W., van der Eerden, A.M., Jansen, J.B.H. (1988) Nitrogen storage in biotite: An experimental study of the ammonium and potassium partitioning between 1M-phlogopite and vapour at 2 kb. *Geochim. Cosmochim. Acta* **52**, 1275-1283.

Bourbonnais, A., Lehmann, M.F., Butterfield, D.A., Juniper, S.K. (2012) Subseafloor nitrogen transformations in diffuse hydrothermal vent fluids of the Juan de Fuca Ridge evidenced by the isotopic composition of nitrate and ammonium. *Geochem. Geophys. Geosyst.* **13**, Q02T01.

Brady, P.V., Gíslason, S.R. (1997) Seafloor weathering controls on atmospheric CO 2 and global climate. *Geochim. Cosmochim. Acta* **61**, 965-973.

Brandes, J.A., Boctor, N.Z., Cody, G.D., Cooper, B.A., Hazen, R.M., Yoder Jr, H.S. (1998) Abiotic nitrogen reduction on the early Earth. *Nature* **395**, 365.

Breeding, C.M., Ague, J.J., Bröcker, M. (2004) Fluid – metasedimentary rock interactions in subduction-zone mélange: Implications for the chemical composition of arc magmas. *Geology* **32**, 1041-1044.

Busigny, V., Bebout, G.E. (2013) Nitrogen in the silicate Earth: Speciation and isotopic behavior during mineral–fluid interactions. *Elements* **9**, 353-358.

Busigny, V., Cartigny, P., Laverne, C., Teagle, D., Bonifacie, M., Agrinier, P. (2019) A re-assessment of the nitrogen geochemical behavior in upper oceanic crust from Hole 504B: Implications for subduction budget in Central America. *Earth Planet Sci. Lett.* **525**, 115735.

Busigny, V., Cartigny, P., Philippot, P. (2011) Nitrogen isotopes in ophiolitic metagabbros: A re-evaluation of modern nitrogen fluxes in subduction zones and implication for the early Earth atmosphere. *Geochim. Cosmochim. Acta* **75**, 7502-7521.

Busigny, V., Cartigny, P., Philippot, P., Ader, M., Javoy, M. (2003a) Massive recycling of nitrogen and other fluid-mobile elements (K, Rb, Cs, H) in a cold slab environment: evidence from

HP to UHP oceanic metasediments of the Schistes Lustrés nappe (western Alps, Europe). *Earth Planet Sci. Lett.* **215**, 27-42.

Busigny, V., Cartigny, P., Philippot, P., Javoy, M. (2003b) Nitrogen recycling in subduction zones: A strong geothermal control. *Geochim. Cosmochim. Acta* **67**, A51.

Busigny, V., Laverne, C., Bonifacie, M. (2005) Nitrogen content and isotopic composition of oceanic crust at a superfast spreading ridge: a profile in altered basalts from ODP Site 1256, Leg 206. *Geochem. Geophys. Geosyst.* **6**, Q12O01.

Cannaò, E., Tiepolo, M., Bebout, G., Scambelluri, M. (2020) Into the deep and beyond: Carbon and nitrogen subduction recycling in secondary peridotites. *Earth Planet Sci. Lett.* **543**, 116328.

Cannat, M. (1993) Emplacement of mantle rocks in the seafloor at mid-ocean ridges. *J. Geophys. Res: Solid Earth* **98**, 4163-4172.

Cannat, M. (1996) How thick is the magmatic crust at slow spreading oceanic ridges? *J. Geophys. Res.* **101**, 2847-2857.

Cannat, M., Mevel, C., Maia, M., Deplus, C., Durand, C., Gente, P., Agrinier, P., Belarouchi, A., Dubuisson, G., Humler, E. (1995) Thin crust, ultramafic exposures, and rugged faulting patterns at the Mid-Atlantic Ridge (22–24 N). *Geology* **23**, 49-52.

Carlson, R., Herrick, C. (1990a) Densities and porosities in the oceanic crust and their variations with depth and age. *J. Geophys. Res. Solid Earth* **95**, 9153-9170.

Carlson, R.L. (2011) The effect of hydrothermal alteration on the seismic structure of the upper oceanic crust: Evidence from Holes 504B and 1256D. *Geochem. Geophys. Geosyst.* **12**.

Carlson, R.L., Herrick, C.N. (1990b) Densities and porosities in the oceanic crust and their variations with depth and age. *J. Geophys. Res. Solid Earth* **95**, 9153-9170.

Castelain, T., 2011. Hydrothermal fluid flow through gabbros at IODP site 1309, Atlantis Massif, Mid-Atlantic Ridge. University of Leeds.

Chan, L.-H., Alt, J.C., Teagle, D.A.H. (2002) Lithium and lithium isotope profiles through the upper oceanic crust: a study of seawater–basalt exchange at ODP Sites 504B and 896A. *Earth Planet Sci. Lett.* **201**, 187-201.

Chen, Y.J. (1992) Oceanic crustal thickness versus spreading rate. *Geophys. Res. Lett.* **19**, 753-756.

Chen, Z., Schellart, W.P., Duarte, J.C., Strak, V. (2017) Topography of the Overriding Plate During Progressive Subduction: A Dynamic Model to Explain Forearc Subsidence. *Geophys. Res. Lett.* **44**, 9632-9643.

Clift, P. (2017) A revised budget for Cenozoic sedimentary carbon subduction. *Rev. Geophys.* **55**, 97-125.

Cogné, J.-P., Humler, E. (2004) Temporal variation of oceanic spreading and crustal production rates during the last 180 My. *Earth Planet Sci. Lett.* **227**, 427-439.

Coogan, L.A. (2014) 4.14 - The Lower Oceanic Crust,. In *Treatise on Geochemistry (Second Edition),* (eds. In Heinrich D. Holland, K.K.T.), Elsevier,. pp. 497-541.

Coogan, L.A., Gillis, K.M. (2013) Evidence that low-temperature oceanic hydrothermal systems play an important role in the silicate-carbonate weathering cycle and long-term climate regulation. *Geochem. Geophys. Geosyst.* **14**, 1771-1786.

Coogan, L.A., Gillis, K.M. (2018) Low-Temperature Alteration of the Seafloor: Impacts on Ocean Chemistry. *Annu. Rev. Earth Planet. Sci.* **46**, 21-45.

Coogan, L.A., Parrish, R.R., Roberts, N.M. (2016) Early hydrothermal carbon uptake by the upper oceanic crust: Insight from in situ U-Pb dating. *Geology* **44**, 147-150.

Dasgupta, R. (2013) Ingassing, storage, and outgassing of terrestrial carbon through geologic time. *Rev. Mineral. Geochem.* **75**, 183-229.

Dauphas, N., Marty, B. (1999) Heavy Nitrogen in Carbonatites of the Kola Peninsula: A Possible Signature of the Deep Mantle. *Science* **286**, 2488-2490.

de Moor, J.M., Fischer, T.P., Plank, T. (2022) Constraints on the sulfur subduction cycle in Central America from sulfur isotope compositions of volcanic gases. *Chem. Geol.* **588**, 120627.

Debret, B., Albers, E., Walter, B., Price, R., Barnes, J.D., Beunon, H., Facq, S., Gillikin, D.P., Mattielli, N., Williams, H. (2019) Shallow forearc mantle dynamics and geochemistry: New insights from IODP Expedition 366. *Lithos* **326-327**, 230-245.

deMartin, B.J., Sohn, R.A., Pablo Canales, J., Humphris, S.E. (2007) Kinematics and geometry of active detachment faulting beneath the Trans-Atlantic Geotraverse (TAG) hydrothermal field on the Mid-Atlantic Ridge. *Geology* **35**, 711-714.

Deschamps, F., Godard, M., Guillot, S., Hattori, K. (2013) Geochemistry of subduction zone serpentinites: A review. *Lithos* **178**, 96-127.

Dhuime, B., Hawkesworth, C.J., Cawood, P.A., Storey, C.D. (2012) A change in the geodynamics of continental growth 3 billion years ago. *Science* **335**, 1334-1336.

Dick, H.J., Lin, J., Schouten, H. (2003) An ultraslow-spreading class of ocean ridge. *Nature* **426**, 405-412.

Dick, H.J.B., Kvassnes, A.J.S., Robinson, P.T., MacLeod, C.J., Kinoshita, H. (2019) The Atlantis Bank Gabbro Massif, Southwest Indian Ridge. *Prog. Earth Planet. Sci.* **6**, 64.

Dick, H.J.B., Natland, J.H., Alt, J.C., Bach, W., Bideau, D., Gee, J.S., Haggas, S., Hertogen, J.G.H., Hirth, G., Holm, P.M., Ildefonse, B., Iturrino, G.J., John, B.E., Kelley, D.S., Kikawa, E., Kingdon, A., LeRoux, P.J., Maeda, J., Meyer, P.S., Miller, D.J., Naslund, H.R., Niu, Y.-L., Robinson, P.T., Snow, J., Stephen, R.A., Trimby, P.W., Worm, H.-U., Yoshinobu, A. (2000) A long in situ section of the lower ocean crust: results of ODP Leg 176 drilling at the Southwest Indian Ridge. *Earth Planet Sci. Lett.* **179**, 31-51.

Edmond, J.M., Measures, C., McDuff, R.E., Chan, L.H., Collier, R., Grant, B., Gordon, L.I., Corliss, J.B. (1979) Ridge crest hydrothermal activity and the balances of the major and minor elements in the ocean: The Galapagos data. *Earth Planet Sci. Lett.* **46**, 1-18.

Eiler, J.M., Farley, K.A., Valley, J.W., Hauri, E., Craig, H., Hart, S.R., Stolper, E.M. (1997) Oxygen isotope variations in ocean island basalt phenocrysts. *Geochim. Cosmochim. Acta* **61**, 2281-2293.

Eiler, J.M., Schiano, P., Kitchen, N., Stolper, E.M. (2000) Oxygen-isotope evidence for recycled crust in the sources of mid-ocean-ridge basalts. *Nature* **403**, 530-534.

Elkins, L.J., Fischer, T.P., Hilton, D.R., Sharp, Z.D., McKnight, S., Walker, J. (2006) Tracing nitrogen in volcanic and geothermal volatiles from the Nicaraguan volcanic front. *Geochim. Cosmochim. Acta* **70**, 5215-5235.

Exley, R.A., Boyd, S.R., Mattey, D.P., Pillinger, C.T. (1987) Nitrogen isotope geochemistry of basaltic glasses: implications for mantle degassing and structure? *Earth Planet Sci. Lett.* **81**, 163-174.

Expedition 304/305 Scientists. (2006a) Expedition 304/305 summary. In *Proc. IODP* (eds. In Blackman, D.K., Ildefonse, B., John, B.E., Ohara, Y., Miller, D.J., MacLeod, C.J., and the Expedition 304/305 Scientists), College Station TX (Integrated Ocean Drilling Program Management International, Inc.).

Expedition 304/305 Scientists. (2006b) Site U1309. In *Proc. IODP* (eds. In Blackman, D.K., Ildefonse, B., John, B.E., Ohara, Y., Miller, D.J., MacLeod, C.J., and the Expedition 304/305 Scientists), college Station TX (Integrated Ocean Drilling Program Management International, Inc.). pp. 1-60.

Expedition 309/312 Scientists. (2006) Site 1256. In *Proc. IODP* (eds. Teagle, D.A.H., Alt, J.C., Umino, S., Miyashita, S., Banerjee, N.R., Wilson, D.S., and the Expedition 309/312 Scientists.), Integrated Ocean Drilling Program Management International, Inc. Washington, DC. pp. 1–549. pp. 1-509.

Expedition 335 Scientists. (2012) Deep drilling of intact ocean crust: harnessing past lessons to inform future endeavors. . In *Proc. IODP,* (eds. In Teagle, D.A.H., Ildefonse, B., Blum, P., and the Expedition 335 Scientists, Expedition 304/305), Tokyo (Integrated Ocean Drilling Program Management International, Inc.). pp. 1-45.

Faak, K., Gillis, K.M. (2016) Slow cooling of the lowermost oceanic crust at the fast-spreading East Pacific Rise. *Geology* **44**, 115-118.

Fischer, T.P., Arellano, S., Carn, S., Aiuppa, A., Galle, B., Allard, P., Lopez, T., Shinohara, H., Kelly, P., Werner, C. (2019) The emissions of CO_2 and other volatiles from the world's subaerial volcanoes. *Sci. Rep.* **9**, 1-11.

Fischer, T.P., Hilton, D.R., Zimmer, M.M., Shaw, A.M., Sharp, Z.D., Walker, J.A. (2002) Subduction and recycling of nitrogen along the Central American margin. *Science* **297**, 1154-1157.

Fischer, T.P., Takahata, N., Sano, Y., Sumino, H., Hilton, D.R. (2005) Nitrogen isotopes of the mantle: Insights from mineral separates. *Geophys. Res. Lett.* **32**, L110305.

Fisher, A.T. (1998) Permeability within basaltic oceanic crust. *Rev. Geophys.* **36**, 143-182.

Freundt, A., Grevemeyer, I., Rabbel, W., Hansteen, T.H., Hensen, C., Wehrmann, H., Kutterolf, S., Halama, R., Frische, M. (2014) Volatile (H_2O, CO_2, Cl, S) budget of the Central American subduction zone. *Int. J. Earth Sci* **103**, 2101-2127.

Früh-Green, G.L., Plas, A., Lécuyer, C. (1996) Petrologic and stable isotope constraints on hydrothermal alteration and serpentinization of the EPR shallow mantle at Hess Deep (Site 895). In *Proc. ODP, Sci. Results* (eds. Mével, C., Gillis, K.M., Allan, J.F., and Meyer, P.S. (Eds.)), College Station, TX (Ocean Drilling Program). pp. 255–291.

Fryer, P. (1992) A synthesis of Leg 125 drilling of serpentine seamounts on the Mariana and Izu-Bonin forearcs. In *Proc. ODP, Sci. Results* (eds. Fryer, P., Pearce, J.A., Stokking, L.B., et al.,), College Station, TX (Ocean Drilling Program). pp. 593–614.

Fryer, P. (1996) Evolution of the Mariana Convergent Plate Margin System. *Rev. Geophys.* **34**, 89-125.

Fryer, P. (2012) Serpentinite mud volcanism: observations, processes, and implications. Ann. Rev. Mar. Sci. **4**, 345-373.

Fryer, P., Wheat, C.G., Williams, T., Kelley, C., Johnson, K., Ryan, J., Kurz, W., Shervais, J., Albers, E., Bekins, B., Debret, B., Deng, J., Dong, Y., Eickenbusch, P., Frery, E., Ichiyama, Y., Johnston, R., Kevorkian, R., Magalhaes, V., Mantovanelli, S., Menapace, W., Menzies, C., Michibayashi, K., Moyer, C., Mullane, K., Park, J.-W., Price, R., Sissmann, O., Suzuki, S., Takai, K., Walter, B., Zhang, R., Amon, D., Glickson, D., Pomponi, S. (2020) Mariana serpentinite mud volcanism exhumes subducted seamount materials: implications for the origin of life. *Philosophical Transactions of the Royal Society A: Mathematical, Physical and Engineering Sciences* **378**, 20180425.

Fryer, P., Wheat, C.G., Williams, T., Albers, E. Bekins, B., Debret, B.P.R., Deng, J., Dong, Y., Eickenbusch, P., Frery, E.A., Ichiyama, Y., Johnson, K., Johnston, R.M., Kevorkian, R.T., Kurz, W., , Magalhaes, V., Mantovanelli, S.S., Menapace, W., Menzies, C.D., Michibayashi, K., Moyer, C.L., Mullane, K.K., Park, J.-W., Price, R.E., Ryan, J.G., Shervais, J.W., Sissmann, O.J., Suzuki, S., , Takai, K., Walter, B., and Zhang, R. (2018a) Expedition 366 summary. In *Mariana Convergent Margin and South Chamorro Seamount. Proceedings of the International Ocean Discovery Program* (eds. Fryer, P., Wheat, C.G., Williams, T., and the Expedition 366 Scientists), College Station, TX (International Ocean Discovery Program). pp. 1-23.

Fryer, P., Wheat, C.G., Williams, T., Albers, E., Bekins, B., Debret, B.P.R., Deng, J., Dong, Y., Eickenbusch, P., Frery, E.A., Ichiyama, Y., Johnson, K., Johnston, R.M., Kevorkian, R.T., Kurz, W., , Magalhaes, V., Mantovanelli, S.S., Menapace, W., Menzies, C.D., Michibayashi, K., Moyer, C.L., Mullane, K.K., Park, J.-W., Price, R.E., Ryan, J.G., Shervais, J.W., Sissmann, O.J., Suzuki, S., , Takai, K., Walter, B., and Zhang, R. (2018b) Site 1498. In *Mariana Convergent Margin and South Chamorro Seamount. Proceedings of the International Ocean Discovery Program* (eds. Fryer, P., Wheat, C.G., Williams, T., and the

Expedition 366 Scientists), College Station, TX (International Ocean Discovery Program). pp. 1-35.

Fullerton, K.M., Schrenk, M.O., Yücel, M., Manini, E., Basili, M., Rogers, T.J., Fattorini, D., Di Carlo, M., d'Errico, G., Regoli, F., Nakagawa, M., Vetriani, C., Smedile, F., Ramírez, C., Miller, H., Morrison, S.M., Buongiorno, J., Jessen, G.L., Steen, A.D., Martínez, M., de Moor, J.M., Barry, P.H., Giovannelli, D., Lloyd, K.G. (2021) Effect of tectonic processes on biosphere–geosphere feedbacks across a convergent margin. *Nat. Geosci.* **14**, 301-306.

Füri, E., Portnyagin, M., Mironov, N., Deligny, C., Gurenko, A., Botcharnikov, R., Holtz, F. (2021) In situ quantification of the nitrogen content of olivine-hosted melt inclusions from Klyuchevskoy volcano (Kamchatka): Implications for nitrogen recycling at subduction zones. *Chem. Geol.* **582**, 120456.

Furnes, H., McLoughlin, N., Muehlenbachs, K., Banerjee, N., Staudigel, H., Dilek, Y., de Wit, M., Van Kranendonk, M., Schiffman, P. (2008) Oceanic pillow lavas and hyaloclastites as habitats for microbial life through time – A Review. In *Links Between Geological Processes, Microbial Activities&Evolution of Life: Microbes and Geology* (eds. Dilek, Y., Furnes, H., Muehlenbachs, K.). Springer Netherlands, Dordrecht. pp. 1-68.

Furnes, H., Muehlenbachs, K., Tumyr, O., Torsvik, T., Thorseth, I.H. (1999) Depth of active bio-alteration in the ocean crust: Costa Rica Rift (Hole 504B). *Terra Nova-Oxford* **11**, 228.

Furnes, H., Staudigel, H. (1999) Biological mediation in ocean crust alteration: how deep is the deep biosphere? *Earth Planet Sci. Lett.* **166**, 97-103.

Gale, A., Dalton, C.A., Langmuir, C.H., Su, Y., Schilling, J.G. (2013) The mean composition of ocean ridge basalts. *Geochem. Geophys. Geosyst.* **14**, 489-518.

Galvez, M.E., Pubellier, M. (2019) How do subduction zones regulate the carbon cycle? In *Deep carbon: Past to present*. Cambridge University Press. pp. 276-312.

Gao, Y., Vils, F., Cooper, K., Banerjee, N., Harris, M., Hoefs, J., Teagle, D., Casey, J., Elliott, T., Laverne, C. (2012) Downhole variation of lithium and oxygen isotopic compositions of oceanic crust at East Pacific Rise, ODP Site 1256. *Geochem. Geophys. Geosyst.* **13**, Q10001.

Ge, M.H., Zhang, J.J., Li, L., Liu, K., Ling, Y.Y., Wang, J.M., Wang, M. (2017) Geochronology and geochemistry of the Heilongjiang Complex and the granitoids from the Lesser Xing'an-Zhangguangcai Range: Implications for the late Paleozoic-Mesozoic tectonics of eastern NE China. *Tectonophysics* **717**, 565-584.

Ge, M.H., Zhang, J.J., Liu, K., Ling, Y.Y., Wang, M., Wang, J.M. (2016) Geochemistry and geochronology of the blueschist in the Heilongjiang Complex and its implications in the late Paleozoic tectonics of eastern NE China. *Lithos* **261**, 232-249.

Geilert, S., Albers, E., Frick, D.A., Hansen, C.T., von Blanckenburg, F. (2021) Systematic changes in serpentine Si isotope signatures across the Mariana forearc – a new proxy for slab dehydration processes. *Earth Planet Sci. Lett.* **575**, 117193.

Geldmacher, J., Höfig, T.W., Hauff, F., Hoernle, K., Garbe-Schönberg, D., Wilson, D.S. (2013) Influence of the Galápagos hotspot on the East Pacific Rise during Miocene superfast spreading. *Geology* **41**, 183-186.

Gilbert, L.A., Bona, M.L. (2016) Permeability of oceanic crustal rock samples from IODP Hole 1256D. *Geochem. Geophys. Geosyst.* **17**, 3825-3832.

Gillis, K., Coogan, L. (2011) Secular variation in carbon uptake into the ocean crust. *Earth Planet Sci. Lett.* **302**, 385-392.

Gillis, K.M., Coogan, L.A., Brant, C. (2015) The role of sedimentation history and lithology on fluid flow and reactions in off-axis hydrothermal systems: A perspective from the Troodos ophiolite. *Chem. Geol.* **414**, 84-94.

Gillis, K.M., Snow, J.E., Klaus, A., Abe, N., Adrião, Á.B., Akizawa, N., Ceuleneer, G., Cheadle, M.J., Faak, K., Falloon, T.J., Friedman, S.A., Godard, M., Guerin, G., Harigane, Y., Horst, A.J., Hoshide, T., Ildefonse, B., Jean, M.M., John, B.E., Koepke, J., Machi, S., Maeda, J., Marks, N.E., McCaig, A.M., Meyer, R., Morris, A., Nozaka, T., Python, M., Saha, A., Wintsch, R.P. (2014a) Primitive layered gabbros from fast-spreading lower oceanic crust. *Nature* **505**, 204-207.

Gillis, K.M., Snow, J.E., Klaus, A., Guerin, G., Abe, N., Akizawa, N., Ceuleneer, G., Cheadle, M.J., Adrião, Á. (2014b) Expedition 345 summary. In *Proc. IODP* (eds. In Gillis, K.M., Snow, J.E., Klaus, A., and the Expedition 345 Scientists), College Station, TX (Integrated Ocean Drilling Program). pp. 1-49.

Gillis, K.M., Snow, J.E., Klaus, A., Guerin, G., Abe, N., Akizawa, N., Ceuleneer, G., Cheadle, M.J., Adrião, Á., Faak, K. (2014c) Hole U1415P. In *Proc. IODP* (eds. In Gillis, K.M., Snow, J.E., Klaus, A., and the Expedition 345 Scientists), College Station, TX (Integrated Ocean Drilling Program). pp. 1-106.

Gillis, K.M., Thompson, G., Kelley, D.S. (1993) A view of the lower crustal component of hydrothermal systems at the Mid-Atlantic Ridge. *J. Geophys. Res. Solid* **98**, 19597-19619.

Grady, M.M., Wright, I.P. (2003) Elemental and Isotopic Abundances of Carbon and Nitrogen in Meteorites. *Space Sci. Rev* **106**, 231-248.

Grevemeyer, I., Ranero, C.R., Flueh, E.R., Kläschen, D., Bialas, J. (2007) Passive and active seismological study of bending-related faulting and mantle serpentinization at the Middle America trench. *Earth Planet Sci. Lett.* **258**, 528-542.

Grimes, C.B., John, B.E., Cheadle, M.J., Wooden, J.L. (2008) Protracted construction of gabbroic crust at a slow spreading ridge: Constraints from ^{206}Pb/^{238}U zircon ages from Atlantis Massif and IODP Hole U1309D (30˚ N, MAR). *Geochem. Geophys. Geosyst.* **9**, Q08012.

Gruber, N. (2008) The marine nitrogen cycle: overview and challenges. *Nitrogen in the marine environment* **2**, 1-50.

Gudbrandsson, S., Wolff-Boenisch, D., Gislason, S.R., Oelkers, E.H. (2011) An experimental study of crystalline basalt dissolution from 2- pH$\leqslant$ 11 and temperatures from 5 to 75°C. *Geochim. Cosmochim. Acta* **75**, 5496-5509.

Guerin, G., Becker, K., Gable, R., Pezard, P.A. (1996) Temperature measurements and heat-flow analysis in Hole 504B. In *Proc. ODP, Sci. Results* (eds. Alt, J.C., Kinoshita, H., Stokking, L.B., and Michael, P.J.), Ocean Drilling Program, College Station, TX. pp. 291–296.

Guerin, G., Goldberg, D.S., Iturrino, G.J. (2008) Velocity and attenuation in young oceanic crust: New downhole log results from DSDP/ODP/IODP Holes 504B and 1256D. *Geochem. Geophys. Geosyst.* **9**, Q12014.

Hacker, B.R. (2008) H2O subduction beyond arcs. *Geochemistry, Geophysics, Geosystems* **9**.

Haendel, D., Mühle, K., Nitzsche, H.-M., Stiehl, G., Wand, U. (1986) Isotopic variations of the fixed nitrogen in metamorphic rocks. *Geochim. Cosmochim. Acta* **50**, 749-758.

Halama, R., Bebout, G. (2021) Earth's Nitrogen and Carbon Cycles. *Space Sci. Rev* **217**, 45.

Halama, R., Bebout, G.E., John, T., Scambelluri, M. (2014) Nitrogen recycling in subducted mantle rocks and implications for the global nitrogen cycle. *Int. J. Earth Sci.* **103**, 2081-2099.

Halama, R., Bebout, G.E., John, T., Schenk, V. (2010) Nitrogen recycling in subducted oceanic lithosphere: the record in high-and ultrahigh-pressure metabasaltic rocks. *Geochim. Cosmochim. Acta* **74**, 1636-1652.

Halama, R., Bebout, G.E., Marschall, H.R., John, T. (2017) Fluid-induced breakdown of white mica controls nitrogen transfer during fluid–rock interaction in subduction zones. *Int. Geol. Rev.* **59**, 702-720.

Hall, A. (1989) Ammonium in spilitized basalts of southwest England and its implications for the recycling of nitrogen. *Geochem. J.* **23**, 19-23.

Halldórsson, S.A., Hilton, D.R., Barry, P.H., Füri, E., Grönvold, K. (2016) Recycling of crustal material by the Iceland mantle plume: New evidence from nitrogen elemental and isotope systematics of subglacial basalts. *Geochim. Cosmochim. Acta* **176**, 206-226.

Haraguchi, S., Ishii, T. (2006) Data report: petrological and geochemical features of igneous basement at Site 1224. In *Proc. ODP, Sci. Results* (eds. In Kasahara, J., Stephen, R.A., Acton, G.D., and Frey, F.A.), College Station, TX (Ocean Drilling Program). pp. 1-19.

Harris, B.J.R., de Hoog, J.C.M., Halama, R. (2022) The behaviour of nitrogen during subduction of oceanic crust: Insights from in situ SIMS analyses of high-pressure rocks. *Geochim. Cosmochim. Acta* **321**, 16-34.

Harris, M., Coggon, R.M., Smith-Duque, C.E., Cooper, M.J., Milton, J.A., Teagle, D.A. (2015) Channelling of hydrothermal fluids during the accretion and evolution of the upper oceanic crust: Sr isotope evidence from ODP Hole 1256D. *Earth Planet Sci. Lett.* **416**, 56-66.

Harris, M., Coggon, R.M., Wood, M., Smith-Duque, C.E., Henstock, T.J., Teagle, D.A.H. (2017) Hydrothermal cooling of the ocean crust: Insights from ODP Hole 1256D. *Earth Planet Sci. Lett.* **462**, 110-121.

Harris, R.N., Sakaguchi, A., Petronotis, K., Baxter, A.T., Berg, R., Burkett, A., Charpentier, D., Choi, J., Diz Ferreiro, P., Hamahashi, M., Hashimoto, Y., Heydolph, K., Jovane, L., Kastner, M., Kurz, W., Kutterolf, S.O., Li, Y., Malinverno, A., Martin, K.M., Millan, C., Nascimento, D.B., Saito, S., Sandoval Gutierrez, M.I., Screaton, E.J., Smith-Duque, C.E., Solomon, E.A., Straub, S.M., Tanikawa, W., Torres, M.E., Uchimura, H., Vannucchi, P., Yamamoto, Y., Yan, Q., and Zhao, X.,. (2013a) Input Site U1414. In *Proc IODP,* (In Harris, R.N., Sakaguchi, A., Petronotis, K., and the Expedition 344 Scientists eds.), College Station, TX (Integrated Ocean Drilling Program). pp. 1-87.

Harris, R.N., Sakaguchi, A., Petronotis, K., Baxter, A.T., Berg, R., Burkett, A., Charpentier, D., Choi, J., Diz Ferreiro, P., Hamahashi, M., Hashimoto, Y., Heydolph, K., Jovane, L., Kastner, M., Kurz, W., Kutterolf, S.O., Li, Y., Malinverno, A., Martin, K.M., Millan, C., Nascimento, D.B., Saito, S., Sandoval Gutierrez, M.I., Screaton, E.J., Smith-Duque, C.E., Solomon, E.A., Straub, S.M., Tanikawa, W., Torres, M.E., Uchimura, H., Vannucchi, P., Yamamoto, Y., Yan, Q., and Zhao, X., . (2013b) Input Site U1381. In *Proc. IODP,* (In Harris, R.N., Sakaguchi, A., Petronotis, K., and the Expedition 344 Scientists eds.), College Station, TX (Integrated Ocean Drilling Program). pp. 1-59.

Hattori, K.H., Guillot, S. (2007) Geochemical character of serpentinites associated with high- to ultrahigh-pressure metamorphic rocks in the Alps, Cuba, and the Himalayas: Recycling of elements in subduction zones. *Geochem. Geophys. Geosyst.* **8**, Q09010.

Hayman, N.W., Rioux, M., Anma, R., Tani, K., Dunkley, D.J., Crowley, J., Schmitz, M. (2019) Accretion and oxidation of a superfast-spread axial melt lens: TIMS and SIMS zircon analyses of the IODP Hole 1256D gabbros. *Lithos* **348-349**, 105184.

Hilton, D.R., Fischer, T.P., Marty, B. (2002) Noble gases and volatile recycling at subduction zones. *Rev. Mineral. Geochem.* **47**, 319-370.

Honma, H., Itihara, Y. (1981) Distribution of ammonium in minerals of metamorphic and granitic rocks. *Geochim. Cosmochim. Acta* **45**, 983-988.

Hopson, C.A., Coleman, R.G., Gregory, R.T., Pallister, J.S., Bailey, E.H. (1981) Geologic section through the Samail Ophiolite and associated rocks along a Muscat-Ibra Transect, southeastern Oman Mountains. *J. Geophys. Res. Solid* **86**, 2527-2544.

Hulme, S.M., Wheat, C.G., Fryer, P., Mottl, M.J. (2010) Pore water chemistry of the Mariana serpentinite mud volcanoes: A window to the seismogenic zone. *Geochem. Geophys. Geosyst.* **11**, Q01X09.

Humphris, S.E., Thompson, G. (1978) Hydrothermal alteration of oceanic basalts by seawater. *Geochim. Cosmochim. Acta* **42**, 107-125.

Humphris, S.E., Thompson, R.N., Marriner, G.F. (1980) The Mineralogy and Geochemistry of Basalt Weathering, Holes 417A and 418A. In *Initial Reports of the Deep Sea Drilling Project,* (eds. In Donnelly, T., Francheteau, J., Bryan, W., Robinson, P., Flower, M., Salisbury, M., et al.,), Washington (U.S. Government Printing Office),. pp. 1201-1217.

Hussain, S.A., Demirci, Ş., Özbayoğlu, G. (1996) Zeta Potential Measurements on Three Clays from Turkey and Effects of Clays on Coal Flotation. *J. Colloid Interface Sci.* **184**, 535-541.

Hyndman, R.D., Peacock, S.M. (2003) Serpentinization of the forearc mantle. *Earth and Planetary Science Letters* **212**, 417-432.

Ichiyama, Y., Tsujimori, T., Fryer, P., Michibayashi, K., Tamura, A., Morishita, T. (2021) Temporal and spatial mineralogical changes in clasts from Mariana serpentinite mud volcanoes: Cooling of the hot forearc-mantle at subduction initiation. *Lithos* **384-385**, 105941.

Ildefonse, B., Blackman, D., John, B., Ohara, Y., Miller, D., MacLeod, C.J. (2007) Oceanic core complexes and crustal accretion at slow-spreading ridges. *Geology* **35**, 623-626.

Inguaggiato, S., Taran, Y., Grassa, F., Capasso, G., Favara, R., Varley, N., Faber, E. (2004) Nitrogen isotopes in thermal fluids of a forearc region (Jalisco Block, Mexico): Evidence for heavy nitrogen from continental crust. *Geochemistry, Geophysics, Geosystems* **5**.

Ishizuka, O., Tani, K., Reagan, M.K., Kanayama, K., Umino, S., Harigane, Y., Sakamoto, I., Miyajima, Y., Yuasa, M., Dunkley, D.J. (2011) The timescales of subduction initiation and subsequent evolution of an oceanic island arc. *Earth Planet Sci. Lett.* **306**, 229-240.

Jackson, C.R., Cottrell, E., Andrews, B. (2021) Warm and oxidizing slabs limit ingassing efficiency of nitrogen to the mantle. *Earth Planet Sci. Lett.* **553**, 116615.

Jahn, B.M. (2004) The Central Asian Orogenic Belt and growth of the continental crust in the Phanerozoic. *Geol. Soc. Spec. Publ.* **226**, 73-100.

Jarrard, R.D. (2003) Subduction fluxes of water, carbon dioxide, chlorine, and potassium. *Geochem. Geophys. Geosyst.* **4**, 1-21.

Jarrard, R.D., Abrams, L.J., Pockalny, R., Larson, R.L., Hirono, T. (2003) Physical properties of upper oceanic crust: Ocean Drilling Program Hole 801C and the waning of hydrothermal circulation. *J. Geophys. Res. Solid* **108(B4)**, 2188.

Javoy, M. (1997) The major volatile elements of the Earth: Their origin, behavior, and fate. *Geophys. Res. Lett.* **24**, 177-180.

Javoy, M. (1998) The birth of the Earth's atmosphere: the behaviour and fate of its major elements. *Chem. Geol.* **147**, 11-25.

Javoy, M., Pineau, F. (1991) The volatiles record of a “popping” rock from the Mid-Atlantic Ridge at ^{14}N: chemical and isotopic composition of gas trapped in the vesicles. *Earth Planet Sci. Lett.* **107**, 598-611.

Jia, Y. (2006) Nitrogen isotope fractionations during progressive metamorphism: A case study from the Paleozoic Cooma metasedimentary complex, southeastern Australia. *Geochim. Cosmochim. Acta* **70**, 5201-5214.

Jo, J., Yamanaka, T., Kashimura, T., Okunishi, Y., Kuwahara, Y., Kadota, I., Miyoshi, Y., Ishibashi, J.-i., Chiba, H. (2018) Mineral nitrogen isotope signature in clay minerals formed under high ammonium environment conditions in sediment associated with ammonium-rich sediment-hosted hydrothermal system. *Geochem. J.* **52**, 317-333.

John, T., Scherer, E.E., Haase, K., Schenk, V. (2004) Trace element fractionation during fluid-induced eclogitization in a subducting slab: trace element and Lu–Hf–Sm–Nd isotope systematics. *Earth Planet Sci. Lett.* **227**, 441-456.

Johnson, B., Goldblatt, C. (2015) The nitrogen budget of Earth. *Earth-Sci. Rev.* **148**, 150-173.

Johnson, B.W., Goldblatt, C. (2018) EarthN: A New Earth System Nitrogen Model. *Geochem. Geophys. Geosyst.* **19**, 2516-2542.

Johnston, R.M., 2019. Fluid-mobile Trace Element Variability of Serpentinites and Entrained Crustal Rocks across the Mariana Forearc System. University of South Florida.

Jöns, N., Bach, W., Rosner, M., Plessen, B., 2013. Formation of late-stage mineral veins in the footwall of an oceanic detachment fault (ODP Leg 304/305), Geophys. Res. Abstr.

Kagoshima, T., Sano, Y., Takahata, N., Maruoka, T., Fischer, T.P., Hattori, K. (2015) Sulphur geodynamic cycle. *Sci. Rep.* **5**, 8330.

Karson, J.A., Lawrence, R.M. (1997) Tetonic setting of serpentinite exposures on the western median valley wall of the MARK area in the vicinity of Site 920. In *Proc. ODP, Sci. Results* (eds. Karson, J.A., Cannat, M., Miller, D.J., Elthon, D.), Ocean Drilling Program, College Station, TX. pp. 47-559.

Kawahata, H., Nohara, M., Ishizuka, H., Hasebe, S., Chiba, H. (2001) Sr isotope geochemistry and hydrothermal alteration of the Oman ophiolite. *J. Geophys. Res. Solid* **106**, 11083-11099.

Kelemen, P.B., Manning, C.E. (2015) Reevaluating carbon fluxes in subduction zones, what goes down, mostly comes up. *Proc. Natl. Acad. Sci. U.S.A.* **112**, E3997-E4006.

Kelley, K.A., Plank, T., Ludden, J., Staudigel, H. (2003) Composition of altered oceanic crust at ODP Sites 801 and 1149. *Geochem. Geophys. Geosyst.* **4(6)**, 8910.

Kendrick, M.A. (2019) Halogens in altered ocean crust from the East Pacific Rise (ODP/IODP Hole 1256D). *Geochim. Cosmochim. Acta* **261**, 93-112.

Kendrick, M.A., Hémond, C., Kamenetsky, V.S., Danyushevsky, L., Devey, C.W., Rodemann, T., Jackson, M.G., Perfit, M.R. (2017) Seawater cycled throughout Earth's mantle in partially serpentinized lithosphere. *Nat. Geosci.* **10**, 222-228.

Kendrick, M.A., Honda, M., Pettke, T., Scambelluri, M., Phillips, D., Giuliani, A. (2013) Subduction zone fluxes of halogens and noble gases in seafloor and forearc serpentinites. *Earth Planet Sci. Lett.* **365**, 86-96.

Kendrick, M.A., Scambelluri, M., Honda, M., Phillips, D. (2011) High abundances of noble gas and chlorine delivered to the mantle by serpentinite subduction. *Nat. Geosci.* **4**, 807-812.

Knoll, A.H., Canfield, D.E., Konhauser, K., 2012. Fundamentals of geobiology. Wiley Online Library.

Krantz, J.A., Parman, S.W., Kelley, S.P. (2019) Recycling of heavy noble gases by subduction of serpentinite. *Earth Planet Sci. Lett.* **521**, 120-127.

Labidi, J., Barry, P.H., Bekaert, D.V., Broadley, M.W., Marty, B., Giunta, T., Warr, O., Sherwood Lollar, B., Fischer, T.P., Avice, G., Caracausi, A., Ballentine, C.J., Halldórsson, S.A., Stefánsson, A., Kurz, M.D., Kohl, I.E., Young, E.D. (2020) Hydrothermal 15N15N abundances constrain the origins of mantle nitrogen. *Nature* **580**, 367-371.

Labidi, J., Young, E.D. (2022) The origin and dynamics of nitrogen in the Earth's mantle constrained by 15N15N in hydrothermal gases. *Chem. Geol.* **591**, 120709.

Labidi, J., Young, E.D., Fischer, T.P., Barry, P.H., Ballentine, C.J., de Moor, J.M. (2021) Recycling of nitrogen and light noble gases in the Central American subduction zone: Constraints from $^{15}N^{15}N$. *Earth Planet Sci. Lett.* **571**, 117112.

Lafay, R., Montes-Hernandez, G., Janots, E., Munoz, M., Auzende, A.L., Gehin, A., Chiriac, R., Proux, O. (2016) Experimental investigation of As, Sb and Cs behavior during olivine serpentinization in hydrothermal alkaline systems. *Geochim. Cosmochim. Acta* **179**, 177-202.

Laureijs, C.T., Coogan, L.A., Spence, J. (2021a) In-situ Rb-Sr dating of celadonite from altered upper oceanic crust using laser ablation ICP-MS/MS. *Chem. Geol.* **579**, 120339.

Laureijs, C.T., Coogan, L.A., Spence, J. (2021b) Regionally variable timing and duration of celadonite formation in the Troodos lavas (Cyprus) from Rb-Sr age distributions. *Chem. Geol.* **560**, 119995.

Laurora, A., Brigatti, M.F., Malferrari, D., Galli, E., Rossi, A., Ferrari, M. (2011) The crystal chemistry of lizardite-1T from Northern Apennines ophiolites near Modena, Italy. *Canad Mineral* **49**, 1045-1054.

Laverne, C., Agrinier, P., Hermitte, C.D., Bohn, M. (2001) Chemical fluxes during hydrothermal alteration of a 1200-m long section of dikes in the oceanic crust, DSDPrODP Hole 504B. *Chem. Geol.* **181**, 73-98.

Lee, H., Fischer, T.P., de Moor, J.M., Sharp, Z.D., Takahata, N., Sano, Y. (2017) Nitrogen recycling at the Costa Rican subduction zone: The role of incoming plate structure. *Sci. Rep.* **7**, 1-10.

Li, G.Y., Zhou, J.B., Li, L. (2021e) A new tectonic framework for the composite orogenic metallogenic systems in the east of North China: The role of the Heilongjiang Ocean in the Late Paleozoic to Mesozoic. *Ore Geol. Rev.* **136**, 104293.

Li, J., Chen, B., Mookherjee, M., Morard, G., 2019a. Carbon versus other light elements in Earth's core. Cambridge University Press.

Li, J., Niu, B., Song, B., Xu, W., Zhang, Y., Zhao, Z. (1999) Crustal formation and evolution of northern Changbai Mountains, northeast China. *Geological Publishing House, Beijing (in Chinese with English abstract)* 1-137.

Li, J.Y. (2006) Permian geodynamic setting of Northeast China and adjacent regions: closure of the Paleo-Asian Ocean and subduction of the Paleo-Pacific Plate. *J. Asian Earth Sci.* **26**, 207-224.

Li, K., Li, G.-Y., Du, Y.-F., Han, W., Zhang, J., Chen, L.-H., Zhou, J.-B., Li, L. (2021c) Intraslab remobilization of nitrogen during early subduction facilitates deep nitrogen recycling: Insights from the blueschists in the Heilongjiang Complex in NE China. *Chem. Geol.* **583**, 120474.

Li, K., Li, L., Aubaud, C., Muehlenbachs, K. (2020) Efficient Carbon Recycling at the Central-Northern Lesser Antilles Arc: Implications to deep carbon recycling in global subduction zones. *Geophys. Res. Lett. 47, e2020GL086950.*

Li, K., Li, L., Pearson, D.G., Stachel, T. (2019b) Diamond isotope compositions indicate altered igneous oceanic crust dominates deep carbon recycling. *Earth Planet Sci. Lett.* **516**, 190-201.

Li, K., Li, L., 2022. Nitrogen enrichments in sheeted dikes and gabbros from DSDP/ODP/IODP Hole 504B and 1256D: Insights into nitrogen recycling in Central America and global subduction zones. *Geochim. Cosmochim. Acta* 335, 197-210.

Li, L., Bebout, G.E. (2005) Carbon and nitrogen geochemistry of sediments in the Central American convergent margin: insights regarding subduction input fluxes, diagenesis, and paleoproductivity. *J. Geophys. Res: Solid Earth* **110**.

Li, L., Bebout, G.E., Idleman, B.D. (2007) Nitrogen concentration and δ^{15}N of altered oceanic crust obtained on ODP Legs 129 and 185: insights into alteration-related nitrogen enrichment and the nitrogen subduction budget. *Geochim. Cosmochim. Acta* **71**, 2344-2360.

Li, L., He, Y., Zhang, Z., Liu, Y. (2021d) Nitrogen isotope fractionations among gaseous and aqueous NH_4^+, NH_3, N_2, and metal-ammine complexes: Theoretical calculations and applications. *Geochim. Cosmochim. Acta* **295**, 80-97.

Li, L., Li, K., Li, Y., Zhang, J., Du, Y., Labbe, M. (2021a) Recommendations on offline combustion-based nitrogen isotopic analysis of silicate minerals and rocks. *Rapid Commun. Mass Spectrom.* **35**, e9075.

Li, L., Zheng, Y.F., Cartigny, P., Li, J. (2014) Anomalous nitrogen isotopes in ultrahigh-pressure metamorphic rocks from the Sulu orogenic belt: Effect of abiotic nitrogen reduction during fluid–rock interaction. *Earth Planet Sci. Lett.* **403**, 67-78.

Li, Y.H., Li, L., Wu, Z.Q. (2021b) First-principles calculations of equilibrium nitrogen isotope fractionations among aqueous ammonium, silicate minerals and salts. *Geochim. Cosmochim. Acta* **297**, 220-232.

Liao, S., Tao, C., Jamieson, J.W., Liu, J., Zhu, C., Barriga, F.J.A.S., Li, W., Liang, J., Yang, W., Zhou, J., Deng, X., Yu, J. (2022) Oxidizing fluids associated with detachment hosted hydrothermal systems: Example from the Suye hydrothermal field on the ultraslow-spreading Southwest Indian Ridge. *Geochim. Cosmochim. Acta* **328**, 19-36.

Libourel, G., Marty, B., Humbert, F. (2003) Nitrogen solubility in basaltic melt. Part I. Effect of oxygen fugacity. *Geochim. Cosmochim. Acta* **67**, 4123-4135.

Lilley, M.D., Butterfield, D.A., Olson, E.J., Lupton, J.E., Macko, S.A., McDuff, R.E. (1993) Anomalous CH4 and NH_4^+ concentrations at an unsedimented mid-ocean-ridge hydrothermal system. *Nature* **364**, 45-47.

Liu, Y., Liu, X., Hu, Z., Diwu, C., Yuan, H., Gao, S. (2007) Evaluation of accuracy and long-term stability of determination of 37 trace elements in geological samples by ICP-MS. *Acta Petrologica Sinica* **23**, 1203-1210 (in Chinese with English abstract).

Lonsdale, P. (1988) Structural Pattern of the Galapagos Microplate and Evolution of the Galapagos Triple Junctions. *J. Geophys. Res. Solid* **93**, 13551-13574.

Maekawa, H., Shozui, M., Ishii, T., Saboda, K.L., Ogawa, Y. (1992) Metamorphic rocks from the serpentinite seamounts in the Mariana and Izu-Ogasawara forearcs. In *Proc. ODP, Sci. Results* (eds. Fryer, P., Pearce, J.A., Stokking, L.B., et al.,), College Station, TX (Ocean Drilling Program). pp. 415–430.

Maekawa, H., Shozul, M., Ishll, T., Fryer, P., Pearce, J.A. (1993) Blueschist metamorphism in an active subduction zone. *Nature* **364**, 520-523.

Mallik, A., Li, Y., Wiedenbeck, M. (2018) Nitrogen evolution within the Earth's atmosphere–mantle system assessed by recycling in subduction zones. *Earth Planet Sci. Lett.* **482**, 556-566.

Mann, U., Müller, G. (1979) X-ray mineralogy of Deep Sea Drilling Project legs 51 through 53, western North Atlantic. In *Initial Reports of the Deep Sea Drilling Project* (eds. In Donnelly, T., Francheteau, J., Bryan, W., Robinson, P., Flower, M., Salisbury, M., et al.,), Washington (U.S. Government Printing Office). pp. 721-729.

Marschall, H.R., Ludwig, T., Altherr, R., Kalt, A., Tonarini, S. (2006) Syros Metasomatic Tourmaline: Evidence for Very High-δ^{11}B Fluids in Subduction Zones. *J. Petrol.* **47**, 1915-1942.

Marschall, H.R., Schumacher, J.C. (2012) Arc magmas sourced from mélange diapirs in subduction zones. *Nat. Geosci.* **5**, 862-867.

Marty, B. (1995) Nitrogen content of the mantle inferred from N_2–Ar correlation in oceanic basalts. *Nature* **377**, 326-329.

Marty, B., Almayrac, M., Barry, P.H., Bekaert, D.V., Broadley, M.W., Byrne, D.J., Ballentine, C.J., Caracausi, A. (2020) An evaluation of the C/N ratio of the mantle from natural CO2-rich gas analysis: Geochemical and cosmochemical implications. *Earth Planet Sci. Lett.* **551**, 116574.

Marty, B., Dauphas, N. (2003) The nitrogen record of crust–mantle interaction and mantle convection from Archean to present. *Earth Planet Sci. Lett.* **206**, 397-410.

Marty, B., Humbert, F. (1997) Nitrogen and argon isotopes in oceanic basalts. *Earth Planet Sci. Lett.* **152**, 101-112.

Marty, B., Zimmermann, L. (1999) Volatiles (He, C, N, Ar) in mid-ocean ridge basalts: Assesment of shallow-level fractionation and characterization of source composition. *Geochim. Cosmochim. Acta* **63**, 3619-3633.

McCaig, A.M., Harris, M. (2012) Hydrothermal circulation and the dike-gabbro transition in the detachment mode of slow seafloor spreading. *Geology* **40**, 367-370.

McCaig, A.M., Titarenko, S.S., Savov, I.P., Cliff, R.A., Banks, D., Boyce, A., Agostini, S. (2018) No significant boron in the hydrated mantle of most subducting slabs. *Nat. Commun.* **9**, 4602.

Melzer, S., Wunder, B. (2000) Island-arc basalt alkali ratios: Constraints from phengite-fluid partitioning experiments. *Geology* **28**, 583-586.

Ménez, B., Pasini, V., Brunelli, D. (2012) Life in the hydrated suboceanic mantle. *Nat. Geosci* **5**, 133-137.

Meschede, M., Weiss, R., Schmiedl, G., Hemleben, C. (2002) Benthic foraminiferal distribution and sedimentary structures suggest tectonic erosion at the Costa Rica convergent plate margin. *Terra Nova* **14**, 388-396.

Mevel, C. (1980) Mineralogy and Chemistry of Secondary Phases in Low Temperature Altered Basalts from Deep Sea Drilling Project Legs 51, 52, and 53. In *Initial Reports of the Deep Sea Drilling Project,* (eds. In Donnelly, T., Francheteau, J., Bryan, W., Robinson, P., Flower, M., Salisbury, M., et al.), Washington (U.S. Government Printing Office). pp. 1299-1371.

Mével, C., Cannat, M., Gente, P., Marion, E., Auzende, J.M., Karson, J.A. (1991) Emplacement of deep crustal and mantle rocks on the west median valley wall of the MARK area (MAR, 23°N). *Tectonophysics* **190**, 31-53.

Mével, C., Stamoudi, C. (1996) Hydrothermal alteration of the upper-mantle section at Hess Deep. . In *Proc. ODP, Sci. Results* (Mével, C., Gillis, K.M., Allan, J.F., and Meyer, P.S. eds.), College Station, TX (Ocean Drilling Program). pp. 293-309.

Mingram, B., Bräuer, K. (2001) Ammonium concentration and nitrogen isotope composition in metasedimentary rocks from different tectonometamorphic units of the European Variscan Belt. *Geochim. Cosmochim. Acta* **65**, 273-287.

Mitchell, E.C., Fischer, T.P., Hilton, D.R., Hauri, E.H., Shaw, A.M., de Moor, J.M., Sharp, Z.D., Kazahaya, K. (2010) Nitrogen sources and recycling at subduction zones: Insights from the Izu-Bonin-Mariana arc. *Geochem. Geophys. Geosyst.* **11**.

Mottl, M.J., Komor, S.C., Fryer, P., Moyer, C.L. (2003) Deep-slab fluids fuel extremophilic Archaea on a Mariana forearc serpentinite mud volcano: Ocean Drilling Program Leg 195. *Geochemistry, Geophysics, Geosystems* **4**, Q02X11.

Mottl, M.J., Wheat, C.G., Fryer, P., Gharib, J., Martin, J.B. (2004) Chemistry of springs across the Mariana forearc shows progressive devolatilization of the subducting plate. *Geochim. Cosmochim. Acta* **68**, 4915-4933.

Muehlenbachs, K. (1980) The alteration and aging of the basaltic layer of the sea floor: oxygen isotope evidence from DSDP/IODP Legs 51, 52, and 53. In *Init. Repts. DSDP* (eds. Donnelly, T., Francheteau, J., Bryan, W., Robinson, P., Flower, M.,Salisbury, M., Blei, U., Borella, P.E., Gartner, S., Juteau, T., Kelts, K., Orr, W.N., Quisefit, J.P., Rusinov, V., Sinton, J.M., Smith, B.M., Swift, S.A., Ui, T., Bollinger, C., Byerly, G., Emmermann, R., Hamano, Y., Levi, S., Miles, G.A., Pertsev, N., Ricou,, L.E., Siesser, W.G., Stephen,, R.A., Swanson,, D.A., White, S., Bohrer, D., Hobart, M., Johnson, D., Mathez,, E., Mevel, C., Pertsev, N., Pritchard, R.G., Puchelt, H., Rigotti, P.A., Staudigel, H.), U.S. Government Printing Office, Washington. pp. 1159-1167.

Muehlenbachs, K., Clayton, R. (1976) Oxygen isotope composition of the oceanic crust and its bearing on seawater. *J. Geophys. Res.* **81**, 4365-4369.

Müller, P.J. (1977) CN ratios in Pacific deep-sea sediments: Effect of inorganic ammonium and organic nitrogen compounds sorbed by clays. *Geochim. Cosmochim. Acta* **41**, 765-776.

Müller, R.D., Dutkiewicz, A. (2018) Oceanic crustal carbon cycle drives 26-million-year atmospheric carbon dioxide periodicities. *Sci. Adv.* **4**, eaaq0500.

Mysen, B. (2019) Nitrogen in the Earth: abundance and transport. *Prog. Earth Planet. Sci.* **6**, 38.

Natland, J., Tarney, J., Marsh, N., Melson, W., OHearn, T. (1984) Compositions, stratigraphy, and alteration of pillow basalts, deep-sea drilling project Hole-543A, near the Barbados Ridge. In *Init. Repts. DSDP* (eds. Biju-Duval, B., Moore, J. C., Bergen, J. A., Blackinton, G., Claypool, G. E., Cowan, D. S., Davis, D., Guerra, R. T., Hemleben, C. H. J., Marlow, M. S., Pudsey, C., Renz, G. W., Tardy, M., Wilson, S. D., Wright, A. W.), U.S. Govt. Printing Office, Washington. pp. 393-399.

Nehlig, P., Juteau, T. (1988) Flow porosities, permeabilities and preliminary data on fluid inclusions and fossil thermal gradients in the crustal sequence of the Sumail ophiolite (Oman). *Tectonophysics* **151**, 199-221.

Nielsen, S.G., Klein, F., Kading, T., Blusztajn, J., Wickham, K. (2015) Thallium as a tracer of fluid–rock interaction in the shallow Mariana forearc. *Earth Planet. Sci. Lett.* **430**, 416-426.

Nielsen, S.G., Marschall, H.R. (2017) Geochemical evidence for mélange melting in global arcs. *Sci. Adv.* **3**, e1602402.

Nozaka, T., Fryer, P. (2011) Alteration of the Oceanic Lower Crust at a Slow-spreading Axis: Insight from Vein-related Zoned Halos in Olivine Gabbro from Atlantis Massif, Mid-Atlantic Ridge. *J. Petro.l* **52**, 643-664.

Nozaka, T., Fryer, P., Andreani, M. (2008) Formation of clay minerals and exhumation of lower-crustal rocks at Atlantis Massif, Mid-Atlantic Ridge. *Geochemistry, Geophysics, Geosystems* **9**.

Oakley, A.J., Taylor, B., Moore, G.F. (2008) Pacific Plate subduction beneath the central Mariana and Izu-Bonin fore arcs: New insights from an old margin. *Geochem. Geophys. Geosyst.* **9**, Q06003.

Ohtani, E., Litasov, K., Hosoya, T., Kubo, T., Kondo, T. (2004) Water transport into the deep mantle and formation of a hydrous transition zone. *Phys. Earth Planet. Inter.* **143-144**, 255-269.

Pagé, L., Hattori, K., Guillot, S. (2018) Mantle wedge serpentinites: A transient reservoir of halogens, boron, and nitrogen for the deeper mantle. *Geology* **46**, 883-886.

Palot, M., Pearson, D., Stern, R., Stachel, T., Harris, J. (2014) Isotopic constraints on the nature and circulation of deep mantle C–H–O–N fluids: Carbon and nitrogen systematics within ultra-deep diamonds from Kankan (Guinea). *Geochim. Cosmochim. Acta* **139**, 26-46.

Paul, H.J., Gillis, K.M., Coggon, R.M., Teagle, D.A. (2006) ODP Site 1224: A missing link in the investigation of seafloor weathering. *Geochem. Geophys. Geosyst.* **7**, Q02003.

Peacock, S.A. (1990) Fluid processes in subduction zones. *Science* **248**, 329-337.

Peacock, S.M. (1993) The importance of blueschist → eclogite dehydration reactions in subducting oceanic crust. *GSA Bulletin* **105**, 684-694.

Peacock, S.M. (1996) Thermal and Petrologic Structure of Subduction Zones. In *Subduction*. pp. 119-133.

Pedersen, R.B., Rapp, H.T., Thorseth, I.H., Lilley, M.D., Barriga, F.J.A.S., Baumberger, T., Flesland, K., Fonseca, R., Früh-Green, G.L., Jorgensen, S.L. (2010) Discovery of a black smoker vent field and vent fauna at the Arctic Mid-Ocean Ridge. *Nat. Commun.* **1**, 126.

Penniston-Dorland, S.C., Kohn, M.J., Manning, C.E. (2015) The global range of subduction zone thermal structures from exhumed blueschists and eclogites: Rocks are hotter than models. *Earth Planet Sci. Lett.* **428**, 243-254.

Penrose Conference Participants. (1972) Penrose field conference on ophiolites. *Geotimes* **17**, 24-25.

Philippot, P., Busigny, V., Scambelluri, M., Cartigny, P. (2007) Oxygen and nitrogen isotopes as tracers of fluid activities in serpentinites and metasediments during subduction. *Mineral Petrol.* **91**, 11-24.

Plank, T. (2014) The chemical composition of subducting sediments. In *Treatise on Geochemistry* (eds. Keeling, R.F.E., Amsterdam). Elsevier. pp. 607-629.

Plank, T., Langmuir, C.H. (1998) The chemical composition of subducting sediment and its consequences for the crust and mantle. *Chem. Geol.* **145**, 325-394.

Plank, T., Manning, C.E. (2019) Subducting carbon. *Nature* **574**, 343-352.

Plunder, A., Agard, P., Dubacq, B., Chopin, C., Bellanger, M. (2012) How continuous and precise is the record of P–T paths? Insights from combined thermobarometry and thermodynamic modelling into subduction dynamics (Schistes Lustrés, W. Alps). *J. Metamorph. Geol.***30**, 323-346.

Poli, S., Schmidt, M.W. (1995) H_2O transport and release in subduction zones: Experimental constraints on basaltic and andesitic systems. *J. Geophys. Res. Solid Earth* **100**, 22299-22314.

Pöter, B., Gottschalk, M., Heinrich, W. (2004) Experimental determination of the ammonium partitioning among muscovite, K-feldspar, and aqueous chloride solutions. *Lithos* **74**, 67-90.

Purdy, G.M. (1987) New observations of the shallow seismic structure of young oceanic crust. *J. Geophys. Res. Solid Earth* **92**, 9351-9361.

Ranero, C.R., Phipps Morgan, J., McIntosh, K., Reichert, C. (2003) Bending-related faulting and mantle serpentinization at the Middle America trench. *Nature* **425**, 367-373.

Regier, M.E., Pearson, D.G., Stachel, T., Luth, R.W., Stern, R.A., Harris, J.W. (2020) The lithospheric-to-lower-mantle carbon cycle recorded in superdeep diamonds. *Nature* **585**, 234-238.

Richardson, S.H., Hart, S.R., Staudigel, H. (1980) Vein mineral ages of old oceanic crust. *J. Geophys. Res. Solid Earth* **85**, 7195-7200.

Rioux, M., Johan Lissenberg, C., McLean, N.M., Bowring, S.A., MacLeod, C.J., Hellebrand, E., Shimizu, N. (2012) Protracted timescales of lower crustal growth at the fast-spreading East Pacific Rise. *Nat. Geosci* **5**, 275-278.

Rowan, C.J., Rowley, D.B. (2014) Spreading behaviour of the Pacific-Farallon ridge system since 83 Ma. *Geophys. J. Int.* **197**, 1273-1283.

Saboda, K.L., Fryer, P., Maekawa, H. (1992) Metamorphism of ultramafic clasts from Conical Seamount: Sites 778, 779, and 780. In *Proc. ODP, Sci. Results* (eds. Fryer, P., Pearce, J.A., Stokking, L.B., et al.,), College Station, TX (Ocean Drilling Program). pp. 431-443.

Sadofsky, S.J., Bebout, G.E. (2003) Record of forearc devolatilization in low-T, high-P/T metasedimentary suites: Significance for models of convergent margin chemical cycling. *Geochem. Geophys. Geosyst.* **4(4)**, 9003.

Sadofsky, S.J., Bebout, G.E. (2004) Nitrogen geochemistry of subducting sediments: New results from the Izu-Bonin-Mariana margin and insights regarding global nitrogen subduction. *Geochem. Geophys. Geosyst.* **5**, Q03115.

Saha, A., Basu, A.R., Wakabayashi, J., Wortman, G.L. (2005) Geochemical evidence for a subducted infant arc in Franciscan high-grade-metamorphic tectonic blocks. *GSA Bulletin* **117**, 1318-1335.

Sakai, H., Des Marais, D., Ueda, A., Moore, J. (1984) Concentrations and isotope ratios of carbon, nitrogen and sulfur in ocean-floor basalts. *Geochim. Cosmochim. Acta* **48**, 2433-2441.

Salters, V.J.M., Stracke, A. (2004) Composition of the depleted mantle. *Geochem. Geophys. Geosyst.* **5**, Q05B07.

Sano, Y., Takahata, N., Nishio, Y., Fischer, T.P., Williams, S.N. (2001) Volcanic flux of nitrogen from the Earth. *Chem. Geol.* **171**, 263-271.

Savov, I.P., Ryan, J.G., D'Antonio, M., Fryer, P. (2007) Shallow slab fluid release across and along the Mariana arc-basin system: Insights from geochemistry of serpentinized peridotites from the Mariana fore arc. *J. Geophys. Res. Solid Earth* **112**.

Savov, I.P., Ryan, J.G., D'Antonio, M., Kelley, K., Mattie, P. (2005) Geochemistry of serpentinized peridotites from the Mariana Forearc Conical Seamount, ODP Leg 125: Implications for the elemental recycling at subduction zones. *Geochem. Geophys. Geosyst.* **6**, Q04J15.

Schmidt, M.W. (1996) Experimental Constraints on Recycling of Potassium from Subducted Oceanic Crust. *Science* **272**, 1927-1930.

Schmidt, M.W., Poli, S. (1998) Experimentally based water budgets for dehydrating slabs and consequences for arc magma generation. *Earth Planet Sci. Lett.* **163**, 361-379.

Schoolmeesters, N., Cheadle, M.J., John, B.E., Reiners, P.W., Gee, J., Grimes, C.B. (2012) The cooling history and the depth of detachment faulting at the Atlantis Massif oceanic core complex. *Geochem. Geophys. Geosyst.* **13**, Q0AJ12.

Schwartz, J.J., John, B.E., Cheadle, M.J., Reiners, P.W., Baines, A.G. (2009) Cooling history of Atlantis Bank oceanic core complex: Evidence for hydrothermal activity 2.6 Ma off axis. *Geochem. Geophys. Geosyst.* **10**, Q08020.

Şengör, A.M.C., Natal'in, B.A., Burtman, V.S. (1993) Evolution of the Altaid tectonic collage and Palaeozoic crustal growth in Eurasia. *Nature* **364**, 299-307.

Seyedali, M., Coogan, L., Gillis, K. (2021) Li-isotope exchange during low-temperature alteration of the upper oceanic crust at DSDP Sites 417 and 418. *Geochim. Cosmochim. Acta* **294**, 160-173.

Seyfried Jr, W. (1987) Experimental and theoretical constraints on hydrothermal alteration processes at mid-ocean ridges. *Annu. Rev. Earth Planet. Sci.* **15**, 317-335.

Seyfried, W.E., Bischoff, J.L. (1979) Low temperature basalt alteration by sea water: an experimental study at 70°C and 150°C. *Geochim. Cosmochim. Acta* **43**, 1937-1947.

Shannon, R.T., Prewitt, C.T. (1969) Effective ionic radii in oxides and fluorides. *Acta Crystallographica Section B: Structural Crystallography and Crystal Chemistry* **25**, 925-946.

Shilobreeva, S., Martinez, I., Busigny, V., Agrinier, P., Laverne, C. (2011) Insights into C and H storage in the altered oceanic crust: Results from ODP/IODP Hole 1256D. *Geochim. Cosmochim. Acta* **75**, 2237-2255.

Shipboard Scientific Party. (1980) Site 417. In *Initial Reports of the Deep Sea Drilling Project* (eds. In Donnelly, T., Francheteau, J., Bryan, W., Robinson, P., Flower, M., Salisbury, M., et al.,), Washington (U.S. Government Printing Office),. pp. 23-350.

Shipboard Scientific Party. (1984) Site 543: Oceanic Referenc Site East of the Barbados Ridge Complex. In *Init. Repts. DSDP* (eds. Biju-Duval, B., Moore, J. A.M., Blackinton, G., Claypool, G.E., Cowan, D.S.,), U.S. Govt. Printing Office, Washington. pp. 227-298.

Shipboard Scientific Party. (1985) Site 556. In *Init. Repts. DSDP* (eds. In Bougault, H., Cande, S. C, et al.,), Washington (U.S. Govt. Printing Office), pp. 61-113.

Shipboard Scientific Party. (1989) Site 735. In *Proc. ODP, Init. Repts* (eds. In Robinson, P.T., Von Herzen, R., et al.), College Station, TX (Ocean Drilling Program), pp. 89-222.

Shipboard Scientific Party. (1990) Site 784. In *Proc. ODP, Init. Repts.,* (eds. Fryer, P., Pearce, J.A., Stokking, L.B., et al.,), College Station, TX (Ocean Drilling Program), pp. 273-305.

Shipboard Scientific Party. (1993a) Site 504. In *Proc. ODP, Sci. Results* (eds. Alt, J.C., Kinoshita, H., Stokking, L.B.), Ocean Drilling Program, College Station, TX. pp. 27-121.

Shipboard Scientific Party. (1993b) Site 895. In *Proc. ODP, Init. Repts* (eds. Gillis, K., Mével, C, Allan, J., et al), College Station, TX (Ocean Drilling Program). pp. 109-159.

Shipboard Scientific Party. (1995) Site 920. In *Proc. ODP, Sci. Results* (eds. Cannat, M., Karson, J.A., Miller, D.J.), Ocean Drilling Program, College Station, TX. pp. 45-119.

Shipboard Scientific Party. (1999) Site 735. In *Proc. ODP, Sci. Results* (eds. Dick, H.J.B., Natland, J.H., Miller, D.J., et al.), Ocean Drilling Program, College Station, TX. pp. 1-314.

Shipboard Scientific Party. (2000a) Site 801. In *Proc. ODP, Sci. Results* (eds. Plank, T., Ludden, J.N., Escutia, C.), Ocean Drilling Program, College Station, TX. pp. 1-222.

Shipboard Scientific Party. (2000b) Site 1149. In *Proc. ODP, Init. Repts.,* (eds. In Plank, T., Ludden, J.N., Escutia, C., et al.,), College Station, TX (Ocean Drilling Program). pp. 1–190.

Shipboard Scientific Party. (2002) Site 1200. In *Proc. ODP, Init. Repts* (eds. Salisbury, M.H., Shinohara, M., Richter, C., et al.,), College Station, TX (Ocean Drilling Program). pp. 1–173.

Shipboard Scientific Party. (2003a) Leg 206 summary. In *Proc. ODP, Sci. Results* (eds. Wilson, D.S., Teagle, D.A.H., Acton, G.D. et al.,), Ocean Drilling Program, College Station, TX. pp. 1–117.

Shipboard Scientific Party. (2003b) Site 1224. In *Proc. ODP, Sci. Results* (eds. Stephen, R.A., Kasahara, J., Acton, G.D.), Ocean Drilling Program, College Station, TX. pp. 1–178.

Shipboard Scientific Party. (2003c) Site 1256. In *Proc. ODP, Sci. Results* (eds. Wilson, D.S., Teagle, D.A.H., Acton, G.D., et al.), Ocean Drilling Program, College Station, TX. pp. 1-396.

Shipboard Scientific Party. (2004a) Site 1271. In *Proc. ODP, Sci. Results* (eds. Kelemen, P.B., Kikawa, E., Miller, D.J.), Ocean Drilling Program, College Station, TX. pp. 1–129.

Shipboard Scientific Party. (2004b) Site 1274. In *Proc. ODP, Sci. Results* (eds. Kelemen, P.B., Kikawa, E., Miller, D.J.), Ocean Drilling Program, College Station, TX. pp. 1–116.

Shirey, S.B., Richardson, S.H. (2011) Start of the Wilson cycle at 3 Ga shown by diamonds from subcontinental mantle. *Science* **333**, 434-436.

Shirey, S.B., Wagner, L.S., Walter, M.J., Pearson, D.G., van Keken, P.E. (2021) Slab Transport of Fluids to Deep Focus Earthquake Depths—Thermal Modeling Constraints and Evidence From Diamonds. *AGU Advances* **2**, e2020AV000304.

Sidey, V. (2016) On the effective ionic radii for ammonium. *Acta Crystallographica Section B: Structural Science, Crystal Engineering Materials* **72**, 626-633.

Sievers, N.E., Tenore, J., Penniston-Dorland, S.C., Bebout, G.E. (2017) Fingerprints of forearc element mobility in blueschist-facies metaconglomerates, Catalina Schist, California. *Int. Geol. Rev.* **59**, 741-752.

Smart, K.A., Tappe, S., Stern, R.A., Webb, S.J., Ashwal, L.D. (2016) Early Archaean tectonics and mantle redox recorded in Witwatersrand diamonds. *Nat. Geosci.* **9**, 255.

Smith, D.K., Schouten, H. (2018) Opening of Hess Deep Rift at the Galapagos Triple Junction. *Geophys. Res. Lett.* **45**, 3942-3950.

Smith, E.M., Ni, P., Shirey, S.B., Richardson, S.H., Wang, W., Shahar, A. (2021) Heavy iron in large gem diamonds traces deep subduction of serpentinized ocean floor. *Sci. Adv.* **7**, eabe9773.

Smith, E.M., Shirey, S.B., Richardson, S.H., Nestola, F., Bullock, E.S., Wang, J., Wang, W. (2018) Blue boron-bearing diamonds from Earth's lower mantle. *Nature* **560**, 84.

Snelgrove, S.H., Forster, C.B. (1996) Impact of seafloor sediment permability and thickness on off-axis hydrothermal circulation: Juan de Fuca Ridge eastern flank. *J. Geophys. Res. Solid* **101**, 2915-2925.

Snyder, G., Poreda, R., Fehn, U., Hunt, A. (2003) Sources of nitrogen and methane in Central American geothermal settings: Noble gas and 129I evidence for crustal and magmatic volatile components. *Geochem. Geophys. Geosyst.* **4**, 1-28.

Snyder, G., Poreda, R., Hunt, A., Fehn, U. (2001) Regional variations in volatile composition: Isotopic evidence for carbonate recycling in the Central American volcanic arc. *Geochem. Geophys. Geosyst.* **2(10)**.

Sorensen, Sorena S., Grossman, J.N., Perfit, M.R. (1997) Phengite-hosted LILE Enrichment in Eclogite and Related Rocks: Implications for Fluid-Mediated Mass Transfer in Subduction Zones and Arc Magma Genesis. *J. Petrol.* **38**, 3-34.

Spandler, C., Hermann, J., Faure, K., Mavrogenes, J.A., Arculus, R.J. (2008) The importance of talc and chlorite "hybrid" rocks for volatile recycling through subduction zones; evidence from the high-pressure subduction mélange of New Caledonia. *Contrib. Miner. Petrol.* **155**, 181-198.

Speelmanns, I.M., Schmidt, M.W., Liebske, C. (2018) Nitrogen solubility in core materials. *Geophys. Res. Lett.* **45**, 7434-7443.

Stakes, D., 1991. Oxygen and hydrogen isotope composition of oceanic plutonic rocks: high-temperature deformation and metamorphism of oceanic layer 3, Stable isotope geochemistry: A tribute to Samuel Epstein, pp. 77-90.

Staudigel, H. (2003) 4 - Hydrothermal alteration processes in the oceanic crust. *Treatise on geochemistry* **3**, 659.

Staudigel, H. (2014) 4.16 - Chemical Fluxes from Hydrothermal Alteration of the Oceanic Crust. In *Treatise on Geochemistry (Second Edition)* (eds. Holland, H.D., Turekian, K.K.). Elsevier, Oxford. pp. 583-606.

Staudigel, H., Hart, S.R. (1983) Alteration of basaltic glass: Mechanisms and significance for the oceanic crust-seawater budget. *Geochim. Cosmochim. Acta* **47**, 337-350.

Staudigel, H., Hart, S.R., Richardson, S.H. (1981) Alteration of the oceanic crust: processes and timing. *Earth Planet Sci. Lett.* **52**, 311-327.

Staudigel, H., Hart, S.R., Schmincke, H.-U., Smith, B.M. (1989) Cretaceous ocean crust at DSDP Sites 417 and 418: Carbon uptake from weathering versus loss by magmatic outgassing. *Geochim. Cosmochim. Acta* **53**, 3091-3094.

Staudigel, H., Plank, T., White, B., Schmincke, H.-U. (1996) Geochemical fluxes during seafloor alteration of the basaltic upper oceanic crust: DSDP Sites 417 and 418. *GMS* **96**, 19-38.

Stein, C.A., Stein, S. (1994) Constraints on hydrothermal heat flux through the oceanic lithosphere from global heat flow. *J. Geophys. Res: Solid Earth* **99**, 3081-3095.

Stephen, R.A., J. Kasahara., G. D. Acton. (2003) Drilling at the Hawaii-2 Observatory (H2O) and the Nuuanu Landslide Sites 1223 and 1224. *Proc. Ocean Drill. Program Initial Rep* **200**, 1-72.

Sun, S.S., McDonough, W.F. (1989) Chemical and isotopic systematics of oceanic basalts: implications for mantle composition and processes. *Geol. Soc. Spec. Publ.* **42**, 313-345.

Sun, W., Zhang, L., Li, H., Liu, X. (2020) The synchronic Cenozoic subduction initiations in the west Pacific induced by the closure of the Neo-Tethys Ocean. *Science Bulletin* **65**, 2068-2071.

Syracuse, E.M., Abers, G.A. (2006) Global compilation of variations in slab depth beneath arc volcanoes and implications. *Geochem. Geophys. Geosyst.* **7**, Q05017.

Syracuse, E.M., van Keken, P.E., Abers, G.A. (2010) The global range of subduction zone thermal models. *Phys. Earth Planet. Inter.* **183**, 73-90.

Tamblyn, R., Zack, T., Schmitt, A.K., Hand, M., Kelsey, D., Morrissey, L., Pabst, S., Savov, I.P. (2019) Blueschist from the Mariana forearc records long-lived residence of material in the subduction channel. *Earth Planet Sci. Lett.* **519**, 171-181.

Tao, C., Seyfried, W.E., Lowell, R.P., Liu, Y., Liang, J., Guo, Z., Ding, K., Zhang, H., Liu, J., Qiu, L., Egorov, I., Liao, S., Zhao, M., Zhou, J., Deng, X., Li, H., Wang, H., Cai, W., Zhang, G., Zhou, H., Lin, J., Li, W. (2020) Deep high-temperature hydrothermal circulation in a detachment faulting system on the ultra-slow spreading ridge. *Nat. Commun.* **11**, 1300.

Tesdal, J.E., Galbraith, E.D., Kienast, M. (2013) Nitrogen isotopes in bulk marine sediment: linking seafloor observations with subseafloor records. *Biogeosciences* **10**, 101-118.

Torsvik, T., Furnes, H., Muehlenbachs, K., Thorseth, I.H., Tumyr, O. (1998) Evidence for microbial activity at the glass-alteration interface in oceanic basalts. *Earth Planet Sci. Lett.* **162**, 165-176.

Tumiati, S., Godard, G., Martin, S., Malaspina, N., Poli, S. (2015) Ultra-oxidized rocks in subduction mélanges? Decoupling between oxygen fugacity and oxygen availability in a Mn-rich metasomatic environment. *Lithos* **226**, 116-130.

Turner, S., Rushmer, T., Reagan, M., Moyen, J.-F. (2014) Heading down early on? Start of subduction on Earth. *Geology* **42**, 139-142.

Van Avendonk, H.J.A., Holbrook, W.S., Lizarralde, D., Denyer, P. (2011) Structure and serpentinization of the subducting Cocos plate offshore Nicaragua and Costa Rica. *Geochem. Geophys. Geosyst.* **12**, Q06009.

van Keken, P.E., Wada, I., Abers, G.A., Hacker, B.R., Wang, K. (2018) Mafic High-Pressure Rocks Are Preferentially Exhumed From Warm Subduction Settings. *Geochem. Geophys. Geosyst.* **19**, 2934-2961.

Vanko, D.A., Stakes, D.S., 1991. Fluids in oceanic layer 3: evidence from veined rocks, Hole 735B, Southwest Indian Ridge, Proc. Ocean Drill. Program Sci. Results, pp. 181-215.

VanTongeren, J.A., Kelemen, P.B., Garrido, C.J., Godard, M., Hanghoj, K., Braun, M., Pearce, J.A. (2021) The composition of the lower oceanic crust in the Wadi Khafifah section of the southern Samail (Oman) ophiolite. *J. Geophys. Res: Solid Earth* **126(11)**, e2021JB021986.

Von Damm, K. (1990) Seafloor hydrothermal activity: black smoker chemistry and chimneys. *Annu. Rev. Earth Planet. Sci.* **18**, 173-204.

Von Damm, K.L., Edmond, J.M., Grant, B., Measures, C.I., Walden, B., Weiss, R.F. (1985) Chemistry of submarine hydrothermal solutions at 21°N, East Pacific Rise. *Geochim. Cosmochim. Acta* **49**, 2197-2220.

Wacey, D., McLoughlin, N., Saunders, M., Kong, C. (2014) The nano-scale anatomy of a complex carbon-lined microtube in volcanic glass from the ~92Ma Troodos Ophiolite, Cyprus. *Chem. Geol.* **363**, 1-12.

Wada, I., Wang, K., He, J., Hyndman, R.D. (2008) Weakening of the subduction interface and its effects on surface heat flow, slab dehydration, and mantle wedge serpentinization. *J. Geophys. Res: Solid Earth* **113**, B04402.

Walter, M.J., Kohn, S.C., Araujo, D., Bulanova, G.P., Smith, C.B., Gaillou, E., Wang, J., Steele, A., Shirey, S.B. (2011) Deep mantle cycling of oceanic crust: evidence from diamonds and their mineral inclusions. *Science*, 1209300.

Walther, C.H.E. (2003) The crustal structure of the Cocos ridge off Costa Rica. *J. Geophys. Res: Solid Earth* **108(B3)**, 2136.

Walther, C.H.E., Flueh, E.R., Ranero, C.R., Von Huene, R., Strauch, W. (2000) Crustal structure across the Pacific margin of Nicaragua:evidence for ophiolitic basement and a shallow mantle sliver. *Geophys. J. Int.* **141**, 759-777.

Wang, J., Liu, X. (2016) Proficiency testing of the XRF method for measuring 10 major elements in different rock types. *Rock and Mineral Analysis* **35**, 145-151 (in Chinese with English abstract).

Watenphul, A., Wunder, B., Wirth, R., Heinrich, W. (2010) Ammonium-bearing clinopyroxene: a potential nitrogen reservoir in the Earth's mantle. *Chem. Geol.* **270**, 240-248.

White, W., Klein, E. (2014) 4.13-Composition of the oceanic crust. *Treatise on Geochemistry (second edition)*, 457-496.

Wilson, D.S., Teagle, D.A., Alt, J.C., Banerjee, N.R., Umino, S., Miyashita, S., Acton, G.D., Anma, R., Barr, S.R., Belghoul, A. (2006) Drilling to gabbro in intact ocean crust. *Science* **312**, 1016-1020.

Wu, F.Y., Yang, J.H., Lo, C.H., Wilde, S.A., Sun, D.Y., Jahn, B.M. (2007) The Heilongjiang Group: a Jurassic accretionary complex in the Jiamusi Massif at the western Pacific margin of northeastern China. *Island Arc* **16**, 156-172.

Xu, S., Su, W., Liu, Y., Jiang, L., Ji, S., Okay, A.I., Sengör, A.M.C. (1992) Diamond from the Dabie Shan metamorphic rocks and its implication for tectonic setting. *Science* **256**, 80-82.

Yamamoto, T., Nakahira, M. (1966) Ammonium ions in sericites. *American Mineralogist: Journal of Earth and Planetary Materials* **51**, 1775-1778.

Yamaoka, K., Ishikawa, T., Matsubaya, O., Ishiyama, D., Nagaishi, K., Hiroyasu, Y., Chiba, H., Kawahata, H. (2012) Boron and oxygen isotope systematics for a complete section of oceanic crustal rocks in the Oman ophiolite. *Geochim. Cosmochim. Acta* **84**, 543-559.

Yang, Y., Huang, W., Qi, Z., Xia, Q. (2022) Nitrogen Retention in Feldspar: Implications for Nitrogen Transport in Subduction Zones. *J. Geophys. Res: Solid Earth* **127**, e2021JB023347.

Ye, K., Cong, B., Ye, D. (2000) The possible subduction of continental material to depths greater than 200 km. *Nature* **407**, 734-736.

Yokochi, R., Marty, B., Chazot, G., Burnard, P. (2009) Nitrogen in peridotite xenoliths: Lithophile behavior and magmatic isotope fractionation. *Geochim. Cosmochim. Acta* **73**, 4843-4861.

Zack, T., Rivers, T., Foley, S. (2001) Cs–Rb–Ba systematics in phengite and amphibole: an assessment of fluid mobility at 2.0 GPa in eclogites from Trescolmen, Central Alps. *Contrib. Mineral. Petrol.* **140**, 651-669.

Zhou, J.B., Cao, J.L., Wilde, S.A., Zhao, G.C., Zhang, J.J., Wang, B. (2014) Paleo-Pacific subduction-accretion: Evidence from Geochemical and U-Pb zircon dating of the Nadanhada accretionary complex, NE China. *Tectonics* **33**, 2444-2466.

Zhou, J.B., Han, J., Wilde, S., Guo, X., Zeng, W., Cao, J. (2013) A primary study of the Jilin-Heilongjiang high-pressure metamorphic belt: Evidence and tectonic implications. *Acta Petrol. Sin.* **29**, 386-398.

Zhou, J.B., Li, L. (2017) The Mesozoic accretionary complex in Northeast China: Evidence for the accretion history of Paleo-Pacific subduction. *J. Asian Earth Sci.* **145**, 91-100.

Zhou, J.B., Wilde, S.A., Zhang, X.Z., Zhao, G.C., Zheng, C.Q., Wang, Y.J., Zhang, X.H. (2009) The onset of Pacific margin accretion in NE China: evidence from the Heilongjiang high-pressure metamorphic belt. *Tectonophysics* **478**, 230-246.

Zhou, J.B., Wilde, S.A., Zhao, G.C. (2010) New SHRIMP U-Pb Zircon Ages from the Heilongjiang ComplexinNEChina: Constraints on the Mesozoic Evolution of NE China. *Am. J. Sci.* **310**, 1024-1053.

Zhu, C.Y., Zhao, G., Sun, M., Eizenhöfer, P.R., Liu, Q., Zhang, X., Han, Y., Hou, W. (2017) Geochronology and geochemistry of the Yilan greenschists and amphibolites in the Heilongjiang complex, northeastern China and tectonic implications. *Gondwana Res.* **43**, 213-228.

Zhu, C.Y., Zhao, G., Sun, M., Liu, Q., Han, Y., Hou, W., Zhang, X., Eizenhofer, P.R. (2015) Geochronology and geochemistry of the Yilan blueschists in the Heilongjiang Complex, northeastern China and tectonic implications. *Lithos* **216**, 241-253.

Zimmer, M.M., Fischer, T.P., Hilton, D.R., Alvarado, G.E., Sharp, Z.D., Walker, J.A. (2004) Nitrogen systematics and gas fluxes of subduction zones: insights from Costa Rica arc volatiles. *Geochem. Geophys. Geosyst.* **5**, Q05J11.

Appendix A – Supplementary material for Chapter 2.1

A1 Supplementary tables

Table A 1. Summary of N concentrations, $\delta^{15}N$ values and sample descriptions of altered basalts.

Site	ID (Leg-Hole-Core-Section Interval)	Depth (mbsf)	N (ppm)	$\delta^{15}N$ (‰)	Lithology	Visual Description	Alteration Type*	Ref
556	82-556-2R-2W 68-70	463	13.5	1.6	pillow basalt breccia	Highly altered (the rim is associated with brown alteration halos)	basalt breccia intercalated with limestone	this study
556	82-556-5R-4W 21-23	495	7.0	1.3	glass	moderately altered	BGR	this study
556	82-556-8R-2W 60-62	518	8.2	3.6	pillow basalt	moderately altered	BGR	this study
556	82-556-10R-2W 114-116	536	6.2	1.6	basalt fragment	slightly altered	BGR	this study
1224F	200-1224F-1R-2W 55-60	28.5	5.7	-0.8	massive basalt	slightly altered	BGR	this study
1224F	200-1224F-2R-1W 20-25	40	12.9	0.1	massive basalt	moderately altered	BGR + brown alteration halos	this study
1224F	200-1224F-3R-1W 12-17	47	5.2	0.0	massive basalt	slightly altered	BGR	this study
1224F	200-1224F-4R-5W 33-38	61	5.5	1.5	massive basalt	slightly altered	BGR	this study
1224F	200-1224F-9R-1W 12-16	103	8.5	0.8	pillow basalt	slightly altered	BGR	this study
1224F	200-1224F-13R-1W 32-38	133	9.0	-0.4	massive basalt	slightly altered	BGR	this study
1224F	200-1224F-14R-2W 18-23	145	9.9	0.8	massive basalt	moderately altered	BGR + brown alteration halos	this study
417A	51-417A-24R-1W 101-103	218.5	25.8	-20.1	basalt breccia	highly altered	basalt breccia in a matrix of green palagonite, smectite and zeolite	this study
417A	51-417A-39R-2W 72-74	363	12.8	-10.9	pillow basalt	moderately to highly altered	BGR	this study
417A	51-417A-28R-4W 85-86	256	6.3	2.0	pillow basalt	moderately to highly altered	BGR	this study

Site	ID (Leg-Hole-Core-Section Interval)	Depth (mbsf)	N (ppm)	$\delta^{15}N$ (‰)	Lithology	Visual Description	Alteration Type*	Ref
417A	51-417A-29R-2W 64-65	273	11.3	0.7	pillow basalt	moderately to highly altered	BGR	this study
417A	51-417A-33R-4W 22-23	307	7.1	1.0	pillow basalt	moderately to highly altered	BGR	this study
417A	51-417A-37R-5W 44-45	352	4.6	3.4	pillow basalt	moderately to highly altered	BGR	this study
417A	51-417A-40R-2W 115-116	365.1	5.1	1.4	pillow basalt	moderately to highly altered	BGR	this study
417A	51-417A-42R-4W 94-96	387.8	6.6	3.9	pillow basalt	moderately to highly altered	BGR	this study
417A	51-417A-43R-2W 38-39	389.9	6.4	1.5	pillow basalt	moderately to highly altered	BGR	this study
417A	51-417A-44R-1W 45-48	395.7	2.7	1.0	massive basalt	moderately to highly altered	BGR	this study
417A	51-417A-46R-1W 25-27	407.6	3.4	2.5	massive basalt	moderately to highly altered	BGR	this study
417A	51-417A-38R-8	362	14.6	0.6	Pillow basalt	moderately to highly altered	BGR	Li et al., 2007
417A	41-417A-44R-4	397	11.9	8.3	Pillow basalt	moderately to highly altered	BGR	Li et al., 2007
543A	78-543A-010-01W 57-58	408	31.3	7.1	pillow basalt	moderately altered	BGR + brown alteration halos	this study
543A	78-543A-10-02W 103-105	409	48.4	5.9	pillow basalt	moderately alteraed	BGR + brown alteration halos	this study
543A	78-543A-10-03W 28-30	410	17.5	-1.0	pillow basalt	slightly altered	BGR	this study
543A	78-543A-11-01W 30-33	412	21.1	3.9	pillow basalt	moderately altered	BGR + brown alteration halos	this study
543A	78-543-12-02W 72-75	419	21.0	3.8	pillow basalt	slightly altered	BGR	this study
543A	78-543A-12-04W 128-133	422	24.3	3.5	pillow basalt	slightly altered	BGR	this study
543A	78-543A-13-01W 18-21	425	20.9	1.8	pillow basalt	slightly altered	BGR	this study
543A	78-543A-13-05W 85-86	430	21.5	2.4	pillow basalt	slightly altered	BGR	this study

Site	ID (Leg-Hole-Core-Section Interval)	Depth (mbsf)	N (ppm)	$\delta^{15}N$ (‰)	Lithology	Visual Description	Alteration Type*	Ref
543A	78-543A-14-01W 37-39	433	17.5	1.5	pillow basalt	slightly altered	BGR	this study
543A	78-543A-15-01W 49-51	440	29.6	2.0	pillow basalt	slightly altered	BGR	this study
543A	78-543A-15-03W 99-100	442	27.6	1.6	pillow basalt	slightly altered	BGR	this study
543A	78-543A-16-01W 88-90	443	23.3	2.8	pillow basalt	slightly altered	BGR	this study
543A	78-543A-16-03W 116-118	449	19.7	2.6	pillow basalt	slightly altered	BGR	this study
543A	78-543A-6R-1 51-52	370.51	318.1	3.8	Claystone (basal sediments)	n.p	n.p	this study
543A	78-543A-7R-1 101-102	380.51	325.1	5.1	Claystone (basal sediments)	n.p	n.p	this study
543A	78-543A-8R-1 87-88	389.87	247.8	5.4	Claystone (basal sediments)	n.p	n.p	this study
1256D	206-1256D-02R-01W 86-87	276	11.3	-0.2	massive basalt	moderately altered	BGR	Li and Li, 2022
1256D	206-1256D-6R-05W 99-100	300	19.1	3.8	massive basalt	slightly altered	BGR	Li and Li, 2022
1256D	206-1256D-015R-01W 63-64	364	18.3	-1.4	massive basalt	moderately altered	BGR	Li and Li, 2022
1256D	206-1256D-032R-02W 8-9	470	9.3	-0.9	massive basalt	slightly altered	BGR	Li and Li, 2022
1256D	206-1256D-065R-03W 22-23	705	9.8	0.3	sheeted flow	moderately altered	BGR	Li and Li, 2022
1256D	309-1256D-075R-01W 112-113	752	10.5	-1.0	sheeted flow	moderately altered	BGR	Li and Li, 2022
1256D	309-1256D-092R-01W 95-96	869	10.3	1.0	sheeted flow	slightly altered	BGR	Li and Li, 2022
1256D	309-1256D-100R-01W 133-134	910	7.9	0.5	massive basalt	moderately altered	BGR	Li and Li, 2022
1256D	206-1256D-21R-1 124-130	398.4	6.4	0.1	sheet flow	not available	n.a	Bebout et al., 2018
1256D	206-1256D-26R-1 42-50	439	12.1	1.4	massive basalt	not available	n.a	Bebout et al., 2018

Site	ID (Leg-Hole-Core-Section Interval)	Depth (mbsf)	N (ppm)	δ^{15}N (‰)	Lithology	Visual Description	Alteration Type*	Ref
1256D	206-1256D-41R-2 26-33	526	11.1	1.7	massive basalt	not available	n.a	Bebout et al., 2018
1256D	206-1256D-47R-2 121-126	574	17.8	4.5	sheet flow	not available	n.a	Bebout et al., 2018
1256D	206-1256D-49R-1 69-76	583	11	2.1	sheet flow	not available	n.a	Bebout et al., 2018
1256D	206-1256D-51R-1 45-51	597	13.2	0.2	sheet flow	not available	n.a	Bebout et al., 2018
1256D	206-1256D-52R-1 8-15	601	9.1	1.3	sheet flow	not available	n.a	Bebout et al., 2018
504B	70-504B-36R-4W 0-2	547.65	3.6	-2.4	pillow basalt	moderately altered	BGR	Li and Li, 2022
504B	70-504B-52R-1W 67-72	679.17	2.7	0.7	pillow basalt	moderately altered	BGR	Li and Li, 2022
504B	70-504B-66R-2W 101-106	793.51	3.0	-1.9	pillow basalt	slightly altered	BGR	Li and Li, 2023
504B	83-504B-71R-1W 32-38	836.32	14.8	2.3	pillow basalt	moderately altered	BGR	Li and Li, 2024
504B	83-504B-84R-1W 60-68	947.1	6.2	0.4	transition zone pillow basalt	moderately altered	BGR	Li and Li, 2025
504B	83-504B-94R-2W 10-16	1032.1	3.9	0.0	transition zone pillow basalt	moderately altered	BGR	Li and Li, 2026
504B	70-504B-8R-1 69-72	317.2	13.7	5.1	pillow basalt	not available	BGR	Busigny et al., 2019
504B	70-504B-13R-1 81-84	362.4	8.1	3	pillow basalt	not available	BGR	Busigny et al., 2019
504B	70-504B-29R-2 16-19	485.2	14.1	1.2	pillow basalt	not available	BGR	Busigny et al., 2019
504B	70-504B-39R-1 62-66	571.2	9.1	3.7	pillow basalt	not available	BGR	Busigny et al., 2019
504B	70-504B-43R-1 17-19	602.2	9.3	5.5	pillow basalt	not available	BGR	Busigny et al., 2019
504B	70-504B-60R-1 46-49	742	7.8	7.7	pillow basalt	not available	BGR	Busigny et al., 2019
504B	70-504B-69R-1 95-99	819	10.7	4.2	pillow basalt	not available	BGR	Busigny et al., 2019

Site	ID (Leg-Hole-Core-Section Interval)	Depth (mbsf)	N (ppm)	$\delta^{15}N$ (‰)	Lithology	Visual Description	Alteration Type*	Ref
504B	83-504B-77R-2 71-73	890.9	6.4	0.1	transition zone pillow basalt	not available	BGR	Busigny et al., 2019
504B	83-504B78R-1 6-11	897.6	10.9	0.5	transition zone pillow basalt	not available	BGR	Busigny et al., 2019
504B	83-504B-81R-1 128-132	920.8	7.6	3.8	transition zone pillow basalt	not available	BGR	Busigny et al., 2019
504B	83-504B-88R-1 12-16	976.7	5.7	7.3	transition zone pillow basalt	not available	BGR	Busigny et al., 2019
504B	83-504B96R-1 125-127	1049.7	5.8	2.9	transition zone pillow basalt	not available	BGR	Busigny et al., 2019
801B	129-801B-41R-1 26-30	483.2	7.8	0.7	alkalic basalt	slightly to moderately altered	BGR	Li et al., 2007
801B	129-801B-43R-1 22-27	492.4	9.5	0.2	alkalic basalt	slightly altered	BGR	Li et al., 2007
801B	129-801B-43R-1 132-135	493.5	2.8	-3	alkalic basalt	slightly altered	BGR	Li et al., 2007
801C	129-801C-1R-1 109-141	494.8	7.5	-1.6	alkalic basalt	moderately altered	BGR	Li et al., 2007
801C	129-801C-1R-5 80-82	499.3	2.4	-4.9	alkalic basalt	moderately altered	BGR + carbonate vein	Li et al., 2007
801C	129-801C-4R-1 72-77	522.4	3	0	hydrothermal deposit	hydrothermal deposit	not available	Li et al., 2007
801C	129-801C-5R-2 12-17	532.9	13.4	0.5	breccia	highly altered	contain smectite veins	Li et al., 2007
801C	129-801C-5R-2 123-130	533.7	17.1	0.9	breccia	highly altered	contain smectite veins	Li et al., 2007
801C	129-801C-5R-3 99-104	534.8	16.3	1.2	pillow basalt	highly altered	BGR	Li et al., 2007
801C	129-801C-5R-3 125-131	535.0	15.3	0.7	massive flow	highly altered	BGR	Li et al., 2007
801C	129-801C-7R-3 0-5	552.9	12.4	0.1	massive flow	slightly altered	BGR + smectite in veins and vesicles	Li et al., 2007
801C	129-801C-8R-1 18-21	559.7	18.2	0.7	massive flow	moderately to highly altered	BGR + clay and carbonate in vesicles	Li et al., 2007
801C	129-801C-8R-1 65-67	560.1	9.3	-0.2	massive flow	highly altered	BGR + iron hydroxide in the margin	Li et al., 2007

Site	ID (Leg-Hole-Core-Section Interval)	Depth (mbsf)	N (ppm)	$\delta^{15}N$ (‰)	Lithology	Visual Description	Alteration Type*	Ref
801C	129-801C-10R-6 67-70	576.8	6.7	0.5	massive flow	slightly altered	BGR	Li et al., 2007
801C	129-801C-11R-2 131-136	580.1	6.7	-0.1	massive flow	slightly to moderately altered	BGR	Li et al., 2007
801C	129-801C-12R-1 101-104	588.3	13.7	1	massive flow	slightly altered	BGR	Li et al., 2007
801C	129-801C-12R-3 57-62	590.8	4.8	0.9	massive flow	slightly altered	BGR + halos	Li et al., 2007
801C	185-801C-15R-7 31-34	621.7	3.4	-0.4	massive flow	bleached basalt	BGR	Li et al., 2007
801C	185-801C-17R-4 15-18	637.4	3	-11.4	breccia	moderately to highly altered?	BGR + green celadonite breccia cement	Li et al., 2007
801C	185-801C-19R-2 24-27	653.43	1.8	-6.8	hyaloclastite	hyaloclastite (highly altered?)	not available	Li et al., 2007
801C	185-801C-21R-12 69-71	672.12	2.8	-6.3	massive flow	moderately altered	BGR	Li et al., 2007
801C	185-801C-25R-1 10-13	700.8	2.3	-7	pillow/flow	slightly altered	BGR	Li et al., 2007
801C	185-801C-34R-1 93-96	786.23	1.3	-3.9	massive flow	slightly altered	BGR + halos	Li et al., 2007
801C	185-801C-37R-5 112-114	819.58	2.5	-3.1	massive flow	highly altered	smectite vein + halos	Li et al., 2007
801C	185-801C-40R-1 24-27	841.74	3.6	-11.6	breccia	moderately to highly altered?	not available	Li et al., 2007
801C	185-801C-43R-1 13-15	869.23	3.8	-9.4	massive flow	slightly altered	BGR	Li et al., 2007
801C	185-801C-43R-3 50-55	872.42	2.3	-3	massive flow	highly altered	celadonite veins + halos	Li et al., 2007
801C	185-801C-44R-3 23-26	881.79	2.4	-5.9	massive flow	highly altered	calcite veins and halos	Li et al., 2007
1149B	185-1149B-30R-1 61-66	417.4	1.4	-4.9	pillow breccia	breccia	BGR?	Li et al., 2007
1149B	185-1149B-30R-2 56-62	418.4	2.3	-1.8	pillow	highly altered	green halo	Li et al., 2007
1149C	185-1149C-10R-2 47-51	409.3	2.7	-2.8	pillow	slightly altered	BGR	Li et al., 2007

Site	ID (Leg-Hole-Core-Section Interval)	Depth (mbsf)	N (ppm)	$\delta^{15}N$ (‰)	Lithology	Visual Description	Alteration Type*	Ref
1149D	185-1149D-7R-1 37-42	320.0	2.5	-0.8	hyaloclastite	hyaloclastite (highly altered?)	not available	Li et al., 2007
1149D	185-1149D-9R-3 30-32	341.7	2.1	-7.9	pillow	moderately altered?	BGR + orange/brown/green halos	Li et al., 2007
1149D	185-1149D-11R-2 86-92	360.1	1.5	-6.9	breccia	moderately to highly altered?	BGR?	Li et al., 2007
1149D	185-1149D-16R-3 2-8	408.9	1.7	-6.5	pillow	slightly altered	BGR	Li et al., 2007
1149D	185-1149D-17R-1 92-98	416.4	1.4	-4.3	breccia	slightly altered	BGR	Li et al., 2007
1149D	185-1149D-19R-1 85-89	435.5	2.5	-10.5	pillow	slightly altered	BGR	Li et al., 2007
279A	29-279A-13R-2 0-2	n.a	3.3	0.5	basalt	n.a	not available	Li et al., 2007
279A	29-279A-13R-2 116-120	n.a	4.7	4.2	basalt	n.a	not available	Li et al., 2007
319A	34-319A-3R-4 50-53	n.a	2.6	0.1	basalt	n.a	not available	Li et al., 2007
332B	37-332B-33R-2 77-80	n.a	7.8	-5.4	basalt	n.a	not available	Li et al., 2007
396B	46-396B-15R-3 83-89	n.a	12.1	4.8	basalt	n.a	not available	Li et al., 2007
448A	59-448A-41R-1 2-7	n.a	6.5	3.3	basalt	n.a	not available	Li et al., 2007
448	59-448-61	n.a	11.7	3.8	basalt	n.a	not available	Li et al., 2007
458	60-458-33R-2 74-77	n.a	13.4	5.5	basalt	n.a	not available	Li et al., 2007
459B	60-459B-66R-1 100-102	n.a	15.2	6.2	basalt	n.a	not available	Li et al., 2007
462A	61-46222R-2 120-124	n.a	7.6	-0.6	basalt	n.a	not available	Li et al., 2007

*BGR: background alteration.

Table A 2. Summary of parameters employed in the calculation of N input flux into the world's major subduction zones.

Subduction Zones	Length (km)[a]	CR[a] (mm/yr)	Age (Ma)[a]	Reference site[b]	Basement reached?	Basal Sed type[c]	Assigned Sed N[d] (ppm)	AOC N (ppm)[e]
Southern Chile	1218	16	16	n.p	no	n.p	n.p	$10.1^{\pm7.8}$
Central Chile	1306	71	23	n.p	no	n.p	n.p	$10.1^{\pm7.8}$
North Chile	1579	74	41	320,321	yes	nanno ooze	$171.4^{\pm71.8}$	$13.0^{\pm5.3}$
Peru	1599	65	37	320,321	yes	nanno ooze	$171.4^{\pm71.8}$	$13.0^{\pm5.3}$
Columbia-Ecuador	1355	65	21	677,678	yes	chalk	$171.4^{\pm71.8}$	$13.0^{\pm5.3}$
Central America[f]	1400	85	16	1256,504	yes	chalk	n.p	$9.9^{\pm2.7}$
Mexico	1383	49	9	487	yes	clay	$297.0^{\pm42.8}$	$21.3^{\pm4.2}$
Kurile	1243	75	128	1179	yes	chert	$20.5^{\pm3.5}$	$2.0^{\pm0.4}$
Kamchatka	900	74	115	192	yes	nannofossil chalk and calcareous claystone	$171.4^{\pm71.8}$	$13.0^{\pm5.3}$
NE Japan	1061	76	132	436	no	n.p	n.p	$10.1^{\pm7.8}$
Izu-Bonin-Mariana[f]	2450	41	140	801	yes	Chert + radiolarite	n.p	$7.0^{\pm5.4}$
Ryukyu	1153	57	46	294,195	yes	clay	$297.0^{\pm42.8}$	$21.3^{\pm4.2}$
Philippine	1509	64	43	291	yes	silty clay to zeolite-rich clay	$297.0^{\pm42.8}$	$21.3^{\pm4.2}$
Tonga	1460	148	100	204	no	n.p	n.p	$10.1^{\pm7.8}$
Kermadec	1422	52	100	1124	no	n.p	n.p	$10.1^{\pm7.8}$
Hikurangi	794	21	100	1124	no	n.p	n.p	$10.1^{\pm7.8}$
South Sandwich	1005	44	57	701	yes	nannofossil chalk + siliceous ooze	$171.4^{\pm71.8}$	$13.0^{\pm5.3}$
Lesser Antilles†	800	24	81	543,144	yes	clay	n.p	$24.9^{\pm8.3}$

Subduction Zones	Length (km)[a]	CR[a] (mm/yr)	Age (Ma)[a]	Reference site[b]	Basement reached?	Basal Sed type[c]	Assigned Sed N[d] (ppm)	AOC N (ppm)[e]
Aleutians,	1102	18	72	n.p	no	n.p	n.p	$10.1^{\pm 7.8}$
Aleutians, E	1246	59	56	183	no	n.p	n.p	$10.1^{\pm 7.8}$
Alaska	1490	56	49	178	yes	clay	$297.0^{\pm 42.8}$	$21.3^{\pm 4.2}$
Nankai	824	38	23	1173,1177	yes	clay	$297.0^{\pm 42.8}$	$21.3^{\pm 4.2}$
Sumatra	2462	50	61	211	yes	clay	$297.0^{\pm 42.8}$	$21.3^{\pm 4.2}$
Java	1200	71	100	260, 261	yes	clay	$297.0^{\pm 42.8}$	$21.3^{\pm 4.2}$
Sunda E.	950	71	145	260, 261	yes	clay	$297.0^{\pm 42.8}$	$21.3^{\pm 4.2}$
Andaman-Burma	1089	23	83	218, 718	no	n.p	n.p	$9.9^{\pm 7.6}$
Markan	950	37	97	222, 223	yes	clay	$297.0^{\pm 42.8}$	$21.3^{\pm 4.2}$
Aegean	850	5	90	374, 131	no	n.p	n.p	$10.1^{\pm 7.8}$
Cascadia	990	36	5	174, 888	no	n.p	n.p	$10.1^{\pm 7.8}$
Manlia	1050	10	30	n.p	no	n.p	n.p	$10.1^{\pm 7.8}$
Negros	400	20	16	n.p	no	n.p	n.p	$10.1^{\pm 7.8}$
Sulawesi. N	600	30	42	n.p	no	n.p	n.p	$10.1^{\pm 7.8}$
Sulu	500	20	16	n.p	no	n.p	n.p	$10.1^{\pm 7.8}$
Cotabato	500	20	42	n.p	no	n.p	n.p	$10.1^{\pm 7.8}$
San Cristobal	1050	49	50	n.p	no	n.p	n.p	$10.1^{\pm 7.8}$
Yap-Palau	550	3	32	n.p	no	n.p	n.p	$10.1^{\pm 7.8}$
Torbriand	590	20	50	n.p	no	n.p	n.p	$10.1^{\pm 7.8}$
Vanuatu	1189	111	40	n.p	no	n.p	n.p	$10.1^{\pm 7.8}$
New Britain	600	110	50	n.p	no	n.p	n.p	$10.1^{\pm 7.8}$

a. Convergence rate (CR), trench length, age data are from Jarrard. (2003).
b. Reference site information is from Clift. (2017).
c. The sediments type of basal sediments section that were deposited directly overlying the igneous basement.
d. Assigned N concentration of the basal sediments according to the sediments type.
e. The N concentration of the upper oceanic crust was calculated by equation in Fig. 5.
f. Along Central American, Izu-Bonin-Mariana and Lesser Antilles, N input fluxes were calculated employing their reference sites (Holes 1256D and 504B: Central America; Hole 801C: Izu-Bonin-Mariana; Hole 543A: Lesser Antilles).
g. n.p: not applicable

Appendix B – Supplementary material for Chapter 2.2

B1 Supplementary tables

Table B 1. Lithology, N concentrations and $\delta^{15}N$ values of the gabbroic samples in this study.

Sample ID	Depth （mbsf)	Lithology[a]	N (ppm)	$\delta^{15}N$ (‰)
304-1309D-4R-2W 136-137	34.26	G	8.6	3.3
304-1309D-22R-2W 41-42	127.93	Troc	9.0	2.5
304-1309D-49R-2W 25-27	258.95	Ol G	5.1	1.2
304-1309D-78R-3W 38-39	399.61	Ol G	4.6	1.3
305-1309D-120R-2W 34-35	594.12	G	3.5	0.1
305-1309D-155R-2W 20-21	759.14	G	6.9	0.7
305-1309D-160R-2W 119-120	782.49	G	3.5	-0.7
305-1309D-170R-3W 18-20	830.24	G	8.3	2.7
305-1309D-196R-2W 51-52	950.97	G	3.9	2.1
304-1309D-225R-1W 75-77	1083.15	Ol G	3.5	-0.9
305-1309D-244R-1W 13-15	1172.83	G	3.8	1.8
305-1309D-264R-1W 47-49	1317.59	G	4.2	2.7
305-1309D-280R-1W 15-17	1344.15	G	3.6	1.7
345-U1415P-3R-1W 16-17	12.8	Ol G	6.6	1.5
345-U1415P-6R-2W 18-19	24.3	Ol G	4.9	0.5
345-U1415P-7R-1W 21-22	27.3	Ol G	8.3	2.7
345-U1415P-11R-1W 60-61	46.1	Ol G	8.5	2.1
345-U1415P-15R-1W 34-35	64.2	Ol G	9.8	5.1
345-U1415P-16R-1W 78-79	68.5	Troc	6.4	1.9
345-U1415P-17R-1W 28-30	73.2	Troc	8.7	3.4
345-U1415P-20R-1W 69-70	82.8	Troc	4.0	-1.3
345-U1415P-22R-2W 45-46	91.3	Troc	8.5	3.5
345-U1415P-23R-1W 65-66	99.5	Troc	5.8	0.7
118-735B-1D-01-WW 69-73	0.69	G	18.7	3.8
118-735B-10D-02-WW 17-21	37.72	G	8.3	0.3
118-735B-16R-05-WW 40-43	66.773	G	8.5	2.9
118-735B-23R-02WW 29-30	101.371	Ol G	11.9	-1.9
118-735B-37R-01WW 22-25	176.22	G	6.3	-1.3
118-735B-52R-04-WW 60-61	252.334	G	5.2	-2.7
118-735B-80R-06WW 16-17	430.913	Ol G	4.4	1.9
176-735B-90R-1WW 105-107	508.764	Ol G	6.0	-0.2
176-735B-95R-01WW 105-109	545.65	Ol G	9.2	0.6

Sample ID	Depth （mbsf)	Lithology[a]	N (ppm)	$\delta^{15}N$ (‰)
176-735B-108R-2WW 36-37	625.33	Ol G	2.7	0.4
176-735B-122R-02-WW 11-15	730.794	G	4.5	0.9
176-735B-130R-04WW 116-119	799.3	Ol G	6.7	-1.7
176-735B-149R-07-WW 118-121	968.651	G	6.3	3.1
176-735B-180R-05WW 38-40	1236.66	Ol G	7.0	2.6
176-735B-200R-04-WW 37-38	1406.537	Ol G	5.4	1.0

a. Trco: troctolite; Ol G: olivine gabbro; G: gabbro.

B2 Supplementary information

Estimation of the unit N input flux of the gabbroic oceanic crust in the lower-endmember case scenario

In the lower-endmember case scenario for the estimation of the 5000 m-thick gabbroic section, we assumed that N concentrations exponentially decrease from $7.9^{\pm 4.1}$ ppm (the average value of gabbros of Holes 1256D, 1309D, 735B and 1415P) at 2000 m to 1.5 ppm (the value of fresh oceanic crust; Marty, 1995; Li et al., 2007; Marty et al., 2020) at 7000 m. The N concentration along depth can be described by Equation (1):

$$C_{N(D)} = A \cdot e^{-b \cdot D} \tag{1}$$

where $C_{N(D)}$ is the N concentration in ppm at the depth of D (in m); A and b are constants, which are determined to be $15.4^{+12.2}_{-9.8}$ and $3.0^{+0.1}_{-0.1}\times 10^{-4}$, respectively, by fitting Equation (1) to $7.9^{\pm 4.1}$ ppm at 2000 m to 1.5 ppm at 7000 m.

The unit N input flux (F_N) for subduction of 1 m × 1 m (in surface area) gabbroic section can then be calculated by Equation (2):

$$F_N = \int_{2000}^{7000} C_{N(D)} \cdot \rho \cdot L \cdot R \cdot dD \tag{2}$$

where ρ is the average dry density of 3.0 $g \cdot cm^{-3}$ of the gabbroic lower oceanic crust; L is the unit trench length (1 m); R is the unit width (1 m). This calculation gave a unit N input flux of $5.0^{+1.1}_{-2.2}\times 10^{3}$ $mol \cdot m^{-2}$. This parameter can integrate with subduction rate (in $m \cdot yr^{-1}$) and trench length (in m) to calculate the input flux for individual or global subduction zones.

Appendix C – Supplementary material for Chapter 2.3

C1 Supplementary tables

Table C 1. Lithologies, N concentrations and $\delta^{15}N$ values of the examined oceanic serpentinites in this study.

Sample ID	Protolith	Lithology	Depth (mbsf)	N (ppm)	$\delta^{15}N$ (‰)
147-895D-1R-1W 28-31	Harzburgite	Serpentinite	0	6.9	0.6
147-895D-2R-2W 8-9†		serpentine vein	18	94.0	5.9
147-895D-2R-2W 8-9††	Dunite	Serpentinite	18	7.6	-2.2
147-895D-4R-2W 38-40†		serpentine vein	35	34.9	5.7
147-895D-4R-2W 38-40††	Harzburgite	Serpentinite	35	5.3	2.6
147-895D-6R-1W 58-60	Harzburgite	Serpentinite	56	14.6	2.4
147-895D-7R-1W 2-4	Dunite	Serpentinite	65	13.6	0.4
148-895D-8R-2W 88-90	Harzburgite	Serpentinite	76	7.2	1.4
147-895D-8R-2W 96-98	Dunite	Serpentinite	77	4.7	-1.3
147-895D-9R-2W 24-26	Dunite	Serpentinite	86	4.9	-2.9
153-920D-2R-1W 37-40	Harzburgite	Serpentinite	8	6.1	3.8
153-920D-5R-4W 12-13	Harzburgite	Serpentinite	41	9.2	0.3
153-920D-10R-3W 74-75	Harzburgite	Serpentinite	82	5.3	1.1
153-920D-12R-5W 37-38	Harzburgite	Serpentinite	101	16.8	0.1
153-920D-19R-2W 15-17	Harzburgite	Serpentinite	164	9.1	2.8
153-920D-20R-2W 28-31	Harzburgite	Serpentinite	173	5.5	-3.3
153-920D-22R-2W 75-78	Harzburgite	Serpentinite	193	3.2	-0.7
209-1271B-5R-1W 48-50	Dunite	Serpentinite	28	12.9	-0.5
209-1271B-10R-1W 102-104	Harzburgite	Serpentinite	52	5.9	2.0
209-1271B-12R-1W 112-115	Dunite	Serpentinite	61	7.6	4.4
209-1271B-18R-1W 43-45	Dunite	Serpentinite	90	6.5	1.0
209-1271B-19R-2W 18-21	Dunite	Serpentinite	96	18.6	1.8
209-1274A-2R-1W 19-22	Harzburgite	Serpentinite	12	10.8	2.2
209-1274A-6R-1W 43-45	Harzburgite	Serpentinite	31	7.5	1.3
209-1274A-11R-1W 38-41	Harzburgite	Serpentinite	55	6.3	1.9
209-1274A-16R-2W 61-63	Harzburgite	Serpentinite	86	12.4	2.2
209-1274A-20R-1W 51-54	Dunite	Serpentinite	103	6.9	-1.4
209-1274A-25R-1W40-43	Dunite	Serpentinite	137	13.1	-1.9

†. Serpentine vein minerals that were drilled from 1–2 mm wide veins in the sample.

††. Bulk-rock N analysis with 1–2 mm serpentine veins completely removed by drill bit.

C2 Supplementary information

Detailed core descriptions

(1) ODP Hole 895D

Serpentinites from Hole 895D were exhumed onto the seafloor due to deep faulting associated with the westward propagation of the east-west trending Cocos-Nazca spreading center, which opens up the eastern flank of the young oceanic crust generated at the fast-spreading East Pacific Rise (Früh-Green et al., 1996). Serpentinites from this hole include serpentinized harzburgite and dunite, which are highly to completely altered (~60% – 100%). These serpentinites record an alteration history from early greenschist-facies alteration represented by a secondary mineral assemblage of serpentine + magnetite ± tremolite ± brucite ± chlorite ± talc to late zeolite-facies alteration represented by a secondary mineral assemblage of clay ± carbonate (Shipboard Scientific Party, 1993b). The serpentinization is estimated to occur at high temperatures of 200 – 400 ºC based on the low $\delta^{18}O$ values of serpentine mineral separates (+3.2‰ – +4.1‰; Agrinier et al., 1995; Früh-Green et al., 1996; Mével and Stamoudi, 1996; Alt et al., 2013).

(2) ODP Holes 1271B and 1274A

ODP Holes 1271B and 1274A were drilled on the western wall of the axial valley north and south of the 15°20'N fracture zone at the Mid-Atlantic Ridge (MAR) during ODP Leg 209 (Shipboard Scientific Party, 2004a, b). Serpentinites from Holes 1271B and 1274A were exposed by crustal thinning along long-lived low-angle detachment faults (Alt et al., 2007). ODP Hole 1271B penetrated 103.6 m into a complex association of altered peridotite and gabbroic rocks. Dunite accounts for 56% in the 16 m recovered rocks, with the remainder consisting of 9% harzburgite and 35% gabbroic rocks. Serpentinites from this hole were highly to completely altered (~60% –

100%) and recorded a history from early greenschist- to late zeolite-facies alterations (Shipboard Scientific Party, 2004a). The dominant secondary mineral assemblage includes serpentine + brucite + magnetite, with local presence of minor orange clay + iron oxyhydroxide from the late-stage zeolite-facies alteration (Shipboard Scientific Party, 2004a). Black serpentine + magnetite veins are the dominant vein type in Hole 1271B, forming anastomosing networks (Shipboard Scientific Party, 2004a). The elevated sulfide-sulfur contents and high δ^{34}S values (up to ~2 wt.% and 4 – 10 ‰), suggesting hydrothermal addition of sulfides, indicates that serpentinization occurs at high temperature of ~250 – 400 ºC (Alt et al., 2007). The 1271B samples for this study are highly to completely (90–100%) serpentinized harzburgite/dunite.

Hole 1274A penetrated 156 m into the basement and the recovered 34 m rocks were comprised of 77% serpentinized harzburgite, 20% dunite, and 3% gabbro. The uppermost 90 m are affected by oxidative seawater alteration, forming centimeter-wide halos (Fe-oxyhydroxide) along carbonate veins. Systematic downhole increase of alteration degree to nearly 100% serpentinization is probably associated with large faults in the lower section of the hole (Shipboard Scientific Party, 2004b). The lower half of the hole is completely altered (> 95 vol% secondary minerals) to brucite + serpentine + magnetite (Shipboard Scientific Party, 2004b). The serpentinization is estimated to occur at low temperature of < 150 ºC as revealed by the generally high bulk-rock δ^{18}O values (up to ~8.1‰; Alt et al., 2007, 2013). This is consistent with the elevated high sulfide-sulfur contents (up to ~3000 ppm) with negative δ^{34}S values down to -32.1‰ reflecting low-temperature microbial reduction (Alt et al., 2007). The 1274A samples for this study are serpentinized harzburgite/dunite that are highly to completely altered (65–100%).

(3) ODP Hole 920D

Hole 920D is located in the 2 km wide western median valley wall of the MAR and nearly 30 km south of the Kane Transform (MARK) (Shipboard Scientific Party, 1995) (Fig. 13). Gabbroic rocks and peridotite (< 1 Ma-old) are exposed near seafloor localities by lithospheric extension along a detachment fault (Karson and Lawrence, 1997). The 95.08 m recovered rocks from Hole 920D are dominantly serpentinized harzburgite (83%) and dunite (12%). The recovered rocks from Hole 920D display 75 – 100% alteration and are characterized by extensive development of mesh-textured serpentine and minor amounts of talc, amphibole and chlorite, with carbonate minerals being formed during the latest generation of veining (Shipboard Scientific Party, 1995). The generally low bulk-rock $\delta^{18}O$ values (2.6 – 3.7‰) of these serpentinites indicate a high serpentinization temperature of > 350 ºC (Agrinier and Cannat, 1997), consistent with high sulfide-sulfur concentrations and elevated $\delta^{34}S$ values (up to 1 w.% and 12.7‰) pointing to the addition of sulfide during high-temperature hydrothermal alteration (Alt and Shanks, 2003) .

Appendix D – Supplementary material for Chapter 3.1

D1 Supplementary tables

Table D 1. Nitrogen concentrations, $\delta^{15}N$ values, major and trace element data of the serpentinites.

Sample ID	Depth (mbsf)	Lithology*	N (ppm)	$\delta^{15}N$ (‰)	SiO_2 (wt.%)	TiO_2 (wt.%)	Al_2O_3 (wt.%)	Fe_2O_3 (wt.%)	MgO (wt.%)	MnO (wt.%)	CaO (wt.%)	Na_2O (wt.%)	K_2O (wt.%)	LOI (wt.%)	Total	Li (ppm)	B (ppm)	Cs (ppm)
1200A-3R-1W 77-80	19.0	Serp	5.7	0.2	37.99	0.014	0.35	7.4	40	0.11	0.37	0.13	0.02	14.51	100.89	9.0	39.8	1.185
1200A-6R-1W 44-47	41.8	Serp	5.4	1.0	37.2	0.018	0.41	7.36	40.61	0.105	0.52	0.13	0.01	14.315	100.68	2.6	12.3	0.247
1200A-7R-1W 09-11	51.2	Serp	6.1	0.1	38.24	0.015	0.65	6.95	38.69	0.112	0.57	0.18	0.02	14.885	100.31	2.1	44.3	0.476
1200A-7R-2W 130-133	53.0	Serp	5.4	-0.6	39.99	0.018	0.81	7.45	40.03	0.111	0.83	0.11	0.01	11.164	100.52	2.4	47.1	0.364
1200A-11R-1W 37-40	89.8	Serp	7.4	1.3	34.96	0.013	0.06	7.29	40.3	0.104	0.28	0.22	0.01	17.403	100.64	2.2	51.5	0.131
1200A-16R-1W 81-84	138.4	Serp	10.0	0.6	n.d	n.d	n.d	n.d	n.d	n.d	n.d	n.d	n.d	n.d	n.d	n.d	n.d	n.d
1200A-17G-2W 08-10	GC	Serp	10.4	-0.5	38.7	0.016	0.43	7.42	40.84	0.106	0.47	0.14	0.01	12.7	100.83	1.7	10.9	0.254
780C-6R-1W25-28	42.8	Serp	4.5	-0.4	40.53	0.014	0.39	7.96	43	0.112	0.57	0.09	0	7.989	100.65	5.2	19.7	0.291
780C-6R-1W 72-75	43.2	Serp	4.5	-0.6	39.81	0.013	0.64	7.3	40	0.111	0.65	0.12	0.01	11.544	100.2	5.4	62.2	0.304
780C-9R-1W 50-53	71.6	Serp	7.5	2.8	36.78	0.02	0.43	7	40.12	0.101	0.43	0.22	0.01	16.44	101.55	0.6	59.3	0.052
780C-13R-1W 60-64	107.1	Serp	6.8	0.8	37.39	0.019	0.9	7.22	40.01	0.114	0.61	0.21	0.01	13.555	100.04	4.0	15.0	0.127
780C-16R-1W 52-55	145.5	Serp	6.1	2.0	30.13	0.016	0.29	5.81	31.5	0.086	0.52	0.16	0	12.124	80.636	n.d	n.d	n.d
780C-18R-1W 4-8	154.0	Serp	5.1	1.2	37.23	0.017	0.6	7.66	41.92	0.106	0.38	0.11	0.01	11.717	99.749	3.8	16.8	0.218
780C-18R-1W 85-87	154.9	Serp	5.9	1.8	40.29	0.013	0.8	7.57	39.5	0.116	1.17	0.11	0	10.845	100.41	1.4	15.9	0.044

Sample ID	Depth (mbsf)	Lithology*	N (ppm)	$\delta^{15}N$ (‰)	SiO_2 (wt.%)	TiO_2 (wt.%)	Al_2O_3 (wt.%)	Fe_2O_3 (wt.%)	MgO (wt.%)	MnO (wt.%)	CaO (wt.%)	Na_2O (wt.%)	K_2O (wt.%)	LOI (wt. %)	Total	Li (ppm)	B (ppm)	Cs (ppm)
780C-18R-1W 133-136	155.3	Serp	3.7	1.3	n.d	n.d	n.d	n.d	n.d	n.d	n.d	n.d	n.d	n.d	n.d	n.d	n.d	n.d
779A-5R-1W 57-60	30.2	Serp	9.2	-0.2	34.44	0.013	0.07	7.19	40.87	0.104	0	0.14	0	17.41	100.24	5.4	59.0	0.023
779A-5R-2W 47-50	31.6	Serp	6.5	1.2	n.d	n.d	n.d	n.d	n.d	n.d	n.d	n.d	n.d	n.d	n.d	n.d	n.d	n.d
779A-8R-1W 46-49	59.0	Serp	3.6	0.0	37.39	0.013	0.99	8.11	40.54	0.114	0.42	0.12	0.01	3.82	91.531	8.1	24.0	0.249
779A-10R-1W 28-31	78.0	Serp	4.1	-0.2	39.92	0.017	0.49	8.46	43.6	0.12	0.52	0.11	0	7.31	100.55	2.2	23.9	0.091
779A-14R-2W 28-32	118.0	Serp	4.3	1.9	40.62	0.014	0.74	8.06	41.29	0.117	0.82	0.12	0.01	8.64	100.44	3.8	17.2	0.109
779A-16R-2W 21-25	137.2	Serp	6.1	-1.3	37.55	0.015	0.55	7.26	39.92	0.111	0.41	0.19	0	14.4	100.46	1.9	46.3	0.059
779A-18R-1W 1-4	154.9	Serp	5.4	1.2	41.97	0.02	0.76	7.56	40.96	0.117	0.73	0.12	0.02	8.21	100.47	3.9	23.6	0.415
779A-18R-1W 126-129	156.2	Serp	10.6	-0.3	39.42	0.012	0.12	5.95	39.04	0.075	0.04	0.52	0.01	15.44	100.63	1.1	12.6	0.013
779A-22R-3-W 53-56	173.6	Serp	5.2	2.4	39.06	0.012	0.06	7.84	43.96	0.109	0.07	0.11	0	9.037	100.26	4.6	11.2	0.127
779A-25R-2W 5-9	198.4	Serp	6.3	2.2	38.26	0.014	0.2	7.59	43.1	0.108	0.3	0.11	0	10.88	100.56	2.7	31.9	0.264
779A-31R-1W 13-17	254.8	Serp	5.0	-0.3	40.41	0.012	0.38	6.88	37.03	0.081	1.84	0.18	0	13.17	99.988	2.2	8.0	0.031
U1498B-3R-1W 46-50	19.7	Serp	5.8	0.7	32.57	0.014	0	5.32	43.43	0.092	0.03	0.13	0	19.38	100.94	0.8	61.3	0.018
U1498B-3R-3W 95-100	21.4	Serp	3.9	-3.4	35.68	0.016	0.29	6.13	40.44	0.091	0.3	0.12	0	17.68	100.74	1.9	33.0	0.023
U1498B-4R-1W 103-106	29.9	Serp	12.0	0.9	34	0.014	0	6.45	41.42	0.089	0.18	0.16	0	18.34	100.59	1.2	19.5	0.006
U1498B-5R-1W 93-96	35.6	Serp	12.8	-0.8	31.49	0.015	0	7.02	42.99	0.089	0.27	0.16	0	18.41	100.37	3.2	19.7	0.006

Sample ID	Depth (mbsf)	Lithology*	N (ppm)	$\delta^{15}N$ (‰)	SiO_2 (wt.%)	TiO_2 (wt.%)	Al_2O_3 (wt.%)	Fe_2O_3 (wt.%)	MgO (wt.%)	MnO (wt.%)	CaO (wt.%)	Na_2O (wt.%)	K_2O (wt.%)	LOI (wt. %)	Total	Li (ppm)	B (ppm)	Cs (ppm)
U1498B-7R-4W 3-6	56.6	Serp	4.4	-1.4	34.67	0.019	0.49	7.35	39.39	0.125	0.4	0.15	0	18.02	100.61	2.1	18.5	0.011
U1498B-7R-4W 132-135	57.9	Serp	5.1	-1.3	37.73	0.017	0.34	6.68	40.73	0.089	0.65	0.09	0	14.19	100.52	2.1	29.4	0.138
U1498B-7R-1W 69-72	54.8	Serp M	11.8	-1.6	38.98	0.014	0.38	7.07	37.27	0.08	2.34	0.32	0	14.26	100.71	0.4	13.2	0.003
1498B-11R-2W 0-3	94.6	Serp M	15.4	-1.8	38.42	0.019	0.41	6.85	39.18	0.082	0.04	0.33	0	15.55	100.88	0.8	13.4	0.023
U1498B-14R-3W 0-3	125.1	Serp M	11.1	-3.8	38.9	0.015	0.33	6.04	39.19	0.07	0.35	0.39	0.01	15.19	100.48	0.5	13.5	0.008
1498B-23R-1W 145-147	201.5	Serp M	16.4	-0.7	39.5	0.023	0.65	6.21	39.34	0.088	0.06	0.32	0	14.34	100.53	0.4	20.2	0.009
U1498B-23R-2W 0-3	201.6	Serp M	9.7	-1.1	39.1	0.03	0.68	6.46	38.9	0.094	0.09	0.37	0.01	14.21	99.947	0.2	21.0	0.008
784A-38R-2W 50-52	350.3	Serp	7.1	0.8	35.74	0.015	0.23	6.92	39.54	0.109	0.04	0.26	0	18.06	100.91	0.7	67.0	0.029
784A-40R-2W 72-74	369.7	Serp	8.2	2.5	33.5	0.015	0.03	7.79	41.65	0.108	0.13	0.11	0	17.48	100.8	0.4	54.4	0.014
784A-45R-1W 75-79	416.4	Serp	4.7	0.9	36.3	0.016	0.39	7.02	39.63	0.106	0.32	0.11	0	16.46	100.34	0.9	51.2	0.060
784A-45R-1W 125-129	415.7	Serp	5.9	0.5	38.59	0.017	0.55	6.88	37.58	0.114	1.37	0.12	0	15.21	100.43	5.5	56.3	0.388
784A-45R-2W 08-11	417.2	Serp	7.0	1.0	34.63	0.013	0	7.55	41.54	0.105	0.16	0.09	0	16.96	101.02	0.9	43.1	0.012

*. Serp = serpentinite; Serp M = serpentinite mud

D2 Supplementary figures

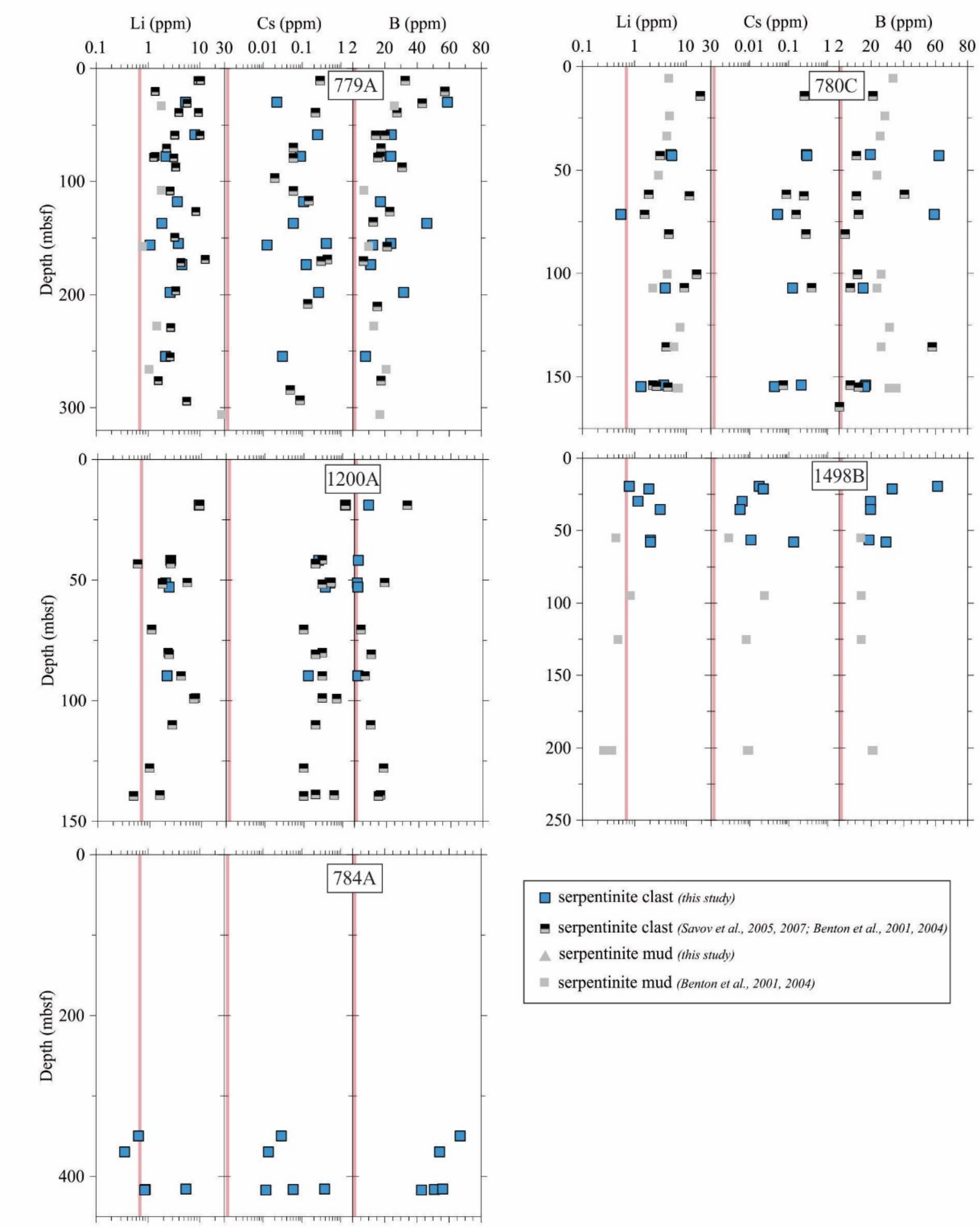

Fig. D1 Downhole variations of Li, Cs and B concentrations in Holes 779A, 780C, 1200A, 1498B and 784A. Note that B concentrations show a stepwise decrease trend along depth due to the interaction with seawater at the top section of the hole. The red lines mark the Li (0.7 ppm), Cs (0.0013 ppm) and B (0.06 ppm) concentrations of the depleted mantle (Salters and Stracke, 2004).

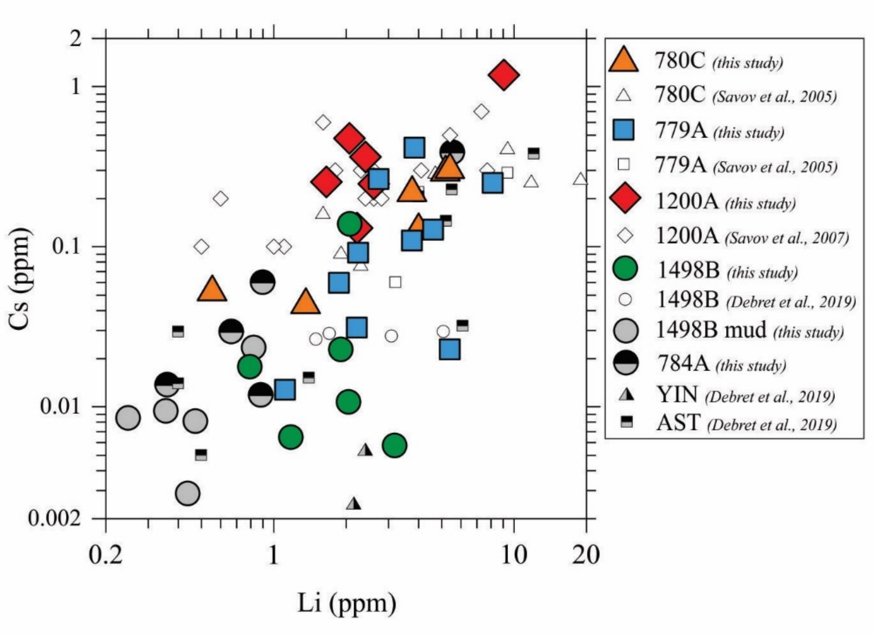

Fig. D2 Diagram showing positive correlation between Li and Cs concentrations of serpentinite clasts and muds (data source: Savov et al., 2005, 2007; Debret et al., 2019).

Appendix E - Supplementary material for Chapter 3.2

E1 Supplementary tables

Table E 1. Nitrogen concentrations, $\delta^{15}N$ values, major and trace element compositions of blueschists from Heilongjiang Complex, Northeast China.

	Mudanjiang blueschists												
	20HLJ-14	20HLJ-14-1	20HLJ-14-2	20HLJ-14-3	20HLJ-15	20HLJ-15-1	20HLJ-15-2	20HLJ-15-3	15HLJ-06	15HLJ-02	15HLJ-05B	15HLJ-01	15HLJ-04
SiO_2	45.22	44.21	44.37	42.78	43.65	44.73	46.65	43.15	44.75	45.1	42.87	45.29	40.01
TiO_2	2.48	2.33	2.47	2.24	1.98	1.57	2.06	3.20	1.971	2.105	2.715	2.15	2.368
Al_2O_3	16.36	15.98	15.85	15.61	17.20	13.96	18.43	15.79	14.21	16.27	17.24	16.77	15.51
TFe_2O_3	12.46	12.91	11.76	11.91	12.90	11.41	12.98	14.95	11.3	13.23	15.37	12.36	12.21
MnO	0.12	0.17	0.12	0.23	0.10	0.11	0.08	0.11	0.128	0.144	0.144	0.159	0.178
MgO	3.78	6.93	4.74	5.00	2.99	2.97	3.27	3.02	2.69	3.94	3.83	3.55	4.01
CaO	8.92	7.01	9.38	11.63	9.10	11.05	5.48	8.26	12.6	9.24	9.64	10.49	14.47
Na_2O	3.85	3.98	3.62	2.94	3.21	3.51	3.81	3.09	3.86	3.66	2.29	3.6	3.08
K_2O	1.38	0.53	1.22	0.77	2.51	1.67	2.89	2.53	1.95	1.43	2.12	1.31	1.03
P_2O_5	0.39	0.37	0.36	0.35	0.27	0.29	0.31	0.62	0.31	0.38	0.36	0.52	0.37
LOI	4.61	5.19	5.75	6.51	5.75	8.30	3.73	5.07	5	2.9	3.37	4.09	7.12
Total	99.57	99.61	99.64	99.97	99.66	99.57	99.69	99.79	98.77	98.4	99.94	100.3	100.3
Li (ppm)	23.0	37.1	24.5	28.4	33.4	29.1	34.9	32.0	n.d	n.d	n.d	n.d	n.d
Be	1.28	1.07	1.46	1.02	1.20	0.81	1.35	1.94	2	1	1	1	< 1
Sc	31.6	29.7	27.0	26.3	33.7	25.9	32.9	31.9	24	28	31	27	27
V	214	197	207	220	247	199	259	300	204	203	277	231	214
Cr	224	226	219	224	111	98.4	105	164	190	210	270	220	230
Co	41.7	90.6	67.2	75.1	43.0	70.6	60.4	50.6	25	46	42	40	52
Ni	147	212	180	213	122	119	118	123	100	150	140	160	170
Cu	49.4	58.9	71.2	65.6	50.3	51.0	42.9	50.7	40	40	50	50	40

	Mudanjiang blueschists												
Zn	98.7	135	110	105	89.2	90.5	97.2	112	70	110	120	90	120
Ga	15.4	18.1	15.7	20.2	16.8	13.3	17.4	24.6	12	16	20	18	17
Ge	1.33	1.36	1.33	1.74	1.28	0.97	1.20	2.43	< 1	1	2	2	1
Rb	37.1	15.1	33.5	21.7	54.7	37.2	65.0	64.9	50	36	54	34	24
Sr	235	212	248	412	234	185	164	314	204	212	281	281	371
Y	33.2	29.7	29.4	32.3	26.1	19.1	28.4	58.3	25	30	36	30	29
Zr	184	182	182	168	123	95.3	131	320	153	161	214	165	183
Nb	18.6	19.2	19.0	17.7	10.4	7.98	11.2	30.9	14	15	20	17	17
Cs	1.74	0.65	1.56	1.02	2.94	2.10	3.33	4.25	2.1	1.5	2.4	1.5	1.1
Ba	143	58.6	113	76.1	238	148	280	259	204	140	208	132	96
La	16.0	13.8	12.3	15.5	8.75	6.20	10.1	27.5	13.5	16.4	19.9	15	13.8
Ce	36.1	33.0	29.1	34.7	21.7	16.2	24.0	62.1	29.6	35	44.3	34.7	32.4
Pr	4.56	4.19	3.82	4.43	2.80	2.16	3.16	9.12	4.04	4.77	5.87	4.64	4.38
Nd	22.1	19.9	18.7	21.4	14.3	11.1	16.2	44.8	19	22.7	27.6	21.8	20.3
Sm	5.51	5.22	4.89	5.38	4.03	3.09	4.45	10.9	4.9	5.8	6.9	5.5	5.3
Eu	1.80	1.76	1.60	1.82	1.40	1.07	1.57	3.34	1.71	1.95	2.44	2.01	1.84
Gd	5.73	5.48	5.03	5.47	4.27	3.29	4.80	11.0	5.3	6.4	7.8	6.1	5.8
Tb	0.94	0.89	0.84	0.90	0.74	0.56	0.83	1.81	0.8	1	1.2	1	0.9
Dy	5.77	5.45	5.20	5.60	4.61	3.50	5.15	11.1	5	5.8	7.2	5.7	5.4
Ho	1.19	1.09	1.06	1.14	0.94	0.71	1.06	2.16	1	1.2	1.4	1.1	1.1
Er	3.31	2.98	2.98	3.20	2.63	1.95	2.90	5.87	2.8	3.3	4	3.2	3
Tm	0.49	0.43	0.44	0.48	0.39	0.29	0.42	0.86	0.38	0.44	0.57	0.44	0.44
Yb	3.10	2.71	2.72	2.96	2.38	1.79	2.61	5.27	2.5	2.8	3.6	2.8	2.9
Lu	0.48	0.40	0.42	0.46	0.36	0.27	0.39	0.78	0.36	0.44	0.55	0.41	0.42
Hf	4.10	3.93	4.05	3.73	2.98	2.32	3.21	7.36	3.4	3.9	4.9	3.8	4.1
Ta	1.20	1.20	1.22	1.15	0.67	0.56	0.73	1.97	0.9	1	1.4	1.1	1.1

	Mudanjiang blueschists												
Pb	0.77	0.80	0.84	1.56	0.59	0.43	0.82	1.78	< 5	< 5	< 5	< 5	< 5
Th	1.03	1.02	0.98	0.97	0.62	0.51	0.67	1.99	0.8	1	1.3	1	1
U	0.49	0.38	0.42	0.52	0.39	0.25	0.39	0.76	0.4	0.5	0.6	0.5	0.5
N (ppm)	21.9	49.2	29.7	33.3	48.9	35.0	62.6	83.6	27.5	21.1	25.6	21.6	13.9
δ^{15}N (‰)	0.5	2.1	3.6	1.6	0.5	1.2	1.0	2.2	3.7	1.4	-0.5	1.7	1.1

	Yilan blueschists													
	19HLJ-04	19HLJ-07	19HLJ-08	19HLJ-09	19HLJ-10	19HLJ-11	19HLJ-12	20HLJ-31-1	20HLJ-31-2	20HLJ-31-3	15HLJ-38	15HLJ-39	15HLJ-40	15HLJ-41
SiO$_2$ (wt.%)	47.34	39.86	52.32	51.08	51.10	50.64	50.32	47.31	45.84	45.67	46.04	47.24	45.49	45.63
TiO$_2$	2.64	2.50	3.26	2.69	2.93	2.97	2.86	2.89	1.96	2.92	4.556	3.465	3.303	3.126
Al$_2$O$_3$	14.91	11.28	13.79	14.58	14.86	13.46	13.14	14.63	13.30	18.51	12.59	12.35	12.21	13.16
TFe$_2$O$_3$	12.66	10.82	12.55	11.30	11.51	12.01	13.93	13.12	9.58	10.85	15.91	15.31	13.02	13.43
MnO	0.19	0.22	0.07	0.11	0.08	0.10	0.07	0.16	0.14	0.13	0.132	0.109	0.125	0.125
MgO	6.15	6.32	5.04	5.46	5.32	5.90	3.66	6.23	4.92	5.30	4.94	4.88	4.28	4.28
CaO	9.00	11.92	1.89	3.06	2.30	2.25	3.44	8.41	10.10	8.00	7.62	5.26	10.31	9.63
Na$_2$O	2.85	2.09	3.00	2.79	2.77	3.23	5.48	3.21	5.16	3.26	3.83	3.78	4.48	4.08
K$_2$O	0.61	3.35	5.09	5.37	5.37	4.96	2.95	0.30	0.39	0.78	1.37	2.64	0.85	1.49
P$_2$O$_5$	0.47	0.72	0.22	0.25	0.32	0.82	1.90	0.35	0.34	0.36	0.85	1.25	1.25	1.22
LOI	2.89	11.15	2.77	3.50	3.49	3.62	2.15	3.12	7.96	3.94	2.7	2.77	3.49	4.4
Total	99.71	100.23	100.00	100.19	100.05	99.96	99.90	99.73	99.69	99.72	100.5	99.06	98.81	100.6
Li (ppm)	19.9	30.3	34.3	31.8	36.6	36.8	21.4	8.84	35.7	11.6	n.d	n.d	n.d	n.d
Be	1.47	1.46	1.67	2.11	2.06	1.99	1.53	1.60	1.31	0.88	3	4	3	3
Sc	29.5	19.1	20.3	18.6	19.2	15.1	15.1	35.7	14.6	35.7	9	6	6	6
V	245	122	92.1	78.4	109	92.4	90.9	306	131	256	232	176	164	157
Cr	148	19.5	40.4	28.3	34.3	12.5	9.43	155	138	44.3	30	50	50	50
Co	42.5	27.2	31.6	27.9	28.3	17.7	11.6	51.3	51.6	45.4	46	34	44	35

	Yilan blueschists													
Ni	94.4	24.6	44.3	38.2	43.4	11.6	9.12	64.7	133	32.6	90	70	90	60
Cu	58.3	12.4	13.6	11.7	12.4	12.6	11.8	85.5	104	72.1	10	< 10	10	20
Zn	108	125	128	116	105	137	95.3	111	79.3	88.3	240	240	230	210
Ga	21.6	16.5	19.3	20.9	21.5	20.4	14.4	20.8	11.2	22.0	39	41	40	36
Ge	1.52	1.44	1.70	1.64	1.74	1.58	1.37	1.46	1.37	1.33	1	1	1	1
Rb	9.86	71.1	105	104	106	89.9	52.2	3.95	11.5	10.9	16	35	12	16
Sr	219	592	15.9	61.7	45.8	58.6	111	371	186	494	691	368	970	1024
Y	40.5	32.6	17.6	17.4	22.2	32.2	29.1	33.8	20.9	34.5	39	38	35	33
Zr	218	149	190	219	225	265	253	192	103	200	428	515	500	475
Nb	24.4	38.4	39.4	43.1	45.4	68.6	68.0	22.0	32.4	28.0	26	33	30	29
Cs	0.19	2.02	2.33	2.48	2.86	2.70	1.42	0.025	3.51	0.049	< 0.5	0.8	0.7	1.4
Ba	164	235	374	581	514	308	188	56.8	39.1	175	227	465	110	190
La	21.8	23.2	21.0	51.8	27.4	50.2	29.2	18.8	22.3	22.6	39.8	40.5	37.7	35.7
Ce	47.0	51.8	47.4	100	54.7	105	67.5	42.3	44.8	47.9	101	101	95.8	90.9
Pr	6.55	7.38	4.74	10.5	5.62	11.4	9.27	5.35	5.14	5.78	14.7	15	13.8	12.9
Nd	29.7	34.0	18.5	36.4	22.7	45.5	46.8	26.1	22.7	27.1	75.8	70.8	68.6	65.8
Sm	7.59	8.33	3.77	5.65	4.92	8.96	11.5	6.63	4.86	6.76	21.7	20.7	19.3	18.5
Eu	2.36	2.64	1.23	1.47	1.51	2.94	3.28	2.09	1.60	2.23	8.13	7.16	6.77	6.49
Gd	7.87	7.91	3.93	5.05	5.11	8.90	10.4	6.68	4.62	6.68	23.9	20	19.6	18.4
Tb	1.28	1.16	0.63	0.68	0.82	1.30	1.46	1.08	0.70	1.09	2.8	2.8	2.5	2.2
Dy	7.62	6.41	3.87	3.90	4.84	7.04	7.26	6.40	3.98	6.45	12.1	11.6	10.8	9.9
Ho	1.49	1.17	0.77	0.77	0.93	1.26	1.21	1.26	0.76	1.27	1.6	1.5	1.4	1.3
Er	4.08	2.99	2.15	2.27	2.51	3.35	3.02	3.39	2.01	3.42	2.9	2.8	2.5	2.4
Tm	0.56	0.39	0.31	0.32	0.35	0.45	0.39	0.49	0.29	0.49	0.26	0.24	0.22	0.19
Yb	3.49	2.23	1.88	2.01	2.09	2.65	2.32	2.92	1.69	2.90	1.2	1.1	1	0.9
Lu	0.50	0.30	0.27	0.30	0.30	0.39	0.35	0.43	0.25	0.42	0.14	0.13	0.13	0.1

	Yilan blueschists													
Hf	5.13	3.71	4.58	5.20	5.42	6.17	5.94	4.68	2.49	4.71	11.4	12.4	11.2	10.8
Ta	1.50	1.95	2.53	2.70	2.86	3.69	3.24	1.35	1.83	1.66	1.7	2.1	2	1.9
Pb	1.78	5.83	1.12	1.18	1.19	1.22	1.32	2.17	4.14	2.53	< 5	< 5	< 5	< 5
Th	1.88	2.76	2.98	3.80	3.53	4.64	4.44	1.53	1.55	1.87	2.1	3	2.7	2.6
U	0.56	0.57	0.41	0.53	0.62	1.18	1.11	0.47	0.38	0.77	0.8	0.8	1.4	0.8
N (ppm)	46.9	95.0	122.6	106.9	117.2	117.7	67.9	37.4	50.29	21.20	24.3	39.7	17.3	37.5
δ^{15}N (‰)	-10.9	2.7	3.1	2.9	2.6	2.1	2.5	-7.8	3.2	0.9	-3.8	-10.1	-3.3	-3.3

Appendix F – Supplementary material for Chapter 3.3

F1 Supplementary tables

Table F 1. Nitrogen concentrations and δ^{15}N values of AOC samples from Hole 1256D and Hole 504B.

Sample ID	Depth (mbsf)	Lithology[a]	Alt[b]	N (ppm)	δ^{15}N (%)	Sample ID	Depth (mbsf)	Lithology	Alt	N (ppm)	δ^{15}N (%)
206-1256D-02R-01W 86-87	276	MB	BGR	11.3	-0.2	70-504B-36R-4W 0-2	548	PB	BGR	3.6	-2.4
206-1256D-6R-05W 99-100	300	MB	BGR	19.1	3.8	Duplicate	548	PB	BGR	3.6	-2.3
206-1256D-15R-01W 63-64	364	MB	BGR	18.3	-1.4				Ave.	3.6	-2.4
206-1256D-32R-02W 8-9	470	MB	BGR	9.3	-0.9	70-504B-52R-1W 67-72	679	PB	BGR	2.7	0.7
206-1256D-65R-03W 22-23	705	SF	BGR	9.8	0.3	70-504B-66R-2W 101-106	794	PB	BGR	3.0	-1.9
309-1256D-75R-01W 112-113	752	SF	BGR	10.5	-1.0	83-504B-71R-1W 32-38	836	PB	BGR	14.8	2.3
309-1256D-92R-01W 95-96	869	SF	BGR	10.3	1.0	83-504B-84R-1W 60-68	947	TZPB	BGR	6.2	0.4
309-1256D-100R-01W 133-134	910	MB	BGR	7.9	0.5	83-504B-94R-2W 10-16	1032	TZPB	BGR	3.8	-0.1
309-1256D-130R-02W 49-50	1065	SD	BGR	12.8	-2.8	Duplicate	1032	TZPB	BGR	4.0	0.1
Duplicate	1065	SD	BGR	11.3	-2.5				Ave.	3.9	0.0
			Ave.	12.1	-2.6	83-504B-104R-2W 42-48	1118	SD	BGR	7.4	-0.8
309-1256D-136R-01W 74-75	1094	SD	BGR	32.7	-3.5	83-504B-129R-2W 12-18	1272	SD	BGR	4.0	0.8
Duplicate	1094	SD	BGR	34.3	-3.8	111-504B-157R-1W 20-30	1473	SD	BGR	11.4	1.2
			Ave.	33.5	-3.7	111-504B-161R-1W 13-20	1504	SD	BGR	6.5	1.7
309-1256D-169R-03W 53-54	1247	SD	BGR	13.1	-1.2	140-504B-186R-1W 25-26	1632	SD	BGR	8.1	2.1
312-1256D-173R-1W 12-13	1262	SD	BGR	13.3	0.0	140-504B-193R-1W 20-21	1680	SD	BGR	12.0	3.3
312-1256D-181R-1W 63-65	1300	SD	BGR	18.9	-1.5	140-504B-199R-1W 126-127	1729	SD	BGR	6.5	3.1
312-1256D-189R-1W 70-71	1335	SD	BGR	12.2	-0.5	140-504B-210R-1W 80-81	1799	SD	BGR	5.4	2.4
312-1256D-196R-1W 35-36	1364	GSD	BGR	17.8	-2.2	140-504B-217R-1W 23-25	1847	SD	BGR	8.7	4.2
312-1256D-214R-2 101-102	1411	G	BGR	12.9	-0.4	140-504B-229R-1W 45-47	1953	SD	BGR	7.6	-1.3
312-1256D-215R-1W 52-54	1416	G	BGR	6.2	1.0	140-504B-236R-1W 75-76	1984	SD	BGR	6.4	2.6
312-1256D-217R-1W 69-70	1422	G	BGR	7.3	1.8	148-504B-240R-1W 13-15	2007	SD	BGR	6.8	2.4
312-1256D-218R-1W 21-22	1427	G	BGR	17.8	2.0	148-504B-242R-1W 5-6	2026	SD	BGR	8.7	3.5
312-1256D-220R-1W 19-20	1435	G	BGR	9.5	3.2	148-504B-246R-1W 37-38	2053	SD	BGR	9.4	4.7
312-1256D-222R-1W 81-82	1445	G	BGR	7.3	0.6	Duplicate	2053	SD	BGR	10.0	5.3
312-1256D-223R-1W 95-96	1450	G	BGR	8.6	1.6				Ave.	9.7	5.0
312-1256D-223R-3 24-25	1452	G	BGR	23.8	1.3	148-504B-247R-1W 73-74	2057	SD	BGR	7.1	0.7
312-1256D-230R-1W 5-6	1484	G	BGR	11.2	0.0	148-504B-248R-1W 31-32	2062	SD	BGR	5.9	3.3
312-1256D-232R-2W 42-43	1494	G	BGR	8.2	1.9						
312-1256D-234R-1 30-31	1503	SD	BGR	11.2	1.4						

a. Abbreviations of rock type: MB = massive basalt; SF = sheeted flow; PB = pillow basalt; TZPB = transition zone pillow basalt; SD = sheeted dike; GSD = granoblastic dike; G = gabbro.

b. Alteration type: BGR = background alteration.

F2 Supplementary information

F2.1 Estimation of N input flux of AOC into the Central America (CA) trench.

(1) Sediments:

(a) *The Guatemala-Northern Costa Rica trench*:

The sedimentary N input flux of $9.3^{\pm 0.5} \times 10^8$ mol·yr^{-1} into the 1100 km Guatemala-Northern Costa Rica trench has been estimated by Li and Bebout (2005) employing the sediments recovered from Hole 1039B offboard the Northern Costa Rica trench (Table 5).

(b) *The Central-Southern Costa Rica trench*:

The sedimentary N input flux into the 300 km Central-Southern Costa Rica trench was estimated based on the sediments recovered from Hole U1414A and U1381C offboard the Central-Southern Costa Rica trench. At Hole U1414A, recovered sediments include, from top to bottom, 145m-thick silty clay (average N concentration: $0.17^{\pm 0.05}$ wt.%), 164 m-thick nannofossil calcareous ooze (average N concentration: $0.03^{\pm 0.02}$ wt.%), and 66 m-thick calcareous and siliceous cemented siltstone and sandstone (average N concentration: $0.09^{\pm 0.06}$ wt.%) (Harris, 2013a). At Hole U1381C, recovered sediments include 56 m-thick silty clay (average N concentration: $0.13^{\pm 0.04}$ wt.%) and 48 m-thick nannofossil ooze (average N concentration: $0.08^{\pm 0.02}$ wt.%) (Harris, 2013b). Combining the sedimentary components recovered from these two holes gave an average sedimentary package into the Central-Southern Costa Rica trench: $100.5^{\pm 62}$ m-thick silty clay with average N concentration of $0.15^{\pm 0.03}$ wt.%, $106^{\pm 82}$ m-thick nannofossil ooze with average N concentration of $0.06^{\pm 0.01}$ wt.%, and $66^{\pm 33}$ m-thick calcareous and siliceous cemented siltstone and sandstone with an average N concentration of $0.09^{\pm 0.06}$ wt.%. The average dry densities for silty clay, nannofossil ooze and calcareous and siliceous cemented siltstone and sandstone are 0.44 g·cm^{-3}, 0.59 g·cm^{-3} and 1.19 g·cm^{-3}, respectively

(Harris, 2013a, b). Integrating these data, the sedimentary N input flux into the Central-Southern Costa Rica trench was estimated to be $3.1^{\pm 0.5} \times 10^{8}$ mol·yr^{-1} (Table 5).

Overall, we obtained a total sedimentary N input flux of $1.2^{\pm 0.1} \times 10^{9}$ mol·yr^{-1} into the entire CA trench.

(2) Basaltic section of AOC:

(a) The Guatemala-Northern Costa Rica trench with input from the EPR crust:

The 811 m-thick basalts (including 57 m-thick transition zone) recovered from Hole 1256D have been measured for bulk-rock N concentrations and δ^{15}N values by Bebout et al. (2018) and this study. To estimate the N input flux contributed by this basaltic section, we employed the method that has been widely used in previous studies for calculating elemental input fluxes (Li and Bebout, 2005; Li et al., 2019, 2020). In this method, the N concentration and δ^{15}N value of each sample are assumed to represent the mean value of the AOC section between itself and the next deeper sample, which were then integrated with dry density (Shipboard Scientific Party, 2003) to yield the N inventory in this section. Using the subducting rate (85 mm·yr^{-1}) and trench length (1100 km) of the CA margin (Li and Bebout, 2005), an N input flux of $1.8^{\pm 0.1} \times 10^{8}$ mol·yr^{-1} was yielded for the 811 m-thick basalts with a weighted mean δ^{15}N value of +0.9‰.

(b) The Central-Southern Costa Rica trench with input from the CNS crust:

The 780 m-thick basalts (including 209 m-thick transition zone) recovered from Hole 504B have been measured for bulk-rock N concentrations and δ^{15}N values by Busigny et al. (2019) and this study. With these data, the subducting rate of 85 mm·yr^{-1} and trench length of 300 km, the modeling using same method described above gave an N input flux of $3.2^{\pm 0.2} \times 10^{7}$ mol·yr^{-1} for the 780 m-thick basalts with a weighted mean δ^{15}N value of +2.6‰.

(3) Sheeted dike and gabbro section of AOC:

(a) The Guatemala-Northern Costa Rica trench with input of the EPR crust:

For the 446 m-thick sheeted-dike and gabbroic section recovered from Hole 1256D, we obtained an N input flux of $1.3^{\pm 0.1} \times 10^{8}$ mol·yr^{-1} with a weighted mean δ^{15}N value of -1.2‰ using the same method described above. Together with the N input flux contributed by the upper 811 m basaltic rocks, we obtained an N input flux of $3.1^{\pm 0.1} \times 10^{8}$ mol·yr^{-1} with a weighted mean δ^{15}N value of +0.1‰ into the Guatemala-Northern Costa Rica trench from the 1257 m-thick AOC section recovered from Hole 1256D.

For the residual AOC section, which are dominantly composed of gabbros, two scenarios are used to estimate the upper- and lower-end of the N input flux. In the upper-end scenario, the average N concentration ($11.3^{\pm 5.6}$ ppm) of the recovered gabbros of Hole 1256D was evenly applied to the residual 4743 m-thick gabbroic section by applying the maximum crust thickness of 6000 m (Fig. 35). This gave an N input flux of $1.0^{\pm 0.5} \times 10^{9}$ mol·yr^{-1} (other parameters involved in the calculation: dry density = 2.9 g·cm^{-3}; convergence rate = 0.085 m·yr^{-1}; trench length = 1100 km; Table 5). In the lower-end scenario, for the estimation of the residual 4243 m-thick gabbroic section (applying the minimum crust thickness of 5500 m), we assumed that N concentrations exponentially decrease from $11.3^{\pm 5.6}$ ppm (average N concentration of gabbro at Hole 1256D) at 1257 m to 1.5 ppm (the value of fresh MORB; Marty, 1995; Li et al., 2007) at 5500 m (Fig. 35). The N concentration along depth can be described by Equation (1):

$$C_{N(D)} = A \cdot e^{-b \cdot D} \tag{1}$$

where $C_{N(D)}$ is the N concentration in ppm at the depth of D (in m); A and b are constants, which were determined to be $20.5^{+14.0}_{-12.2}$ and $5.0^{+1.0}_{-2.0} \times 10^{-4}$, respectively, by fitting Equation (1) to

$11.3^{\pm5.6}$ ppm at 1257 m and 1.5 ppm at 5500 m. The N input flux (F_N) of the AOC from 1257 m to 5500 m can then be calculated by Equation (2):

$$F_N = \int_{1257}^{7000} C_{N(D)} \cdot \rho \cdot L \cdot R \cdot dD \quad (2)$$

where ρ is the average dry density of 2.9 g·cm^{-3} of the sheeted dike and gabbro from Hole 1256D (Expedition 309/312 Scientists, 2006); L is the CA trench length (1100 km); R is the convergence rate (0.085 m·yr^{-1}) of the CA margin. This modeling gave the lower-end N input flux of $3.7^{\pm1.1} \times 10^8$ mol·yr^{-1} for the lower 4243 m gabbroic section (Table 5).

(b) The Central-Southern Costa Rica trench with the input from the CNS crust:

With the bulk-rock N concentrations and δ^{15}N values of the 1056 m-thick sheeted dikes recovered from Hole 504B measured by this study, we obtained an N input flux of $2.4^{\pm0.2} \times 10^8$ mol·yr^{-1} with a weighted mean δ^{15}N value of +2.5‰ using the same method described above.

For the residual AOC section dominantly composed of gabbros, we used the same two-endmember scenarios applied to the Guatemala-Northern Costa Rica trench. In the upper-endmember scenario, by applying the average N concentration ($7.6^{\pm2.1}$ ppm) of the recovered sheeted dikes of Hole 504B evenly to the residual 9164 m-thick AOC section (applying the maximum crust thickness of 11000 m) (Fig. 35), we yielded the upper-end N input flux of $3.7^{\pm1.0} \times 10^8$ mol·yr^{-1} (other parameters used: dry density = 2.9 g·cm^{-3}; convergence rate = 0.085 m·yr^{-1}; trench length = 300 km). In the low-end scenario, we assume that N concentrations decrease exponentially from 7.6 ppm at 1836 m to 1.5 ppm at 8000 m (applying the minimum crust thickness of 8000 m) (Fig. 35). The N concentration along depth can be described by following Equation (1) with constants A and b of $12.4^{+4.4}_{-4.1}$ and $4.0^{+0.0}_{-1.0} \times 10^{-4}$, respectively. Following Equation (2), the calculation gave the lower-end N input flux of $1.2^{\pm0.2} \times 10^8$ mol·yr^{-1} for the lower 6164 m gabbroic section (Table 5).

Consequently, the total N input flux of from the subducting AOC (F_{AOC_N}) into the entire CA trench can be determined in the range from $1.1^{\pm0.1} \times 10^9$ mol·yr^{-1} to $2.0^{\pm0.5} \times 10^9$ mol·yr^{-1}. Together with the N input flux of $1.2^{\pm0.1} \times 10^9$ mol·yr^{-1} from sediments and $7.7^{\pm6.3} \times 10^8$ mol·yr^{-1} from material by tectonic erosion, a total N input flux of $3.1^{\pm0.6} \times 10^9$ mol·yr^{-1} to $4.0^{\pm0.8} \times 10^9$ mol·yr^{-1} was obtained for the entire subducting slab into the CA trench (Table 5).

F2.2. Estimation of the N input flux into the Izu-Bonin-Mariana (IBM) trench

(1) Sediments:

An N input flux of 4.4×10^8 mol·yr^{-1} into the 2450-km IBM trench has been determined by Mitchell et al. (2010) using the N concentrations of sediments analyzed by Sadofsky and Bebout (2004) and a convergence rate of 5 cm·yr^{-1}. In this study, we revised the N flux of the subducting sediments to $3.6^{\pm0.2} \times 10^8$ mol·yr^{-1} according to the updated convergence rate of 4.1 cm·yr^{-1} along the IBM trench (Plank, 2014) (Table 5).

(2) Basaltic section:

Employing a convergence rate of 16 cm·yr^{-1}, a unit N flux of 5.7×10^4 mol·yr^{-1}·km^{-1} into the Mariana trench has been determined by Li et al. (2007) using the 470-m thick upper volcanic section recovered from Site 801 and Site 1149. Here, we modified this unit flux to 1.5×10^4 mol·yr^{-1}·km^{-1} by employing an updated convergence rate of 4.1 cm·yr^{-1} along the IBM trench (Plank, 2014). Same to the method by Mitchell et al. (2010), this unit flux was then applied to the 2450-km IBM trench to obtain an N input flux of $3.6^{\pm0.2} \times 10^7$ mol·yr^{-1} for the 470-m thick upper volcanic section into the IBM trench. Assuming an 800-m thick volcanic section, an N input flux of $2.6^{\pm0.1} \times 10^7$ mol·yr^{-1} into the IBM trench carried by the residual 330-m thick lower volcanic section was obtained by applying the weighted average N concentration of 4.1 ppm from the upper 470-m thick volcanic section (Li et al., 2007), dry density (2.7 g·cm^{-3}) and convergence rate of 4.1 cm·yr^{-1} (Plank, 2014) (Table 5).

(3) Sheeted-dike and gabbroic section:

Assuming a typical crustal thickness of 5500 m for the subducting AOC along the IBM trench, the N input flux of the residual 4700-m thick intrusive section (i.e., sheeted dike and gabbro) was modeled using the same two-endmember scenarios described above. By applying the average N concentration of $7.0^{\pm 5.4}$ ppm evenly to the sheeted-dike and gabbroic sections, an upper-end F_{AOC_N} of $6.9^{\pm 5.3} \times 10^8$ mol·yr^{-1} was yielded for the IBM trench (Table 5). In the lower-endmember scenario, N concentrations exponentially decrease from $7.0^{\pm 5.4}$ ppm at 800 m to 1.5 ppm at 5500 m. The constants A and b in Equation (1) were subsequently fitted to be $9.1^{\pm 8.7}$ and $3.0^{+1.0}_{-2.5} \times 10^{-4}$, respectively. Following Equation (2), the lower-end N input flux of the 4700 m sheeted-dike and gabbroic section was determined to be $3.6^{\pm 2.2} \times 10^8$ mol·yr^{-1} (Table 5). Consequently, an F_{AOC_N} range of $4.2^{\pm 2.2} \times 10^8$ mol·yr^{-1} to $7.5^{\pm 5.3} \times 10^8$ mol·yr^{-1} was yielded for the IBM trench. Together with the revised F_{Sed_N} of $3.6^{\pm 0.2} \times 10^8$ mol·yr^{-1}, a total F_{Slab_N} of $7.8^{\pm 2.2} \times 10^8$ mol·yr^{-1} to $1.1^{\pm 0.5} \times 10^9$ mol·yr^{-1} was obtained for the IBM trench (Table 5).